Crystallization and Demixing: Morphological structure analysis in many-body systems

Alexander Böbel

München 2018

Crystallization and Demixing: Morphological structure analysis in many-body systems

Alexander Böbel

Dissertation
an der Fakultät für Physik
der Ludwig–Maximilians–Universität
München

vorgelegt von
Alexander Böbel
aus Ust-Kamenogorsk

München, den 29.10.2018

Erstgutachter: Prof. Dr. Dr. h.c. Gregor Morfill
Zweitgutachter: Prof. Dr. Hartmut Löwen
Tag der mündlichen Prüfung: 23.11.2018

Contents

List of Figures

List of Tables

Zusammenfassung

Räumliche Daten zu beschreiben und zu analysieren ist eine allgegenwärtige Problemstellung sowohl in der Wissenschaft als auch in der Industrie: So spielt beispielsweise in der Nahrungsmittelindustrie die räumliche Verteilung und die Größe von Poren in Backwaren eine Rolle für deren Geschmack. In den wissenschaftlichen Gebieten der Chemie, Biologie und der Physik liefern räumlich strukturierte Systeme Grundlage vieler Forschungsbereiche und sind in allen Größenordnungen aufzufinden: Auf großen Skalen z.B. bei der Struktur des Universums oder bei Erdbeobachtungsdaten. Auf kleinen Skalen bei der Struktur im inneren von Knochen oder im kleinsten bei der Verformung von Nukleonen zu nuklearer Pasta, die z.B. beim Abkühlen von Neutronensternen entstehen soll.

Insbesondere in der statistischen Physik neigen Vielteilchensysteme dazu, sich in komplexen Strukturen selbst anzuordnen. Diese komplexen räumlichen Strukturen lassen oft Rückschlüsse auf die zugrunde liegende Physik zu. Um einen quantitativen Zusammenhang zwischen der Physik von Vielteilchensystemen und ihrer Morphologie, also der Struktur die diese annehmen, herzustellen, ist eine quantitative Beschreibung dieser Struktur unerlässlich. In dieser Dissertation werden daher die räumlichen Strukturen bei Phasenübergängen (Kristallisation und Entmischung) in Vielteilchensystemen beschrieben und analysiert, um damit Rückschlüsse auf die zugrundeliegende Physik ziehen zu können.

Im Hinblick auf die Methoden, die zur Analyse der in dieser Dissertation untersuchten Systeme genutzt werden, gehen wir über konventionelle Methoden, die auf dem Leistungsspektrum oder auf zwei-Punkt Korrelationsfunktionen beruhen, hinaus. Das Ziel ist es die räumlichen Daten vollständig morphologisch zu charakterisieren. Zu diesem Zweck werden Metriken basierend auf der Familie der Minkowski Funktionale und Tensoren abgeleitet. Das sind additive morphologische Maße, die auch Korrelationen höherer Ordnung detektieren können. Sie sind nicht nur mit geometrischen Konzepten wie Volumen, Fläche und Krümmung verwandt, sondern stellen auch Aspekte der Topologie wie z.B. Verbundenheit dar.

Komplexe Plasmen (dielektrische Mikropartikel eingebracht in ein Plasma) stellen ein überaus geeignetes Modellsystem für die Untersuchung von Vielteilchenprozessen auf der kinetischen Ebene individueller Teilchen dar, da durch ihre optische Dünnheit die Bildgebung mehrerer hundert Lagen von Teilchen und die volle Auflöung der Teilchentrajektorien ermöglicht wird. Darüber hinaus können die Teilchenwechselwirkungen in Komplexen Plasmen auf vielfältige Art und Weise manipuliert werden. Da der Gasdruck meist sehr gering ist, sind die Teilchenbewegungen praktisch ungedämpft. Dies stellt eine direkte Analogie

zur Dynamik von Atomen in Flüssigkeiten oder Festkörpern dar.

Flüssig-fest Phasenübergänge in zwei-dimensionalen Systemen wurden lange Zeit als unmöglich erachtet, da das Mermin-Wagner Theorem langreichweitige Ordnung in zwei (oder weniger) Dimensionen verbietet. Kosterlitz und Thouless umgingen diese Problem jedoch, indem sie die langreichweitige Ordnung durch eine quasi-langreichweitige Ordnung ersetzten und einen topologischen Phasenübergang vorstellten, der durch Interaktionen von Kristalldefekten vonstatten geht. Diese allgemein akzeptierte KTHNY Theorie sagt eine anisotrope Zwischenphase vorher, die so genannte hexatische Phase. Im ersten Teil dieser Dissertation werden die Vorhersagen der KTHNY Theorie, anhand von Experimenten und einer Computer Simulation an einzelnen zwei-dimensionalen Komplexen Plasma Kristall-Lagen getestet. Anhand selbiger Experimente wird eine kürzlich neu entwickelte fraktale-Domänen-Struktur (FDS) Theorie getestet. Die FDS Theorie basiert auf der kinetischen Theorie des Schmelzens von Frenkel. Sie postuliert einen fraktalen Zusammenhang zwischen der eingeschlossenen Fläche von kristallinen Domänen und der Länge deren Begrenzung durch Linien aus Kristalldefekten. Es wird gezeigt, dass die KTHNY Theorie nicht auf flüssig-fest Phasenübergänge in zwei-dimensionalen Komplexen Plasmen angewandt werden kann. Die FDS Theorie wird hingegen validiert.

Desweiteren wird in dieser Dissertation die morphologische Beschreibung der Entmischungsdynamik von Flüssigkeiten behandelt. Der allgemein anerkannte Mechanismus, der für die Flüssigkeitsentmischung verantwortlich ist, ist die spinodale Dekomposition. Diese wird durch das quenchen (z.B. abkühlen) in den inneren Bereich der spinodalen Kurve im Phasendiagramm ausgelöst. Das charakteristische Merkmal der spinodalen Dekomposition ist der Beginn der Entmischung durch das exponentielle Wachstum von Dichtefluktuationen mit großen Wellenlängen. Die Vorhersagen der Molekularfeldtheorie der spinodalen Dekomposition sind jedoch nicht mit experimentellen Beobachtungen und Simulationen vereinbar. Diese Tatsache zeigt den Bedarf an Studien auf, die es vermögen einzelnen Teilchen zu folgen und bei denen man die Interaktionen zwischen den Teilchen beeinflussen kann. Deshalb werden in dieser Doktorarbeit sowohl Simulationen von Komplexen Plasmen (in drei-dimensionaler Euklidscher Geometrie) als auch Dichtefunktionaltheorie Berechnungen auf der zwei-dimensionalen Sphäre untersucht. In beiden Fällen können verschiedene Stadien in der Dynamik der Entmischung unterschieden werden. Das interessanteste Ergebnis ist die Entdeckung von universellem Verhalten im Entmischungsprozess. Universalität kann in dieser Arbeit im Hinblick auf verschiedene Interaktionspotentiale, bzw. im Hinblick auf verschiedene Mischungsverhältnisse und Sphärenradien gezeigt werden. Um diese universellen Eigenschaften zu entdecken, ist die Anwendung nicht-linearer Maße zwingend erforderlich, konventionelle auf dem Leistungsspektrum basierende Maße sind hierfür unzureichend. Dies zeigt, dass die nicht-linearen Eigenschaften des Entmischungsprozesses eine wichtige Rolle spielen und ist deshalb ein Fokus künftiger Arbeiten zu diesem Thema.

Abstract

The description and analysis of spatial data is an omnipresent task in both science and industry: In the food industry the distribution and size of pores in baked goods plays a role in their taste. In chemistry, biology and physics spatial data arises in manifold disciplines and on all length scales. On large scales one finds them in the structure of the universe or in earth surveillance data. On small scales one observes highly structured data in inner bones or on minute scales in the deformation of nucleons in nuclear pasta, which is theorized to form during the cooling of a neutron star.

In particular in statistical physics many-body-systems have a tendency to collectively form complex structures by self-organization. These complex structures often allow to draw conclusions about the underlying physics. In order to formulate a quantitative relation between the physics of many-body-systems and their morphology, i.e. the spatial structure they assume, a quantitative description of this structure is essential. In this dissertation the spatial structure of phase transitions (crystallization and demixing) in many-body-systems is quantitatively described and analyzed in order to achieve an improved understanding of the physics involved.

Regarding the analysis methods applied in this thesis we go beyond conventional linear measures based on two-point correlation functions or the power spectrum. Instead, the aim is a full nonlinear morphological characterization of the spatial data with measures derived from the family of Minkowski functionals and tensors. They are additive, morphological measures related to, not only geometrical concepts like volume, area and curvature, but also to topological aspects such as connectivity and are sensitive to higher order correlation.

Complex plasmas (dielectric microparticles immersed in a plasma) are a well suited model system for the particle resolved investigation of many-body processes. Their optical thinness allows for the optical imaging and tracking of the fully resolved trajectories of hundreds of particle layers. Additionally interactions can be tuned over a large range allowing to manipulate the shape and magnitude of the interparticle potential. Since the gas density is typically very low, the particle motion is practically undamped resulting in a direct analogy to the atomistic dynamics in solids or fluids.

Liquid-solid phase transition have been considered impossible for a long time since the Mermin-Wagner theorem forbids long-range order in two (or less) dimensions. However, Kosterlitz and Thouless (Nobel prize 2016) circumvented this by replacing the long-range order with a quasi-long-range order and by introducing a topological phase transition mediated by defects. The well accepted KTHNY theory predicts an intermediate anisotropic

phase, the hexatic phase. In the first part of this thesis the KTHNY theory is tested for experiments and a simulation of the crystallization of two-dimensional complex plasma sheets. For the same experiments the hypothesis and prediction of the recently developed fractal-domain-structure (FDS) theory is tested. The FDS theory is based on the Frenkel kinetic theory of melting. It postulates a fractal relationship between crystalline domains separated by boundaries of defect lines and predicts a scale-free relation between the system energy and the defect fraction. It is found that the KTHNY theory is not applicable to the liquid-solid phase transition in complex plasmas. The FDS theory however, is validated.

The other focus of this thesis is the morphological characterization of fluid-fluid demixing dynamics. The generally accepted mechanism for fluid-fluid demixing is spinodal decomposition. Spinodal decomposition is achieved by a quench deep inside the spinodal curve of the phase diagram. It is characterized by the exponential growth of long-wavelength density fluctuations. However the mean-field theory predictions of spinodal decomposition are not consistent with experiments and simulations. This shows the need for particle resolved studies with tunable interactions. To this end complex plasma simulations in flat three-dimensional space and density-functional theory calculations on the two-dimensional sphere are analyzed. In both cases different stages of demixing are identified with distinct domain growth rates during spinodal decomposition. Most importantly, universal demixing behavior is found for different interaction potentials, respectively for different mixture fractions and sphere sizes. These universal features could only be resolved by applying nonlinear measures, going beyond conventional methods based on the power spectral density. This suggests that nonlinear features in the demixing kinetics play an important role and that it is crucial to address this issue in future works.

Chapter 1

Introduction

Spatial structures can be found everywhere in nature. From minuscule structures in nuclear pasta [173, 50, 89] to the large-scale structure of the universe [83, 126] they occur on all length scales. Nuclear pasta is an exotic degenerate state of matter that is postulated to exist e.g. in the crust of neutron stars. At matter densities of about 10^{14} g/cm^3, nuclear attractive forces and electrostatic repulsion forces become similar in magnitude. The balance of these forces allows for the emergence of complex structures built from deformed nuclei. These structures resemble types of pasta and are called e.g. spaghetti phase, lasagna phase, bucatini phase or Swiss cheese phase. The galaxy distribution in the universe is not homogeneous and isotropic on large scales. Rather huge clusters of galaxies are gravitationally bound in a filament structure. These filaments, typically 160-260 million light years in length, make up the boundaries of large voids. Theory suggests that these large-scale structures originate from primordial inhomogeneities due to quantum fluctuations that are stretched to galactic scales during inflation. These primordial inhomogeneities can today be observed in the temperature fluctuations of the cosmic microwave background (CMB). Another example of the relevance in understanding complex filament structure can be found in the human body: the trabecular bone structure. When the trabecular structure is compromised by Osteoporosis the fracture risk is increased. In a healthy bone the trabecular structure is anisotropic, aligned in the direction of its mechanical load. By the detection of deviations of the trabecular structure form the anisotropy in the preferred direction, osteoporosis can be diagnosed and it is possible to predict the bone strength [39, 44, 168, 142, 127, 19]. In the field of material science the goal is to predict mechanical material properties by the knowledge of their microstructure and their material composition [164, 165]. When these predictions can be made it is possible to design materials that comply with specific requirements [130, 154]. Even in the food industry [5, 41, 49] spatial structure data is analyzed, since the distribution and size of pores or ingredients has an impact on the taste.

The physical principals governing these complex system are closely related to their spatial structure. In such cases a quantitative characterization of their structure is essential to facilitate an understanding of the underlying physics. This can be outlined by considering the prominent example of the characterization of the thermal fluctuations of the cosmic

microwave background (CMB). The application of morphological measures to the detection of non-Gaussian contributions to the CMB can provide insight about their primordial origin. These results may be used to validate or falsify theories about the primordial origin of the non-homogeneous, anisotropic large-scale structure of the universe.

In particular in the field of statistical physics, complex many-body systems can be found that exhibit emergent complex structure dependent on the microscopic nature of their interparticle interactions [72, 135, 136]. An illustrative example can be found in [105]: In confined colloidal suspensions competing interactions lead to a variety of complex structures into which the particles can self-assemble. Depending on the shape of the interaction potential the particles assume compact discs, fringed disks, rods or spherical clusters with superficial entrances. In this thesis the spatial structure of many body systems and its evolution during phase transitions, in particular crystallization and demixing, is characterized and analyzed quantitatively. This quantitative spatial description is performed in order to gain insight into the governing physical laws of the analyzed systems.

Traditionally the analysis of spatial structure is performed via the structure factor which is obtained by the power spectral density. This is analogous to the two-point density correlation function in position space. The structure factor and the power spectral density were useful in times when scattering experiments were the standard experimental setup to study microstructure. Today, however, the advanced capabilities of digital image processing open the door for more sophisticated structural measures to be applied in position space. An example for such methods are Minkowski functionals and their extension to tensor valued quantities, the Minkowski tensors. Their main advantage compared to power spectrum methods is their sensitivity to higher order correlations characterizing nonlinearities. The extension of traditional power spectrum or two-point correlation measures is, in contrast, computationally expensive [169]. The use of Minkowski functionals and tensors is compelling due to their straightforward interpretability. They are related to simple concepts as volume, area, curvature and connectedness, while being founded on a solid mathematical framework and provide a complete characterization of additive morphological properties of spatial data.

Scalar Minkowski functionals were fist described by Hermann Minkowski in 1903 [120] and have since been known in the field of integral geometry [175, 149]. Subsequently they became a prominent tool for morphological data analysis [114] and recently the family of scalar Minkowski functionals has been extended and generalized to tensor valued quantities known as Minkowski tensors [152]. Their attractiveness is not only based on the wide range of possible applications, but in particular on a strong completeness theorem by Alesker [6] and their sensitivity to higher order correlations [114]. Minkowski functionals are measures that can describe the shape and the topological connectedness of patterns. They have been applied to calculate e.g. the curvature energy of membranes [69], or as an order parameter in Turing patterns [113]. They also play a role in a density functional theory for fluids (as hard balls or ellipsoids) [144, 112]. In cosmology Minkowski functionals are a well known tool for the characterization of point distributions (find clusters, filaments, underlying point-processes) or for the search for non-Gaussian signatures in the cosmic microwave background (CMB) [148, 177, 121, 145, 122]. Minkowski tensors are sensitive to directional

properties such as the elongation of a body. They have been used in the context of cellular, granular or porous structures and have been applied to detect and classify crystal types [71, 82, 147, 151, 43, 90]. It was shown that they provide advantages [119] compared to the conventional bond-order metrics [157]: The choice of the neighborhood definition affects the value and trend of the bond-order parameters and they are not robust in the sense that they are not a continuous function of the particle coordinates. These issues can be avoided by the use of Minkowski tensor metrics.

With regard to the possibility of the experimental observation of fluid-solid phase transitions in two dimensions only few physical systems prove to be suitable candidates. Experiments have been performed with compressed Langmuir films of stearic acid [137], trapped atomic gases [62], the electron solid [59, 123] or monolayers of xenon on graphite [68]. Even fewer systems allow for the resolution and the tracing of trajectory dynamics of individual particles. This however, is possible in colloidal dispersions [128, 161, 180, 129] or in complex plasmas [91, 66, 132, 93]. Complex plasmas are the soft matter state of plasmas: Dielectric particles are immersed into a plasma where they get charged due to electron and ion fluxes. In complex plasmas the dynamic time scale, e.g. the inverse Einstein frequency, is in the range of 10 ms, the particle diameters are in the range of μm and their separation is in the range of 100 μm [52, 124]. These optically thin systems can easily be visualized and allow the three-dimensional imaging of hundreds of particle layers. Complex plasmas are a soft matter state complementary to colloidal dispersions. The dynamics in a complex plasma are virtually undamped (analogous to the dynamics of atoms in liquids), whereas the colloid dynamics in the solvent is highly damped [74].

Several theories [37, 140] have been proposed to explain fluid-solid phase transitions in planar systems. Before, they have been thought impossible for a long time because long-range order is forbidden in two dimensions by the Mermin-Wagner theorem [117]. The most prominent of the theories explaining two-dimensional phase transitions is the Nobel price-winning (2016) KTHNY theory [94, 63, 131, 179], named after Kosterlitz, Thouless, Halperin, Nelson and Young. It explains the melting of a crystal into a fluid via an intermediate hexatic phase. This topological phase transition is mediated by lattice defects: Initially bound paired dislocations dissociate in the hexatic phase mainly consisting of free dislocations. The free dislocations in turn dissociate into free disclinations in the liquid state. Disclinations are crystal defects violating rotational symmetry, dislocations violate translational symmetry. The well-known long-range order in the case of three dimensional solids is replaced with a quasi-long-range order consistent with the Mermin-Wagner theorem [117]. Recently a scale-free fractal-domain-structure theory [125, 92, 93] has been introduced, based on the kinetic theory of Frenkel [53]. It is built on the hypothesis that the solid phase consists of crystalline domains that are separated from neighboring crystalline domains via boundaries of defect lines. The relation between the length of boundary lines and the areas of crystalline domains is postulated to be fractal. In this thesis experiments of the crystallization process in two-dimensional complex plasma sheets are analyzed and compared with theory and computer simulation results.

Furthermore this thesis deals with the topic of binary fluid demixing: Computer simulations of demixing binary three-dimensional complex plasmas, and dynamic density-

functional (DDFT) calculations of demixing binary fluids bound to the surface of a sphere are analyzed. When two immiscible fluids are mixed they start to dynamically separate until two phases coexist in a thermodynamically stable equilibrium. This phenomenon is well known in the case of the everyday example of oil in water [17], but is observed in a variety of fields among which there are molecular fluids [146], granular media [143], passive [64] and active colloidal suspensions [31], mixtures of active and passive particles [158], active particle with different mobilities [111] and active particles in external fields [96]. It was shown that particles with different diffusivity demix [174] and only recently experiments in complex plasmas showed demixing for particles with size disparities of only 3 % [88]. This suggests a mechanism beyond mere spinodal decomposition which requires size disparities of at least 30 % [75]. Spinodal decomposition is mainly understood in the context of mean field theory approaches. However, these approaches have drawbacks [74] and it was shown that their predictions are not validated in experiments [22, 110]. This suggests the need of particle resolved studies: Such studies may facilitate the better understanding of spinodal decomposition which so far has mainly been studied in the context of mean field theory and has provided unsatisfactory agreement with experiments.

Complex plasmas are a well suited model system for the particle resolved study of phase separation dynamics. The fluid-fluid phase separation dynamics crucially depend on competing interactions between constituent particles [65]. Complex plasma systems are conveniently tunable: The particle interaction potential can be adjusted and the interaction range varied on scales significantly larger than the interparticle separation [52, 124, 87]. In the complementary field of colloidal dispersions interaction ranges are typically short [74]. Again the possibility to investigate individual particle kinetics plays a crucial role in understanding the origin of collective behavior based on its constituents.

The calculations on spherical geometries are based on a dynamical density-functional theory [12, 109] applied to the Gaussian core model [159]. This approach provides a simple model for polymers in solution and is chosen due to its simplicity and its generic demixing properties. The density-functional theory is based on the assumption that the free energy of a fluid is a unique functional of its equilibrium density and is independent of external fields. For a specific interaction potential the inhomogeneous fluid density and all n-point correlation functions can be obtained by functional differentiation of the free energy functional. The Gaussian core model is a soft particle interaction potential that consists of a pairwise sum of additive Gaussian components for which terms in a series expansion of the free energy can be calculated analytically.

In spatially confined systems the dynamics of demixing are less well understood compared to boundaryless systems. Possible confining methods are by external fields or obstacles [102, 103]. However, spatial confinement can also be imposed by the intrinsic geometry of space itself [26]. Recent studies of phase transitions on spherical geometries have shown the richness of physical effects due to their confinement on curved surfaces. An icosahedrically symmetric order parameter explained the long-range order a colloidal suspension crystal on a spherical surface [60]. The distribution of defects could be predicted by the projection of inhomogeneous crystals onto homogeneous crystals on curved surfaces [156]. Emergent structures in reaction-diffusion systems on spherical surfaces were investigated

in [95].

This thesis is structured as follows: Section 2 introduces the theoretical aspects of two-dimensional liquid-solid phase transitions. In section 3 theoretical considerations on fluid-fluid phase separation are presented. A brief introduction to the systems, i.e. complex plasmas and dynamic density functional theory calculations, upon which the analysis methods explained in section 5 are performed is given in section 4. The publications enclosed at the end of this thesis are summarized and complementary information is presented in section 6, 7 and 8. Section 9 gives a short summary and outlook.

Chapter 2

Liquid-solid phase transition in two dimensions

The melting transition in two dimensions is a highly interesting topic since it is completely different to the usual three-dimensional case. A theorem by Mermin and Wagner [117] forbids any translational long-range order in two (or less) dimensions as it is necessary in the case of a three-dimensional solid. The Mermin-Wagner theorem states that, in systems with sufficiently short-range interactions and in dimensions smaller or equal to two, no continuous symmetries can be spontaneously broken at finite temperatures. This means that no long-range order is possible in these systems since there is little energy cost to create long-range fluctuations. These long-range fluctuations are thermodynamically favoured, since they increase the system entropy. The Goldstone theorem [56] states that in systems with spontaneous symmetry breaking massless Goldstone modes are bound to exist. In two, or less, dimensions these massless Goldstone modes cannot exist since they would imply a divergent correlation function. Thus, no spontaneous symmetry breaking is possible, and therefore also no phase transition from disorder to long-range order.

2.1 KTHNY theory

The most prominent theory that is able to circumvent the restrictions of Mermin and Wagner is the KTHNY theory [94, 63, 131, 179, 160], named after Kosterlitz, Thouless, Halperin, Nelson and Young. They describe a melting transition driven by topological defects called vortices in the XY model: A phase transition is predicted via the unbinding of vortex pairs at an interaction strength dependent temperature. The XY model is a lattice model in statistical physics. It assigns a two-dimensional (therefore XY) spin vector to any lattice site on a lattice of arbitrary dimension. It is the $n = 2$ case of the general n-vector model. $n = 1$ is the well known Ising model, $n = 3$ the Heisenberg model.

In the two-dimensional solid the KTHNY theory description of the melting transition is more complicated as in the XY model since the two-dimensional particle system exhibits two types of topological defects. A dislocation is an extra row of particles between two

regular lattice rows, breaking the translational symmetry of the crystal. Dislocations are described by a Burgers vector: It is the difference between start and endpoint of a rectangular path in the ideal crystal compared to the path enclosing a dislocation. A dislocation is illustrated in Fig. 2.1. The other type of lattice defect is the disclination. It is violating the rotational symmetry of the crystal: When enclosing it by a path in the lattice it leads to a mismatch of orientation. Another possibility of describing a disclination is via the Voronoi tessellation of its lattice points. The Voronoi tessellation is the generalization of the Wigner-Seitz cell. It is the partition of space into convex polytopes, the Voronoi cells, with the lattice points as center points, that each contain the set of points that is closer to its center than to any other lattice point. In this description the next-neighbors are well defined as the lattice points of Voronoi cells sharing a boundary. A disclination then has another number of next neighbors than an ideal crystal cell. A dislocation can be described a pair of bound disclinations. Free disclinations are illustrated in Fig. 2.2. A pair of bound disclinations resulting in a dislocation is presented in Fig. 2.3.

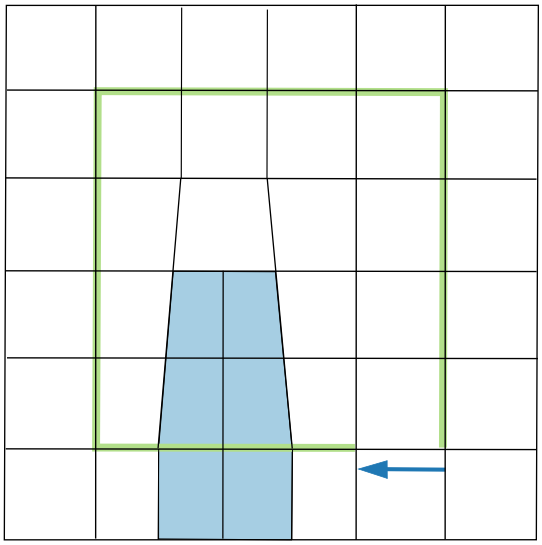

Figure 2.1: Illustration of a dislocation in a square lattice. The Burgers vector is shown. It is the difference of the start and endpoint of a regular path around the dislocation.

The two-dimensional solid is described by a quasi-long range order defined by an algebraic decay of the translational density correlation function, and a long range order in the orientation of next-neighbor bonds. The first step in the melting transition at temperature T_m is the destruction of the translational order by free dislocations: The dislocation unbinding transition is similar to the vortex-unbinding transition in the XY model. However, even after the dislocation unbinding transition the liquid phase is not reached yet since it is not isotropic. This anisotropic liquid is the hexatic phase, characterized by a quasi-long-range orientational order, a power-law decay of the orientational correlation function. Here

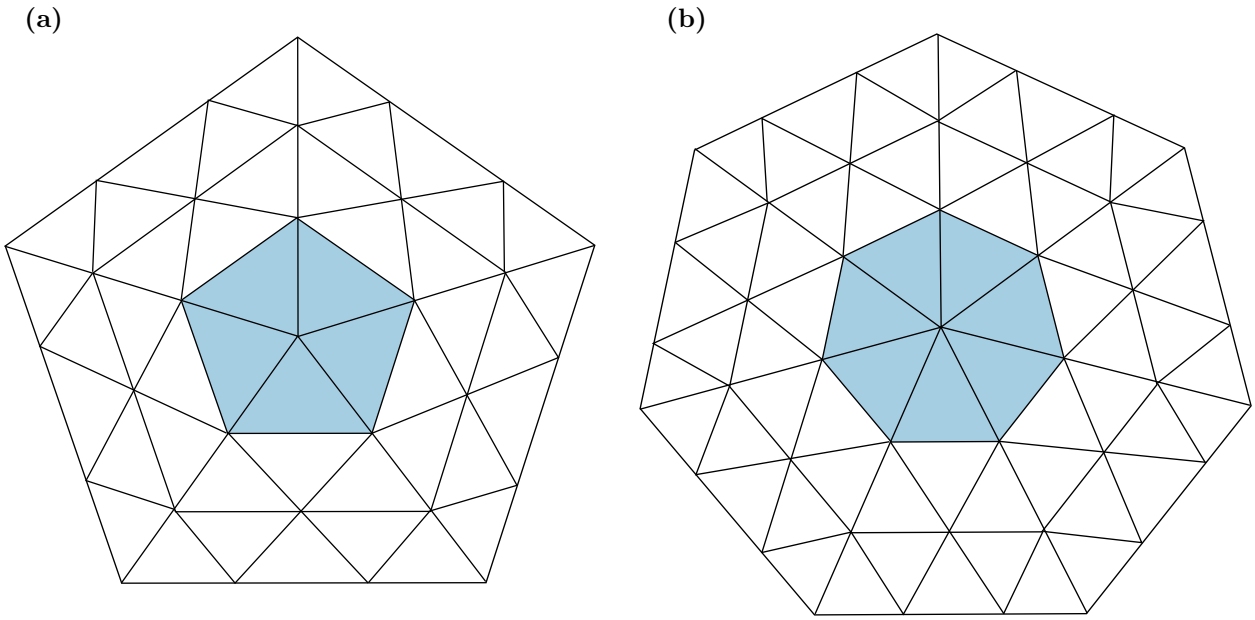

Figure 2.2: Illustration of disclinations in a hexagonal lattice. In panel (a) the center site has only five neighbors instead of six. In panel (b) The center cite has seven neighbors instead of six. For a path around the disclination the orientation of triangular cells changes by $+\pi/3$ in panel (a) and by $-\pi/3$ in panel (b).

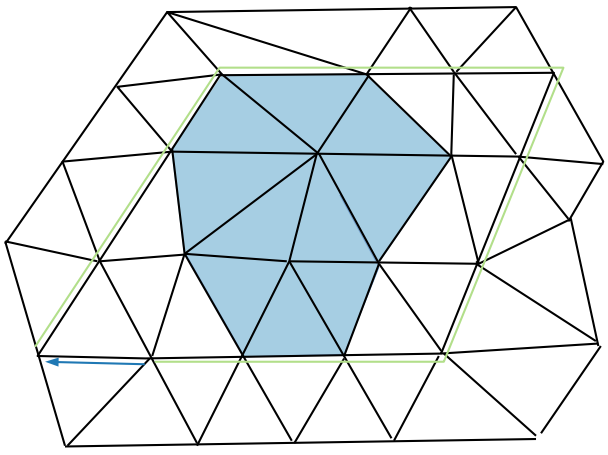

Figure 2.3: Illustration of a dislocation made up by paired 5/7 disclinations. The Burgers vector is shown. It is the difference of the start and endpoint of a regular path around the dislocation.

the disclinations are bound in pairs. At a higher temperature $T_i > T_m$ the disclinations continuously unbind and the isotropic liquid state is reached. Table 2.1 gives a summary of the stages in the liquid-solid transition according to the KTHNY theory. Mathematical

definitions of the pair- and bond correlation functions and expressions for the functional shape of their long-range long range decay in the liquid, hexatic and solid phase can be found in section 5.

Table 2.1: Stages in the liquid-solid transition according to the KTHNY theory.

	solid	hexatic	liquid
temperature	$T < T_m$	$T_m < T < T_i$	$T_i < T$
dislocations	bound pairs	free	free
disclinations	bound quartets	bound pairs	free
translational order range	quasi-long	short	short
rotational order range	long	quasi-long	short

2.2 Frenkel kinetic theory of melting

Jakow Iljitsch Frenkel described the liquid-solid phase transition on a kinetic level in his book [53] written in 1942. It was, however, published four years later due to "mailing difficulties connected to the war".

A solid is defined by a regular lattice representing fixed equilibrium particle positions. The particles oscillate around their equilibrium positions due to thermal motion. When the kinetic energy of a particle exceeds the activation energy U_D set by the potential of neighboring particles is can transition to an interstitial site, leaving a vacancy on its original position. Thus, the degree of dissociation is dependent on the temperature T. Vacancies and interstitial particles are subject to diffusion in the lattice.

Consider the crystal consisting of N_D vacancies and N_I interstitial particles with N particles in total. Then the particles and vacancies can be distributed at $N + N_\mathrm{D} - N_\mathrm{I}$ sites. The number of possibilities to distribute N_D holes on theses sites is:

$$P_\mathrm{D} = \frac{(N + N_\mathrm{D} - N_\mathrm{I})!}{N_\mathrm{D}!(N - N_\mathrm{I})!} \approx \frac{N!}{N_\mathrm{D}!(N - N_\mathrm{D})!} \tag{2.1}$$

for $N_\mathrm{D} \ll N$. The entropy then is $S = k\ln(P_\mathrm{D})$, where k is the Boltzmann constant. The free energy $F = U - TS$ generated by the holes then is

$$F_\mathrm{D} = N_\mathrm{D}U_\mathrm{D} - kT\big[\ln(N!) - \ln(N_\mathrm{D}!) - \ln((N - N_\mathrm{D})!)\big]. \tag{2.2}$$

Using the approximation $\partial/\partial x \ln(x!) = \partial/\partial x \sum_{i=1}^{x} \ln(i) \approx \partial/\partial x \int_1^x \ln(y)\,\mathrm{d}y = \ln(x)$ one can find that F_D assumes its minimum at:

$$N_\mathrm{D} = N \exp\left(\frac{-U_\mathrm{D}}{kT}\right) \tag{2.3}$$

for $N_\mathrm{D} \ll N$. This relation, called the Arrhenius law, was observed in two-dimensional complex plasma experiments [132]. The Arrhenius law was first used to describe chemical kinetics of monomolecular reactions [167], it states that the logarithm of the reaction rate (in this case the defect fraction) is proportional to the inverse of the temperature.

Frenkel argues that the structure of a liquid is similar to a solid since the volume increase at the melting transition is only about 10 %. The thermal fluctuations of the particle positions around their equilibrium points should be the same, however in the liquid state the average duration a particle stays at a specific equilibrium position is much shorter compared to the solid state, since cohesive forces are smaller for larger particle separations. The long-range order in the crystalline state is lost in the liquid state due to the high mobility of particles.

In the case of liquid crystals Frenkel described their melting transition via the formation of "swarms" of particles that retain their orientational order within their group, while the translational order and the orientational order across particle groups is lost. This however is only an intermediate state. By continued heating the larger ordered domains become ever smaller. Thus, the average number of particles $\langle N_\mathrm{D} \rangle$ within an ordered domain is temperature dependent.

Consider a system of N particles divided in $z = N/\langle N_\mathrm{D} \rangle$ ordered domains. The internal energy of the system is increased by an amount E compared to the ideal case because neighboring domains are not oriented in the same direction. E depends on the surface tension σ and the domain volume V:

$$E = \sigma V^{2/3} z^{1/3}. \tag{2.4}$$

The number of possibilities to distribute N particles on z domains becomes

$$P_\mathrm{D} = \frac{N!}{[(N/z)!]^z} \approx z^N. \tag{2.5}$$

using Stirlings formula $\ln(N!) \approx N\ln(N) - N$ for large N. This leads to an increase of entropy $S_\mathrm{D} = k \ln(P_\mathrm{D})$ by $S_\mathrm{D} = kN \ln(z)$. The increase in Helmholtz free energy F_D becomes:

$$F_\mathrm{D} = E - TS = \sigma V^{2/3} z^{1/3} - TkN\log(z), \tag{2.6}$$

which assumes its minimal value at

$$z = \frac{3NkT}{\sigma V^{2/3}}. \tag{2.7}$$

Then the average number of particles within an ordered domain is given by:

$$\langle N_\mathrm{D} \rangle = \frac{N}{V} \left(\frac{\sigma V}{3NkT} \right)^3 \tag{2.8}$$

This derivation is the basis for the fractal-domain-structure theory explained in the next section.

2.3 Fractal-domain-structure theory

In experiments with two-dimensional complex plasma sheets it was discovered that the liquid-solid phase transition in those systems might not be of KTHNY type. Experiments showed inconsistencies between the predicted and observed long-range decay functional shape of the pair correlation function [93]. Since the experiments were also not consistent with the Arrhenius law (eq. (2.3)) a new out-of-equilibrium theory had to be developed. The fractal-domain-structure (FDS) theory was first described in [125, 92]. It is rederived in this thesis. Based on the kinetic theory of Frenkel [53], described in section 2.2 above, it describes a scale-free liquid-solid phase transition of a N-particle system in two dimensions when the temperature T is varied.

For any system energy $E = k_B T$, the N-particle system is divided into

$$z = \frac{N}{\langle N_d \rangle} \tag{2.9}$$

homogeneous domains. On average each domain is comprised of $\langle N_d \rangle$ particles. These domains are separated by defect lines as their boundaries. Defects are e.g. pairs of 5/7 dislocations (represented by pentagons/septagons in the Voronoi tessellation). No correlation of structural order is required at the inter-domain level.

Given the mean interparticle separation Δ the mean domain radius $\langle r \rangle$ is determined by the domain area. The domain area is the sum of all unit cell areas $\pi \langle r \rangle^2 = \pi (\Delta/2)^2 (N/z)$ within the domain. Then the domain radius is given by

$$\langle r \rangle = \frac{1}{2} \left(\frac{N}{z} \right)^{1/2} \Delta. \tag{2.10}$$

The sole contribution to the interface energy is assumed to be given by the line energy $\langle E \rangle = 2\pi \langle r \rangle z\sigma$, where σ is the line tension. Substituting $\langle r \rangle$ gives

$$\langle E \rangle = \pi \Delta (Nz)^{1/2} \sigma. \tag{2.11}$$

The system entropy increases with the number of domains z since the number of distinct realizations P of the particle arrangement is a measure for the degree of disorder of the system. P can be obtained by calculating the number of possibilities to distribute N particles on z domains, each containing $\langle N_d \rangle$ particles. In a first step one can choose $\langle N_d \rangle$ particles from an ensemble of N particles. Then, $\langle N_d \rangle$ particles can be chosen from the remaining $N - \langle N_d \rangle$ particles with the number of possibilities p, where

$$p = \binom{N - \langle N_d \rangle}{\langle N_d \rangle}. \tag{2.12}$$

This process, repeated the domains are fully occupied, yields P by multiplication of all independent possibilities:

$$P = \prod_{i=0}^{z-1} \binom{N - i \langle N_d \rangle}{\langle N_d \rangle} = \frac{N!}{(\langle N_d \rangle !)^z} \cdot \frac{1}{(N - z \langle N_d \rangle)!} = \frac{N!}{[(N/z)!]^z}. \tag{2.13}$$

With Stirlings formula for sufficiently large N and N/z this can be approximated by

$$P \simeq z^N. \tag{2.14}$$

Then the entropy is $S = k \ln(P)$ and the resulting average Helmholtz free energy is

$$\begin{aligned} \langle F \rangle &= \langle E \rangle - TS \\ &= \pi\Delta \left(Nz\right)^{1/2} \sigma - NkT \ln(z). \end{aligned} \tag{2.15}$$

Assuming homogeneity of pressure and temperature throughout the system and that the value of the free energy is independent of the realization of domain distribution, the minimization of the free energy $\partial \langle F \rangle / \partial z = 0$ provides a relation between the number of domains and the system temperature:

$$z = \left(\frac{2kT}{\pi\Delta\sigma}\right)^2 N. \tag{2.16}$$

The scaling nature of the domain structure is introduced as the hypothesis of the FDS theory:

$$\langle N_d \rangle \Delta^2 B = \left[\Delta \langle N_s \rangle\right]^{1+\alpha}. \tag{2.17}$$

B and α are constants depending on the shape of the domains. Values for regular shapes are given in table 2.2. For fractal domains $0 < \alpha < 1$ is expected. An illustration of the fractal domain structure for two experiments in two-dimensional complex plasmas is given in Fig. 2.4.

Table 2.2: Values of the shape constants B and α in the FDS theory hypothesis $\langle N_d \rangle \Delta^2 B = \left[\Delta \langle N_s \rangle\right]^{1+\alpha}$ (eq. (2.17)) for regular domains.

domain shape	B	α
circular	π^2	1
compact ($\langle N_d \rangle \to \langle N_s \rangle$)	$1/\Delta$	0
narrow	$2/\Delta$	0

Substituting the scaling relation of the domain structure Eq. (2.17) in Eq. (2.16), yields a power-law for the relation between the density of the total number of particles in all domain boundaries $N_T \equiv z\langle N_s \rangle$ and the system temperature:

$$\frac{N_T}{N} = B^{1/(1+\alpha)} \Delta^{(1-\alpha)/(1+\alpha)} \left(\frac{2kT}{\pi\Delta\sigma}\right)^{(2\alpha)/(1+\alpha)} \tag{2.18}$$

The hypothesis of the FDS theory as formulated in Eq. (2.17) and the implication Eq. (2.18) are tested in section 6 for experiments of the crystallization of two-dimensional complex plasma sheets.

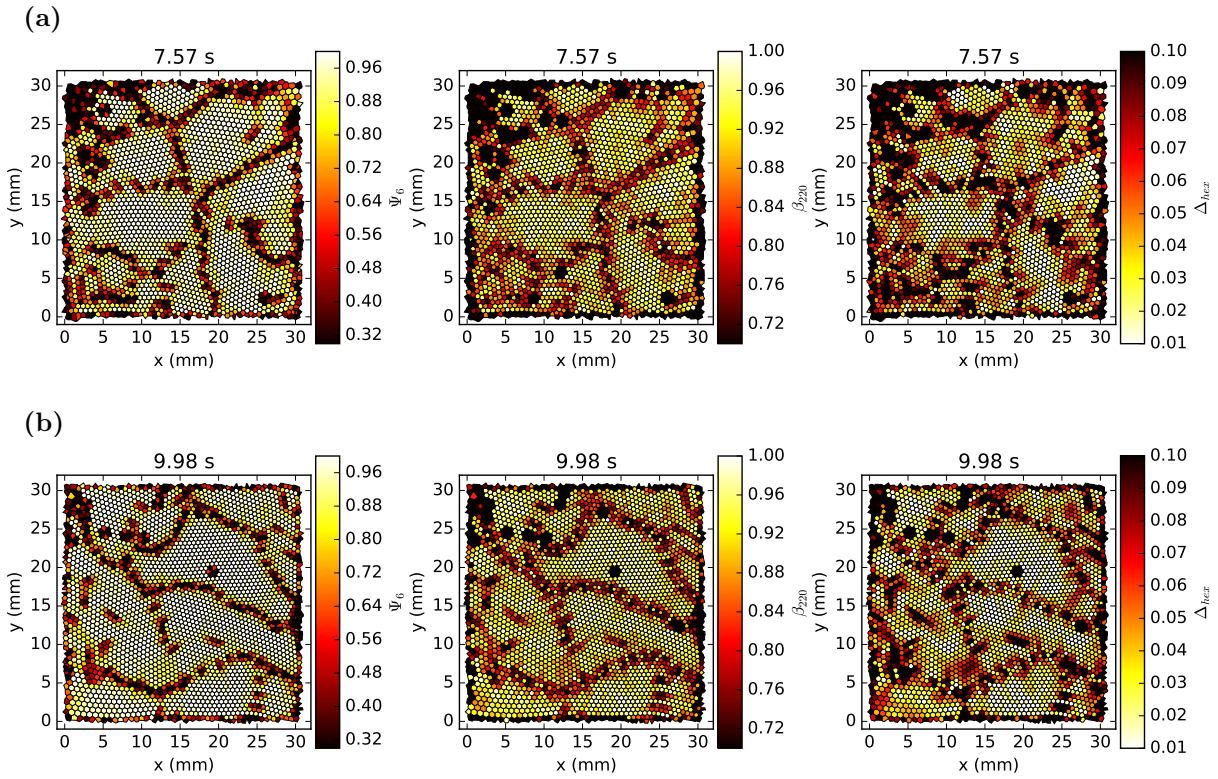

Figure 2.4: Illustration of the fractal domain structure for two experiments in two-dimensional complex plasmas. (a) presents data from experiment III, (b) from experiment IX of [24]. Light yellow colors indicate states of high crystallinity, whereas dark red colors indicate defects. Columns correspond to different morphological measures as explained in chapter 5.

Chapter 3

Fluid demixing

3.1 Phase coexistence

The elementary thermodynamic principles of phase separation are known since Gibbs presented his extensive work in 1878 [55]. They are also explained in e.g. [98].

The state of a homogeneous body in equilibrium is completely described by the two thermodynamic quantities energy E and volume V. However, the body is not necessarily homogeneous for any combination of E and V. There is a possibility that it decomposes into two distinct, homogeneous parts in different states. This kind of equilibrium states are called phases. The conditions for the equilibrium of two phases is that their temperatures T_1 and T_2, their pressures P_1 and P_2, and their chemical potentials μ_1 and μ_2 match:

$$\begin{aligned} T_1 &= T_2 \\ P_1 &= P_2 \\ \mu_1(P,T) &= \mu_2(P,T) \end{aligned} \tag{3.1}$$

For systems of several particle species the condition is the constancy of the chemical potentials

$$\mu_i = \left(\frac{\partial G}{\partial N_i}\right)_{P,T} \tag{3.2}$$

for every component of the mixture. The chemical potentials μ_i are the derivatives of the Gibbs free energy G with respect to the particle numbers N_i of a component under constant pressure and temperature. The differential of G depends also on the entropy S:

$$\mathrm{d}G = -S\mathrm{d}T + V\mathrm{d}P + \sum_i \mu_i \mathrm{d}N_i. \tag{3.3}$$

3.2 Mean field theory

The state of a binary mixture can be described by three variables. P, T and the concentration x. A state of two phases in equilibrium can be represented by a surface in

the P-T-x coordinate system. An example of a phase diagram (in the plane of constant P) for a typical binary system that can exist in a mixed or a demixed state is shown in Fig. 3.1. The curve of coexistence is the binodal curve, its maximum is the critical point. Inside the curve a heterogeneous demixed state is possible, whereas outside the curve the mixture is homogeneous. Binary mixtures belong to the Ising universality class [138] along with liquid-vapor transitions, coulombic systems, micellar systems and uniaxial magnetic systems. This means that the considerations for binary systems explained in this chapter also apply to one component systems of the Ising class.

A mean field theory for the characterization of the equilibrium of a binary mixture of species 1 and 2 can be formulated for the order parameter $\Psi = \rho_1 - \rho_2$, where ρ_i is the local density of species i [134]. The control parameter can be the temperature T or the total density ρ. There are two distinct states of this system: The homogeneous state of a single mixed phase can be described by the order parameter Ψ_1, the heterogeneous demixed state with rich phases of species 1 or species 2 particles can be described by order parameters Ψ_1 and Ψ_2 respectively. During demixing the order parameter is conserved by the lever rule

$$\Psi_0 = x_1\Psi_1 + (1 - x_1)\Psi_2, \tag{3.4}$$

where x_1 is the fraction of the phase rich with particles of species 1. In the mean field approach surface and inhomogeneity effects are neglected. Then the Helmholtz free energy in the demixed state F_d is given by:

$$F_d = x_1 F(\Psi_1) + (1 - x_1)F(\Psi_2) \tag{3.5}$$

The binodal curve (solid line in Fig. 3.1) determines the heterogeneous phase of coexistence and can be obtained by the minimization of F_d. The conservation of the order parameter can be imposed by the Lagrange multiplier λ by minimizing $\widetilde{F_d} = F_d + \lambda\,[x_1\Psi_1 + (1 - x_1)\Psi_2 - \Psi_0]$. The minimization leads to the Maxwell double-tangent construction [98]:

$$F'|_{\Psi=\Psi_{1,2}} = \frac{F(\Psi_2) - F(\Psi_1)}{\Psi_2 - \Psi_1} = -\lambda. \tag{3.6}$$

F' denotes the derivative of F with respect to Ψ.

The unstable region is bound by the spinodal line (dashed line in Fig. 3.1) defined by the condition $\partial^2 F/\partial\Psi^2 < 0$.

There are two mechanisms for a fluid-fluid phase separation. The first possibility is a quench to a state point inside the coexistence regime in the vicinity of the binodal curve. Then the phase separation mechanism is the nucleation of droplets of one phase in the second phase [76, 134]. The second mechanism can occur if the quench happens deeper inside the binodal curve, in the spinodal region of the phase diagram. Here it is generally expected that the phase separation happens due to the exponential growth of long-wavelength density fluctuations [76, 134]. This mechanism is called spinodal decomposition. Both mechanisms are believed to lead to domain growth stages that are self-similar in time [134, 30]. This means that the domain morphology is preserved in time and that there exists a specific characteristic length scale whose time evolution is governed by a

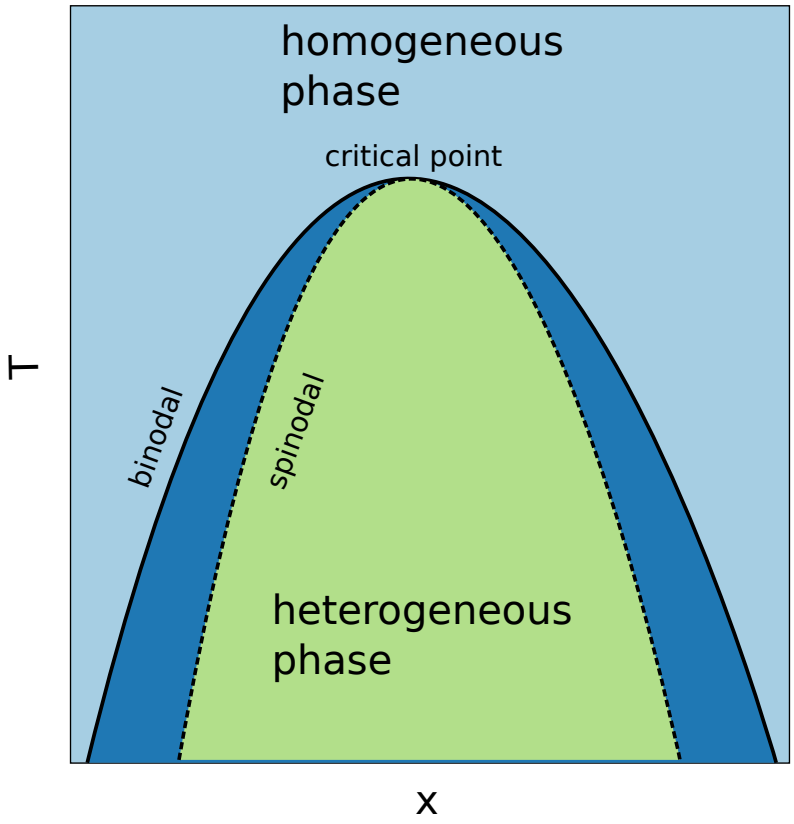

Figure 3.1: Phase diagram of a binary system. Temperature T vs. concentration x.

power-law growth $L(t) \propto t^{\alpha}$. The exponents α may vary between distinct stages of the demixing dynamics. This scaling hypothesis has only been proven in some simple models, as e.g. in the one-dimensional Glauber model [28]. However, it is generally accepted since it is evidenced in many cases [134].

Three consecutive stages can be distinguished during the spinodal decomposition: Initially the density fluctuations are small, such that it is possible to model them linearly [32, 33, 42, 76, 134, 48, 4]. In the second stage the density fluctuations grow large but no sharp interfaces between phases exist yet [42]. In the late stage the phases are separated by sharp interfaces [8].

3.3 Cahn-Hillard theory

The accepted mean field theory describing the dynamics of spinodal decomposition is the Cahn-Hillard model [32, 33]. It is formulated for the order parameter $\Psi(\mathbf{r}, t)$ in the

Ginzburg-Landau free energy [134]

$$F[\Psi] = \int \mathrm{d}\mathbf{r} \left[F(\Psi) + \frac{1}{2} K (\nabla \Psi)^2 \right], \tag{3.7}$$

with the coefficient $K > 0$ as a measure of surface tension. The chemical potential μ can be obtained by the functional derivative

$$\mu(\mathbf{r}, t) = \frac{\delta F[\Psi]}{\delta \Psi} = F'(\Psi) - K \nabla^2 \Psi. \tag{3.8}$$

F' denotes the derivative of F with respect to Ψ. The gradient term in the free energy Eq. (3.7) takes large scale correlations into account. The use of the gradient term is only valid for large values of the correlation length ξ and Eq. (3.7) is only exact near the critical point where the correlation length diverges. The diffusive flux $\mathbf{J}$ is given by Fick's law:

$$\mathbf{J} = -\frac{D}{kT} \nabla \mu \tag{3.9}$$

Adding the advection term $\mathbf{v} \cdot \nabla \Psi$ for the hydrodynamic flow, the continuity equation (Cahn-Hillard equation [134, 30]) obtained from Eq. (3.7) reads

$$\frac{\partial \Psi}{\partial t} + \mathbf{v} \cdot \nabla \Psi = \frac{D}{kT} \nabla^2 \mu. \tag{3.10}$$

After simplification of the Navier-Stokes equation for incompressible fluids with pressure p, viscosity η, constant density ρ, and after adding the term $\Psi \nabla \mu$ (accounting for the free energy change due to chemical potential gradients resulting from phase interfaces) the velocity field $\mathbf{v}$ obeys

$$\rho \left(\frac{\partial \mathbf{v}}{\partial t} + (\mathbf{v} \cdot \nabla) \mathbf{v} \right) = \eta \nabla^2 \mathbf{v} - \nabla p - \Psi \nabla \mu. \tag{3.11}$$

The continuity equation for the density is

$$\frac{\partial \rho}{\partial t} + \nabla \cdot (\rho \mathbf{v}) = 0. \tag{3.12}$$

The Cahn-Hillard equation 3.10 can be used to explain the different stages of the spinodal decomposition dynamics:

(1) Linear stage: Introducing $\delta\Psi = \Psi - \Psi_0$ and linearizing the chemical potential $\mu = (F''|_{\Psi_0} - K\nabla^2)\,\delta\Psi$ Eq. (3.10) yields

$$\lambda \propto -k^2 \left(F''|_{\Psi_0} + K k^2 \right) \tag{3.13}$$

for the ansatz $\delta\Psi \propto \exp(\lambda t + i\mathbf{k} \cdot \mathbf{r})$. $F'' < 0$ inside the spinodal curve, therefore $\lambda > 0 \equiv k < k_{cr} = \sqrt{-K^{-1} F''|_{\Psi_0}}$. Long-wavelength fluctuations grow exponentially for $k < k_{cr}$, with the maximum rate for $k = 1/2\, k_{cr}$. This means that the fastest growth rate is for domains of size:

$$L \propto \frac{1}{k_{cr}} \tag{3.14}$$

The growth is time-independent in the initial linear stage.

(2) Diffusive stage: In the first nonlinear stage the hydrodynamic term $\mathbf{v} \cdot \nabla\Psi$ can be neglected in Eq. (3.10). Sharp interfaces are formed between the phases and surface tension plays a role. For two-dimensional and three-dimensional systems the growth exponent is $\alpha = 1/3$ [30]. This is the same result as the Lifshitz-Slyozov-Wagner theory [104, 170] for the nucleation and growth regime. On the one hand the Gibbs-Thomas boundary condition provides the dependence of the chemical potential $\mu \propto \gamma/L$. On the other hand $\partial\Psi/\partial t \propto (\rho/L)\,\mathrm{d}L/\mathrm{d}t$, leading to:

$$L(t) \propto \left(\frac{\gamma D m t}{\rho k T}\right)^{1/3}. \tag{3.15}$$

The transition from the linear to the diffusive regime happens at time scales of $L \propto (D\eta/kT)^2$.

(3) Viscous hydrodynamic stage: The hydrodynamics come into play. The Cahn-Hillard equation Eq. (3.10) has to be coupled with the Navier-Stokes equation Eq. (3.11) and the continuity equation Eq. (3.12). For a quench near the critical point neighboring domains can coalesce with the surface tension as the driving force which is balanced by the viscous friction [153]. The surface tension term in the Navier-Stokes equation 3.11 is $\Psi\nabla\mu \propto \gamma/L$, whereas the viscous term is $\eta\nabla^2\mathbf{v} \propto (\eta/L^2)\mathrm{d}L/\mathrm{d}t$ leading to a linear growth

$$L(t) \propto \frac{\gamma t}{\eta} \tag{3.16}$$

in the viscous stage. The transition from diffusive to viscous growth happens at length scales $L \propto (D\eta m/\rho k T)^{1/2}$. In the case of a quench far away from criticality, i.e. for small values of the mixing fraction x_1, the individual droplets cannot connect in order to coalesce, thus disabling the mechanism responsible for viscous growth. In this case the behavior is the same as in the nucleation and growth case where the diffusive stage transitions into the coalescence due to the Brownian motion [153] of the demixed phase domains. Then the growth rate is $L(t) \propto (kTt/\eta)^{1/3}$.

(4) Inertial stage. When for late times the domain sizes become large, the characteristic Reynolds numbers become of the order of unity and inertia starts to play a crucial role. The surface tension is balanced against the inertial term $(\mathbf{v} \cdot \nabla)\,\mathbf{v} \propto \rho/L\,(\mathrm{d}L/\mathrm{d}t)^2$ in the Navier-Stokes equation Eq. (3.11), resulting in the growth

$$L(t) \propto \left(\frac{\gamma t^2}{\rho}\right)^{1/3}. \tag{3.17}$$

The transition between viscous and inertial growth happens at length scales $L \propto \eta^2/\rho\gamma$.

The same exponents can be obtained by simple dimensional considerations [30] and were systematically derived for a Lennard-Jones fluid in [48]. Table 3.1 summarizes these results.

Table 3.1: Stages during spinodal decomposition with power-law growth $L(t) \propto t^{\alpha}$ in the mean field approximation.

stage	$L(t) \propto$	regime	α
linear	$\frac{1}{k_{cr}}$	$L \ll \left(\frac{D\eta}{kT}\right)^2$	0
diffusive	$\left(\frac{\gamma D t}{\rho k T}\right)^{1/3}$	$\left(\frac{D\eta}{kT}\right)^2 \ll L \ll \left(\frac{D\eta m}{\rho k T}\right)^{1/2}$	$\frac{1}{3}$
viscous	$\frac{\gamma t}{\eta}$	$\left(\frac{D\eta m}{\rho k T}\right)^{1/2} \ll L \ll \frac{\eta^2}{\rho\gamma}$	1
inertial	$\left(\frac{\gamma t^2}{\rho}\right)^{1/3}$	$L \gg \frac{\eta^2}{\rho\gamma}$	$\frac{2}{3}$

3.4 Particle resolved studies

Mean field theory approaches provide several drawbacks in understanding phase separation dynamics . For example, the spinodal line is only defined for sufficiently long-range interactions [74]. In general a gradual transition is expected between the regimes of nucleation and growth and spinodal decomposition. Theories trying to describe the gradual transition [100, 21] show significant drawbacks [22]. Another disadvantage is that the position of the spinodal curve depends on the system size $\mathcal{L}$ compared to the correlation length ξ. The mean field theory is only valid in the case $\mathcal{L}/\xi \ll 1$ where the phase separation is inhibited. In the case $\mathcal{L}/\xi \gtrsim 1$ the free energy depends strongly on $\mathcal{L}$ such that for large systems the spinodal curve completely disappears [101, 139, 99]. In the linear stage of spinodal decomposition it was shown that the mean field prediction of a time independent characteristic length scale and the exponential growth of fluctuations are not confirmed [22, 110]. This suggests that particle resolved studies with tunable interaction potential ranges are suitable to enrich the general understanding of phase separation dynamics provided by mean field theory.

Consider a mixture of $N = \sum_i N_i$ molecules that consist of different species i. Then, according to [65] a function of mixing, denoted by the superscript M can be written for any thermodynamic property F as

$$F^M(P,T) = F_m(P,T,\{N_i\}) - \sum_i x_i F_i(P,T,N_i) \tag{3.18}$$

with the value for the mixture F_m and F_i for the pure component. $x_i = N_i/N$ is the concentration of species i. A mixture of particles that are labeled but identical is called

an ideal mixture and has a Gibbs free energy of

$$G^M = NkT \sum_i x_i \ln(x_i) \tag{3.19}$$

Real mixtures are not ideal mixtures, thus one can introduce excess properties of mixing as the difference between the actual and the ideal mixing function. Excess properties are denoted by a superscript E. The simplest model of a real binary mixture is that G^E is a quadratic function of composition [146] and proportional to the interchange energy w:

$$G^E = x_1 x_2 w \tag{3.20}$$

Eq. (3.20) provides a good approximation for many mixtures [65]. For mixtures where the pure and pair potentials $V_{a,b}(r)$ are of the form

$$V_{a,b}(r) = \epsilon_{a,b} f\left(\frac{r}{\sigma_{a,b}}\right) \tag{3.21}$$

(where $\epsilon_{a,b}$ is a characteristic energy scale, $\sigma_{a,b}$ is a characteristic length scale and f an arbitrary function) the cross-interaction parameters, i.e. for cases $a \neq b$ are given by (phenomenological) combining rules. The Lorentz rule (which is exact for hard sphere mixtures) is given by

$$\sigma_{a,b} = \frac{1}{2}(\sigma_{aa} + \sigma_{bb}) \tag{3.22}$$

and the Berthelot rule is formulated as

$$\epsilon_{a,b} = \sqrt{\epsilon_{aa}\epsilon_{bb}}. \tag{3.23}$$

When a mixture satisfies these rules it is called a Lorentz-Berthelot mixture. It can be shown that when the Berthelot mixing rule is violated by a positive nonadditivity $\delta > 0$ the energy cost for unlike species being neighbors leads to demixing in high density conditions [70]. The excess free energy favours phase separation.

The Berthelot mixing rule nonadditivity parameter for a system of binary particles with pair interaction energy $V_{ij}(r)$ with $i, j \in \{1, 2\}$ is defined by:

$$V_{ij} = (1 + \delta)\sqrt{V_{11}V_{22}}. \tag{3.24}$$

In the particle resolved picture the tendency of particles of different species to demix is determined by the relative strengths of their interactions [65]. In single species systems an attractive interaction is necessary to facilitate demixing [65, 98]. Within systems of several components this is however, not required. For a binary mixture of particles of species 1 and species 2, demixing is possible when the interaction strength between species 1 and species 2 is more repulsive than the geometric mean of the interaction strengths among particles of the same species. The degree of difference in these interaction strengths is the interaction nonadditivity δ. Demixing/mixing is preferred when $\delta > 0/\delta < 0$.

Particle resolved studies of fluid-fluid demixing simulations of a three-dimensional complex plasma are discussed in the second enclosed publication [25] that is summarized in chapter 7 and can be found in the attachment in section D.2.

Chapter 4

Physical and model systems

4.1 Complex plasmas

A plasma is an ionized gas, consisting of atoms, ions and electrons, that exhibits quasi-neutrality and collective behavior [35]. Quasi-neutrality is the apparent neutrality at large scales, while effects of charge are observed at length scales smaller than the Debye length λ_D. λ_D is the distance at which the electrostatic potential of a charged particle has decreased its magnitude by a factor of $1/e$. Since the plasma constituent particles interact via long-range Coulomb forces every particle interacts simultaneously with a large number of other particles in the plasma. Thus, the plasma can show a cooperative response to external stimuli and exhibit collective behavior. In contrast, for instance in a gas, the particles interact mainly via short-range repulsion forces and the disturbance of an individual atom has practically no effect on the collective.

When dielectric (micro-) particles are introduced into a plasma, they get negatively charged due to electron and ion currents to their surface. Due to their charge they can interact among themselves and with the plasma particles and thus form the soft matter state of the plasma called complex plasma (or dusty plasma). Plasma crystals were discovered in 1994 [36, 67, 163] (for reviews consult e.g. [52, 124, 74]). Complex plasmas extend the hierarchy of soft matter systems of which there are granular solids, complex liquids (gels, polymers etc.) and aerosols to the plasma state of matter. The molecular component of a complex plasma is the ionized gas whereas the supramolecular component can exist in the solid, liquid or gaseous state.

Some of their properties are:

- The complex plasma particles are individually observable.
- The particles diameters are in the range of μm, their separation in the range of 100 μm. These optically thin systems can easily be visualized and allow the three-dimensional imaging of hundreds of particle layers.
- The dynamic time scale, e.g. the inverse Einstein frequency, is in the range of 10 ms. This allows for a high resolution tracing of the dynamics of microparticles.

- Analogous to the dynamics of atoms in liquids or solids, the dynamics of microparticles in a complex plasma are virtually undamped due to the dilute ionized gas as the molecular component. The momentum transfer between supramolecular microparticles is much greater than the momentum transfer of microparticles and plasma constituents.
- The composition of four components allows a great variety of configurations and the modeling of many physical processes.
- The system can be manipulated manifold in experiments. For example electrostatic and magnetic fields, thermal gradients or electromagnetic pressure by laser can be applied.
- The strong coupling and collective behavior provide an opportunity to study highly non linear and self-organization processes.

Therefore complex plasmas provide the unique opportunity to study a cornucopia of (self-organizing) physical processes on the kinetic individual particle level.

4.1.1 Two-dimensional plasma crystals

Two-dimensional crystals are an important research subject since they show fundamentally different properties compared to the three-dimensional case. In three dimensions a solid is characterized by its long-range order. However, as explained in section 2, in two (or less) dimensions the Mermin-Wagner [117] theorem forbids any long-range order and an alternative characterization of the solid state is necessary. Another interesting point is that such two-dimensional systems are not frequently observed and hence the theory can only be tested for few experimental setups. Examples for two-dimensional systems are e.g. compressed Langmuir films of stearic acid [137], trapped atomic gases [62], the electron solid [59, 123] or monolayers of xenon on graphite [68]. Complex plasmas provide an additional system where two dimensional solids can be observed and their unique properties even allow the complete tracing of individual particle trajectories.

In 1986 [73] it was proposed that small particles can form a coulomb lattice in a plasma. The coupling parameter Γ is the ratio of the mean energy of pair electrostatic interactions to the thermal particle energy:

$$\Gamma = \frac{Q^2}{kT\Delta} \tag{4.1}$$

It is a measure for the strength of the electrostatic coupling between particles. A coulomb lattice is formed if the coupling parameter exceeds a critical value $\Gamma > \Gamma_c \simeq 170$. This condition is hard to meet experimentally in a one component plasma. The charge is equal to the elementary charge and Γ_c can only be exceeded for very high densities and low temperatures. The charge of the supramolecular component in a complex plasma, the microparticles, is much greater and can vary over a wide range of about $Q \in [10^3, 10^4]e$ allowing the formation of plasma Coulomb crystals at moderate temperatures of about $T \simeq 300K$. The first experimental evidence for two-dimensional complex plasma crystals was reported in 1994 [36, 67, 163]. In a radio frequency (rf) discharge the particles were

confined to a monolayer that crystallized into a two-dimensional hexagonal Bravais lattice. In nature two-dimensional systems are not easy to find. In complex plasmas however, it is straightforward to levitate a single layer of plasma particles in a rf discharge chamber. Vertical fluctuations due to fluctuations in the particle charges are usually negligible. An image of two-dimensional plasma crystal, electrostatically levitated in laboratory conditions on the ground, is presented in Fig. 4.1.

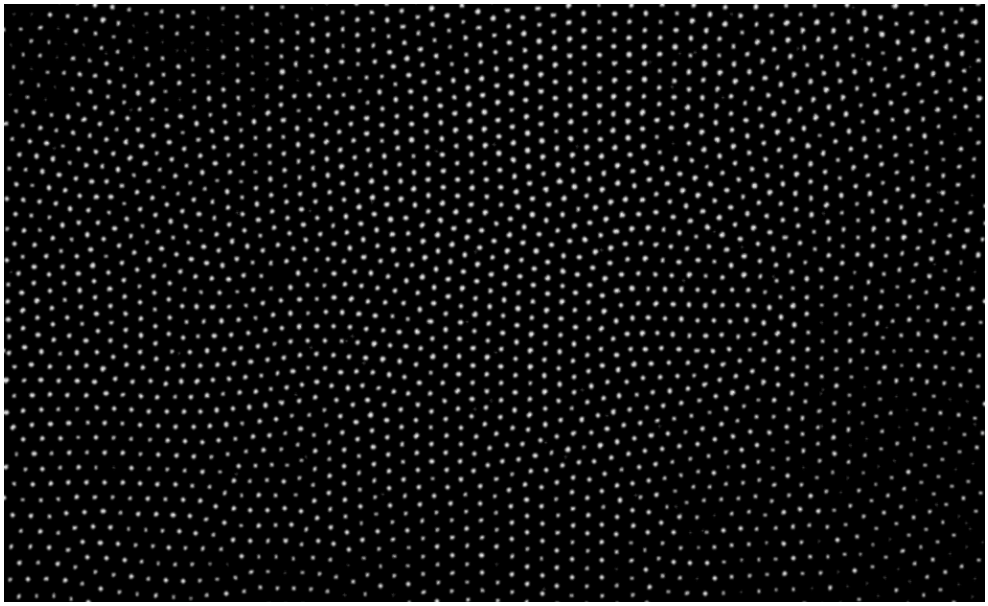

Figure 4.1: Two-dimensional plasma crystal levitated in a rf chamber in ground-based laboratory. The experiment was performed by C. A. Knapek. The field of view was 18 mm x 25 mm. Particles are melamine formaldehyde spheres of 9.19 μm diameter, the mean interparticle separation is 0.59 mm. The gas pressure is 1.94 Pa and the electrode peak-to-peak voltage is 172 V. The image was adapted from [24].

Experiments of a the crystallization of a two-dimensional complex plasma are discussed and analyzed in the publication in appendix D.1 and summarized in section 6.

4.1.2 Charging

Since the supramolecular microparticles interact via coulomb forces depending on their charge Q, the start of the description of their interactions has to begin with the nature of their charging. Microparticles are charged due to the electron flux I_e and the ion flux I_i to their surfaces. The charge evolves in time according to:

$$\frac{\mathrm{d}Q}{\mathrm{d}t} = I_i - I_e \tag{4.2}$$

Electrons have a higher mobility than ions leading to an initially high I_e and a large negative charge Q of the particle. The negative charge repulses incoming electrons and attracts ions until the fluxes match and Q stays constant for long times t.

The standard approach to describe the electron and ion fluxes is the orbital-motion-limited (OML) approximation [38, 7, 57]. The assumptions of the OML approximation are:

- Microparticles are isolated. Electron and ion motions in the vicinity of a specific microparticles are not affected by other particles.
- The plasma is collisionless. Electrons and ions do not collide during their approach to the microparticle.
- The effective potential has no barriers.

Solving the conservation equations of energy and angular momentum provides the following expression for the cross section for the collection of electrons and ions:

$$\sigma(v) = \begin{cases} \pi a^2(1 - 2q\phi_s/mv^2) & \text{for } q\phi_s < 1/2mv^2 \\ 0 & \text{otherwise.} \end{cases} \tag{4.3}$$

Here q and m are the charge and mass or either electrons or ions, v is the velocity in the microparticle coordinate system, a is the radius of the microparticle and $\phi_s \propto T_e/e$ is the stationary surface potential depending on the electron temperature T_e. e is the elementary charge. The currents can be obtained by integration of the velocity distribution functions $f(v)$:

$$I = qn \int \mathrm{d}^3v \; v\sigma(v)f(v), \tag{4.4}$$

with number densities n. Assuming Maxwellian velocity distributions this yields for ion I_i and electron fluxes I_e:

$$\begin{aligned} I_e &= \sqrt{8\pi}a^2 e n_e v_{T_e} \exp\left(-\frac{|Q|e}{aT_e}\right) \\ I_i &= \sqrt{8\pi}a^2 e n_i v_{T_i} \left(1 + \frac{T_e}{T_i}\frac{|Q|e}{aT_e}\right) \end{aligned} \tag{4.5}$$

Equal currents lead to the equilibrium charge

$$Q = a\phi_s. \tag{4.6}$$

This turns out to be a good approximation for sufficiently small particles $a < 0.2\,\lambda$ compared to the screening length λ [40, 85].

4.1.3 Interaction potential and interaction nonadditivity

For the approximation of an isolated spherical particle the distribution of the electrostatic potential ϕ can be obtained from the charge distribution ρ by the Poisson equation

$$\Delta\phi(r) = -4\pi\rho(r) \tag{4.7}$$

with boundary conditions $\phi(r \to \infty) = 0$ and $\phi(r = a) = \phi_s$. The surface potential is related to the particle charge by:

$$\left.\frac{\mathrm{d}\phi}{\mathrm{d}r}\right|_{r=a} = -\frac{Q}{a^2} \tag{4.8}$$

Boltzmann electrons and ions distributions can be linearized for $q|\phi_s|/kT \lesssim 1$, then the Poisson equation Eq. (4.7) is solved by the Yukawa (or Debye-Hückel) potential:

$$\phi(r) = \frac{Q}{r}\exp\left(-\frac{r}{\lambda_D}\right) \tag{4.9}$$

with the linearized Debye length λ_D. It is composed of the electron and ion Debye length given by:

$$\frac{1}{\lambda_D^2} = \frac{1}{\lambda_{De}^2} + \frac{1}{\lambda_{Di}^2} = 4\pi\left(\frac{en_e}{kT_e} + \frac{q_i n_i}{kT_i}\right). \tag{4.10}$$

The exponential screening of the interaction potential can be explained by the redistribution of electrons and ions around the microparticle.

There are different screening mechanisms possible in complex plasmas which play an important role in the distribution of charges around microparticles. When there is no plasma production, i.e. ionization, or loss in the neighborhood of a microparticle, the long-range asymptote of the potential is determined by the conservation of fluxes to the particle surface. This leads to a power-law decay of the far potential. In collisionless plasmas this asymptote is predicted to decay quadratically $\phi(r) \propto r^{-2}$ [9, 166] For highly collisional plasmas the potential is predicted to be Coulomb-like $\phi(r) \propto r^{-1}$ [84]. A so-called shadowing force between neighboring particles resulting from mutual distortions of their ion and neutral fluxes can also lead to a Coulomb asymptote $\phi(r) \propto r^{-1}$ [97].

A particularly crucial role in determining the shape of the long-range asymptote is plasma production and loss. Several mechanisms can be responsible: Electron-neutral collisions is considered to be the main cause of plasma production due to impact ionization. Plasma loss can be due to electron-ion recombination in high pressure gas discharges [51], due to ambipolar diffusion to the walls of the plasma chamber in low and moderate pressure [34], combinations of those [86], or plasma loss on the microparticles for high densities [46]. These processes lead, in general, to the emergence of two asymptotes of the interaction potential $\phi(r)$ that both exhibit exponential screening of the Yukawa form. This is called a double-Yukawa repulsive potential [86]:

$$\Phi(r) \;=\; \frac{1}{r}\left(Q^*_{\mathrm{SR}}e^{-r/\lambda_{\mathrm{SR}}} + Q^*_{\mathrm{LR}}e^{-r/\lambda_{\mathrm{LR}}}\right) \tag{4.11}$$

Here Q^* indicates effective charge, λ indicates the screening length scale for long-range (LR) and short-range (SR) interactions respectively. In fact, the length scales can be quite different. λ_{SR} is determined by the Debye-Hückel screening and therefore has similar magnitude as the Debye length which is typically smaller than the interparticle separation. The value of λ_{LR} depends on the balance between plasma loss and production and can therefore vary over a broad
, typically much larger than the interparticle separation. The screening length ratio, providing a measure or the dominance of long-range over short-range interactions, is defined as:

$$\Lambda \;=\; \lambda_{\mathrm{LR}}/\lambda_{\mathrm{SR}}. \tag{4.12}$$

The pair interaction energy of particles i, j in a binary mixture is determined by the potential of charge Q_i at the position of charge Q_j:

$$V_{ij}(r) = \frac{1}{2} \sum_{\beta\in\{\mathrm{SR,LR}\}} \left(Q_i Q^*_{\beta,j} + Q_j Q^*_{\beta,i}\right) \frac{e^{-r/\lambda_\beta}}{r} \tag{4.13}$$

It follows that the Berthelot mixing interaction nonadditivity parameter

$$\delta = \frac{\left(\sqrt{\dfrac{\nu_{2,\mathrm{SR}} + \nu_{2,\mathrm{LR}}\left(e^{-r/\lambda_{\mathrm{LR}}}/e^{-r/\lambda_{\mathrm{SR}}}\right)}{\nu_{1,\mathrm{SR}} + \nu_{1,\mathrm{LR}}\left(e^{-r/\lambda_{\mathrm{LR}}}/e^{-r/\lambda_{\mathrm{LR}}}\right)}} - 1\right)^2}{2\sqrt{\dfrac{\nu_{2,\mathrm{SR}} + \nu_{2,\mathrm{LR}}\left(e^{-r/\lambda_{\mathrm{LR}}}/e^{-r/\lambda_{\mathrm{SR}}}\right)}{\nu_{1,\mathrm{SR}} + \nu_{1,\mathrm{LR}}\left(e^{-r/\lambda_{\mathrm{LR}}}/e^{-r/\lambda_{\mathrm{LR}}}\right)}}} \geq 0 \tag{4.14}$$

(see section 3) is always positive. Therefore the binary complex plasma system always exhibits phase separation in bulk conditions, also for a double-Yukawa potential. $\nu_{i,\beta}, \beta \in \{\mathrm{SR}, \mathrm{LR}\}$ are the normalized charge ratios $\nu_{i,\beta} = Q^*_{i,\beta}/Q_i$.

For a complex plasma with only one (generic) far field asymptote $Y(r)$ and interaction potential $\phi_{ij} = Q^*_i Y(r_{ij})$, depending on the far-field effective charge $Q^*_i(Q_i)$, the nonadditivity parameter reduces to:

$$\delta = \frac{\left(\sqrt{\nu_2/\nu_1} - 1\right)^2}{2\sqrt{\nu_2/\nu_1}} \geq 0 \tag{4.15}$$

with the normalized charge ratio $\nu_i = Q^*_i/Q_i$. Thus, for a complex plasma demixing is always stimulated in bulk conditions. This is a remarkable result since it is independent of the particular form of the far-field radial profile $Y(r)$. This implies that complex plasmas always demix independent of the particular charging mechanisms e.g. ion/neutral particle collisions or ion absorption to the microparticle surface. The only quantity influencing the value of the interaction nonadditivity is the ratio between the actual particle charge and the effective charge determining the far-field interaction potential. An image of a phase separating binary complex plasma is presented in Fig. 4.2.

Particle resolved demixing simulations of a binary three-dimensional complex plasma are analyzed for different screening length ratios Λ in the publication "Kinetics of fluid

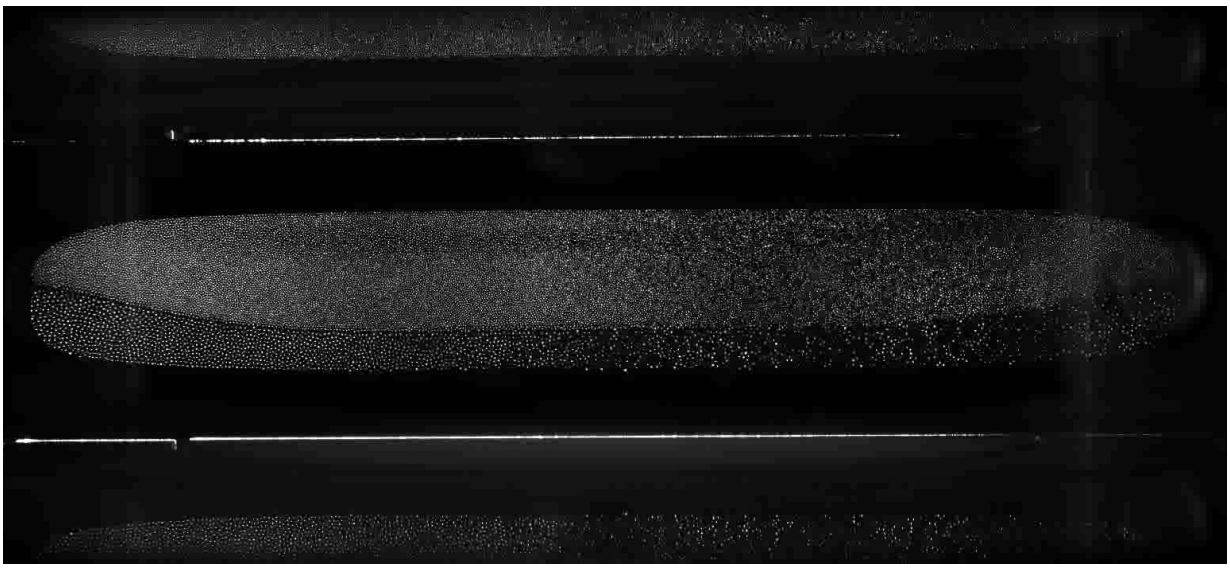

Figure 4.2: Phase separating binary complex plasma consisting of different sized particles. The image is a cross section of a three-dimensional cloud. The experiment was performed by E. Zaehringer on the PlasmaLab/Ekoplasma setup in a parabolic flight campaign in 2016 under microgravity conditions. Particles are melamine formaldehyde spheres of 4.41 μm, respectively 9.19 μm diameter. The chamber is cylindrical with an electrode diameter of 11.4 cm, the vertical electrode separation is adjusted to 30 mm. Voltage is applied in push-pull mode between upper and lower electrodes in the range of $U_{\mathrm{pp}} \simeq 27\,\mathrm{V}$. The gas pressure is 10 Pa.

demixing in complex plasmas: Domain growth analysis using Minkowski tensors" in the appendix D.2. This work is summarized in section 7.

4.2 Dynamic density-functional theory

The dynamical density functional theory (DDFT) with a Gaussian core model (GCM) provides a simple model for polymers in solution. The model is chosen due to its simplicity and its generic demixing properties.

This section gives an overview of methods used in [26] to model fluid demixing on spherical geometries. The dynamics of a fluid, bound to the surface of a sphere, is investigated using a dynamical density functional theory [12, 109] with a Gaussian core model [159] for the particle interaction potential. The density-functional theory is based on the assumption that the free energy of a fluid is a unique functional of its equilibrium density and is independent of external fields. For a specific interaction potential the inhomogeneous fluid density and all n-point correlation functions can be obtained by functional differentiation of the free energy functional. The Gaussian core model is a soft particle interaction potential that consists of a pairwise sum of additive Gaussian components for which terms in a series expansion of the free energy can be calculated analytically.

4.2.1 The Gaussian Core Model

The Gaussian core model (GCM) was introduced by Stillinger [159] in order to study phase separation in binary mixtures. It has been studied extensively in the bulk as also at interfaces [10, 11, 12, 15, 14, 16].

Consider a binary fluid consisting of a mixture of particles of two distinct species. The particles of species i and j interact via the soft repulsive pair potential:

$$\beta v_{ij}(r) = \beta\epsilon_{ij} \exp\{-r^2/R_{ij}^2\}, \tag{4.16}$$

Here $\beta = (kT)^{-1}$. The positive parameter $\epsilon_{ij} > 0$ is a measure for the interaction strength, $R_{ij} > 0$ is the length scale of the interaction range.

The mean field approximation of the free energy in the GCM is in agreement with computer simulations of the full model [108]. Another advantage is its straightforward application in density functional theories.

4.2.2 Mean-field free energy functional

The Helmholtz free energy functional F describing of the particles on the sphere can be approximated by

$$\begin{aligned}\beta F[\{\rho_q(\mathbf{r})\}] = &\sum_q \int d\mathbf{r}\rho_q(\mathbf{r})\big(\ln(\rho_q(\mathbf{r})) - 1\big) \\ &+ \frac{1}{2}\sum_{ql}\int d\mathbf{r}\int d\mathbf{r}'\rho_q(\mathbf{r})\rho_l(\mathbf{r}')\beta v_{ql}(|\mathbf{r}-\mathbf{r}'|).\end{aligned} \tag{4.17}$$

The first is the ideal term, the second the excess term that describes the interactions. F has a functional dependence on the density profiles $\rho_q(\mathbf{r}, t)$ for both species $q \in \{1, 2\}$. Since the thermal wavelength is physically irrelevant it is set to unity.

The number density of species q is $\rho_q = N_q/V$ in the bulk. Here N_q is the number of particles of species q, and V is the area. The total particle number density is the sum of the contributions of both species $\rho = \rho_1 + \rho_2$, similar $N = N_1 + N_2$. The mixing parameter x is the concentration of particles of species 2, $x = N_2/N$. Then $\rho_1 = (1-x)\rho$ and $\rho_2 = x\rho$ with the lever rule $\rho = (1-x)\rho + x\rho$. The free energy per particle $f = f/N$ can be written as sum of the ideal term f_{id} and the excess term f_{ex}:

$$f = f_{\text{id}} + f_{\text{ex}}. \tag{4.18}$$

The ideal term can be expressed as

$$\beta f_{\text{id}} = \ln(\rho) - 1 + (1-x)\ln(1-x) + x\ln(x), \tag{4.19}$$

and the excess term as

$$\beta f_{\text{ex}} = \frac{1}{2\rho}\big(\rho_1\rho_1\hat{v}_{11} + 2\rho_1\rho_2\hat{v}_{12} + \rho_2\rho_2\hat{v}_{22}\big). \tag{4.20}$$

Here the coefficients are transformed via $\hat{v}_{ij} = \epsilon^*_{ij} R^2_{ij} \pi$ and $\epsilon^*_{ij} = \beta \epsilon_{ij}$. In [26] following parameters are chosen: $R_{11} = R_{22} = R_{12} = 1$, $\epsilon^*_{11} = \epsilon^*_{22} = 2$ and $\epsilon^*_{12} = 1.035 \epsilon^*_{11}$.

With these parameters a phase diagram is calculated in the case of flat geometry acting as guide for the behavior in the case of spherical geometry [26]: The GCM demixes when sufficiently high densities $\rho > \rho_c$ are reached.

4.2.3 Dynamical density-functional theory and numerical implementation

The one-body densities of the particles on the spherical surface can be obtained by the application of dynamical density functional theory [13, 109]. In the DDFT the temporal evolution of the particle densities is given by the equation of motion.

$$\gamma^{-1} \frac{\partial \rho_q(\mathbf{r}, \mathbf{t})}{\partial t} = \frac{\partial}{\partial \mathbf{r}} \cdot \left[\rho_q(\mathbf{r}, t) \frac{\partial}{\partial \mathbf{r}} \frac{\delta F[\{\rho_q(\mathbf{r}, t)\}]}{\delta \rho_q(\mathbf{r}, t)} \right] \tag{4.21}$$

Here γ is the mobility and it is related to the diffusion coefficients D as $\gamma = \beta D$. Eq. (4.21) is a generalized diffusion equation. The evolution of the density is by gradients in the local chemical potentials. The chemical potential depends on the particle interactions encoded in the free energy functional, Eq. (4.17). For the ideal gas functional Eq. (4.21) is reduced to the standard ideal gas diffusion equation.

The DDFT equation of motion Eq. (4.21) is solved on the sphere, with pixels parametrized by the spherical coordinates θ and ϕ. By this parametrization the calculation of gradients and divergences of scalar- and vectors fields can be done by simple finite differences. Convolutions are efficiently calculated by applying the convolution theorem on the unit-sphere [45, 26] via spherical harmonic functions.

Dynamical density-functional theory calculations of a binary fluid confined to the surface of a sphere are analyzed for different sphere sizes and mixture compositions in the study provided in appendix D.3. A summary can be found in section 8.

Chapter 5

Linear and nonlinear spatial statistics

The treatment of spatial data is an omnipresent challenge in many fields of research. The effect of osteoporosis on anisotropic bone structure is investigated in the field of medicine [39, 44, 168, 142, 127, 19], the influence of porous structure on the taste of food is relevant for the food industry [5, 41, 49], biologists study cell packings [18, 20, 78]. Spatial structures occur on all length scales ranging from nuclear pasta [173, 50, 89] to the large scale structure of the universe [83, 126].

In particular in statistical physics many body systems often self-organize in complex structures [72, 135, 136]. Competing interactions in confined colloidal suspension can, for example, lead to particles that self-assemble in compact disks [105]. The particular structure that is assumed depends on the interaction potential shape. Such systems, exhibiting complex structure, have a strong connection between the physical principals that govern their interactions on the microscopic scale and the morphology of the structural patterns they assume.

In order to obtain a quantitative description of the connection between physics and shape, a quantitative morphological description is necessary. Traditionally this description is based on two-point correlation functions or their analogue in Fourier space, the power spectral density. This was a convenient way to compare experiment and theory in a time when scattering experiments were the standard method to analyze microscopic spatial structure. In these days, advanced digital image processing allows the application of sophisticated structural measures in position space. One possibility to describe spatial data more rigorously than power spectrum based measures are Minkowski functionals and tensors. A crucial advantage of Minkowski functional and tensor measures is their sensitivity to higher order correlations. The extension of traditional power spectrum or two-point correlation measures is, in contrast, computationally expensive [169]. Another benefit of Minkowski measures is that they are easy to interpret since they are related to simple concepts as volume, area, curvature and connectedness.

In this section a brief introduction to traditional measures (that are usually applied to characterize demixing dynamics and two-dimensional crystal and liquid systems), both

in position and Fourier space is given. Then, Minkowski functionals and tensors are presented as a complete family of morphological descriptors. Before the actual measures are discussed, a mathematical description of many-body systems is given.

5.1 Random point processes

Many-body systems of physical particles can mathematically be described by a set of points $\{\mathbf{x}_i | i = 1, ..., N, N \in \mathbb{N}\}$ in three dimensional Euclidean space $\mathbb{E}^3$. Any particle configuration can be described by a random point process resulting in this set of points. This point process is determined by its probability distribution function (pdf)

$$\prod_{k=1}^{N} \mathrm{d}\mathbf{x}_k \; \mathcal{P}(\mathbf{x}_1, ..., \mathbf{x}_N). \tag{5.1}$$

The pdf is completely determined when all of its moments, given by the N-point correlation functions

$$\left\langle \mathbf{x}_1^{l_1} ... \mathbf{x}_N^{l_N} \right\rangle = \int \prod_{k=1}^{N} \mathrm{d}\mathbf{x}_k \; \mathbf{x}_1^{l_1} ... \mathbf{x}_N^{l_N}, \tag{5.2}$$

are known. The exponents $l_i \in \mathbb{N}$ are natural numbers. A linear point process (in one-dimensional systems described by an autoregressive-moving-average-model (ARMA) [176, 27]) is homogeneous and isotropic. Thus, its correlation functions are translation and rotation invariant and can only depend on the magnitude of pairwise differences $|\mathbf{x}_i - \mathbf{x}_j|$, leaving the two-point correlation function

$$\xi_{ij}(|\mathbf{x}_i - \mathbf{x}_j|) = \langle \mathbf{x}_i \mathbf{x}_j \rangle \tag{5.3}$$

as the only non-vanishing moment. The pdf determined solely by its two-point correlation function is the pdf for Gaussian random fields (GRF):

$$\prod_{k=1}^{N} \mathrm{d}\mathbf{x}_k \; \mathcal{P}(\mathbf{x}_1, ..., \mathbf{x}_N) = \frac{1}{(2\pi)^{N/2} \det(\xi)^{1/2}} \exp\left(-\frac{1}{2} \sum_{i,j} \mathbf{x}_i (\xi^{-1})_{ij} \mathbf{x}_j \right). \tag{5.4}$$

Thus a linear random point process is completely determined by the knowledge of its two-point correlation function (all higher order correlations vanish) and given by a Gaussian probability distribution function. This means that any nonlinear properties must necessarily lie in the correlation functions of orders larger than two.

5.2 Conventional structure measures in position space

5.2.1 Pair correlation function $g(r)$

The KTHNY theory (see section 2.1) for the melting transition in two-dimensional systems predicts distinct long-range decay asymptotes of the pair correlation function in different phases.

With $\rho = N/V$ in three dimensions, or $\rho = N/A$ in two dimensions, being the number density of the set of N particles $\{\mathbf{x}_i | i = 1, ..., N, N \in \mathbb{N}\}$ occupying the volume V, or area A, the pair correlation function is defined as:

$$g(\mathbf{x}) = \frac{1}{\rho} \left\langle \sum_{i \neq j} \delta(\mathbf{x} - (\mathbf{x}_i - \mathbf{x}_j) \right\rangle . \tag{5.5}$$

$\langle \cdot \rangle$ denotes the ensemble average, $\delta(\mathbf{x})$ is the Dirac delta distribution. By defining the density distribution $\rho(\mathbf{x}) = \sum_i \delta(\mathbf{x} - \mathbf{x}_i)$ the pair correlation function can be written as the two-point density correlation function:

$$g(\mathbf{x}) = \left\langle \sum_{i \neq j} \rho(\mathbf{x} - \mathbf{x}_i) \rho(\mathbf{x} - \mathbf{x}_j) \right\rangle . \tag{5.6}$$

The radially averaged pair correlation function (also known as the translational correlation function or radial density distribution) is given by

$$g(r) = \frac{\pi r^2}{2\pi r N^2} \left\langle \sum_{i \neq j} \delta(r - (r_i - r_j) \right\rangle = \frac{1}{2\pi r N} \left\langle \sum_{i \neq j} \rho(r - r_i) \rho(r - r_j) \right\rangle \tag{5.7}$$

in two dimensions ($\mathbf{x} = (x_1, x_2), r^2 = x_1^2 + x_2^2$). It is a measure for the translational order in a point distribution. It yields the mean probability density for the existence of a particle separated by a distance r from another particle [171]. It is calculated explicitly by choosing one-by-one, each particle i as the center particle $\mathbf{x}_c$, then calculating the probability to find another particle in the neighborhood $U_{\delta r}(r)$, the annulus at the distance r extending to $r + \delta_r$, and averaging over all particles as center particle. In the flat two-dimensional case the neighborhood is the annulus with area $2\pi r \delta r$. N_c center particles are chosen and the distance is scanned between $r = 0$ and $r = r_{max}$ in steps of δr. To get the probability, the particles in the neighborhood have to be counted and then the result normalized by the neighborhood area. Averaging is done by division with N_c and by normalizing with the particle density $N_c / \pi r_{max}^2$:

$$g(r) = \sum_{i=1}^{N_c} \frac{1}{N_c} \frac{\pi r^2}{N_c} \sum_{r + \delta r < |\mathbf{x} - \mathbf{x}_c| < r + \delta r} \frac{i}{2\pi r \delta r} \tag{5.8}$$

The position of the first peak of $g(r)$ is a good estimate of the average interparticle distance δ. It can be used to characterize the degree of translational order via the magnitude of the correlation length ξ. In addition the peak width of $g(r)$ is a measure for the particle temperature.

An example for the shape of $g(r)$ is given in Fig. 5.1. The fist peak indicates the average interparticle distance, the next peaks correspond to the position of the after next neighbors. At large distances the value of $g(r)$ converges to unity.

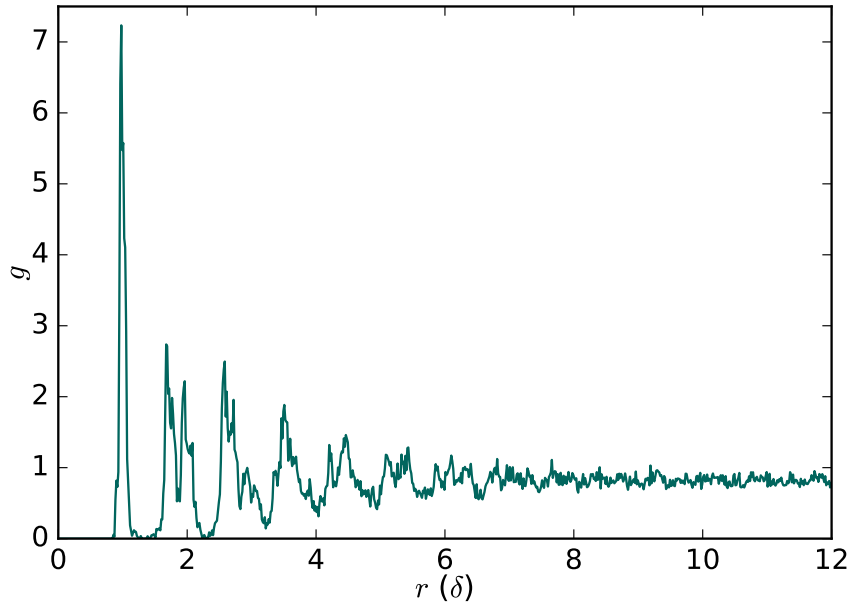

Figure 5.1: Pair correlation function $g(r)$ for a two-dimensional complex plasma sheet. The experiment is the same as presented in Fig. 2.4 (b).

The predictions of the KTHNY theory on the long-range decay of $g(r)$ are summarized in table 5.1. In the publication "Scale-free crystallization of two-dimensional complex plasmas: Domain analysis using Minkowski tensors" in the attachment D.1 these decay shapes are tested for experiments of the crystallization of a two-dimensional complex plasma. This work is summarized in section 6.

Table 5.1: Consequences of the KTHNY theory on the long-range decay of the pair correlation function $g(r)$ in different phase regimes.

phase	temperature regime	$g(r)$ decay
liquid	$(T > T_{c2})$	$g(r) \propto \exp(-r/\xi)$
hexatic	$(T_{c1} < T < T_{c2})$	$g(r) \propto \exp(-r/\xi)$
solid	$(T < T_{c1})$	$g(r) \propto r^{-\eta(T)}, \eta(T \to T_{c1}^{-}) = \max(\eta(T))$

5.2.2 Bond order parameter Ψ_6

A metric for the local hexagonality of a two-dimensional lattice is the bond order parameter Ψ_6 [157]. It can be used to identify defects in two-dimensional lattices. For any lattice site

k it is defined as

$$\Psi_{6,k} = \left| 1/n_k \times \sum_{m=1}^{n_k} \exp\left(6i\Theta_{km}\right) \right|. \tag{5.9}$$

n_k is the number of nearest neighbors of the particle at lattice site k. Θ_{km} is the angle between the bond of particles at sites k and m and an arbitrarily chosen fixed axis. i is the imaginary unit. The value of Ψ_6 for a perfect hexagonal lattice site is 1, it assumes small values for lattices sites with distorted neighborhood shapes. This makes it possible to identify crystalline lattice sites by introducing a threshold value $\Psi_{6,\text{thresh}}$. Then one can consider lattice sites with $\Psi_{6,k} > \Psi_{6,\text{thresh}}$ as crystalline and lattice sites with $\Psi_{6,k} < \Psi_{6,\text{thresh}}$ as lattice defects. When averaged over all lattice sites it is used as a measure for the mean local order of a crystal.

However, it has been show that the bond-order parameter has significant drawbacks [119]: Ψ_6 depends on the choice of the specific neighborhood definition and is inherent discontinuous. These shortcomings are cured when using the morphological Minkowski functional and tensor measures (their introduction follows in section 5.4 below).

5.2.3 Bond correlation function $g_6(r)$

In addition to the predictions on the long-range asymptotes for the pair correlation function $g(r)$, the KTHNY theory has implications regarding the asymptotes of the bond correlation function $g_6(r)$.

Ideal hexagonal crystals exhibit a long-range order of the orientation of their nearest neighbor bonds. The correlation function describing this orientational order is the bond correlation function $g_6(r)$. Following [63, 131] it can be defined as the radially averaged correlation function of $\Psi(\mathbf{x}) = \exp\left(i\theta(\mathbf{x})\right)$:

$$g_6(r) = \left\langle \sum_{k \neq l} \Psi(r - r_k)\Psi^*(r - r_l) \right\rangle. \tag{5.10}$$

$\theta(\mathbf{r})$ denotes the angle between a nearest neighbor bond for a lattice site at position $\mathbf{r}$ and an arbitrary but fixed axis. i is the imaginary unit.

The explicit calculation of the bond correlation function can be performed as the sum

$$g_6(r) = \left| \frac{1}{N_B} \sum_{l=1}^{N_B} \frac{1}{n(l)} \sum_{k=1}^{n(l)} \exp\left\{6i\left(\theta(r_k) - \theta(r_l)\right)\right\} \right|. \tag{5.11}$$

N_B is the total number of bonds in the crystal, $n(l)$ is the number of bonds at distance r from bond l. θ_i the angle of bond i at the position $\mathbf{x}_i$ to an arbitrary, but fixed, axis. For a perfect hexagonal lattice $g_6(r) \equiv 1$ and it is close to 1 and constant for a solid crystalline state [63].

An example for the shape of $g_6(r)$ is given in Fig. 5.2. The peak positions indicate the distance between next neighbors and after next neighbors and so on as in the pair

correlation function $g(r)$. The value of $g_6(r)$ decays for large distances, indicating a non-solid phase.

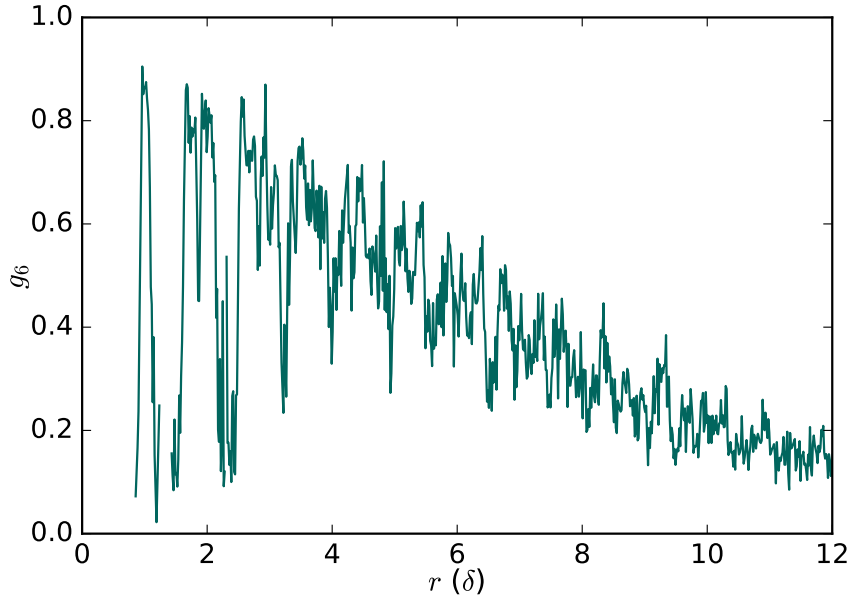

Figure 5.2: Bond correlation function $g_6(r)$ for a two-dimensional complex plasma sheet.

The predictions of the KTHNY theory on the long-range decay of $g_6(r)$ are summarized in table 5.2. These predictions are tested in the publication in the attachment D.1 (summarized in section 6) for the solid-liquid transition in two-dimensional complex plasma sheets.

Table 5.2: Consequences of the KTHNY theory on the long-range decay of the bond correlation function $g_6(r)$ in different phase regimes.

phase	temperature regime	$g_6(r)$ decay
liquid	$(T > T_{c2})$	$g_6(r) \propto \exp(-r/\xi_6(T))$
hexatic	$(T_{c1} < T < T_{c2})$	$g_6(r) \propto r^{-\eta_6(T)}$; $\eta_6 < 0.25$
solid	$(T < T_{c1})$	$g_6(r) = \text{const},\ \text{const} \neq 0$

5.3 Linear methods in Fourier space

As discussed in section 5.1 linear random point processes are characterized by their Gaussian probability distribution function and are completely determined by their two-point correlation function.

On the other hand the Fourier transform of the two-point correlation function $\xi(\mathbf{x})$ is the power spectral density P (also power spectrum or structure factor):

$$P(\mathbf{k}) = \int \mathrm{d}^3\mathbf{x}\, \mathbf{exp}(-i\mathbf{k}\cdot\mathbf{x})\xi(\mathbf{x}). \tag{5.12}$$

Due to the homogeneity and isotropy the power spectral modes are mutually independent:

$$\langle \tilde{\mathbf{x}}(\mathbf{k}_i)\tilde{\mathbf{x}}(\mathbf{k}_j)^*\rangle = (2\pi)^3\delta(\mathbf{k}_i - \mathbf{k}_j)P(|\mathbf{k}_j|). \tag{5.13}$$

Then the pdf of the Fourier components is given by:

$$\prod_{j=1}^{N} \mathrm{d}\tilde{\mathbf{x}}(\mathbf{k}_j)\ \mathcal{P}\left(\tilde{\mathbf{x}}(\mathbf{k}_1), ..., \tilde{\mathbf{x}}(\mathbf{k}_N)\right) = \frac{1}{(2\pi)^{N/2}|\prod_i P(\mathbf{k}_i)|^{1/2}} \exp\left(-\frac{1}{2}\sum_i \frac{|\tilde{\mathbf{x}}(\mathbf{k}_i)|^2}{P(|\mathbf{k}_i|)}\right). \tag{5.14}$$

Since the Fourier transform is bijective the power spectrum contains the same information as the two-point correlation function. This means that all information of a linear process is encoded in the power spectrum and vice versa that the power spectrum only provides information about the linear properties of a signal.

5.3.1 Power spectral density and structure factor

The evolving domain size in demixing experiments is usually characterized by the structure factor (also power spectrum or power spectral density) [3, 54].

The Fourier transform $\mathcal{F}(\mathbf{k})$ of a smooth function $\rho(\mathbf{x}) : \mathbb{R}^N \to \mathbb{R}$ is given by:

$$\mathcal{F}(\mathbf{k}) = \int_{\mathbb{R}^N} \rho(\mathbf{x})\ \mathrm{e}^{i2\pi\mathbf{k}\cdot\mathbf{x}}\mathrm{d}^N\mathbf{x} \tag{5.15}$$

It can be decomposed into the Fourier amplitudes $|\mathcal{F}(\mathbf{k})|$ and the Fourier phases $\Phi(\mathbf{k})$ as

$$\mathcal{F}(\mathbf{k}) = |\mathcal{F}(\mathbf{k})|\,\mathrm{e}^{i\Phi(\mathbf{k})}. \tag{5.16}$$

The absolute square of the Fourier amplitudes is called the power spectrum $\mathcal{P}(\mathbf{k})$ (also structure factor $S(\mathbf{k})$):

$$\mathcal{P}(\mathbf{k}) = \mathcal{F}^*(\mathbf{k})\cdot\mathcal{F}(\mathbf{k}) = |\mathcal{F}(\mathbf{k})|^2\,. \tag{5.17}$$

In the discrete case the Fourier transform $\mathcal{F}_\mathbf{k}$ of a series $\rho_\mathbf{x} : \mathbb{R}^N \to \mathbb{R}, \rho \in \mathbb{R}, \mathbf{x} = (x_1, x_2, ..., x_N) \in \mathbb{R}^N, N \in \mathbb{N}$, sampled at n points $x_i \in \{1, 2, ..., n\}\forall i \in \{1, ..., N\}$ is given by:

$$\mathcal{F}_\mathbf{k} = \sum_{x_1=1}^{n}\sum_{x_2=1}^{n} ... \sum_{x_N=1}^{n} \rho_\mathbf{x}\ \mathrm{e}^{i2\pi\mathbf{k}\cdot\mathbf{x}/n} \tag{5.18}$$

Demixing dynamics are usually investigated by calculating the characteristic scale $L(t)$ of the fluid density distribution $\rho(x) : \mathbb{R} \to \mathbb{R}$. L is obtained by identifying the wave number k_{max} at the position of the maximum of $\mathcal{P}(k)$ as the length scale

$$L = \frac{2\pi}{k_{max}}, \tag{5.19}$$

where

$$k_{max} = \arg\max(P(k)). \tag{5.20}$$

k_{max} can be determined by fitting an off-critical fitting function, proposed in [54], in order to obtain the fitted structure factor $S(k)$:

$$S(k) \propto (k/k_{max})^2 \,/\, \left[2 + (k/k_{max})^6\right]. \tag{5.21}$$

5.3.2 Angular power spectral density

For the analysis of the structure factor in the case of systems on spherical geometry the need arises to define a orthonormal decomposition in harmonic functions on the sphere. To find the basis functions $\Psi(\mathbf{n})$ one has to solve the Laplace equation

$$\nabla^2 \Psi(\mathbf{n}) = 0. \tag{5.22}$$

$\mathbf{n}(\Theta, \Phi)$ is a direction on the sphere. Separation of variables $\Psi(\mathbf{n}) = A(\Theta)B(\Phi)$ leads to:

$$\frac{B(\Phi)}{\sin(\Theta)} \frac{\mathrm{d}}{\mathrm{d}\Theta} \left(\sin(\Theta) \frac{\mathrm{d}A(\Theta)}{\mathrm{d}\Theta} \right) + \frac{A(\Theta)}{\sin^2(\Theta)} \frac{\mathrm{d}^2 B(\Phi)}{\mathrm{d}\Phi^2} + l(l+1)A(\Theta)B(\Phi) = 0. \tag{5.23}$$

The harmonic functions solving Eq. (5.23) are the spherical harmonics $\Psi(\mathbf{n}) = Y_{lm}(\mathbf{n})$ given by

$$Y_{lm}(\mathbf{n}) = \sqrt{\frac{2l+1}{4\pi} \frac{(l-m)!}{(l+m)!}} P_l^m(\cos(\theta)) e^{im\Phi}, \tag{5.24}$$

with indices $l \in \mathbb{N}_0$ and $m \in \mathbb{Z}$ with $-l \leq m \leq l$. P_l^m are the Legendre polynomials. Any scalar function $\rho(\mathbf{n})$ on a spherical geometry can be decomposed in its spherical harmonics representation. The spherical harmonics $Y_{lm}(\mathbf{n})$ form a orthonormal base on the unit sphere.

l is the multipole and determines the "wave length". It counts the number of waves along a meridian. m determines the shape of the mode, it is the number of modes along the equator. This is illustrated in Fig. 5.3: The spherical harmonics $Y_{lm}(\mathbf{n})$ are presented for $l = 5$ and $m = 0, 1, 2, 3, 4, 5$. The average solid angle Ω corresponding to a specific l is $\Omega = 4\pi/2l$. Considering the division of the sphere in $2l$ equal slices, the widest part of these slices corresponds to an angle $\Theta = \pi/l$. This translates into a length scale $L = R \cdot \pi/l$, with the sphere radius R.

The function $\rho(\mathbf{n})$ can be expanded as:

$$\rho(n) = \sum_{l \geq 0} \sum_{|m| \leq l} a_{lm} Y_{lm}(\mathbf{n}), \tag{5.25}$$

with harmonic coefficients a_{lm} given by the projection

$$a_{lm} = \int \mathrm{d}\Omega \; \rho(\mathbf{n}) Y_{lm}^*(\mathbf{n}). \tag{5.26}$$

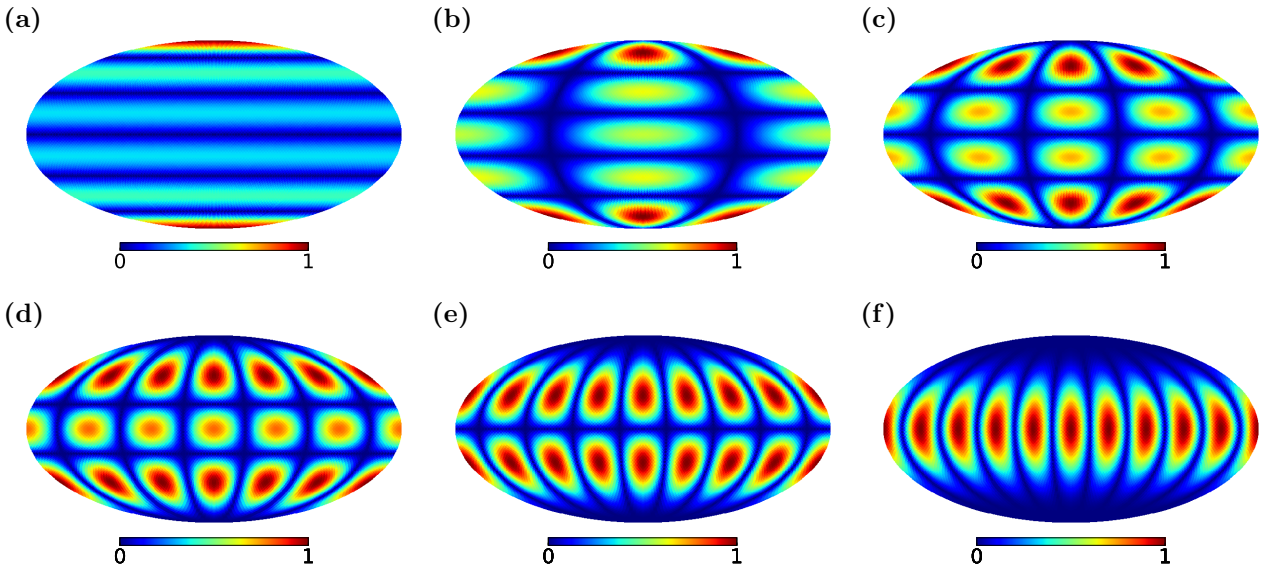

Figure 5.3: The spherical harmonics $Y_{lm}(\mathbf{n})$ an a sphere shown in the Mollweide projection. (a) $l = 5$, $m = 0$, (b) $l = 5$, $m = 1$, (c) $l = 5$, $m = 2$, (d) $l = 5$, $m = 3$, (d) $l = 5$, $m = 4$, (d) $l = 5$, $m = 5$.

The power spectrum C_l of the scalar field $\rho(n)$ can be defined via the harmonic coefficients a_{lm} obeying $\langle a_{lm} a^*_{l'm'} \rangle = \delta_{ll'} \delta_{mm'} C_l$ by

$$C_l = \frac{1}{2l+1} \sum_{|m| \leq l} \langle |a_{lm}|^2 \rangle. \tag{5.27}$$

The C_l are called the angular power spectral density. Since for any l there exist $2l + 1$ modes of m the total power for the multipole l is given by $(2l + 1) \cdot C_l$.

In the following we analyze the position $l_{\max}$ and value $C_{l,\max}$ of the maximum of the power spectral density. $l_{\max}$ is a measure for the length scale of the most dominant pattern. This quantity is the standard metric to characterize the domain growth of demixing processes [29, 169, 162, 178, 25]. Here we also introduce the power $C_{l,\max}$ as a measure for the domain growth. $C_{l,\max}$ is a measure for the dominance of the most predominant pattern (in terms of spherical harmonics) of the function on the sphere.

The position of the maximum is determined via fitting the off-critical fitting function

$$S(l,t) \propto (l \cdot L(t)/2\pi)^2 \,/\, \left[2 + (l \cdot L(t)/2\pi)^6\right] \tag{5.28}$$

[54].

5.4 Nonlinear morphological measures

The power spectrum and the pair correlation function only characterize linear properties as they are defined by two-point density correlation functions. Thus, it can be beneficial to

extend the analysis of spatial data to measures that also capture the nonlinear information encoded in higher order correlation functions. Formulated in Fourier space this means to capture the information decoded in the Fourier phases. The difference between an image analysis based on only the Fourier amplitudes as compared to the Fourier phases is presented in Fig. 5.4. Here two greyscale portraits are Fourier transformed, then the

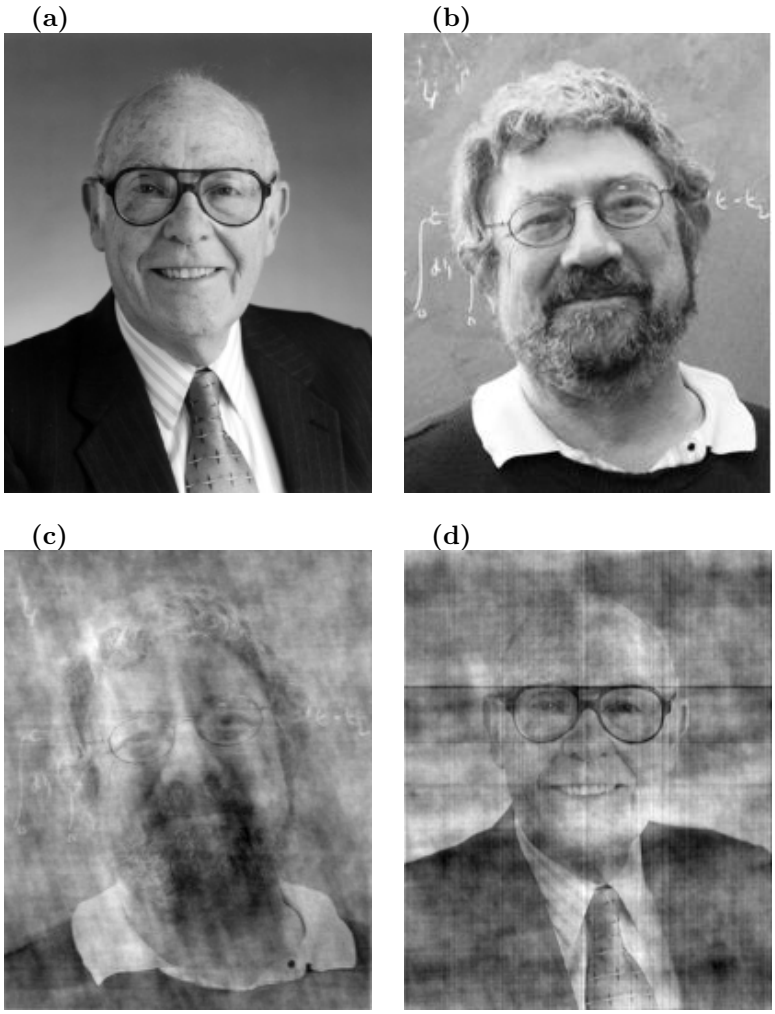

Figure 5.4: Fourier transform of greyscale images. J. W. Cahn is portrayed in panel (a), J. M. Kosterlitz in panel (b). The Fourier transform of panels a,b is given by $\mathcal{F}_{a,b}(\mathbf{k}) = |\mathcal{F}_{a,b}(\mathbf{k})|e^{-i\phi_{a,b}(\mathbf{k})}$. The lower panels present the inverse Fourier transform with exchanged phases and amplitudes: Panel (c) presents $FT^{-1}[|\mathcal{F}_a(\mathbf{k})|e^{-i\phi_b(\mathbf{k})}]$. Panel (d) presents $FT^{-1}[|\mathcal{F}_b(\mathbf{k})|e^{-i\phi_a(\mathbf{k})}]$. Clearly the morphological information is encoded in the Fourier phases. Inspired by C. Räth [141].

amplitudes of the first image are combined with the phases of the second (and vice versa) before the inverse Fourier transform is shown. The portraits can be recognized due to the information in the Fourier phases since they encode the structural information of the

images. This also shows that human texture recognition must be a nonlinear process. (For a theory of human visual perception consult [79, 80]. It was shown that texture discrimination relies on a few conspicuous features, called textons.)

Another example where the linear, isotropic nature of the power spectrum analysis shows is limitation is shown in Fig. 5.5. Here a snapshot of a molecular dynamics simulation of a binary complex plasma is show. The two particle species are initially mixed and then dynamically demix. At first neighboring particles start to agglomerate in disjoint spherical domains. However, at later times these domains start to coalesce. This process is discussed in more detail in section 7. During the coalescence the shape of the domains is anisotropic and can obviously not be described by a single number as would be the case when choosing the maximum of the structure factor. In this case an explicitly anisotropic shape metric is needed.

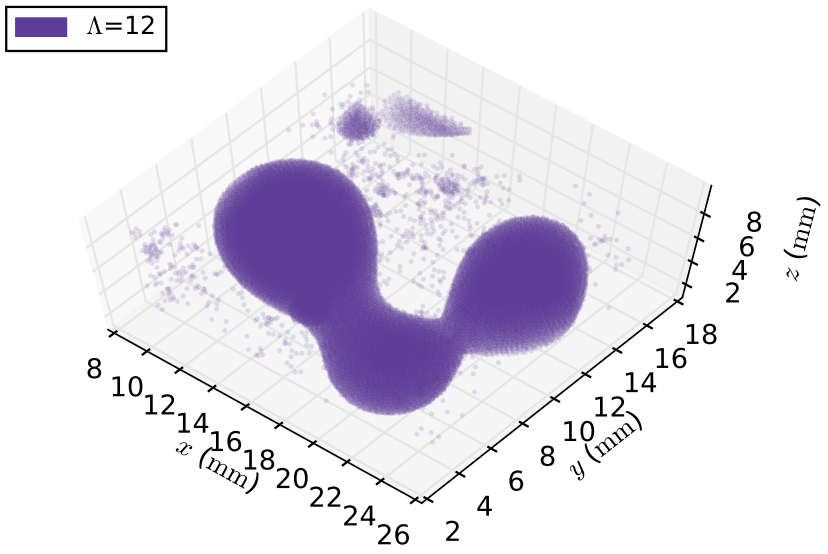

Figure 5.5: Anisotropic domain shape of the minority particles in a binary complex plasma molecular dynamics simulation during demixing. The screening length ratio (Eq. (4.12)) is $\Lambda = 12$.

One possibility to define shape metrics that capture the nonlinear information in higher order correlations are Minkowski functionals. By extending their definition to higher rank tensors it is also possible to define explicit anisotropy measures and metrics sensitive to specific structure symmetries.

5.4.1 Minkowski functionals

In the early 20th century [120] Minkowski functionals have been introduced and discussed in the context of integral geometry [175, 149]. Later their potential for morphological data analysis was discovered after their application to the analysis of the large-scale structure of the universe [114]. They characterize not only the geometrical properties and the shape of structured data but also their topology and connectedness. They can provide insight into physical processes where conventional linear measures cannot since they are sensitive to n-point correlation functions for any order n [114] and thus respond to nonlinear properties.

Definition

The Minkowski functionals can be defined as integrals on smooth bodies and their boundaries. In two dimensions they are familiar quantities: The area, the perimeter and the Euler characteristic. The Euler characteristic is a topological invariant that measures the connectedness of a pattern. In two dimensions it can be calculated as the sum of all connected regions in the pattern minus the number of holes in these regions. In three dimensions they are the volume, the surface area, the integrated mean curvature, which is proportional to the mean width, and again the Euler characteristic. In three dimensions the Euler characteristic is given by the number of connected regions plus the number of holes in those regions minus the number of tunnels piercing through connected regions.

For a body K with a smooth boundary contour ∂K embedded in D-dimensional Euclidean space $\mathbb{E}^D$ the $D+1$ Minkowski functionals are defined as:

$$\begin{aligned} M_0(K) &= \int_K \mathrm{d}^D\mathbf{x} \\ M_\nu(K) &= \int_{\partial K} G_\nu(\mathbf{x})\,\mathrm{d}^{D-1}\mathbf{x} \quad , \quad 1 \le \nu \le D \end{aligned} \tag{5.29}$$

$G_\nu(\mathbf{x})$ are the elementary symmetric polynomials of the local principal curvatures as defined in differential geometry.

Properties

Minkowski functionals are motion invariant, i.e. they are invariant under translations $\mathbf{t}$ or rotations $\hat{O}$:

$$\begin{aligned} M_\nu(K+\mathbf{t}) &= M_\nu(K) \\ M_\nu(\hat{O}\,K) &= M_\nu(K) \end{aligned} \tag{5.30}$$

They are additive

$$M_\nu(K_1 \cup K_2) = M_\nu(K_1) + M_\nu(K_2) - M_\nu(K_1 \cap K_2) \tag{5.31}$$

and conditionally continuous. This means that for a convergent (with respect to the Hausdorff metric) series of bodies $\{K_n \to K | n \to \infty\}$ the series of Minkowski functionals

also converges:

$$\lim_{n\to\infty} M_\nu(K_n) = M_\nu(K) \tag{5.32}$$

They form a complete family of morphological measures. The completeness theorem [61] states that any motion invariant, conditionally continuous and additive functional $\mathcal{F}$, defined on a subset of Euclidean space S that can be represented as a finite union of closed bounded convex sets, necessarily is a Minkowski functional or a linear combination of Minkowski functionals:

$$\mathcal{F}(S) = \sum_{\nu=0}^{D} = c_\nu M_\nu(S) \tag{5.33}$$

with coefficients $c_\nu \in \mathbb{R}$. They are homogenous functions of order $D-\nu$:

$$M_\nu(\lambda K) = \lambda^{D-\nu} M_\nu(K) \tag{5.34}$$

They are proportional to n-point correlation function for any n and thus are sensitive to nonlinear properties. This becomes directly clear when considering the mean value of the Minkowski functional density of a set of points $\{\mathbf{x}_i | i = 1, ..., N, N \in \mathbb{N}\}$ in three dimensional Euclidean space $\mathbb{E}^3$ covered by spherical balls $B_r(\mathbf{x}_i) = \{\mathbf{x} \in \mathbb{E}^3 | \parallel \mathbf{x} - \mathbf{x}_i \parallel \leq r\}$ as $\mathcal{B}(r) = \cup_{i=1}^{N} B_r(\mathbf{x}_i)$ in a volume Ω. Generally the statistics in the point set are characterized by the density correlation functions $\{\rho_n(\mathbf{x}_1, ..., \mathbf{x}_N) | n = 1, ..., N\}$. Then, due to the additivity Eq. (5.31), the mean Minkowski functional density is given by:

$$\left\langle \frac{M_\nu(\mathcal{B}(r))}{\Omega} \right\rangle = \sum_{n=1}^{N} \frac{(-1)^{n+1}}{n!\Omega} \prod_{k=1}^{n} \int_\Omega \mathrm{d}^3\mathbf{x}_k \; \rho_k(\mathbf{x}_1, ..., \mathbf{x}_k)) \; M_\nu(\cap_{i=1}^{N} B_r(\mathbf{x}_k)) \tag{5.35}$$

according to [114]. This is their main advantage in comparison with linear measures. Since they are proportional to n-point correlations for any n, they capture the full nonlinear structural information. In addition they not only characterize shape and geometry, but also topological connectedness. In this sense they are extraordinary useful measures for the full morphological characterization of spatial patterns. Another attractive property is that, while being based on a rigorous mathematical framework, they still are easy to interpret and applications are manifold: For example in the curvature energy of membranes [69], in the order parameter in Turing patterns [113], in a density functional theory for fluids (as hard balls or ellipsoids) [144, 112], for testing point distributions (find clusters, filaments, underlying point-process) or for searching for non-Gaussian signatures in the CMB [148, 177, 121, 145, 122].

Functionals in two dimensions

In two dimensions the three Minkowski functionals $M_0(K)$ (area), $M_1(K)$ (perimeter) and $M_2(K)$ (euler characteristic) are given by:

$$
\begin{aligned}
M_0(K) &= \int_K \mathrm{d}^2\mathbf{x} \\
M_1(K) &= \int_{\partial K} \mathrm{d}\mathbf{x} \\
M_2(K) &= \int_{\partial K} \kappa(\mathbf{x})\, \mathrm{d}\mathbf{x}
\end{aligned}
\tag{5.36}
$$

Here, $\kappa(x)$ is the local Gaussian curvature.

Functionals in three dimensions

In three-dimensional Euclidean space the four Minkowski functionals $M_0(K)$ (volume), $M_1(K)$ (area), $M_2(K)$ (integrated mean curvature) and $M_3(K)$ (euler characteristic) are given by:

$$
\begin{aligned}
M_0(K) &= \int_K \mathrm{d}^3\mathbf{x} \\
M_1(K) &= \int_{\partial K} \mathrm{d}^2\mathbf{x} \\
M_2(K) &= \int_{\partial K} \kappa_1(\mathbf{x}) + \kappa_2(\mathbf{x})\, \mathrm{d}^2\mathbf{x} \\
M_3(K) &= \int_{\partial K} \kappa_1(\mathbf{x})\kappa_2(\mathbf{x})\, \mathrm{d}^2\mathbf{x}
\end{aligned}
\tag{5.37}
$$

$\kappa_1(x)$ and $\kappa_2(x)$ are the local principle curvatures.

Calculation

Due to the additivity (Eq. (5.31)) of the Minkowski functionals they can be calculated by summing up their local contributions. Local contributions can be obtained by the pixelization and binarization of data. Pixelized data $P(\mathbf{r})$ of a set $\mathcal{S}$ can be binarized by setting a threshold value T. The excursion set K_T is the set of all pixels with a value greater than or equal to T:

$$
K_T = \{\mathbf{x} \in \mathcal{S} | P(\mathbf{x}) \geq T\} \tag{5.38}
$$

This divides the set of pixels into a subset of "active" pixels and a subset of "inactive" pixels. An algorithm to compute Minkowski functionals of binary pixelized data was proposed in [118]. In the two-dimensional case every pixel is decomposed into 4 vertices, 4 edges and its interior square. The number of active interiors n_s is counted, as is the number of edges n_e and vertices at the interface between active and inactive pixels. This decomposition is illustrated in Fig. 5.6 for a square of nine pixel of which 8 are active encircling an inactive hole. The Minkowski functionals, the area M_0, the integral mean curvature or perimeter M_1 and the Euler characteristic M_2, can then be calculated as sums, by counting

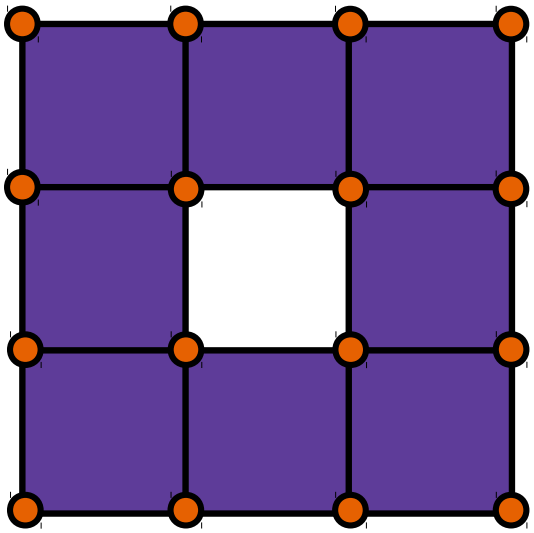

Figure 5.6: Illustration for the calculation of Minkowski functionals. The pixels are decomposed in n_s squares, n_e edges and n_s vertices. Here we have $n_s = 8$, $n_e = 24$ and $n_v = 16$. Active squares are colored. Adapted from [118].

elementary geometric objects:

$$\begin{aligned} M_0 &= n_s \\ M_1 &= -4n_s + 2n_e \\ M_2 &= n_s - n_e + n_v. \end{aligned} \tag{5.39}$$

For the example in Fig. 5.6 this yields $M_0 = 8$, $M_1 = 16$ and $M_2 = 0$.

In the three dimensional case the pixels are decomposed into 8 vertices, 12 edges, 6 faces in their interior cube. The number of cubes n_c, and the number of vertices n_v, edges n_e and faces n_f at the active/inactive pixel interfaces are counted. Then the Minkowski functionals can be calculated simply by the summations:

$$\begin{aligned} M_0 &= n_c \\ M_1 &= -6n_c + 2n_f \\ 2M_2 &= 3n_c - 2n_f + n_e \\ M_3 &= -n_c + n_f - n_e + n_v. \end{aligned} \tag{5.40}$$

To avoid the double counting of any vertices, edges or faces the original images can be build up step by step by starting with a specific active pixel and then individually adding neighboring pixels to a temporary image. This was suggested in [118]. The temporary number of edges, vertices or faces is only added to the total number if all neighboring

pixels have been added. The number of arithmetic operations required to compute M_0, M_1, and M_2 scales linearly with the number of active pixels and the total number of pixels in the image.

5.4.2 Minkowski tensors

With the scalar valued and motion invariant Minkowski functionals it is not possible to define an explicit measure for anisotropy. However, it is natural to extend the scalar Minkowski functionals to tensor valued quantities, called Minkowski tensors (MTs) by introducing tensor products of position and normal vectors. It is straight forward to define explicit anisotropy measures with Minkowski tensors of rank two. By applying higher rank tensors it is also possible to define metrics that are sensitive to specific (high-fold) symmetries.

Definition

Minkowski tensors are defined as [152]:

$$\begin{aligned} W_0^{a,0}(K) &:= \int_K \mathrm{d}^D\mathbf{x}\ \ \mathbf{x}^{\odot a} \\ W_\nu^{a,b}(K) &:= 1/D \int_{\partial K} \mathrm{d}^{D-1}\mathbf{x}\ \ G_\nu(\mathbf{x})\ \ \mathbf{x}^{\odot a} \odot \mathbf{n}^{\odot b} \end{aligned} \tag{5.41}$$

Here, $\odot$ denotes the symmetric tensor product $\mathbf{x} \odot \mathbf{y} = 1/2\,(\mathbf{x} \otimes \mathbf{y} + \mathbf{y} \otimes \mathbf{x})$. Again $G_\nu(\mathbf{x})$ are the elementary symmetric polynomials of the local principal curvatures as defined in differential geometry. a counts the number of position vectors $\mathbf{x}$, b counts the number of normal vectors $\mathbf{n}$ in the tensor product. Thus the rank of each tensor is the tuple (a, b).

Properties

Their properties are as follows: They are isometry covariant, i.e their behavior under translation $\mathbf{t}$ and rotation $\hat{O}$ is given by:

$$\begin{aligned} W_\nu^{a,b}(K + \mathbf{t}) &= \sum_{i=0}^{a} \binom{a}{i} \mathbf{t}^i\, W_\nu^{a-i,b}(K) \\ W_\nu^{a,b}(\hat{O}\,K) &= \hat{O}_{a+b}\, W_\nu^{a,b}(K) \end{aligned} \tag{5.42}$$

They are additive:

$$W_\nu^{a,b}(K_1 \cup K_2) = W_\nu^{a,b}(K_1) + W_\nu^{a,b}(K_2) - W_\nu^{a,b}(K_1 \cap K_2) \tag{5.43}$$

and they are homogeneous of degree $D + a - \nu$, $a \in \mathbb{R}$, $\nu \in \mathbb{R}$ for isotropic scaling with a factor $\lambda \in \mathbb{R}$:

$$W_\nu^{a,b}(\lambda K) = \lambda^{D+a-\nu}\, W_\nu^{a,b}(K) \tag{5.44}$$

Similar to Minkowski functionals the attractiveness of Minkowski tensors is due to their manifold applications. Furthermore, they are founded on a solid mathematical framework: A strong completeness theorem by Alesker [6] states that all morphological information that is relevant for additive properties of a body K is represented by the Minkowski tensors. Any motion covariant, conditionally continuous and additive tensor valued functional $\mathcal{T}$ is a superposition of the (countably many) Minkowski tensors. In the specific case of rank two tensors this can be expressed as:

$$\mathcal{T}(K) = \sum_{\nu=0}^{D} \left(T_\nu^{0,0} \cdot W_\nu(K) E_D + \sum_{a=0}^{2} T_\nu^{a,2-a} \cdot W_\nu^{a,2-a}(K) \right) \tag{5.45}$$

with real coefficients $T_\nu^{a,b}$ that are independent of the particular choice of the body K.

The Minkowski tensors have a very intuitive interpretation. The position vector tensors are proportional to tensors of inertia. $W_0^{2,0}$ has the form of the tensor of inertia when the mass of the body is homogeneously distributed. When all the mass of the body is concentrated on its boundary the tensor of inertia is proportional to $W_1^{2,0}$. For a three-dimensional solid object with its mass located solely on its edges or its vertices, the Minkowski tensor $W_2^{2,0}$ respectively $W_3^{2,0}$ is the tensor of inertia when the masses are weighted with the angles between boundary surfaces or edges. The tensor $W_1^{0,2}$ is the covariance tensor of the normal vector distribution and $W_2^{0,2}$ is proportional to the covariance tensor of its normal distribution weighted by the normal distribution. These interpretations are illustrated in Fig. 5.7 for the two-dimensional case.

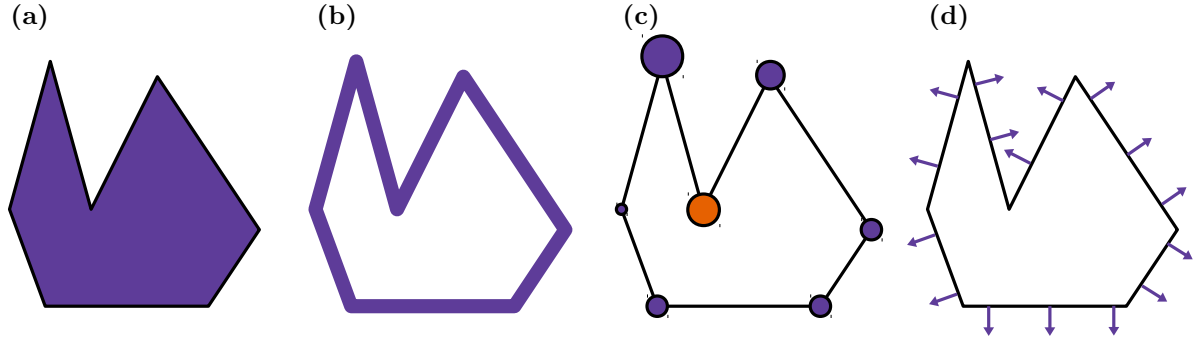

Figure 5.7: Illustration of the interpretation of Minkowski tensors in two dimensions. The Minkowski tensors are the moments of inertia for different mass distributions. (a) $W_0^{2,0}$ for a homogeneous mass distribution. (b) $W_1^{2,0}$ for the mass concentrated on the boundary. (c) $W_2^{2,0}$ for masses proportional to the interior angles (negative for concave vertices) at the vertices. (d) $W_1^{0,2}$ is an tensor representation of the normal vector distribution.

Applications of Minkowski tensors range from the analysis of cellular, granular and porous structures to the classification of crystal types [71, 82, 147, 151, 43, 90, 25].

Calculation

The Minkowski tensors are defined as curvature integrals over smooth boundary surfaces. Digital data, however, is obviously not smooth. This problem can be circumvented by the introduction of a smooth parallel body construction. Due to their continuousness the limit of the Minkowski tensors of a body that is infinitesimally extended and smoothed exists for a vanishing extension and it can be used to calculate explicit finite formulae for Minkowski tensors of triangulated surfaces.

In order to calculate Minkowski tensors for polygonal bodies P we consider the parallel body construction

$$P_\epsilon = P \uplus S_\epsilon \tag{5.46}$$

[150]. S_ϵ is a disk of radius $\epsilon > 0$ and $\uplus$ is the Minkowski sum, defined as:

$$K_1 \uplus K_2 = \{p_1 + p_2 \mid p_1 \in K_1, p_2 \in K_2\}\,. \tag{5.47}$$

Thus, P_ϵ is the union of all disks S_ϵ with origins at all points in P. This extends the boundary of P by an amount ϵ outwards and smooths the kinks at the vertices to circular arcs as illustrated in Fig. 5.8.

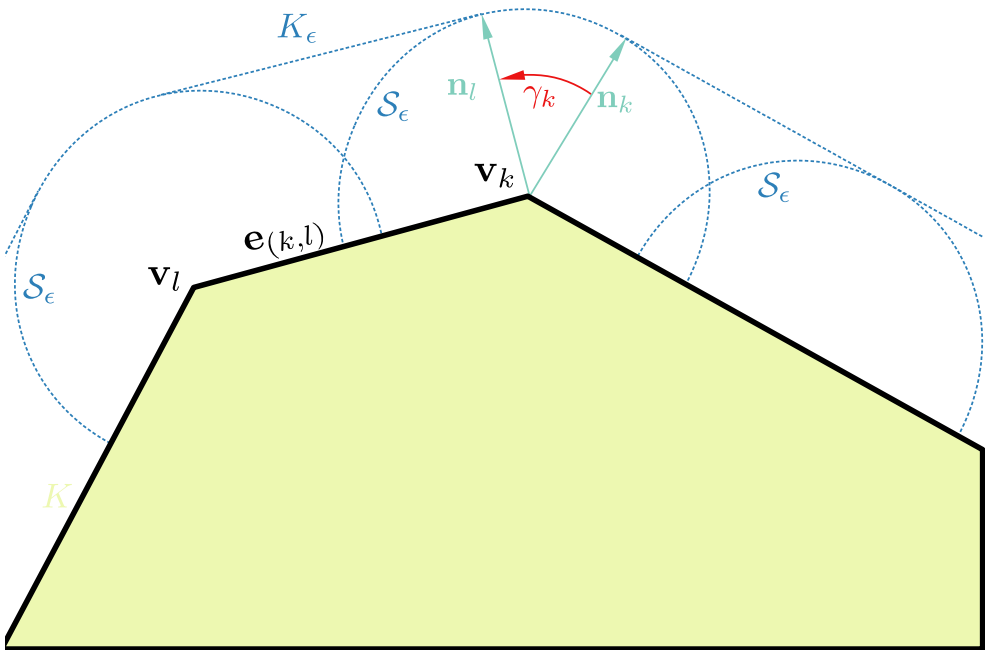

Figure 5.8: Illustration for the explicit calculation of Minkowski tensors of a body K via K_ϵ.

Performing the limit $\epsilon \to 0$ then yields the tensor

$$W_\nu^{a,b}(P) = \lim_{\epsilon \to 0} W_\nu^{a,b}(P_\epsilon). \tag{5.48}$$

In two dimensions, consider the polygonal representation of P by its vertices $\mathbf{v}_k$. Then the edges between vertices $\mathbf{v}_k$ and $\mathbf{v}_l$ are

$$e_{(k,l)} = \mathbf{v}_l - \mathbf{v}_k \tag{5.49}$$

with normal vectors

$$\mathbf{n}_{(k,l)} = \frac{R\,\mathbf{e}_{(k,l)}}{\left|\mathbf{e}_{(k,l)}\right|}. \tag{5.50}$$

Here

$$R = \begin{pmatrix} 0 & -1 \\ -1 & 0 \end{pmatrix} \tag{5.51}$$

is the $\pi/2$ rotation matrix. γ_k is the angle between $\mathbf{n}_{(k-1,k)}$ and $\mathbf{n}_{(k,k+1)}$. Using these definitions we can obtain the explicit formula to calculate e.g. the second rank tensor:

$$\begin{aligned} W_1^{2,0}(P) &= \lim_{\epsilon\to 0}\frac{1}{2}\int_{\partial P_\epsilon} \mathrm{d}\mathbf{x}\;\; \mathbf{x}\odot\mathbf{x} \\ &= \lim_{\epsilon\to 0}\frac{1}{2}\sum_{(k,l)}\left|\mathbf{e}_{(k,l)}\right|\frac{1}{2}\{(\mathbf{v}_k+\epsilon\mathbf{n}_{(k,k+1)})\odot(\mathbf{v}_k+\epsilon\mathbf{n}_{(k,k+1)}) \\ &+ (\mathbf{v}_k+\epsilon\mathbf{n}_{(k,k+1)})\odot(\mathbf{v}_l+\epsilon\mathbf{n}_{(l,l+1)}) + (\mathbf{v}_l+\epsilon\mathbf{n}_{(l,l+1)})\odot(\mathbf{v}_l+\epsilon\mathbf{n}_{(l,l+1)})\} \\ &= \frac{1}{6}\sum_{(k,l)}\left|\mathbf{e}_{(k,l)}\right|\{\mathbf{v}_k\odot\mathbf{v}_k+\mathbf{v}_k\odot\mathbf{v}_l+\mathbf{v}_l\odot\mathbf{v}_l\} \\ &= \frac{1}{6}\sum_{(k,l)}\left|\mathbf{e}_{(k,l)}\right|\cdot\begin{pmatrix} v_{kx}^2+v_{kx}v_{lx}+v_{lx}^2 & v_{kx}v_{ky}+v_{kx}v_{ly}+v_{lx}v_{ly} \\ v_{ky}v_{kx}+v_{ky}v_{lx}+v_{ly}v_{lx} & v_{ky}^2+v_{ky}v_{ly}+v_{ly}^2 \end{pmatrix} \end{aligned} \tag{5.52}$$

For the calculation of expression of the curvature tensors, the parametrization of the normal field to the boundary curve

$$\mathbf{n}(\tau) = \cos(\tau)\mathbf{n}_{(\mathbf{k},\mathbf{l})} + \sin(\tau)\mathbf{t}_{(\mathbf{k},\mathbf{l})} \tag{5.53}$$

is considered. The tangent vectors to ∂P are

$$\mathbf{t}_{(k,l)} = R^{-1}\mathbf{n}_{(k,l)} \tag{5.54}$$

To avoid a lengthy calculation we introduce the variable $\Gamma(\mathbf{n})$ as the angle between $\mathbf{n}$ and the x-axis. This leads to the vanishing of off-diagonal term due to the symmetry of the

trigonometric functions for integration over the closed polygon boundary. E.g.

$$\begin{aligned} W_2^{0,2}(P) &= \lim_{\epsilon\to 0}\frac{1}{2}\int_{\partial P_\epsilon} \mathrm{d}\mathbf{x}\ \ \kappa(x)\ \mathbf{n}\odot\mathbf{n} \\ &= \lim_{\epsilon\to 0}\frac{1}{2}\sum_k \int_0^{\gamma_k} \epsilon \mathrm{d}\tau \frac{1}{\epsilon}\ \mathbf{n}\odot\mathbf{n} \\ &= \frac{1}{2}\sum_k \int_{\Gamma(\mathbf{n}_{(\mathbf{k-1,k})})}^{\Gamma(\mathbf{n}_{(\mathbf{k,k+1})})} \mathrm{d}\Gamma \begin{pmatrix}\cos(\Gamma)\\ \sin(\Gamma)\end{pmatrix}\odot\begin{pmatrix}\cos(\Gamma)\\ \sin(\Gamma)\end{pmatrix} \\ &= \frac{1}{2}\sum_k \int_{\Gamma(\mathbf{n}_{(\mathbf{k-1,k})})}^{\Gamma(\mathbf{n}_{(\mathbf{k,k+1})})} \mathrm{d}\Gamma \begin{pmatrix}\cos^2(\Gamma) & 0\\ 0 & \sin^2(\Gamma)\end{pmatrix} \\ &= \frac{1}{4}\sum_k \left(\Gamma(\mathbf{n}_{(k,k+1)}) - \Gamma(\mathbf{n}_{(k-1,k)})\right)\ E \\ &= \frac{1}{4}\sum_k \gamma_k\ E \\ &= 4\ W_2\ E_2, \end{aligned} \tag{5.55}$$

where E_2 is the two-dimensional unit matrix.

In the three-dimensional case the body K is considered by its triangulated surface. Its vertices are $\mathbf{v}_k$. The vertices $\mathbf{v}_k$ and $\mathbf{v}_l$ are connected by edges $\mathbf{e}_{(k,l)} = \mathbf{v}_l - \mathbf{v}_k$. The facet spanned by the vertices $\mathbf{v}_k$, $\mathbf{v}_l$ and $\mathbf{v}_m$ have area $A_{(k,l,m)}$ and an outward facing normal vector $\mathbf{n}_{(k,l,m)}$. The normalized mean of neighboring facet normal $\mathbf{n}_{(k,l,m)}$ and $\mathbf{n}_{(l,m,n)}$ is called $\mathbf{n}_{(l,m)}$. The angle $\gamma_{(k,l,m)}$ is measured between edges $\mathbf{e}_{(k,l)}$ and $\mathbf{e}_{(l,m)}$. $\gamma_{(k,l)}$ is the dihedral angle of the edge $\mathbf{e}_{(k,l)}$ and γ_k is the angular defect of the vertex v_k, given by:

$$\gamma_k = 2\pi - \sum_{(k,l,m)} \gamma_{(k,l,m)}. \tag{5.56}$$

Minkowski tensor measures

Rank 2 isotropy index β The isotropy of a body K can be characterized as the ratio of the smallest eigenvalue λ_{min} and largest eigenvalue λ_{max} of the DxD representation matrix for each Minkowski tensor $W_\nu^{a,b}$ [152]:

$$\beta_\nu^{a,b}(K) := \frac{\lambda_{min}\left(W_\nu^{a,b}(K)\right)}{\lambda_{max}\left(W_\nu^{a,b}(K)\right)} \tag{5.57}$$

$\beta \in [0,1]$ is dimensionless and a pure shape measure that is invariant under isotropic $\lambda K = \{\lambda\mathbf{x}|\mathbf{x}\in K, \lambda\in\mathbb{R}\}$ scaling of the body K. It assumes its highest value for objects that do not have a preferred directionality in the sense of elongation. E.g. in two dimensions $\beta = 1$ for a circle or a square. For a rectangle with side lengths a, and b, the isotropy

index is $\beta = a/b$. This means that β in not a measure of asphericity (the deviation from a sphere) but of anisotropy with the meaning of directedness.

β can be used as an order parameter in point sets $\{\mathbf{x}_k\}, k \in \mathbb{N}$ in a metric space $\mathcal{M}$. For any point set one can bijectively define its Voronoi tessellation. It is the partition of space into N convex polytopes V_k, the Voronoi cells, that each contain the set of points that is closer to $\mathbf{x}_k$ than to any other $\mathbf{x}_l, l \neq k$:

$$V_k = \{\mathbf{u} \in \mathcal{M} | d(\mathbf{u}, \mathbf{x}_k) < d(\mathbf{u}, \mathbf{x}_l), \forall k \neq l\} \tag{5.58}$$

β is equal to 1 for Voronoi cells of ideal lattices, e.g. fcc, hcp or bcc crystals. When the crystal is disturbed, the value of β of distorted Voronoi cells decreases. Elementary applications are artificially generated point sets of large ideal crystals of type hcp, fcc and bcc superimposed with Gaussian noise $\mathcal{N}(\mu_k = \mathbf{x}_k, \sigma = \delta \cdot l)$. δ is the mean interparticle separation, and $l \in [0, 1]$ scans the space of standard deviations in the range of δ. Fig. 5.9 (left panels) shows the mean isotropy index β averaged over all Voronoi cells of the ideal lattices in relation to the noise level expressed in standard deviations measured in units of the mean interparticle separation. The ideal value of $\langle\beta\rangle = 1$ drops exponentially when the noise level is increased for all tensors and crystal types. The amount it decreases is dependent only on the specific tensor but independent of the crystal type. This illustrates that β can be used as a measure for the order of a crystal (or a general point set), but it is not able to distinguish between particular types of symmetries, e.g. fcc, hcp or bcc.

Rank 4 In order to distinguish between structures of high symmetry, i.e. differentiate between crystalline structures (hcp, fcc, etc.), higher ranked tensors have to be applied. For rank four and higher, isotropic symmetry is distinct from cubic symmetry. (This is evidenced by the appearance of a second independent shear modulus when transitioning from isotropic to cubic symmetry in the theory of linear elasticity, which is formulated using a rank-four tensor, the compliance tensor S_{ijkl} of an arbitrarily anisotropic elastic solid [172]. S_{ijkl} relates stress components linearly to each strain component.) This method has been used in hard sphere systems to characterize random close packings [82].

For brevity, only the simplest rank four Minkowski tensor is considered:

$$W_1^{0,4}(K) = \frac{1}{2} \int_{\partial K} \mathrm{d}\mathbf{x}\, \mathbf{n}(\mathbf{x}) \otimes \mathbf{n}(\mathbf{x}) \otimes \mathbf{n}(\mathbf{x}) \otimes \mathbf{n}(\mathbf{x}). \tag{5.59}$$

In the two-dimensional polygonal representation its components, labeled $\mu, \nu, \tau, \sigma \in (x, y)$ are:

$$\left[W_1^{0,4}(P)\right]_{\mu\nu\tau\sigma} = \frac{1}{2} \sum_{(k,l)} \left|\mathbf{e}_{(k,l)}\right| \cdot \left[\mathbf{n}_{(k,l)}\right]_\mu \left[\mathbf{n}_{(k,l)}\right]_\nu \left[\mathbf{n}_{(k,l)}\right]_\tau \left[\mathbf{n}_{(k,l)}\right]_\sigma . \tag{5.60}$$

In the three-dimensional ($\mu, \nu, \tau, \sigma \in \{x, y, z\}$) triangulated representation the components are:

$$\left[W_1^{0,4}(K)\right]_{\mu\nu\tau\sigma} = \frac{1}{3} \sum_{(k,l,m)} A_{(k,l,m)} \cdot \left[\mathbf{n}_{(k,l,m)}\right]_\mu \left[\mathbf{n}_{(k,l,m)}\right]_\nu \left[\mathbf{n}_{(k,l,m)}\right]_\tau \left[\mathbf{n}_{(k,l,m)}\right]_\sigma . \tag{5.61}$$

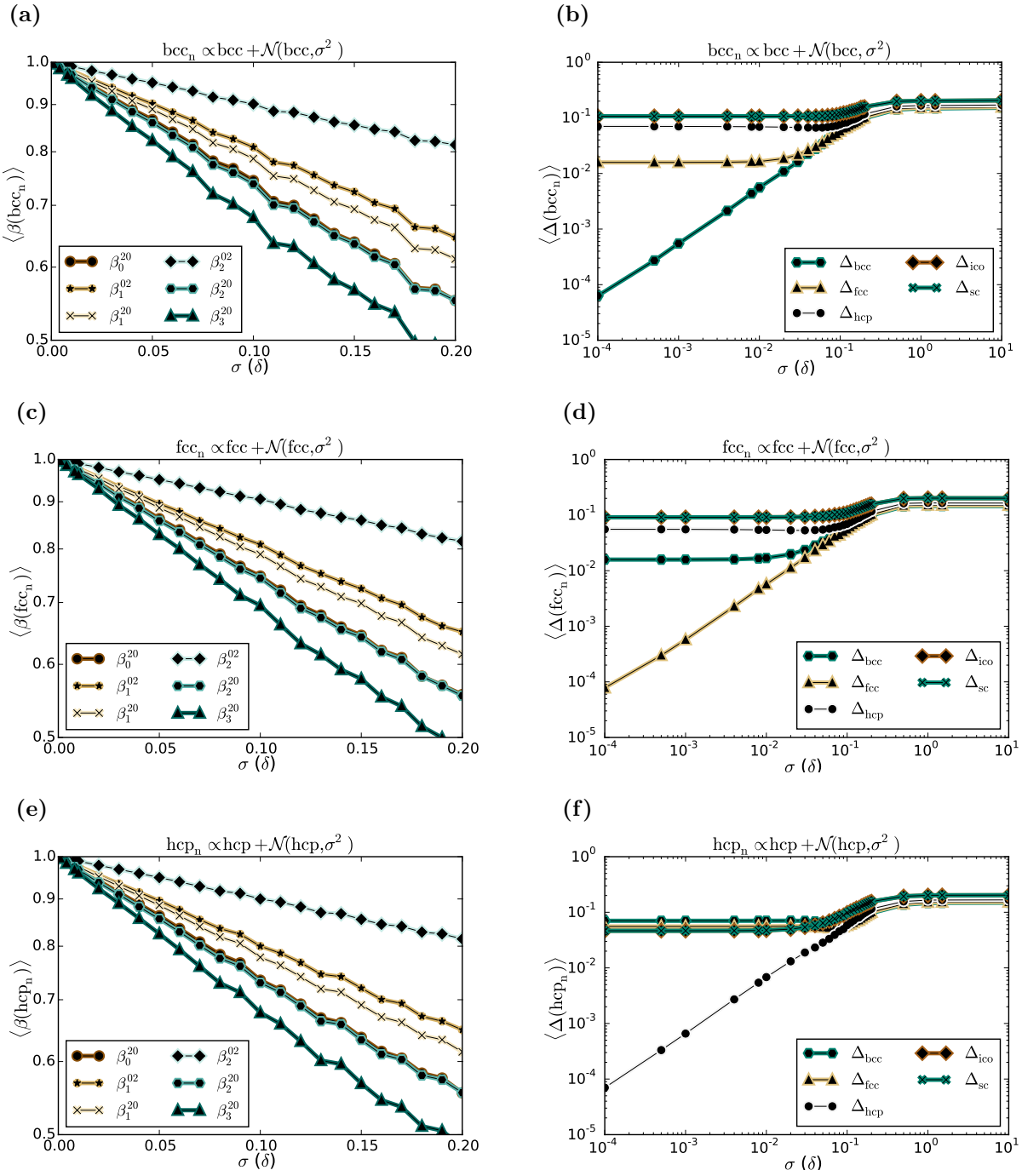

Figure 5.9: Elementary applications of Minkowski tensor measures on ideal crystals superimposed with Gaussian noise of variance σ^2. Left (panel (a),(c),(e)): The mean isotropy index $\langle\beta\rangle$ (Eq. (5.57)) drops exponentially with increasing noise. This can be used to distinguish between ideal crystal and distorted crystal cells. Right (panel (b),(d),(f)): The mean symmetry metric $\langle\Delta\rangle$ (Eq. (5.65)) allows for the identification of specific crystal types.

Since it is translation invariant and symmetric (i.e. it holds for the components $\left[W_1^{0,4}\right]_{\mu\nu\tau\sigma} = \left[W_1^{0,4}\right]_{(\mu\nu\tau\sigma)}$, here the round bracket $(\cdot)$ denotes all cyclic permutations) it has, in two dimensions, only 5 independent elements instead of 16. In three dimensions it only has 15 independent elements instead of 81.

A morphological metric suitable for characterizing systems of spherical particles should be rotationally invariant since the physics does not a priori designate a preferred direction. Thus, the tensor $W_1^{0,4}$ should not be directly used. Instead, rotational invariants are constructed [81]. This is done by borrowing ideas from the theory of the elastic stiffness tensor.

The tensor $W_1^{0,4}(K)$ is rewritten in the Mehrabadi supermatrix notation [116] as a 3×3 matrix in the two-dimensional case

$$M = \begin{bmatrix} S_{xxxx} & S_{xxyy} & S_{xxzz} \\ S_{yyxx} & S_{yyyy} & \sqrt{2}\,S_{yyxy} \\ \sqrt{2}\,S_{xyxx} & \sqrt{2}\,S_{xyyy} & 2S_{xyxy} \end{bmatrix} \tag{5.62}$$

and as a 6×6 matrix in the three-dimensional case:

$$M = \begin{bmatrix} S_{xxxx} & S_{xxyy} & S_{xxzz} & \sqrt{2}\,S_{xxyz} & \sqrt{2}\,S_{xxxz} & \sqrt{2}\,S_{xxxy} \\ S_{xxyy} & S_{yyyy} & S_{yyzz} & \sqrt{2}\,S_{yyyz} & \sqrt{2}\,S_{yyxz} & \sqrt{2}\,S_{yyxy} \\ S_{xxzz} & S_{yyzz} & S_{zzzz} & \sqrt{2}\,S_{zzyz} & \sqrt{2}\,S_{zzxz} & \sqrt{2}\,S_{zzxy} \\ \sqrt{2}\,S_{xxyz} & \sqrt{2}\,S_{yyyz} & \sqrt{2}\,S_{zzyz} & 2\,S_{yzyz} & 2\,S_{yzxz} & 2\,S_{yzxy} \\ \sqrt{2}\,S_{xxxz} & \sqrt{2}\,S_{yyxz} & \sqrt{2}\,S_{zzxz} & 2\,S_{yzxz} & 2\,S_{xzxz} & 2\,S_{xzxy} \\ \sqrt{2}\,S_{xxxy} & \sqrt{2}\,S_{yyxy} & \sqrt{2}\,S_{zzxy} & 2\,S_{yzxy} & 2\,S_{xyxz} & 2\,S_{xyxy} \end{bmatrix}. \tag{5.63}$$

Here $S = W_1^{0,4}(K)/W_1(K)$.

Then, the tuple formed by the eigenvalues ζ_i

$$\mathbf{u}_i M = \zeta_i M \tag{5.64}$$

of M is a fingerprint with respect to the symmetry of the polyhedron K. The fingerprint tuple is invariant under rotation, scaling and translation of the polyhedron K. Examples of the fingerprint tuples ζ_i for common types of symmetries are provided in table 5.3.

Using the signature eigenvalue tuple ζ_i of M it is possible to define a distance measure on the metric space of bodies K induced by the Euclidean distance:

$$\Delta(K_1, K_2) := \left(\sum_{i=1}^{6} \left(\zeta_i(K_1) - \zeta_i(K_2)\right)^2 \right)^{1/2}. \tag{5.65}$$

$\Delta(K_1, K_2)$ is a pseudometric. It is positive definite, symmetric, the triangle inequality holds, however, the coincidence axiom $\Delta(K_1, K_2) = 0 \Leftarrow K_1 = K_2$ is only an implication and not an equivalence. For example $\Delta(\text{sphere}, \text{dodecahedron}) = 0$. To distinguish dodecahedra from spheres one needs to employ even higher rank tensors. Elementary applications

Table 5.3: Symmetry fingerprint tuples ζ_i (Eq. (5.64)) for the three-dimensional Bravais lattices: sc = simple cubic, bcc = body-centered cubic, hcp = hexagonal close packing, fcc = face-centered cubic, for the regular dodecahedron with ico = icosahedral symmetry and for the two-dimensional Bravais lattices square and hexagonal.

	three-dimensional					two-dimensional	
	sc	bcc	hcp	fcc	ico	square	hexagonal
ζ_1	$\frac{1}{3}$	$\frac{1}{3}$	$\frac{1}{3}$	$\frac{1}{3}$	$\frac{1}{3}$	$\frac{1}{3}$	$\frac{1}{2}$
ζ_2	$\frac{1}{3}$	$\frac{8-4/\sqrt{3}}{33}$	$\frac{1}{6}$	$\frac{1}{6}$	$\frac{2}{15}$	$\frac{1}{3}$	$\frac{1}{4}$
ζ_3	$\frac{1}{3}$	$\frac{8-4/\sqrt{3}}{33}$	$\frac{5}{36}$	$\frac{1}{6}$	$\frac{2}{15}$	$\frac{1}{3}$	$\frac{1}{4}$
ζ_4	0	$\frac{8-4/\sqrt{3}}{33}$	$\frac{5}{36}$	$\frac{1}{6}$	$\frac{2}{15}$	–	–
ζ_5	0	$\frac{-1+2\sqrt{3}}{33}$	$\frac{1}{9}$	$\frac{1}{12}$	$\frac{2}{15}$	–	–
ζ_6	0	$\frac{-1+2\sqrt{3}}{33}$	$\frac{1}{9}$	$\frac{1}{12}$	$\frac{2}{15}$	–	–

are presented in Fig. 5.9 (right panels). The same ideal crystal datasets superimposed with Gaussian noise as in the discussion for β above are analyzed. The mean symmetry metric Δ is calculated for every lattice with respect to several symmetries. For low noise values the symmetry metrics corresponding to the crystal symmetry show only small deviations from the perfect symmetry. At noise levels of about $\sigma \simeq 0.1\delta$ (corresponding to the Lindemann criterion [106] of melting) the metrics with respect to any of the symmetries reach similar values. Clearly it is possible to detect crystalline structures and even distinguish their type using the symmetry metric Δ.

Chapter 6

Crystallization of two-dimensional complex plasmas

This section summarizes the following paper and provides complementary information. The paper is published in Ref. [24] and appears in the appendix (section D.1) of this thesis.

> Scale-free crystallization of two-dimensional complex plasmas: Domain analysis using Minkowski tensors,
> A. Böbel, C.A. Knapek and C. Räth, *Phys. Rev. E* **97** (2018), 053201

The experiments were performed by C. A. Knapek, the simulation was implemented and conducted by C. Durniak. The computational data analysis methods were implemented by A. Böbel. The results were obtained, discussed and interpreted by A. Böbel. C. Räth initiated and supervised the work.

6.1 Objectives

Previously preliminary evidence [93] was found that the generally accepted KTHNY theory (section 2.1) is not applicable to the crystallization process in two-dimensional complex plasmas (section 4.1).

The objective of this study is to show that the KTHNY theory is not applicable to a series of experiments, and a simulation, on the crystallization of two-dimensional complex plasma systems and rigorously test and validate the recent FDS theory (section 2.3) for these systems.

Furthermore the aim was to demonstrate the benefits of the robust and continuous Minkowski tensor metrics (section 5.4.2) for the defect detection, as compared to the conventional bond order metric (section 5.2.2).

6.2 Experiments and simulation

Melamine-formaldehyde particles with a diameter of 9.19 μm and a mass of 6.14×10^{-13}kg were injected into an argon radio-frequency (rf) discharge ignited between a horizontal, capacitively coupled electrode mounted on the bottom of a vacuum chamber and the grounded chamber walls. The electric fields in the plasma sheath region above the electrode then levitated the charged particles against gravity. Additionally, an elevated rim on the electrode provided a radial confinement by shaping the electric potential inside the chamber. The injected particles then formed a crystalline single layer with a hexagonal crystal structure, which was temporarily destroyed by applying a negative electric pulse to two parallel wires mounted at approximately the levitation height of the mono-layer. The particle system then was left to re-crystallize under constant pressure and rf-power. Experiments at 12 different plasma conditions were performed: the neutral gas pressure was varied between $1.15 - 2.3$ Pa and the peak-to-peak rf voltages U_{PP} at the electrode were chosen in the range $[-134, -214]$ V. A sketch of the experimental setup is provided in Fig. 6.1. An image of the particles of experiment XII can be found in Fig. 4.1. Parameters of the experiments and simulation can be found in table 6.1.

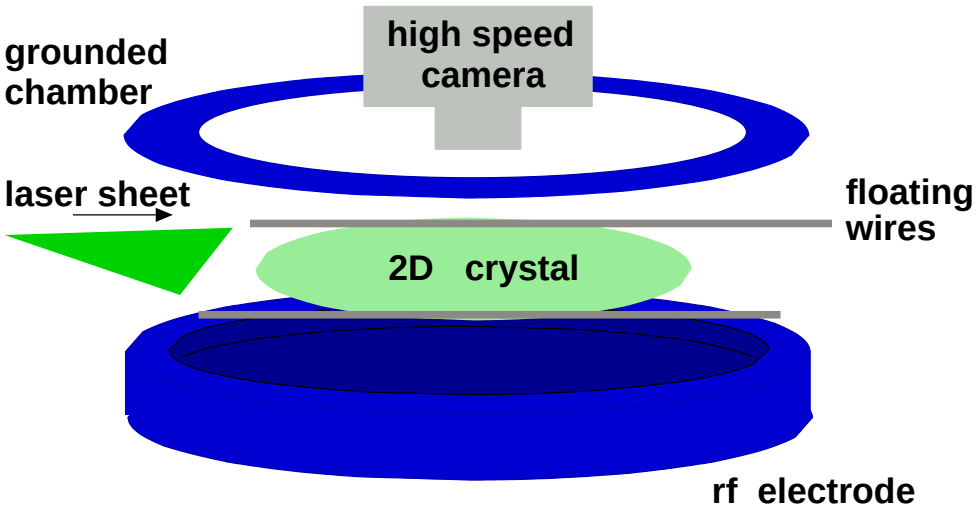

Figure 6.1: Sketch of the experimental setup used for the presented crystallization experiments [92]. A two-dimensional crystal is levitated in the plasma sheath region above the lower rf electrode. A glass window in the upper chamber flange provides optical access for a high speed camera from the top viewpoint. Particles are illuminated by a vertically thin, horizontally spread laser sheet. Two wires are mounted inside the chamber for electric particle manipulation. These are normally floating, but can be fed with a short electric pulse to melt the particle system.

To complement the experimental results, a molecular dynamics simulation of the crystallization of a mono-layer of 3000 particles in a parabolic confinement is considered. The simulation parameters were chosen to meet the experimental conditions: the damping rate was 2 Hz, the time step 0.01 s, particle mass and charge were 6.1×10^{-13} kg and -12000 e,

respectively. The particles were initially heated to 230 eV, and then allowed to cool until they reached a crystalline state.

Table 6.1: Parameters of the experiments and the simulation. Neutral gas pressure p, Epstein damping coefficient ν, peak-to-peak rf voltage U_{PP} at the driven electrode and the mean particle separation Δ obtained from the pair correlation functions. The Epstein damping coefficient ν, a measure for the damping rate of the particle motion due to scattering on neutral gas atoms, was calculated from the discharge parameters given in Ref. [133], using the reflection index $\delta = 1.26$ as measured in Ref. [107].

	p(Pa)	ν(Hz)	U_{PP}(V)	Δ(mm)
I	1.93	2.27	-138	0.60
II	1.36	1.60	-144	0.61
III	2.29	2.69	-134	0.61
IV	1.15	1.35	-184	0.60
V	1.36	1.60	-180	0.60
VI	1.68	1.97	-176	0.60
VII	2.12	2.49	-172	0.60
VIII	2.30	2.70	-172	0.60
IX	1.36	1.60	-214	0.57
X	1.93	2.27	-206	0.51
XI	2.30	2.70	-200	0.53
XII	1.94	2.28	-172	0.59
Simulation (S)	...	2	...	0.8

6.3 Bond correlation function and defect detection

The tracked particle positions are analyzed in a threefold manner. In the first step of the analysis the bond correlation function $g_6(r)$ was calculated in order to test its long-range scaling behavior against predictions of the KTHNY theory as discussed in section 2 and 5. Next the hypothesis Eq. (2.17) $\langle N_d \rangle \Delta^2 B = [\Delta \langle N_s \rangle]^{1+\alpha}$ is tested. Defects in the crystalline lattice are detected with three different order parameters: via the Ψ_6 bond order metric (Sec. 5.2.2), via the MT2 isotropy index β (Sec. 5.4.2) and via the MT4 symmetry metric Δ (Sec. 5.4.2). After deleting the detected crystal defects the remaining, therefore ideal crystal, domains are efficiently clustered into groups using a density based network cluster algorithm (DBSCAN) [1]. This allows the measurement of the area A_i and perimeter l_i of each crystalline domain and the testing of the hypothesis Eq. (2.17) of the FDS theory. Lastly the power law relationship between energy and defect fraction Eq. (2.18) $N_T/N \propto E^{2\alpha/(1+\alpha)}$ predicted by the FDS theory is tested. The defect fraction is obtained with the same defect detection methods as used for the test of the hypothesis.

The system energy is determined using the width of Gaussian fits to the particle velocity distributions in x and y direction.

6.4 Results

The bond correlation function $g_6(r)$ was calculated for all time-steps and datasets and fitted to a linear decay model (crystalline state), an exponential decay model (liquid state) and a power-law decay model (hexatic phase). For brevity of presentation only results of fits for one experimental data set are shown in Fig. 6.2. The findings, however, are qualitatively the same for all data sets. Panel (a) shows fits of the long-range decay behavior of $g_6(r)$ for different time steps. Panel (b) provides the values of the fit parameters c_6, ξ_6 and η_6. The models are (see section 2.1) the crystalline state: $g_6(r) \propto c_6 \cdot r$, the liquid state: $g_6(r) \propto \exp(-r/\xi_6)$ and the hexatic phase: $g_6(r) \propto r^{-\eta_6}$. The goodness of fit χ^2 statistic

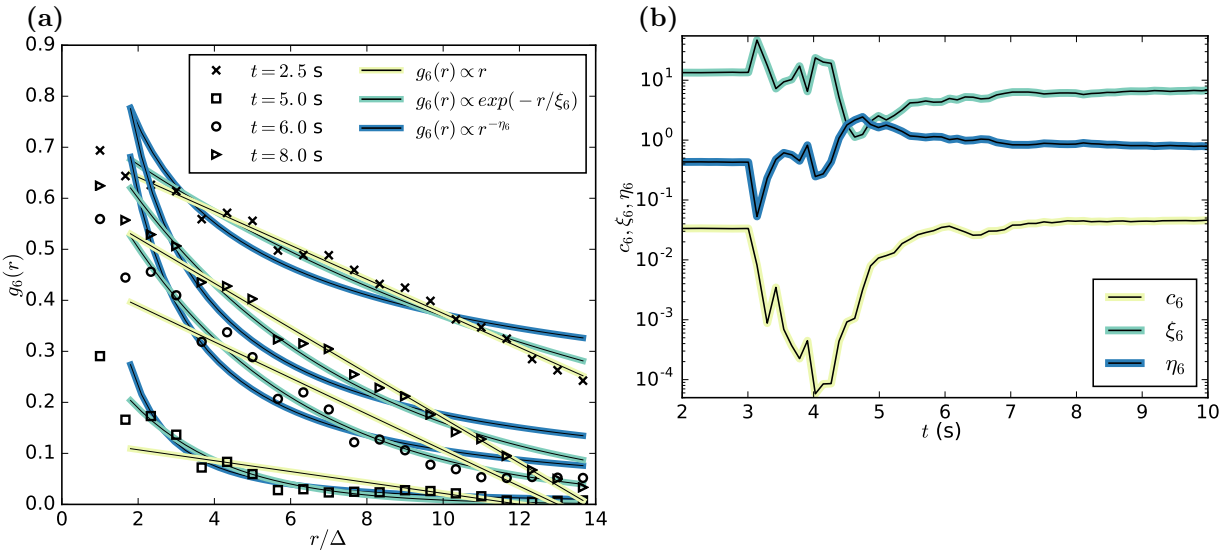

Figure 6.2: Scaling behavior of the long-range decay of the bond correlation function $g_6(r)$. Shown for experimental data set I. (a) Models are fitted to the long-range decay of $g(r)$ at different times t. Crystalline state: $g_6(r) \propto c_6 \cdot r$, liquid state: $g_6(r) \propto \exp(-r/\xi_6)$ and hexatic phase: $g_6(r) \propto r^{-\eta_6}$. (b) Values of the best fit parameters for different models. To enhance the clarity of the strongly fluctuating figures during melting times, panel (b) only show every 20th data point.

is shown in Fig. 6.3 and Fig. 6.4 for all data sets. Small values indicate high goodness of fit and confidence of the validity of the underlying model.

For small times, before melting, and for large times, we find the best model to be the crystalline state in most cases, otherwise the liquid state. This is expected since the initial experiment configuration is a crystalline sheet that is melted by an electric shock and then recrystallizes. During the melting phase no model can be fitted reliably and no model shows an advantage over the other. Before the recrystallization, however a liquid state is

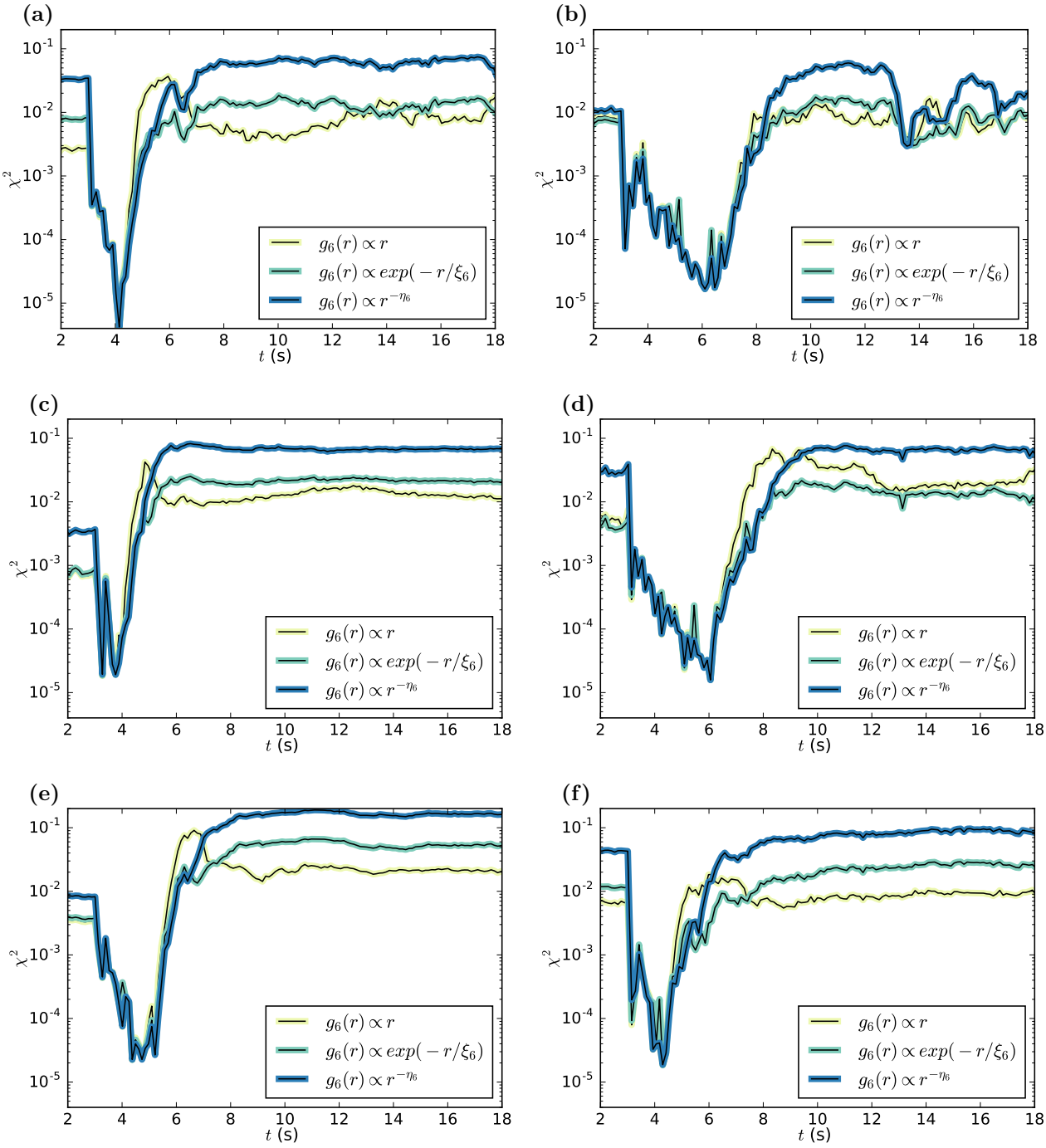

Figure 6.3: Scaling behavior of the long-range decay of the bond correlation function $g_6(r)$. Shown for experimental data set I (a) to XI (f).The χ^2 statistic as a measure of the goodness of fit is presented. Small values indicate the best model. χ^2 is the sum of sqared residuals divided by the fitted values. Models are fitted to the long-range decay of $g(r)$ at different times t. Crystalline state: $g_6(r) \propto c_6 \cdot r$, liquid state: $g_6(r) \propto \exp(-r/\xi_6)$ and hexatic phase: $g_6(r) \propto r^{-\eta_6}$.

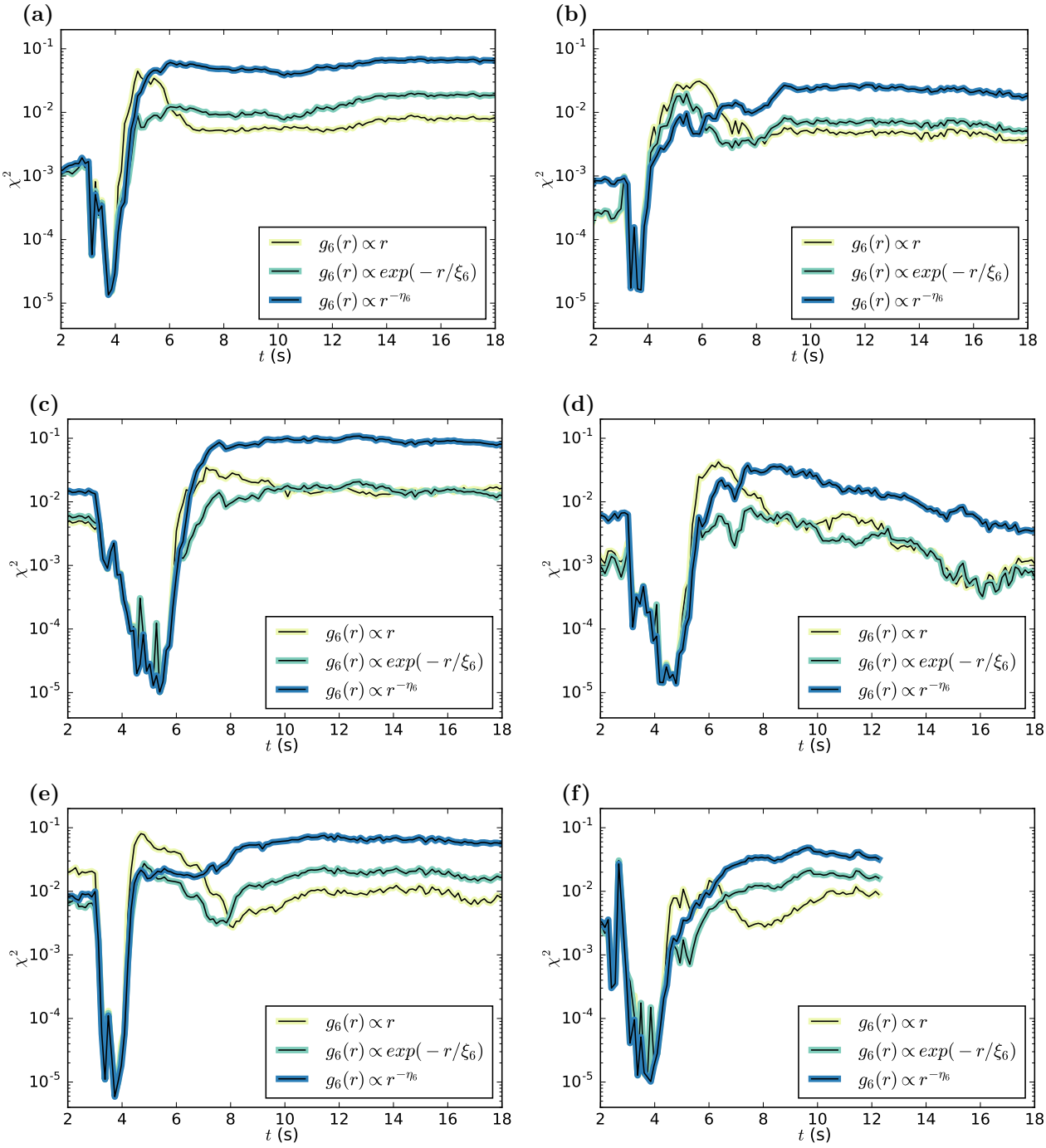

Figure 6.4: Scaling behavior of the long-range decay of the bond correlation function $g_6(r)$. Shown for experimental data set VII (a) to XII (f).The χ^2 statistic as a measure of the goodness of fit is presented. Small values indicate the best model. Models are fitted to the long-range decay of $g(r)$ at different times t. Crystalline state: $g_6(r) \propto c_6 \cdot r$, liquid state: $g_6(r) \propto \exp(-r/\xi_6)$ and hexatic phase: $g_6(r) \propto r^{-\eta_6}$.

evidenced. Since the power law fit at no times shows the best goodness of fit, one cannot infer the existence of a hexatic phase.

In a short time frame between the chaotic melting and the liquid state, both the hexatic phase and the liquid state model can be fitted with high goodness of fit values. However, the value of the power-law exponent η predicted by the KTHNY theory ($\eta < 0.25$) is not in agreement with the observed values, which are much larger. In addition the hexatic phase is predicted in a lower temperature regime, after the liquid cools down before crystallization.

Since no hexatic state can be observed it follows that the KTHNY theory is not valid in the case of two-dimensional complex plasma phase transitions as analyzed here.

Fig. 6.5 (a),(c) and (e) show the relationship between domain areas A_i and their perimeter l_i. The hypothesis of the FDS theory $\langle A_i \rangle \propto \langle l_i \rangle^{1+\alpha}$ is validated for all experiments and the simulation. In Fig. 6.5 (b),(d) and (f) the defect fractions N_T/N is plotted against the kinetic energy E of the particles. On can find an energy range where the scaling relation $N_T/N \propto E^{2\alpha/(1+\alpha)}$ is valid. The observed scaling relation is in agreement with the prediction of the FDS theory. The average line of best fit for the experiments is shifted in a parallel fashion to simulation data energies. The simulation validates the experimental results. Deviations are expected due to the difference in the underlying confinement potential. The simulation uses a parabolic confinement potential resulting in a radially decreasing particle density, whereas the experiments show constant particle densities due to a nonparabolic confinement.

The values of individual α obtained by least-square fits are listed in table 6.2. The mean exponent values for different methods are consistent with the exception of the energy vs. defect fraction measurement performed with the Ψ_6 bond order metric. The bond order metric has a much lower exponent and thus provides a smaller scaling range compared to the Minkowski tensor measures. Ψ_6 is a more binary measure and not as continuously sensitive to crystal distortions as the Minkowski tensor measures. The Minkowski tensors are not only able to distinguish perfect crystal cells from distorted defects, but are able to resolve continuously the range of ever more distorted imperfect cells. This allows the Minkowski tensor measures to verify the prediction of the FDS theory $N_T/N \propto E^{2\alpha/(1+\alpha)}$ for a large energy range.

Illustrations of the domain-structure of nature a complex plasma sheet is given in Fig. 6.6. The Voronoi cells are color coded by the three measures Ψ_6, $\beta_2^{2,0}$ and Δ_{hex}. One can clearly see the that the Minkowski functional measures provide a continuous metric for lattice distortions, whereas the bond order metric is more binary. This leads to the improved sensitivity of Minkowski tenor measures at low energies and allows the verification of the power-law Eq. (2.18) for a much larger scaling range compared to the bond order metric as it is presented above in Fig. 6.5. Illustrations for all experiments and the simulation are presented in the appendix B in Fig. B.2, Fig. B.3 and Fig. B.4.

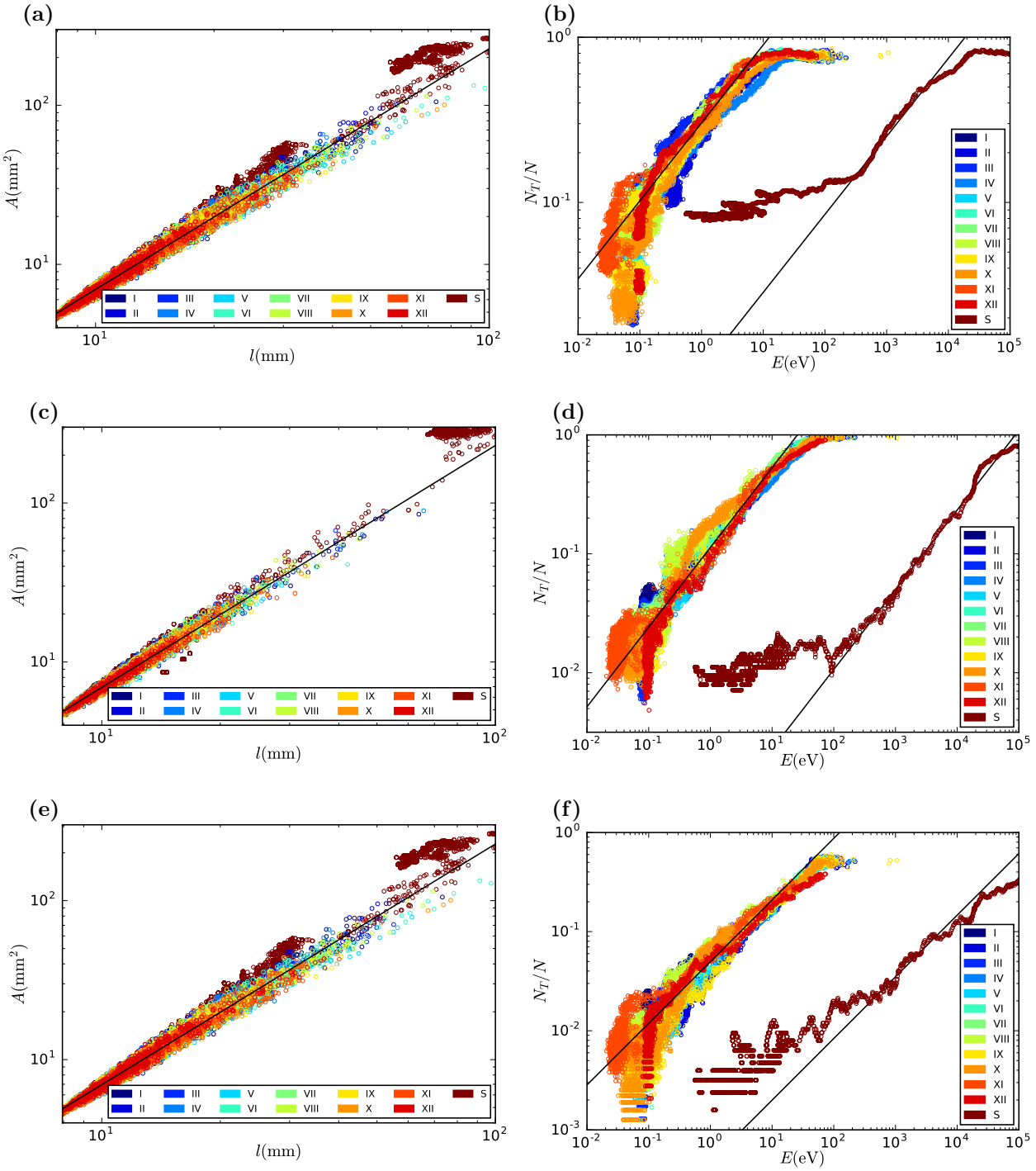

Figure 6.5: The area A_i of crystalline domains plotted against their boundary length l_i (left). The defect fraction N_T/N is plotted against the system energy E (right). Different colors indicate different experiments and the simulation. The solid line is the mean of all least square linear fits to the power law Eq. (2.17) (left) and to Eq. (2.18) (right) for the experiments and the simulation. In Fig. (a),(b) defects are identified via the Ψ_6 bond order metric, in Fig. (c),(d) the particles in crystalline states are identified via the MT2 isotropy index method and in Fig. (e),(f) they are identified via the MT4 symmetry metric.

Table 6.2: Power law exponents α for the area-length scaling in Fig. 6.5 (left) and the defect fraction vs. energy scaling in Fig. 6.5 (right) measured via the Ψ_6, the MT2 and the MT4 methods for experiments I-XII and the simulation. The last row is the mean value of all above with the standard deviation as uncertainty.

	$\langle A_i \rangle \propto \langle l_i \rangle^{1+\alpha}$			$N_T/N \propto E^{2\alpha/(1+\alpha)}$		
	α (Ψ_6)	α (MT2)	α (MT4)	α (Ψ_6)	α (MT2)	α (MT4)
I	0.526	0.505	0.519	0.186	0.454	0.413
II	0.569	0.550	0.570	0.405	0.518	0.593
III	0.503	0.535	0.539	0.266	0.323	0.367
IV	0.550	0.524	0.566	0.295	0.416	0.473
V	0.466	0.487	0.574	0.362	0.618	0.605
VI	0.485	0.494	0.547	0.319	0.453	0.359
VII	0.515	0.540	0.558	0.515	0.540	0.558
VIII	0.501	0.545	0.547	0.405	0.526	0.418
IX	0.527	0.518	0.570	0.358	0.563	0.844
X	0.488	0.545	0.545	0.241	0.254	0.328
XI	0.490	0.479	0.578	0.263	0.103	0.677
XII	0.548	0.543	0.560	0.304	0.550	0.234
S	0.752	0.856	0.529	0.303	0.504	0.471
$\langle$ I...XII $\rangle$	0.51 $\pm$ 0.02	0.52 $\pm$0.02	0.55 $\pm$ 0.02	0.31 $\pm$0.06	0.52 $\pm$ 0.18	0.47 $\pm$0.17

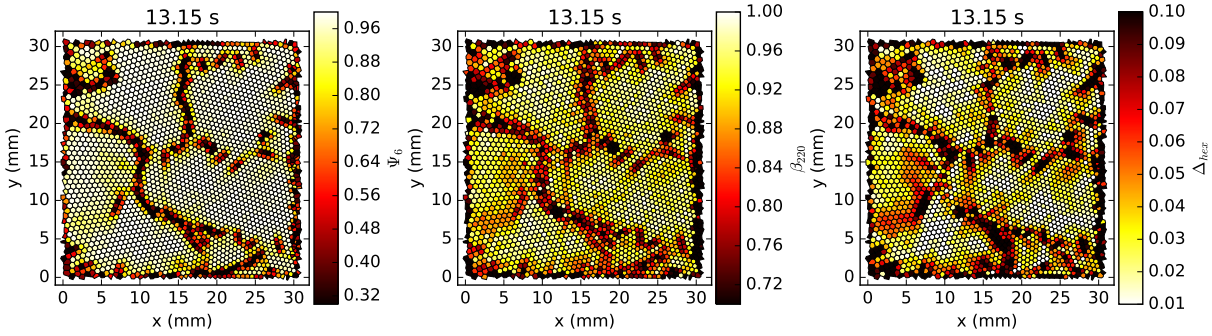

Figure 6.6: Illustration of experiment IV. The Voronoi cells are color coded by Ψ_6 (left panel), $\beta_2^{2,0}$ (middle panel) and Δ_{hex} (right panel).

6.5 Conclusions

Minkowski Tensor methods are able to verify the Fractal Domain Structure (FDS) theory [125] for two-dimensional phase transitions with unprecedented statistical significance. The domain structure observed after the crystallization in experiments and a simulation of two-dimensional complex plasmas is analyzed by detecting the crystal defect lines at the domain

interfaces. The hypothesis and the prediction of a fractal relationship between domain area and boundary of the FDS theory are validated. The detection of defects via Minkowski tensor methods provides a much more reliable basis for the testing of the theory compared to the conventional Ψ_6 bond order metric. The bond order metric proves to be too binary in its nature, not allowing the continuous detection of crystal distortions. This allows the Minkowski measures to resolve defect fraction of about one magnitude smaller than with the bond order metric and verify the power-law prediction of the FDS theory for a scaling range one magnitude larger. Scaling exponents obtained for the hypothesis and the prediction of the FDS theory are consistent for all experiments, the simulation and a wide range of parameters in the detection methods. This suggests that the underlying equations are inherent to the physics of two-dimensional phase transitions in complex plasmas.

The prominent, nobel prize winning KTHNY theory is not found to be valid for the experiments and the simulation performed in this study. By fitting the long-range decay of the bond correlation function $g_6(r)$ to different models it could be shown that no hexatic phase exists in these two-dimensional complex plasma systems, therefore contradicting the KTHNY theory.

Since complex plasmas are non-equilibrium systems these results suggest that the FDS theory is rather applicable to out of equilibrium liquid-solid transitions in two-dimensional systems than the KTHNY theory.

Chapter 7

Demixing of binary complex plasmas in three-dimensional flat space

A summary and complementary information to the following publication appearing as Ref. [25] and in the appendix (section D.2) of this thesis is given in this section.

> Kinetics of fluid demixing in complex plasmas: Domain growth analysis using Minkowski tensors,
> A. Böbel and C. Räth, *Phys. Rev. E* **94** (2016), 013201

The molecular dynamics simulations were carried out by A. Wysocki. The power spectrum analysis was carried out by C. Räth. The Minkowski functional and tensor analysis was performed by A. Böbel. The results were discussed, interpreted and conclusions were drawn by A. Böbel. C. Räth initiated and supervised the work.

7.1 Objectives

Molecular dynamics simulations based on the experimentally evidenced fluid demixing in complex plasmas are compared with theoretical predictions. The objective is to measure and compare the growth of demixed domains using the conventional power spectrum based method and also the novel Minkowski tensor measures. We are interested in comparing the conventional, linear measure with non-linear Minkowski measures. The implications of the findings with the Minkowski tensor analyses should be discussed and their impact on the interpretation of the demixing kinetics shown. In addition we want to emphasized that complex plasmas are a model system well suited to investigate dynamic processes on the individual particle level.

7.2 Molecular dynamics simulation

Molecular dynamics simulations are performed with the Langevin thermostat. A composition of equal particle numbers for two species with in total 729000 particles was randomly distributed in a cube with a side length of 27 mm. The initial mean interparticle distance was 0.3 mm. Periodic boundary conditions were imposed. The particles interact via a double Yukawa potential $\Phi(r)$ of the form (compare section 4.1.3):

$$\Phi(r) = \frac{1}{r}\Big(Z^*_{\mathrm{SR}} \exp\left(-r/\lambda_{\mathrm{SR}}\right) + Z^*_{\mathrm{LR}} \exp\left(-r/\lambda_{\mathrm{LR}}\right) \Big), \tag{7.1}$$

with two distinct screening length scales λ_{SR} for short-range interaction and λ_{LR} for long-range interaction. The effective particle charges are $Z^*_{\mathrm{SR,LR}}$. We introduce the screening length ratio

$$\Lambda = \frac{\lambda_{\mathrm{LR}}}{\lambda_{\mathrm{SR}}} \tag{7.2}$$

as a measure for the dominance of long-range interactions over short-range interactions. The simulation results for the screening length ratios $\Lambda \in \{1, 2, 4, 12\}$ are analyzed and interpreted below. The simulation parameters were chose corresponding to the experiment (see section 4.1.3) in PK-3 Plus where phase separation was observed. The particle mass density was 1.5 g/cm^3, the particle diameters were $2a_1 = 3.4$ μm and $2a_2 = 9.2$ μm, the actual charges were $Z_1 = 4000$ e and $Z_2 = (a_2/a_1)Z_1 = 10824$ e, the friction coefficients were $\zeta_1 = 250$ s^{-1} and $\zeta_2 = (a_1/a_2)\zeta_1 = 92.4$ s^{-1}, the temperature was $k_{\mathrm{B}}T = 0.024$ eV, and the SR screening length was chosen to be $\lambda_{\mathrm{SR}} = 150$ μm. In order to numerically solve the equations of motion, a standard integration scheme with the use of memory functions [47] was employed. A integration time step of $\delta t = 0.0025 < \zeta_1^{-1} < \zeta_2^{-1}$ s was used. Further details can be found in the supplementary material of [178].

7.3 Power spectrum and Minkowski tensor analysis

In the first step of the analysis the average size of demixed domains $L(t)$ is measured via the structure factor $S(k,t)$ [3, 77, 54] based on the power spectrum. The power spectrum is fitted with the off-critical fitting function $S(k) \propto (k/k_{\mathrm{max}})^2 \,/\, \left[2 + (k/k_{\mathrm{max}})^6\right]$ (Eq. (5.21)), and the position of the maximum k_{max} of $S(k)$ is identified as the inverse of the mean average length scale via $k_{\mathrm{max}} = 2\pi/L$. In the second step of the analysis the demixed domain size is identify via Minkowski tensor methods based on the rank two isotropy metric β and the symmetry metric Δ (section 5.4.2).

The Minkowski tensor analysis was carried out by the following procedure for every simulation time-step. The values of M_0 (see section 5.4.1), β_{120} (see Eq. (5.57)) and Δ_{hcp} (see Eq. (5.65)) were calculated locally for the Voronoi cells of each particle of the minority species and then collected in a histogram. Histograms of β_{120} for different time steps are presented in Fig. 7.1. The particles in the demixed domains have isotropic Voronoi cells of hcp symmetry, whereas the fluid particles still dispersed in the majority species have

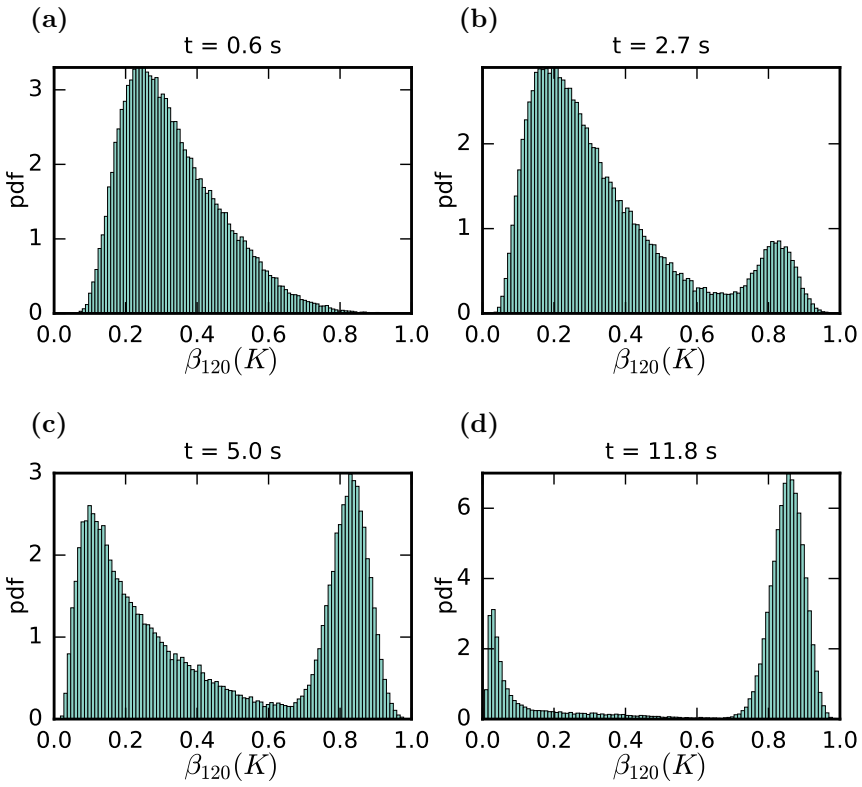

Figure 7.1: Calculating the minority phase domain size via a histogram method. β_{120} of the Voronoi cells for all minority phase particles is plotted for increasing time from the top left to the bottom right panel. The separating parts are interpreted as ordered domains in the case of high β_{120} values in contrast to the disordered particles suspended in the majority species corresponding to low β_{120} values. Here $\Lambda = 12$.

highly non-isotropic and asymmetric Voronoi cells. By simply choosing a cut-off value, e.g. $\beta_{\text{thresh}} = 0.7$ and $\Delta_{\text{thresh}} = 0.12$, one can subdivide the histograms into an ordered and an disordered part. Counting the particles in the ordered part gives a measure for the size of the demixed domains. These measures are called MT2 respectively MT4 measure. The detection of particles in already demixed domains is illustrated for the MT2 measure in Fig. 7.2.

7.4 Results

The long-range interactions facilitate fast demixing kinetics resulting in large demixed domain sizes. A comparison of domain sizes in the final demixed state is given in Fig. 7.3. It shows different screening length ratios Λ in each quadrant. Obviously a large value of Λ results in large sized demixed domains. This is due to the fact that increasing Λ increases the range of the particle interaction potential leading to the coalescence of even far away

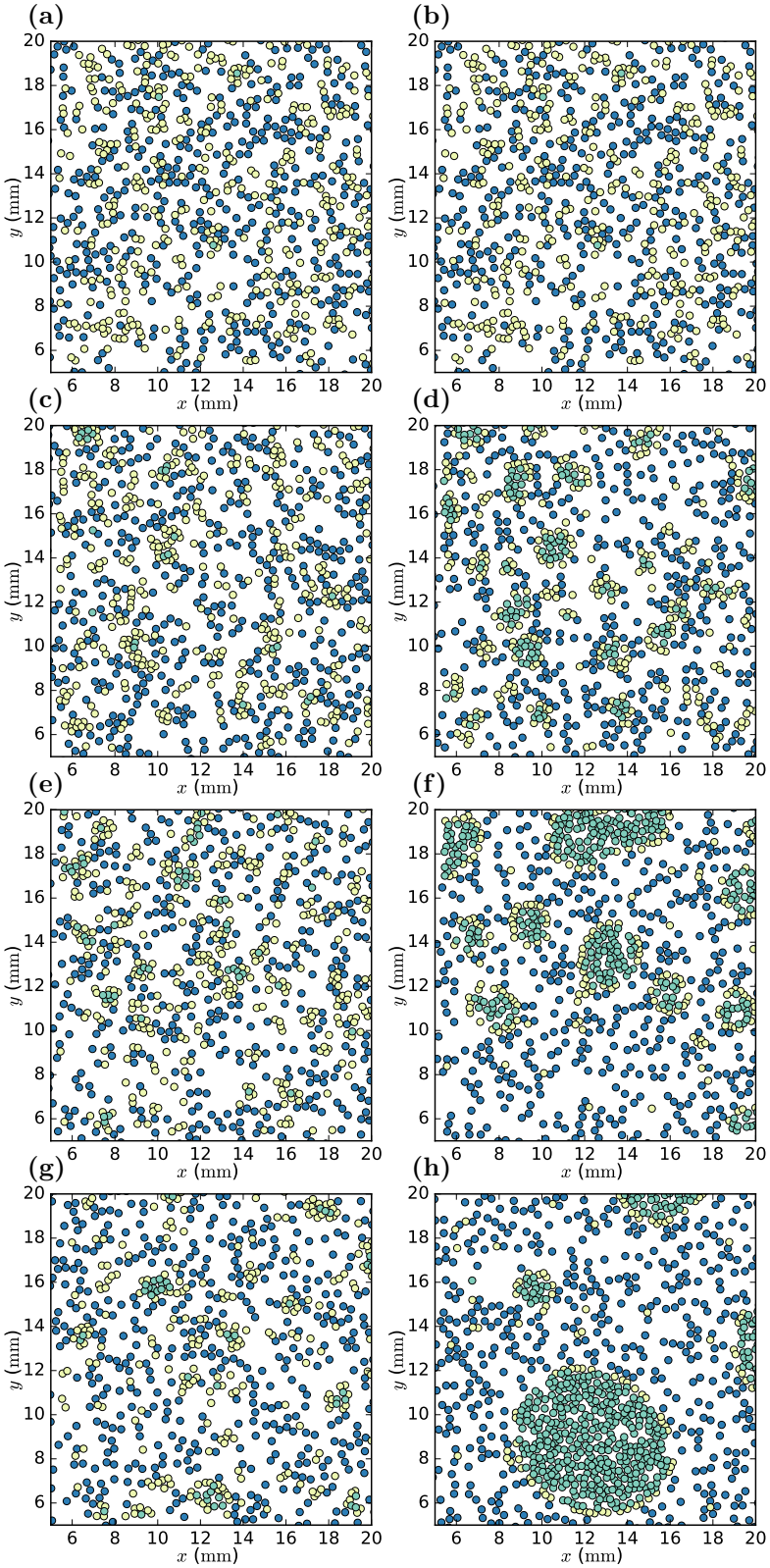

Figure 7.2: Two-dimensional slice ($z \in [11.0\text{mm}, 11.1\text{mm}]$) for the detection of demixed domains via the isotropy index β_2^{20}. (a),(b) $\Lambda = 1$, (c),(d) $\Lambda = 2$, (e),(f) $\Lambda = 4$, (g),(h) $\Lambda = 12$. Left column early time, right column: late time. Particles of species one have blue color, particles of species two are yellow. The particles of species two, detected as already demixed via the β_2^{20} metric, are color coded in green.

initially disjoint domains.

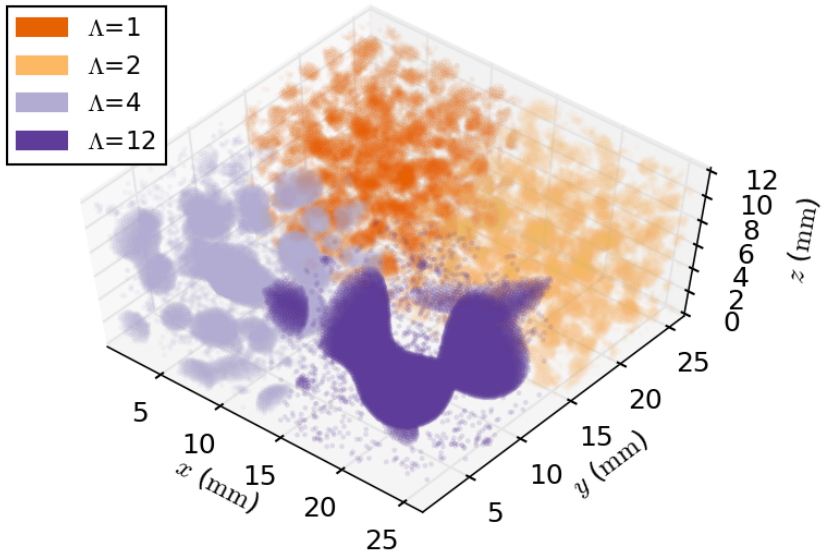

Figure 7.3: Domain size comparison for different screening length ratios Λ.

As presented in Fig. 7.4 the dynamic range of the power spectrum domain size measure is significantly smaller compared to the dynamic range of the Minkowski measures. While the power spectrum and the Minkowski tensor measures are blind to the initial phase of the spinodal decomposition, the scalar Minkowski functional measure is sensitive to changes in the particle distribution from the beginning of the simulations. However, at later times ($t \gtrsim 1$ s) the scalar and tensor Minkowski measures become equivalent. Any of the presented measures evidences a power law growth $L(t) \propto t^{\alpha}$ in the main domain growth phase for $t \gtrsim 1$ s until saturation. By a scaling of the axis of local gradients $d = \Delta \mathrm{m}/\Delta t$ and local power law exponents $d_{\mathrm{LL}} = \Delta \log(\mathrm{m})/\Delta \log(t)$ (Fig. 7.5) the curves for measures $m \in \{\mathrm{MT0}, \mathrm{MT2}, \mathrm{MT4}\}$ coincide well in the cases $\Lambda \in \{2, 4, 12\}$. This hints toward a universal domain growth in these cases. A qualitatively different domain growth is found in the case $\Lambda = 1$, i.e. the short-range dominated interaction potential, since these curves do not coincide with the others. The curves $d(t)$ were transformed to curves $d(t) \to d^*(t^*)$ by the scaling $d \to d^* = d^{\Lambda^{\mu}}$ and $t \to t^* = (t/1s)^{\Lambda^{\tau}}$, with parameters $\mu, \tau \in \mathbb{R}$. For the power spectrum measure no universal behavior can be identified.

7.5 Conclusions and outlook

It is found that Minkowski tensor measures have a significantly larger dynamical range in detecting the growth of demixed domains compared to the power spectrum measure. Thus they also are generally more sensitive to changes in the domain size and to structural

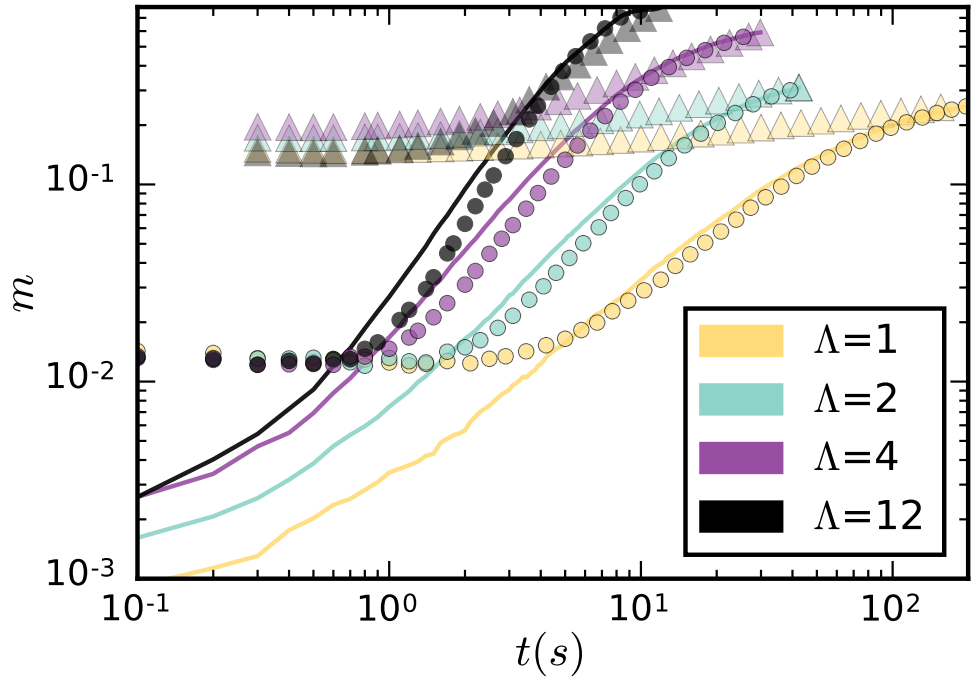

Figure 7.4: Growth of the minority phase domains. The evolution of different domain size measures $m \in \{\mathrm{PS}, \mathrm{MT0}, \mathrm{MT2}\}$ is plotted for increasing simulation time.
Triangles mark the PS method, lines the volume MT0 method and dots the MT2 isotropy index method. Colours indicate different screening length ratios $\Lambda \in \{1, 2, 4, 12\}$. To improve readability only a subset data points are displayed s.t. markers are equidistant.

changes at the onset of the demixing process. However, increasing the Minkowski tensor rank decreases the sensitivity: To measure merely the mean domain size directional shape information is not necessary.

In the long-range dominated cases, for $\Lambda = 2, 4, 12$, demixing occurs in two distinct stages: Initially neighbouring particles agglomerate. Here the number of particles in the demixed domains grows rapidly. In the next stage these agglomerated domains coalesce and grow in cascades. Here, the contribution to the domain size is mainly due to coalescence, diffusion of further particles to the demixed domains happens slowly. For higher screening length ratios Λ the number of cascades is increasing and therefore the final demixed domain size is larger compared to smaller values of Λ. For short-range interactions, in the case $\Lambda = 1$, only the agglomeration stage is observed. This explains the universal behavior found for $\Lambda = 2, 4, 12$ and the qualitative difference for $\Lambda = 1$. This universal behavior can only be detected by Minkowski functional or tensor measures but not for the power spectrum measure. This implies that the universal behavior has an nonlinear origin.

Further study of these universal features is necessary. The hints of universality have to be investigated systematically, utilizing more extensive simulations, for further screening length ratios and for different shapes of the interaction potential. These studies can shed light on the differences in the physics between the universality classes found in this work.

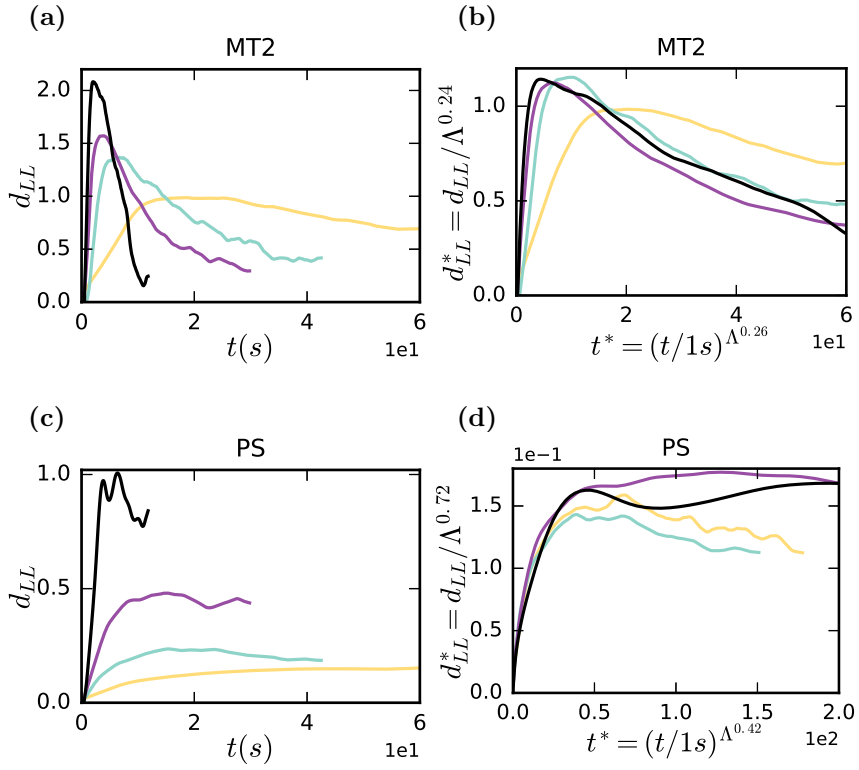

Figure 7.5: Local power law exponents $d_{LL} = \Delta\log(\mathrm{m})/\Delta\log(t)$ are plotted against time t in the left column. In the right column the Scaled local gradients $d^*_{LL} = d_{LL}/\Lambda^{\nu}$, $\nu \in \mathbb{R}$ are plotted against scaled time $t^* = (t/1s)^{\Lambda^{\rho}}$, $\rho \in \mathbb{R}$. The first row shows the $MT2$ measure, the second row presents the PS measure. Only the Minkowski measure shows universal behavior for $\Lambda > 1$.

Since the short-range interaction case only shows agglomeration of particles but no cascades of coalescence, the demixing process for $\Lambda = 1$ might not be in the spinodal decomposition regime of the phase diagram.

Chapter 8

Demixing kinetics on spherical geometry

This section provides complementary information and summarizes the following paper, which appears in the appendix (section D.3) of this thesis.

> Fluid demixing kinetics on spherical geometry: Power spectrum and Minkowski functional analysis
> A. Böbel, M. C. Bott, H. Modest, J.M. Brader and C. Räth, submitted to the *New Journal of Physics*

The density-functional theory calculations were performed by M. C. Bott and J. M. Brader. A. Böbel performed the angular power spectral density analysis. The Minkowski functional calculation was implemented and carried out by A. Böbel based on work of H. Modest. The results were discussed, interpreted and conclusions were drawn by A. Böbel. C. Räth initiated and supervised the work.

8.1 Objectives

The objective of this study is the systematic analysis of fluid-fluid demixing on the sphere with linear power spectrum methods as also by use of the nonlinear Minkowski functionals.

Demixing kinetics have been studies extensively in infinite flat geometries. However, systems subjected to boundary conditions are less well understood. Instead of imposing boundary conditions by introducing obstacles or external fields, a confinement can also be achieved by the geometry of space itself. This approach, recently applied in the context of crystallization [60, 156] and in reaction-diffusion systems [95] showed promising results. Density-functional theory (DDFT) calculations (see section 4.2) for the demixing of a binary fluid on a sphere have been performed in [26] in order to find metastable demixed states. However the dynamics of the demixed domain growth were characterized only superficially. Here these DDFT calculations are analyzed in a systematic manner by firstly,

calculating the average domain size via the angular power spectral density, and secondly, extending this linear analysis with the use of Minkowski functionals.

8.2 Density functional theory calculations

The dynamical density functional theory (DDFT) [12, 109] with a Gaussian core model (GCM) [159] for the particle interaction potential is a simple model for polymers in solution that provides generic demixing properties as it is discussed in section 4.2.

Following parameters are chosen for the excess free energy in Eq. (4.20): $R_{11} = R_{22} = R_{12} = 1$, $\epsilon^*_{11} = \epsilon^*_{22} = 2$ and $\epsilon^*_{12} = 1.035\epsilon^*_{11}$.

The equation of motion Eq. (4.21) is solved on the sphere, with pixels parametrized by the spherical coordinates θ and ϕ. This leads to an oversampling at the poles. This can be improved by using equal sized pixels in future studies. The DDFT calculations were performed for two sphere sizes. A large sphere with radius $R = 10R_{11}$ and a small sphere with radius $R = 2.5R_{11}$. For each sphere five mixture fractions x ($x = N_2/N$ is the concentration of particles of species 2) were analyzed: $x = 0.1$, $x = 0.2$, $x = 0.3$, $x = 0.4$ and $x = 0.5$. The DDFT calculation timesteps are measured in the dimensionless time of $t^* = tD/R_{11}^2$, where D is the bare diffusion coefficient. In the domain growth analyses only one of the species is considered. Its density field is called $\rho(\mathbf{r}, t^*)$. Since the contributions of the particle species are mirror images (where the concentration of one species is low, the other is high and vice versa) their information content is redundant.

8.3 Angular power spectrum and Minkowski functional analysis

For the DDFT calculation data the angular power spectral density (see section 5.3.2) and the three Minkowski functionals (section 5.4.1) are calculated.

The angular power spectral density is fitted via the off-critical function Eq. (5.28). The average domain size $L(t)$ is identified with the position of the maximum $l_{\max}$ of $S(l,t)$ (by fitting $C_{l,\max}$) via $L = R\pi/l_{\max}$. Not only this standard measure for the domain size during demixing is analyzed, but also the maximal value of the structure factor $S(l_{\max})$. Since there are $2(l+1)$ modes the total power of multipole $l_{\max}$ is given by $(2l+1)C_{l,\max}$.

To calculate the Minkowski functionals the spherical coordinate grid (of $181 \cdot 92 = 16652$ pixel) is interpolated on an equal area pixel grid with $N_{\text{pix}} = 12288$ pixel. This rather low resolution size is chosen since the original DDFT calculation data has a similarly low resolution. This will be improved in further studies. To define an equal area pixel grid the python library healpy [2] for HEALPix is used. The HEALPix pixelisation scheme is a partition of a spherical surface into quadrilateral pixels of equal area A_{pix} but varying shape [58]. The pixel size is determined by the HEALPix resolution parameter N_{side} that can be chosen as a power of two, $N_{\text{side}} = 1, 2, 4, 8, ...$ This corresponds to a total number of pixels of $N_{\text{pix}} = 12 \times N_{\text{side}}^2 = 12, 48, 192, 768, ...$ In this thesis $N_{\text{side}} = 32$ is chosen.

The three Minkowski functionals M_0, M_1 and M_2 of the excursion sets $K_{\rho_{\text{th}}}$ (see Eq. (5.38)) of $\rho(\mathbf{r}, t^*)$ are calculated. In this study the threshold levels $\rho_{\text{th},k}$ run over 101 equidistant values where $\rho_{\text{th},0} = 0$ and $\rho_{\text{th},100} = \max(\rho(\mathbf{r}, t^*))$. The Minkowski functionals then can be calculated, following [118] by using Eq. (5.39).

8.4 Results

The results of the DDFT calculations are illustrated in Fig. 8.1 for the large sphere $R = 10R_{11}$ and in Fig. 8.2 for the small sphere $R = 2.5R_{11}$. The initial demixing stage due to the growth of density fluctuations happens very fast. When the first fluctuations become visible to the eye the phases are separated in the next moments only few DDFT calculation time steps later. This change happens in the range of about $\Delta t^* \simeq 100$. In the next stage the fluctuations separate into initially small sized demixed domains during a time scale of about $\Delta t^* \simeq 1000$. The growth and coalescence of these domains subsequently happens at even larger time scales of about $\Delta t^* \simeq 100000$. The onset of the demixing process is earlier for higher mixing ratios x. The initial size of demixed domains is also increasing with higher x. For the small sphere the onset of the demixing process is much later than for the large sphere.

Fig. 8.3 shows the angular power spectral densities obtained for the DDFT calculations on different sphere sizes R and with different mixture parameters x. Results of the power spectrum analysis are presented in Fig. 8.4. Different regimes of the demixing process can be found in both the characteristic length scale $L = R\pi/l_{\text{max}}$, derived from the positions of maximal amplitudes l_{max}, and the maximal amplitudes $C_{l,\text{max}}$.

In the graphs for the characteristic length scale $L(t^*)$ of the domain size (Fig. 8.4 (a)), the initial spinodal decomposition phase of growing density fluctuations cannot be observed, since no domain growth has yet begun. However, the power law growth of L in the second stage can be detected. For the large sphere the slope in the log-log plot varies less than for the small sphere since there are fewer initially demixed domains on the small sphere, the spatial confinement plays a more important role than for the large sphere. In particular for $R = 2.5R_{11}$ and $x = 0.1$ no demixing is observed during the complete DDFT calculation, ending at $t^* = 10^5$. The domain growth is faster for higher mixing parameters, with the exception being $x = 0.1$: Here the demixing processes starts late but domain growth is fast. Contrary to the usual demixing metric L, the power $C_{l,\text{max}}$ is able to detect the growth of density fluctuations in the initial stage of spinodal decomposition in addition to the coalescence stage. In the initial stage it shows a growth of about four orders of magnitude.

The dependence of the Minkowski functionals on the threshold density ρ_{th} is presented in the appendix C in Fig. C.1 for the large sphere and in Fig. C.2 for the small sphere. The time t^* is color coded. Only for very small times the functionals depend on the threshold value, for larger times, when domain interfaces are formed at the crossover time t_c^*, they become constant. They exhibit their largest variations at relative threshold densities in the neighborhood of the mixing parameter at $\rho_{\text{th}}/\rho_{\text{th},100} \simeq x$. For large times M_0 converges

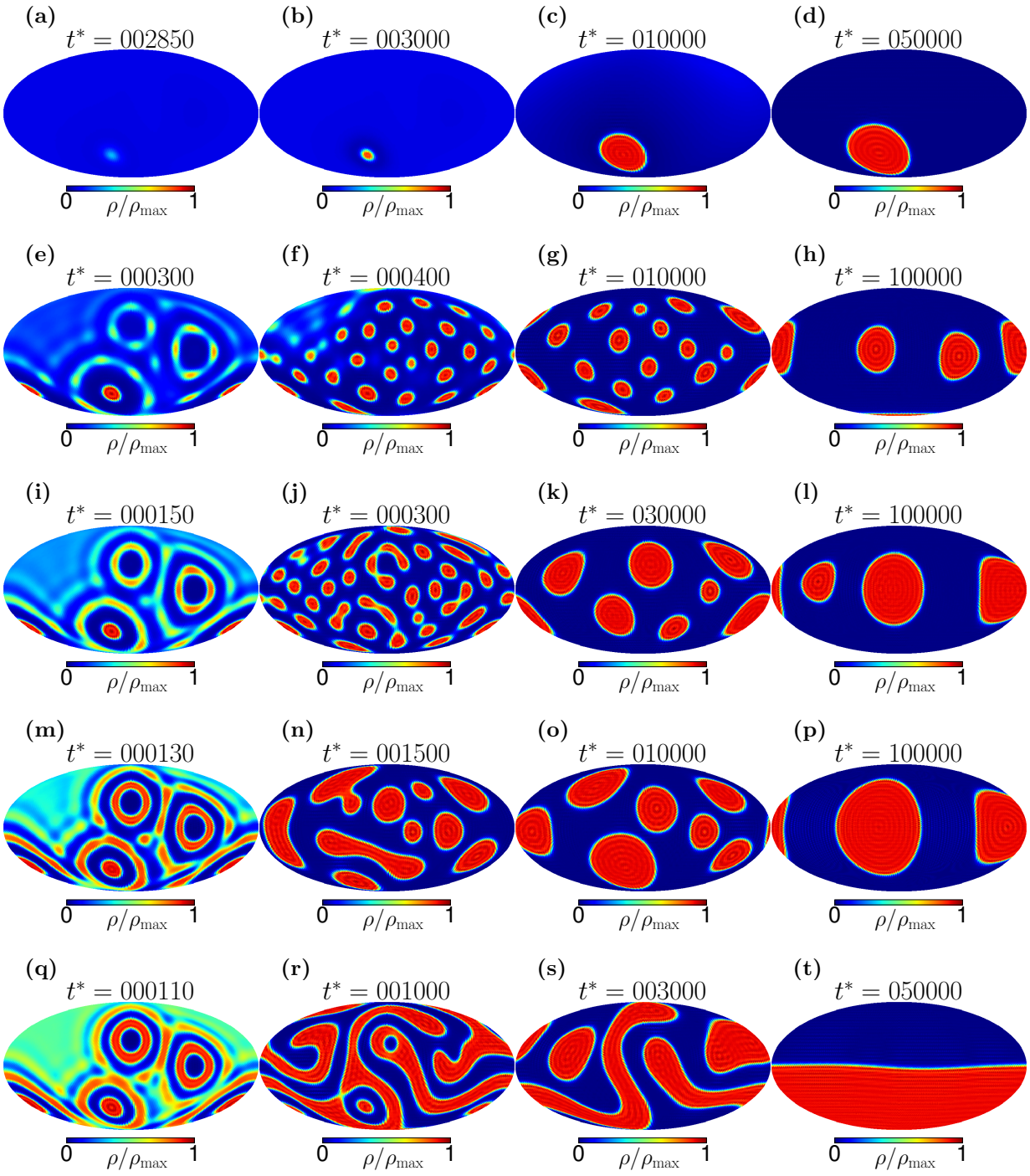

Figure 8.1: Mollweide projection of DDFT demixing dynamics on the large sphere. $\rho(\mathbf{r}, t^*)$ is plotted. In the first row $x = 0.1$, in the second row $x = 0.2$, in the third row $x = 0.3$, in the fourth row $x = 0.4$ and in the fifth row $x = 0.5$. Time t^* increases in the columns form left to right as indicated in each title.

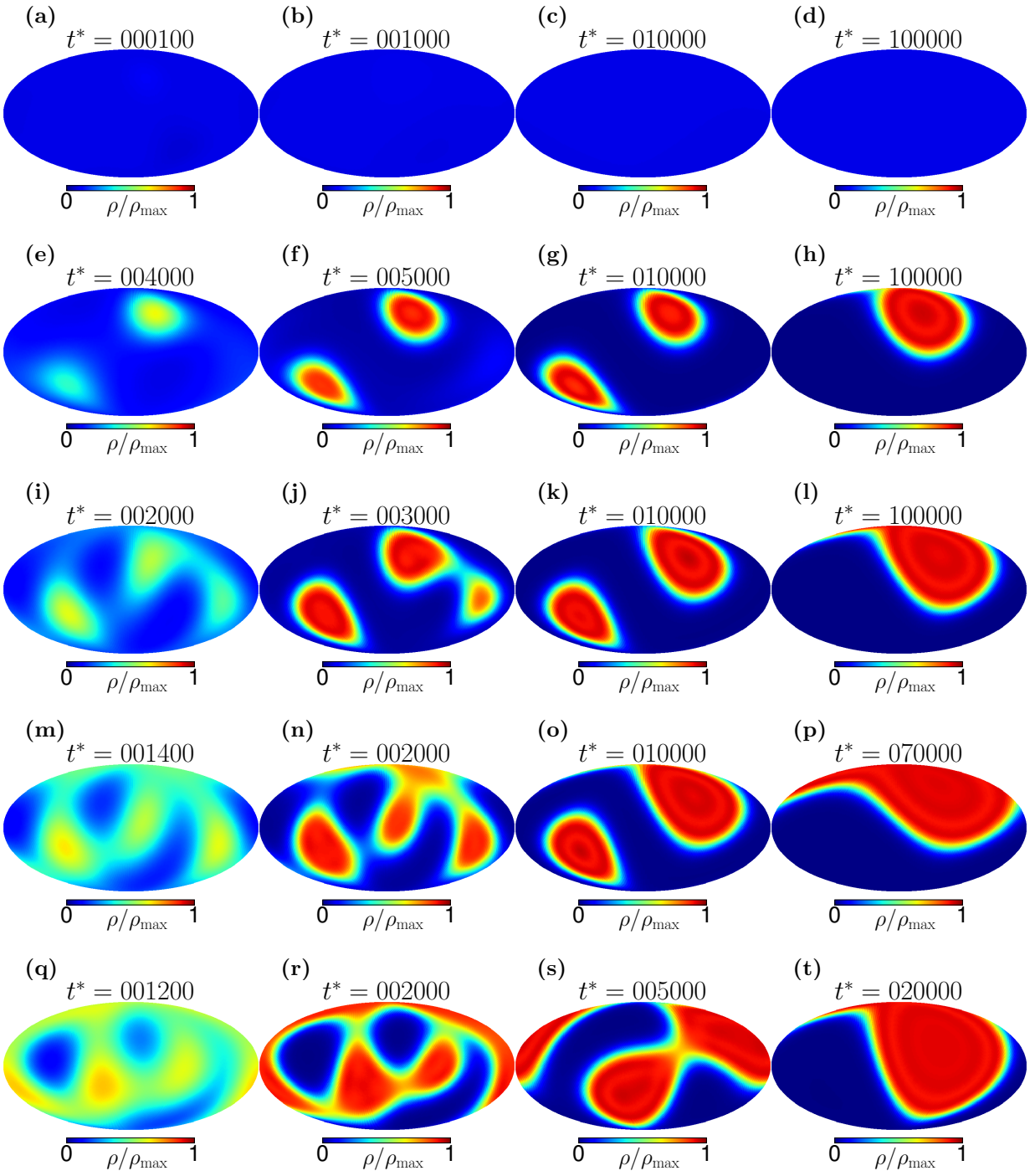

Figure 8.2: Mollweide projection of DDFT demixing dynamics on the small sphere. $\rho(\mathbf{r}, t^*)$ is plotted. In the first row $x = 0.1$, in the second row $x = 0.2$, in the third row $x = 0.3$, in the fourth row $x = 0.4$ and in the fifth row $x = 0.5$. Time t^* increases in the columns form left to right as indicated in each title.

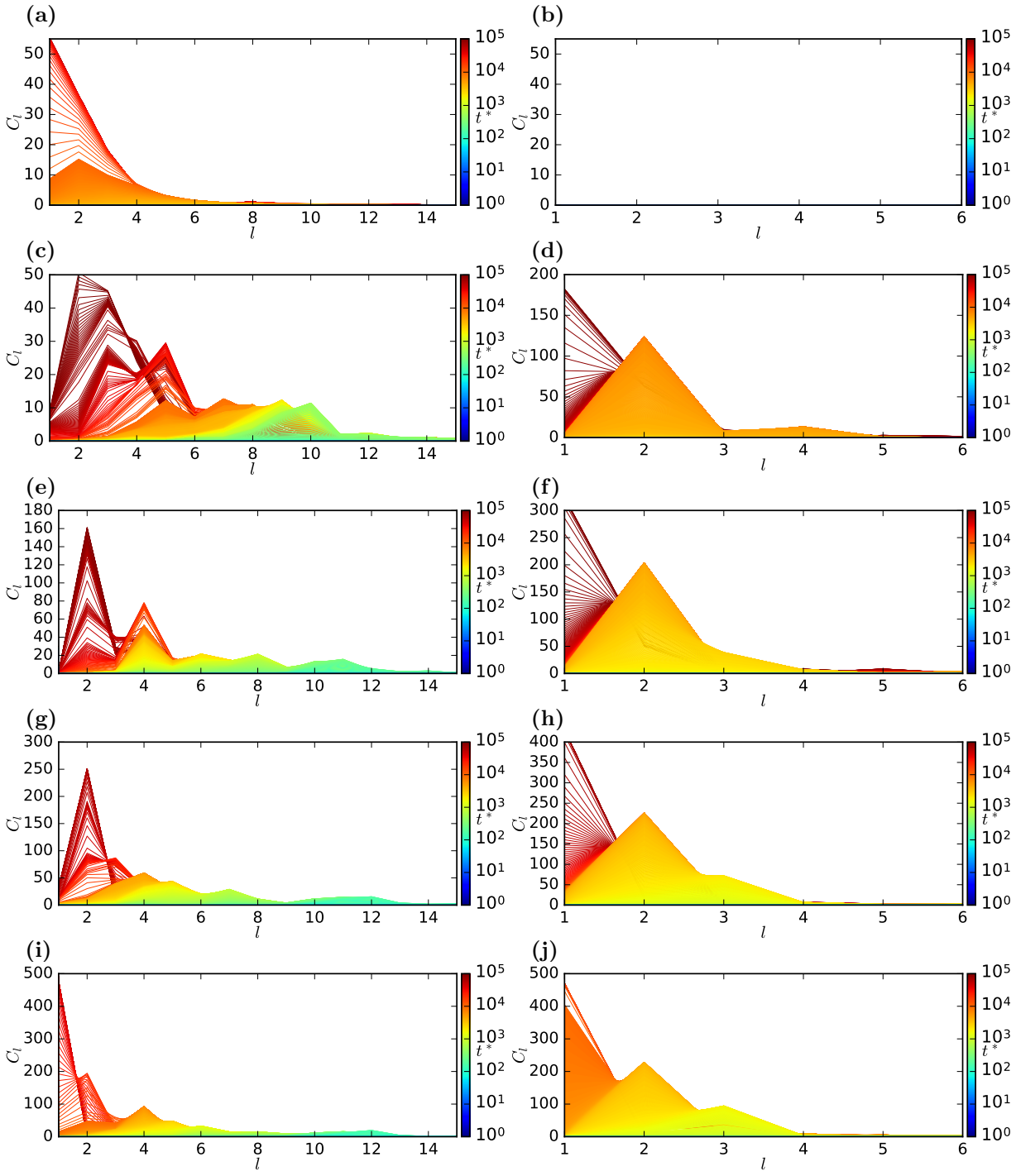

Figure 8.3: Angular power spectral density. Time t^* is color coded. First column: Large sphere $R = 10R_{11}$, second column: Small sphere $R = 2.5R_{11}$. First row: $x = 0.1$, second row: $x = 0.2$, third row: $x = 0.3$, fourth row $x = 0.4$, fifth row: $x = 0.5$.

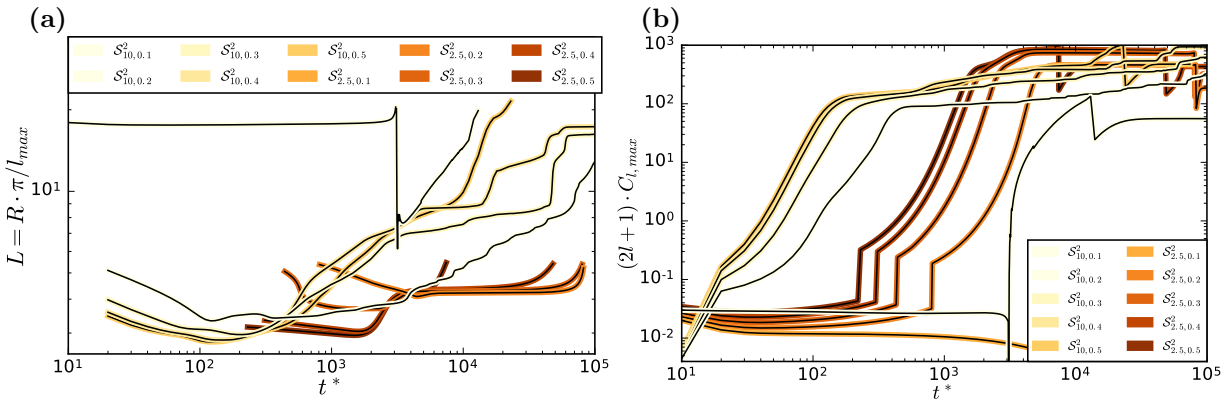

Figure 8.4: Power spectrum analysis: (a) The characteristic length scale $L_{PS} = R \cdot l_{\max}/\pi$ is identified via the position of the maximum of the angular power spectrum $l_{max} = l|_{C_l = C_{l,\max}}$. (b) Total power $(2l+1)C_{l,\max}$ of the maximum of the angular power spectrum $C_{l,\max} = max_{1<l<N}(C_l)$. The radii R and mixture parameters x on the two-sphere $\mathcal{S}^2$ are represented in the legend as: $\mathcal{S}^2_{R/R_{11},x}$.

towards the sphere surface V_0 weighted with the mixing parameter $M_0(t \to \infty) = V_0 x$. This value is only reached if the coalescence is complete with only one remaining domain. M_1 approaches the value of the boundary length of the spherical cap with surface area $V_0 x$, and M_2 is the number of already demixed domains after interfaces are formed. The number of domains can be obtained in a straightforward fashion as the value of the Euler characteristic M_2, since the domains have no holes for non-extreme threshold values. M_2 counts the difference between the number of connected domains minus the number of holes in the domains. Thus, for intermediate threshold values where demixed domains have no holes, M_2 is exactly the number of already demixed domains. The peaks for very small/large values of ρ_{th} are an artefact of the numerical calculation of functional derivatives via convolutions. The convolutions are implemented in the space of spherical harmonics leading to overshoots at pixel boundaries. However this is not a problem, since in the subsequent analysis specific, intermediate values of ρ_{th} are chosen.

Fig. 8.5, respectively Fig. 8.6 show the temporal evolution of the Minkowski functionals for the large, respectively small sphere. The threshold value $\rho_{\text{th}}/\rho_{\text{th},100}$ is color coded. A qualitative difference is observed for the regimes $\rho_{\text{th}}/\rho_{\text{th},100} < x$ and $\rho_{\text{th}}/\rho_{\text{th},100} > x$.

At the crossover value $\rho_{\text{th}}/\rho_{\text{th},100} \simeq x$ the functional show significant deviations from the functional values of neighboring thresholds. This can be explained because initially most binarized pixels for $\rho/\rho_{\text{th},100} \simeq x$ are active for relative thresholds below x. There is a sharp transition to the activation of almost all pixels at relative thresholds slightly above x. Due to this significant change in the Minkowski functionals at $\rho_{\text{th}}/\rho_{\text{th},100} \simeq x$ they can be used to measure x with only the knowledge of the very early initial stage of spinodal decomposition.

After the crossover time t_c^* the Minkowski functionals show only small differences for

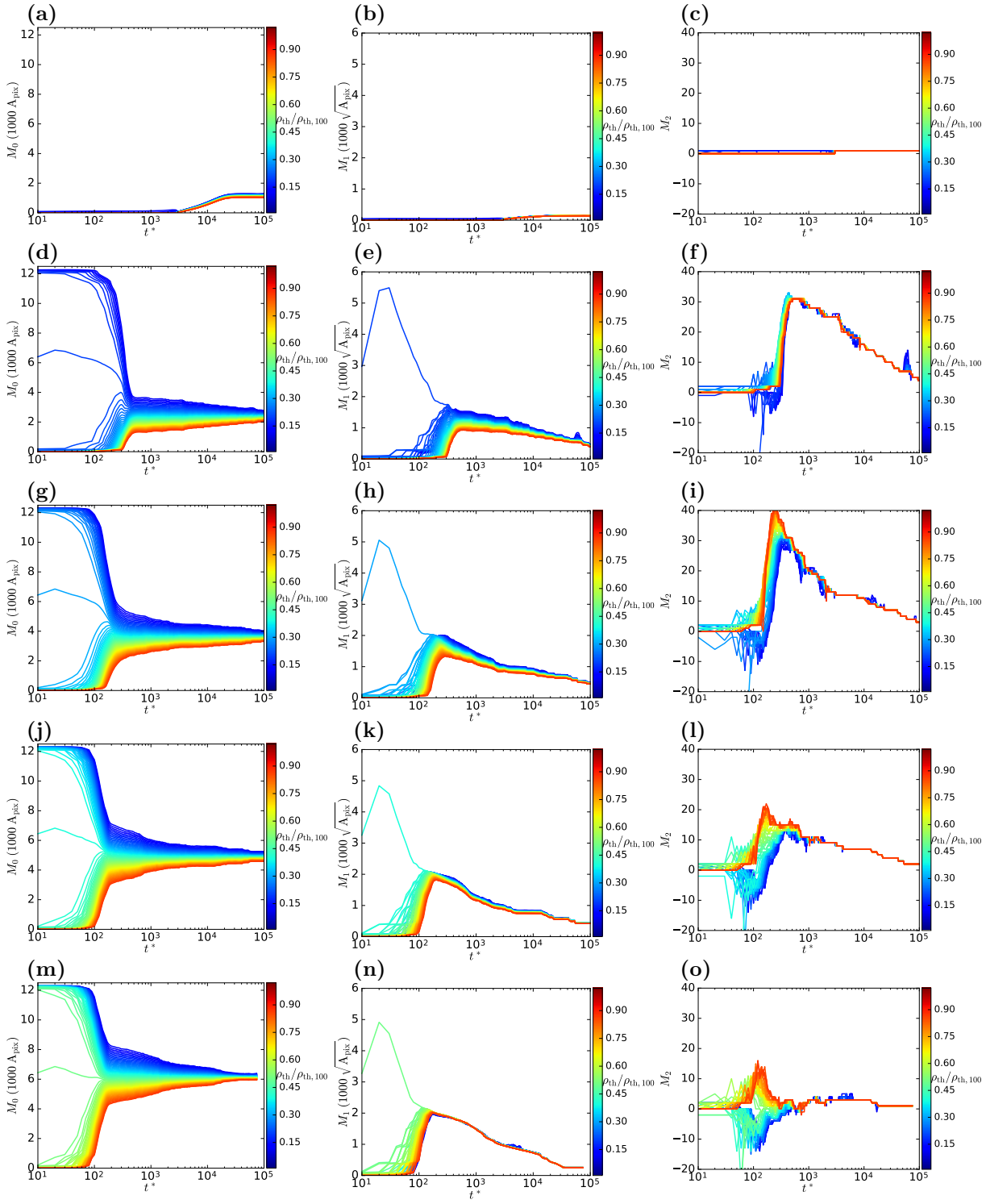

Figure 8.5: Minkowski functionals, dependence on time t^*, for the large sphere $R = 10R_{11}$. Threshold values $\rho_{\mathrm{th}}/\rho_{\mathrm{th},100}$ are color coded. First column: Area functional M_0, second column: perimeter functional M_1, third column: euler functional M_2. First row: $x = 0.1$, second row: $x = 0.2$, third row: $x = 0.3$, fourth row $x = 0.4$, fifth row: $x = 0.5$.

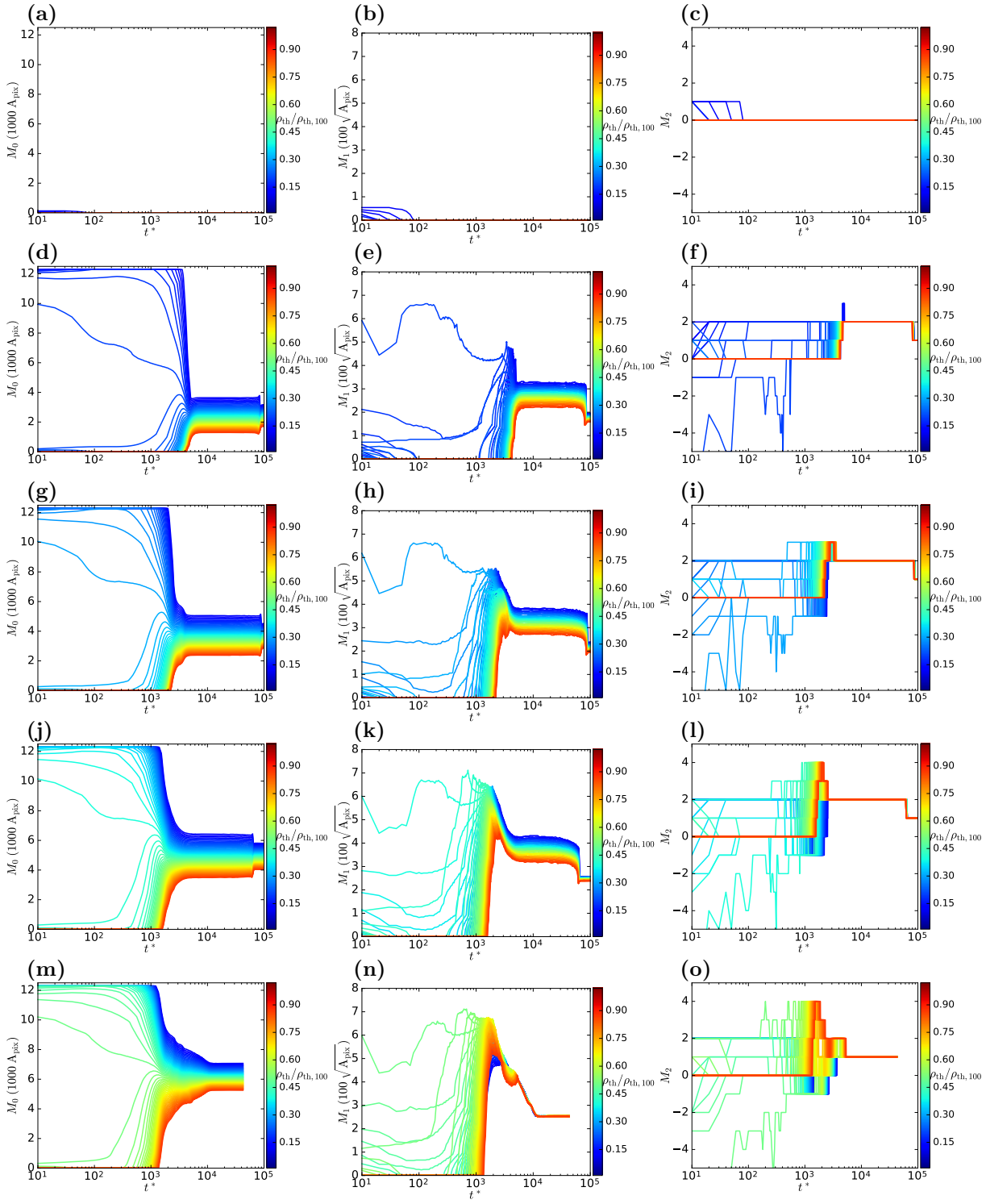

Figure 8.6: Minkowski functionals, dependence on time t^*, for the small sphere $R = 2.5R_{11}$. Threshold values $\rho_{\mathrm{th}}/\rho_{\mathrm{th,100}}$ are color coded. First column: Area functional M_0, second column: perimeter functional M_1, third column: euler functional M_2. First row: $x = 0.1$, second row: $x = 0.2$, third row: $x = 0.3$, fourth row $x = 0.4$, fifth row: $x = 0.5$.

different threshold levels, allowing the precise measurement of t_c^* in a computationally inexpensive manner.

The Minkowski functional graphs obtained on the sphere are in qualitative agreement with Minkowski functionals calculated for spinodal decomposition in flat two-dimensional geometry of a liquid-vapor system [155, 115]. The liquid-vapor system belongs to the same universality class as the fluid-fluid system [138].

In the subsequent analyses specific threshold values are chosen, such that the minimal number of active pixels is close to unity and the Minkowski functionals have their maximal scaling range as $\rho_{\mathrm{th}}/\rho_{\mathrm{th},100} \simeq x$. Such graphs are presented in the appendix C in Fig. C.3 and Fig. C.4. In these graphs two demixing stages can be evidenced since they show a transition at the crossover time t_c^* when the domain interfaces form and coalescence begins. $t_c^* \simeq 2 \cdot 10^2$ in the case of $R = 10R_{11}$ and $t_c^* \simeq 2 \cdot 10^3$ in the case of $R = 2.5R_{11}$.

Logarithmic plots of the Minkowski functionals are presented in the appendix C in Fig. C.4. Compared to the angular power spectral density measures (Fig. 8.4) they provide several advantages: The high sensitivity to changes in the morphology allows the Minkowski functionals to detect transitions in the behavior of domain growth not visible to power spectrum measures. The Minkowski functionals resolve three distinct phases in the early stage of spinodal decomposition: (1) fast growth (2) slower growth, (3) main growth of density fluctuations. In the power spectrum however, only phases (1) and (3) are detected.

The homogeneity of the Minkowski functionals (Eq. (5.34)) leads to a power law for the scaling by a length L:

$$M_0 \propto 1,\ M_1 \propto L^{-1},\ M_2 \propto L^{-2} \tag{8.1}$$

L is interpreted as the characteristic size of demixed domains. The scaling of $1/M_1 \propto L$ and $1/\sqrt{M_2} \propto L$ is presented in Fig. 8.7. A power law growth is evidenced for the domain size in the coalescence stage $L \propto t^{*\alpha}$.

However, the small sphere exhibits only few coalescence events and thus the domain growth is characterized by plateaus connected with rapid size changes at coalescence events. This leads to a bad statistic in detecting the power law by fitting a line in the log-log plot. The power law exponents α, obtained by liner fits, are presented in the appendix C in table C.1.

Most power law exponents are $\alpha \simeq 0.2$, which is similar to the prediction of [23]. This is smaller than the value predicted by mean field theory for the diffusive regime (which is $\alpha = 1/3$ [104, 162]). However for the equal concentration mixture $x = 0.5$ the power law exponent is closer to $1/3$.

By a suitable rescaling $r(R, x)$ of Minkowski functionals and time axis, the graphs for all mixing parameters $x > 0.1$ and sphere sizes R coincide well. This is shown in Fig. 8.8. Explicit scalings are: $t^* \to t^* \cdot x^{-2/3} \cdot (R/R_{11})^{3/2}$, $M_0 \to M_0/x$, $M_1 \to M_1/\sqrt{x}/(R/R_{11})^{0.8}$. This suggest a universal demixing behavior for $x > 0.1$, qualitatively different to the case $x = 0.1$. The measures based on the angular power spectral density fail to show any universal features. This suggests that nonlinearities are responsible. Evidently, the

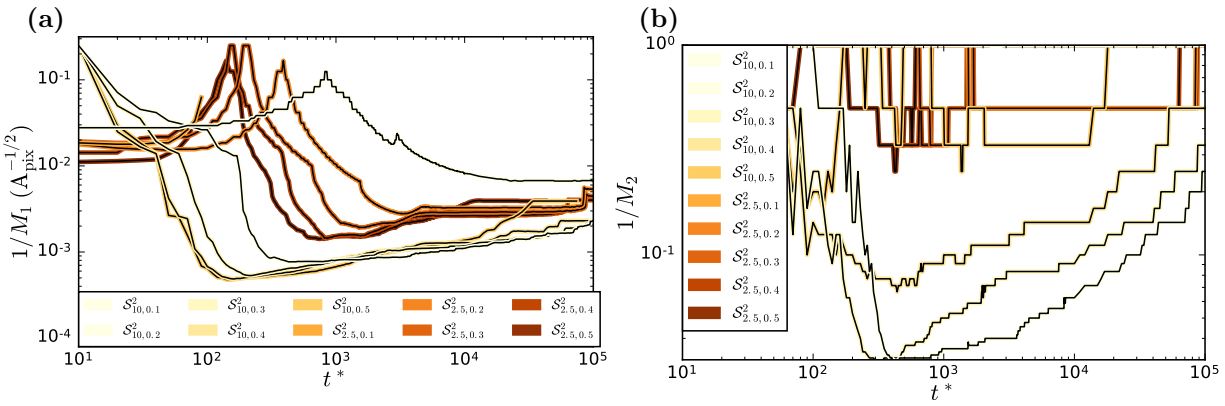

Figure 8.7: Scaling behaviour of $1/M_1 \propto L$ and $1/\sqrt{M_2} \propto L$ reveal power law domain growth $L \propto t^{*\alpha}$ after spinodal decomposition. The radii R and mixture parameters x on the two-sphere $\mathcal{S}^2$ are represented in the legend as: $\mathcal{S}^2_{R/R_{11},x}$.

Minkowski functional measures provide qualitatively new result compared to linear power spectral density measures. They may play a key role in the further investigation of universal features of demixing processes.

8.5 Conclusions and outlook

Distinct stages of spinodal decomposition can be detected in DDFT demixing calculations of a binary fluid. The onset, the main fluctuation growth stage and the coalescence stage of spinodal decomposition can be detected by analyzing the shape of the total power of the fluid density. The usual demixing metric, the average domain size deduced from the position of the maximum of the power spectral density, is however, only responsive to the domain growth during the coalescence stage.

The Minkowski functional analysis provides further advantages in many respects. The most important points are:

– Minkowski functionals can detect a further stage in the phase of early spinodal decomposition.

– They allow the measurement of domain growth rates with high statistical significance.

– Their dynamic range depends only on the resolution of the data, since one can always find a threshold such that only one pixel is detected as active.

– The transitions between demixing stages is more pronounced than in the case of power spectrum measures. This allows the precise measurement of transition times with low computational cost.

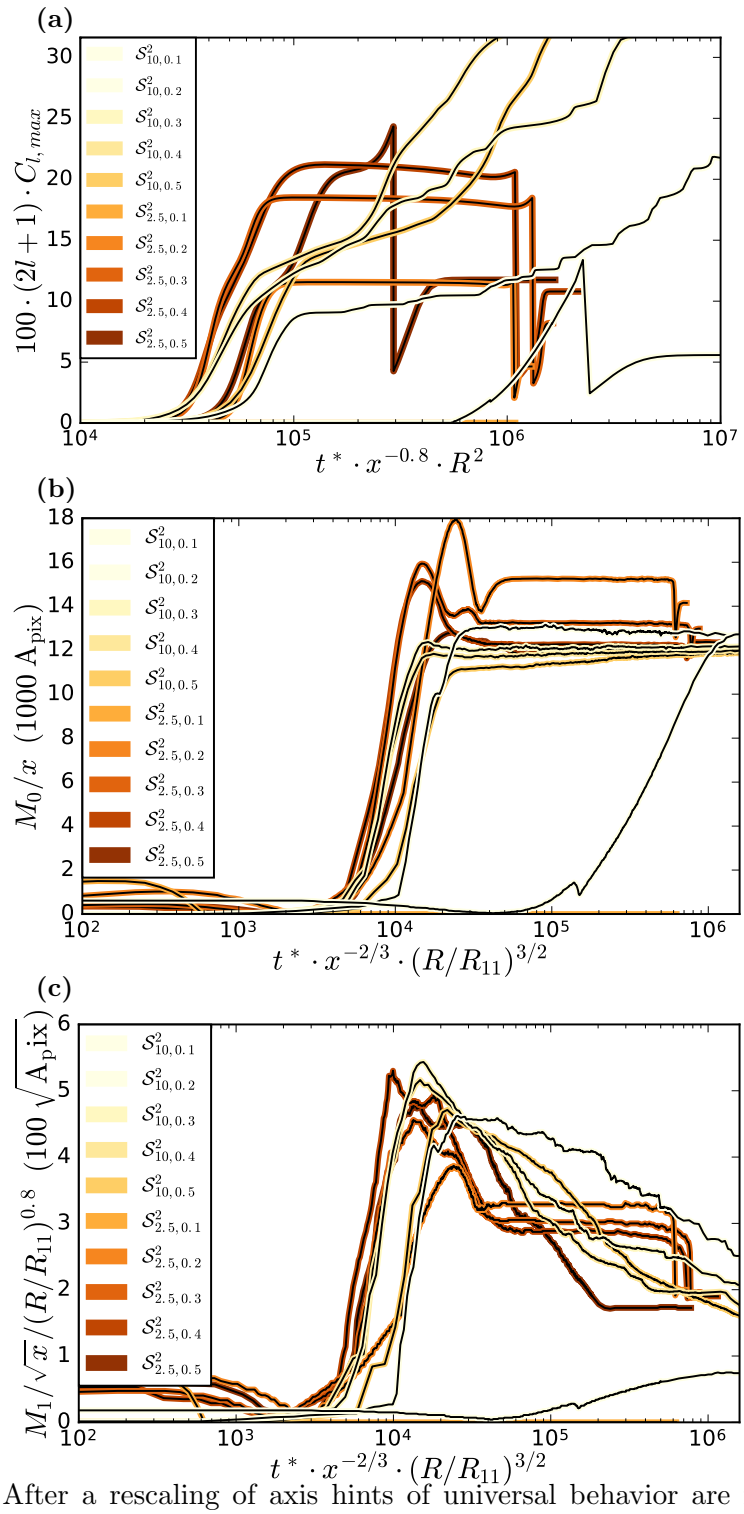

Figure 8.8: After a rescaling of axis hints of universal behavior are found in panel (b) for M_0 and in panel (c) for M_1. However, in panel (a), no universal behavior is found for power spectral density $(2l+1) \cdot C_{l,\max}$. The radii R and mixture parameters x on the two-sphere $\mathcal{S}^2$ are represented in the legend as: $\mathcal{S}^2_{R/R_{11},x}$.

– Using Minkowski functionals the species composition can be measured precisely by only observing the early spinodal decomposition.

– Most importantly: Minkowski functionals reveal universal features in the demixing behavior for a large number of species compositions and sphere sizes and a qualitatively different demixing scenario when one species has a small concentration. Power spectrum measures cannot reveal universal behavior of the domain growth.

Future work will focus on the systematic characterization of these universal features and on the relation to the universal properties described for the flat three-dimensional case in section 7. The nonlinear origin of the universal behavior suggests the application of surrogates [145, 122, 121] to identify the specific nonlinear contributions to the demixing dynamics.

Chapter 9

Summary and outlook

This thesis aimed to provide a contribution to advance the understanding of emergent, self-organized phenomena in the field of many-body statistical physics. Physical systems consisting of many particles out of equilibrium still give rise to the curiosity of scientists all around the world. Even when the interaction between individual constituents is understood, systems with large particle numbers are able to form complex structures of manifold shapes and topologies. In this thesis two examples of such systems have been studied: The crystallization process of two-dimensional complex plasma sheets and the fluid demixing dynamics of both simulations of a complex plasma in three dimensions and density-functional calculations of a binary fluid on the curved geometry of a sphere.

By extending the characterization and analysis of spatial structure from traditional methods as e.g. the power spectral density or the bond-order parameters, to nonlinear structure metrics capturing the complete morphological information of patterns ranging from shape and geometry, to connectedness and topology, it was possible to gain qualitatively new insight into the physical processes studied in this dissertation.

After analyzing the long-range decay of the far asymptotes of the pair correlation and the bond correlation function of experiments as well as of a simulation of the crystallization of two-dimensional complex plasma sheets it could be shown, that the KTHNY theory of melting in two dimensions cannot be applied to these complex plasma systems since no hexatic phase could be detected. A recently developed fractal-domain-structure (FDS) theory was also tested. It assumes that the crystallization process is accompanied by the formation of domains in the crystalline phase that are separated by lines of crystal defects and postulates a fractal relation between the domain area and boundary length. The theory predicts a scale-free dependence of the total defect fraction on the system energy. Both, the postulate and the prediction of the FDS theory are verified in this dissertation by the detection of crystal defects. This suggests that the FDS theory, rather than the KTHNY theory, is applicable to non-equilibrium liquid-solid phase transitions in two-dimensional systems.

In particle resolved simulations of binary complex plasma systems in three-dimensional Euclidean space, a universal behavior of the demixing dynamics for long-range dominated particle interactions is found. In contrast, the formation of demixed domains in the case

of short-range interactions is qualitatively different. In the long-range dominated case two stages of the demixing process are observed. Initially neighboring particles of one species agglomerate, subsequently the agglomerated particles coalesce in cascades. This process is accelerated and demixed domains become larger when the range of the interaction is increased. When interactions are sufficiently short-ranged, no coalescence stage can be observed. Demixing occurs only due to the agglomeration of neighboring particles. In order to address the impact of confinement and of curved geometry on the demixing dynamics, without imposing artificial boundary conditions, density-functional theory (DDFT) calculations on spherical geometries are analzsed. Again universal features of the dynamics of demixed domain growth can be identified. Here the universality is found for different mixing compositions and on different sized sphere embeddings. By the comparison of the growth rates of demixed domains three distinct stages prior to the coalescence are evidenced. A qualitatively different scenario is found for small mixing fractions: Depending on the sphere size there is either no demixing during the DDFT calculation time, or demixing occurs, without transition to the coalescence stage, at much later times compared to larger mixing fractions. The reason for the late demixing seems to be that the particle separation of the low concentration species is high. No demixing during the DDFT calculation time is achieved for the small sphere where finite size effects play an increased role.

In this thesis the spatial data is analzsed on the one hand by using conventional linear measures as the power spectrum, pair correlation functions and bond order parameters. On the other hand a morphological characterization with nonlinear measures, derived from the family of Minkowski functionals and tensors, is performed. These measures describe shape, elongation, symmetry and connectedness and are sensitive to any n-point density correlation function. They show several advantages in comparison with linear measures. For instance it is possible to robustly and continuously detect crystal distortions using Minkowski tensor measures. This allows the verification of the prediction of the FDS theory for defect fractions ranges one order of magnitude larger compared to the conventional bond order parameter. The most significant advantage is the detection of universal features in fluid-fluid demixing systems that cannot be found by utilizing power spectrum measures. This suggests, that the universal features originate from nonlinearities in the underlying physics.

The nonlinear origin of universal behavior is a curial point to be addressed in future work. This can be done by applying the method of surrogates, i.e. by creating copies of the spatial data with preserved linear properties but with the nonlinear features removed (by transforming the Fourier phases such that they become uncorrelated and randomized). In future studies the emergence of universal behavior in demixing systems will be analyzed systematically. The shape and range of the particle interaction potential, the composition of mixed particle species and the confinement of particles are predictor variables the focus will lie on. Another key point of future studies is the description of the demixing kinetics in the context of spinodal decomposition for particle resolved systems, which are not covered in the mean field theory approach.

Appendix A

Explicit formulae for Minkowski tensors of triangulated bodies

This section provides supplementary material to section 5.

A.1 Tensors in two dimensions

The linearly independent two-dimensional Minkowski tensors up to rank two are given in Table A.1. An extensive description of Minkowski tensors for planar patterns can be found in [150].

A.2 Tensors in three dimensions

To simplify the expressions for the triangulated tensors the symmetric tensor $\Lambda^n_{(k,l,m)}$ is introduced in [152]:

$$\Lambda^n_{(k,l,m)} = 2A_{(k,l,m)} \int_0^1 \mathrm{d}\lambda \int_0^{1-\lambda} \mathrm{d}\mu \ \left(\mathbf{v}_k + \lambda\,(\mathbf{v}_l - \mathbf{v}_k) + \mu\,(\mathbf{v}_m - \mathbf{v}_k)^{\odot n}\right) \tag{A.1}$$

The linearly independent three-dimensional Minkowski tensors up to rank two are given in Table A.3. The specific components of the tensor $\Lambda^n_{(k,l,m)}$ (Eq. A.1) that have to be chosen for in the formulae in table A.3 for the indices μ (according to the corresponding Minkowski vector components α or Minkowski tensor components α, β) are given in table A.2.

Table A.1: Linearly independent two-dimensional Minkowski tensors up to tensor rank two. $\mathbf{x} = x\hat{\mathbf{x}} + y\hat{\mathbf{y}}$ are the position vectors, $\mathbf{n}$ the normal vectors of K. The brackets $[\mathbf{x}]_x = x$ indicate the tensor components. In the polygonal representation the vertices $\mathbf{v}_k$ and $\mathbf{v}_l$ are connected by the edge $\mathbf{e}_{(k,l)}$. The normal vector $\mathbf{n}_{(k,l)}$ is orthogonal to $\mathbf{e}_{(k,l)}$. The angle between $\mathbf{n}_{(k,l)}$ and $\mathbf{n}_{(l,m)}$ is γ_l. $E_2 = \hat{\mathbf{x}} \odot \hat{\mathbf{x}} + \hat{\mathbf{y}} \odot \hat{\mathbf{y}}$ is the two-dimensional unit tensor.

tensor	definition	polygonal representation
scalar functionals		
$W_0(K)$	$\int_K \mathrm{d}^2\mathbf{x}$	$\frac{1}{4}\sum_{(k,l)} \lvert\mathbf{e}_{(k,l)}\rvert \cdot \left(\mathbf{n}_{(k,l)} \cdot (\mathbf{v}_k + \mathbf{v}_l)\right)$
$W_1(K)$	$\frac{1}{2}\int_{\partial K} \mathrm{d}\mathbf{x}$	$\frac{1}{2}\sum_{(k,l)} \lvert\mathbf{e}_{(k,l)}\rvert$
$W_2(K)$	$\frac{1}{2}\int_{\partial K} \kappa(\mathbf{x})\,\mathrm{d}\mathbf{x}$	$\frac{1}{2}\sum_k \gamma_k$
vectors		
$\left[W_0^{1,0}(K)\right]_x$	$\int_K x\,\mathrm{d}^2\mathbf{x}$	$\sum_{(k,l)} \left([\mathbf{v}_l]_y - [\mathbf{v}_k]_y\right) \cdot \left([\mathbf{v}_k]_x^2 + [\mathbf{v}_k]_x [\mathbf{v}_l]_x + [\mathbf{v}_l]_x^2\right)$
$W_1^{(1,0)}(K)$	$\frac{1}{2}\int_{\partial K} \mathbf{x}\,\mathrm{d}\mathbf{x}$	$\frac{1}{4}\sum_{(k,l)} \lvert\mathbf{e}_{(k,l)}\rvert (\mathbf{v}_k + \mathbf{v}_l)$
$W_2^{(1,0)}(K)$	$\frac{1}{2}\int_{\partial K} \mathbf{x}\,\kappa(\mathbf{x})\,\mathrm{d}\mathbf{x}$	$\frac{1}{2}\sum_k \gamma_k$
rank two tensors		
$[W_0(K)E_2]_{xx}$	$\int_K \mathrm{d}^2\mathbf{x}$	$\frac{1}{4}\sum_{(k,l)} \lvert\mathbf{e}_{(k,l)}\rvert \cdot \left(\mathbf{n}_{(k,l)} \cdot (\mathbf{v}_k + \mathbf{v}_l)\right)$
$[W_1(K)E_2]_{xx}$	$\frac{1}{2}\int_{\partial K} \mathrm{d}\mathbf{x}$	$\frac{1}{2}\sum_{(k,l)} \lvert\mathbf{e}_{(k,l)}\rvert$
$[W_2(K)E_2]_{xx}$	$\frac{1}{2}\int_{\partial K} \kappa(\mathbf{x})\,\mathrm{d}\mathbf{x}$	$\frac{1}{2}\sum_k \gamma_k$
$W_2^{(1,1)}(K)$	$\frac{1}{2}\int_{\partial K} \mathbf{x} \odot \mathbf{n}\,\kappa(\mathbf{x})\,\mathrm{d}\mathbf{x}$	$\frac{1}{2}\sum_k \lvert\mathbf{e}_{(k,l)}\rvert^{-1} \mathbf{e}_{kl} \odot \mathbf{e}_{kl}$
$\left[W_0^{2,0}(K)\right]_{xx}$	$\int_K x^2\,\mathrm{d}^2\mathbf{x}$	$\frac{1}{12}\sum_{(k,l)} \lvert\mathbf{e}_{(k,l)}\rvert \left[\mathbf{n}_{(k,l)}\right]_x \cdot \left([\mathbf{v}_k]_x^3 + [\mathbf{v}_l]_x^3 + [\mathbf{v}_k]_x^2 [\mathbf{v}_l]_x + [\mathbf{v}_k]_x [\mathbf{v}_l]_x^2\right)$
$\left[W_0^{2,0}(K)\right]_{xy}$	$\int_K x\,y\,\mathrm{d}^2\mathbf{x}$	$\frac{1}{14}\sum_{(k,l)} \left([\mathbf{v}_k]_y [\mathbf{v}_l]_x - [\mathbf{v}_k]_x [\mathbf{v}_l]_y\right) \cdot \left([\mathbf{v}_k]_x \left(2[\mathbf{v}_k]_y - [\mathbf{v}_l]_y\right) - [\mathbf{v}_l]_x \left(2[\mathbf{v}_l]_y - [\mathbf{v}_k]_y\right)\right)$
$W_1^{(2,0)}(K)$	$\frac{1}{2}\int_{\partial K} \mathbf{x} \odot \mathbf{x}\,\mathrm{d}\mathbf{x}$	$\frac{1}{6}\sum_{(k,l)} \lvert\mathbf{e}_{(k,l)}\rvert (\mathbf{v}_k \odot \mathbf{v}_k + \mathbf{v}_k \odot \mathbf{v}_l + \mathbf{v}_l \odot \mathbf{v}_l)$
$W_2^{(2,0)}(K)$	$\frac{1}{2}\int_{\partial K} \mathbf{x} \odot \mathbf{x}\,\kappa(\mathbf{x})\,\mathrm{d}\mathbf{x}$	$\frac{1}{2}\sum_k \gamma_k\,\mathbf{v}_k \odot \mathbf{v}_k$

Table A.2: Tensor components μ of $\Lambda^n_{(k,l,m)}$ (Eq. A.1) that have to be chosen for in the formulae in table A.3 according to the corresponding Minkowski vector (MV) components α or Minkowski tensor (MT) components α, β.

MV α	μ	MT α, β	μ
x	y	x,x	z
y	z	y,y	x
z	x	z,z	y
		x,y	z
		y,z	x
		z,x	y

Table A.3: Linearly independent three-dimensional Minkowski tensors up to tensor rank two. $\mathbf{x} = x\hat{\mathbf{x}} + y\hat{\mathbf{y}} + z\hat{\mathbf{z}}$ are the position vectors, $\mathbf{n}$ the normal vectors of K. The brackets $[\mathbf{x}]_1 = x$ indicate the tensor components. The triangulated surface is a collection of facets (k,l,m) with areas $A_{(k,l,m)}$, edges $\mathbf{e}_{(k,l)}$ and vertices $\mathbf{v}_k$. $\mathbf{n}_{(k,l,m)}$ is the facet normal, $\mathbf{n}_{(k,l)}$ the edge normal. $\gamma_{(k,l,m)}$ are the internal angles of neighboring facets, γ_k is the angular defect. The tensors $\Lambda^n_{k,l,m}$ are given in Eq. A.1 and its components for ω in Table A.2.

tensor	definition	triangulated representation
scalar functionals		
$W_0(K)$	$\int_K \mathrm{d}^3\mathbf{x}$	$\frac{1}{9}\sum_{(k,l,m)} A_{(k,l,m)}\,(\mathbf{v}_k+\mathbf{v}_l+\mathbf{v}_m)\cdot\mathbf{n}_{(k,l,m)}$
$W_1(K)$	$\frac{1}{3}\int_{\partial K} \mathrm{d}^2\mathbf{x}$	$\frac{1}{3}\sum_{(k,l,m)} A_{(k,l,m)}$
$W_2(K)$	$\frac{1}{6}\int_{\partial K} (\kappa_1+\kappa_2)\,\mathrm{d}^2\mathbf{x}$	$\frac{1}{6}\sum_{(k,l)} \lvert\mathbf{e}_{(k,l)}\rvert\,\gamma_{(k,l)}$
$W_3(K)$	$\frac{1}{3}\int_{\partial K} \kappa_1\kappa_2 \mathrm{d}^2\mathbf{x}$	$\frac{1}{3}\sum_k \gamma_k$
vectors		
$\left[W_0^{1,0}(K)\right]_\alpha$	$\int_K \mathbf{x}_\alpha\,\mathrm{d}^3\mathbf{x}$	$\sum_{(k,l,m)} \left[\Lambda^2_{(k,l,m)}\right]_{\alpha,\mu} [\mathbf{n}_{k,l,m}]_\omega$
$W_1^{(1,0)}(K)$	$\frac{1}{9}\int_{\partial K} \mathbf{x}\,\mathrm{d}^2\mathbf{x}$	$\frac{1}{9}\sum_{(k,l,m)} A_{(k,l,m)}\,(\mathbf{v}_k+\mathbf{v}_l+\mathbf{v}_m)$
$W_2^{(1,0)}(K)$	$\frac{1}{6}\int_{\partial K} \mathbf{x}\,(\kappa_1+\kappa_2)\,\mathrm{d}^2\mathbf{x}$	$\frac{1}{12}\sum_{(k,l)} \lvert\mathbf{e}_{(k,l)}\rvert\,\gamma_{(k,l)}\cdot(\mathbf{v}_k+\mathbf{v}_l)$
$W_3^{(1,0)}(K)$	$\frac{1}{3}\int_{\partial K} \mathbf{x}\,\kappa_1\kappa_2\,\mathrm{d}^2\mathbf{x}$	$\frac{1}{3}\sum_k \gamma_k\mathbf{v}_k$
rank two tensors		
$[W_0(K)]_{\alpha,\beta}$	$\int_K \mathrm{d}^3\mathbf{x}$	$\frac{1}{9}\sum_{(k,l,m)} A_{(k,l,m)}\,(\mathbf{v}_k+\mathbf{v}_l+\mathbf{v}_m)\cdot\mathbf{n}_{(k,l,m)}$
$[W_1(K)]_{\alpha,\beta}$	$\frac{1}{3}\int_{\partial K} \mathrm{d}^2\mathbf{x}$	$\frac{1}{3}\sum_{(k,l,m)} A_{(k,l,m)}$
$[W_2(K)]_{\alpha,\beta}$	$\frac{1}{6}\int_{\partial K} (\kappa_1+\kappa_2)\,\mathrm{d}^2\mathbf{x}$	$\frac{1}{6}\sum_{(k,l)} \lvert\mathbf{e}_{(k,l)}\rvert\,\gamma_{(k,l)}$
$[W_3(K)]_{\alpha,\beta}$	$\frac{1}{3}\int_{\partial K} \kappa_1\kappa_2 \mathrm{d}^2\mathbf{x}$	$\frac{1}{3}\sum_k \gamma_k$
$\left[W_0^{2,0}(K)\right]_{\alpha,\beta}$	$\int_K [\mathbf{x}\odot\mathbf{x}]_{\alpha,\beta}\,\mathrm{d}^3\mathbf{x}$	$\sum_{(k,l)} \left[\Lambda^3_{(k,l,m)}\right]_{\alpha,\beta,\mu} \left[\mathbf{n}_{(k,l,m)}\right]_\omega$
$W_1^{(2,0)}(K)$	$\frac{1}{3}\int_{\partial K} \mathbf{x}\odot\mathbf{x}\,\mathrm{d}^2\mathbf{x}$	$\frac{1}{3}\sum_{(k,l,m)} \Lambda^2_{(k,l,m)}$
$W_2^{(2,0)}(K)$	$\frac{1}{6}\int_{\partial K} \mathbf{x}\odot\mathbf{x}\,(\kappa_1+\kappa_2)\,\mathrm{d}^2\mathbf{x}$	$\frac{1}{18}\sum_{(k,l)} \lvert\mathbf{e}_{(k,l)}\rvert\,\gamma_{(k,l)}\,(\mathbf{v}_k\odot\mathbf{v}_k+\mathbf{v}_k\odot\mathbf{v}_l+\mathbf{v}_l\odot\mathbf{v}_l)$
$W_3^{(2,0)}(K)$	$\frac{1}{3}\int_{\partial K} \mathbf{x}\odot\mathbf{x}\,\kappa_1\kappa_2\mathrm{d}^2\mathbf{x}$	$\frac{1}{3}\sum_k \gamma_k\mathbf{v}_k\odot\mathbf{v}_k$
$W_1^{(0,2)}(K)$	$\frac{1}{3}\int_{\partial K} \mathbf{n}\odot\mathbf{n}\,\mathrm{d}^2\mathbf{x}$	$\frac{1}{3}\sum_{(k,l,m)} A_{(k,l,m)}\mathbf{n}_{(k,l,m)}\odot\mathbf{n}_{(k,l,m)}$
$W_2^{(0,2)}(K)$	$\frac{1}{6}\int_{\partial K} \mathbf{n}\odot\mathbf{n}\,(\kappa_1+\kappa_2)\,\mathrm{d}^2\mathbf{x}$	$\sum_{(k,l)} \lvert\mathbf{e}_{(k,l)}\rvert\,\{\left(\gamma_{(k,l)}+\sin(\gamma_{(k,l)})\right)\left(\mathbf{n}_{(k,l)}\right)^{\odot 2} + \left(\gamma_{(k,l)}-\sin(\gamma_{(k,l)})\right)\left(\frac{\mathbf{n}_{(k,l)}\times\mathbf{e}_{(k,l)}}{\lvert\mathbf{e}_{(k,l)}\rvert}\right)^{\odot 2}\}$

Appendix B

Fractal-Domain-Structure in a two-dimensional complex plasma

This section provides supplementary material to section 7.

Illustrations of the domain structure nature of the complex plasma sheets for all experiments and the simulations are given in Fig. B.1, Fig. B.2, Fig. B.3 and Fig. B.4. The Voronoi cells are color coded by the three measures Ψ_6, $\beta_2^{2,0}$ and Δ_{hex}. One can clearly see the that the Minkowski functional measures provide a continuous metric for lattice distortions, whereas the bond order metric is more binary. This leads to the improved sensitivity of Minkowski tenor measures at low energies and allows the verification of the power law Eq. (2.18) for a much larger scaling range compared to the bond order metric as it is presented in Fig. 6.5.

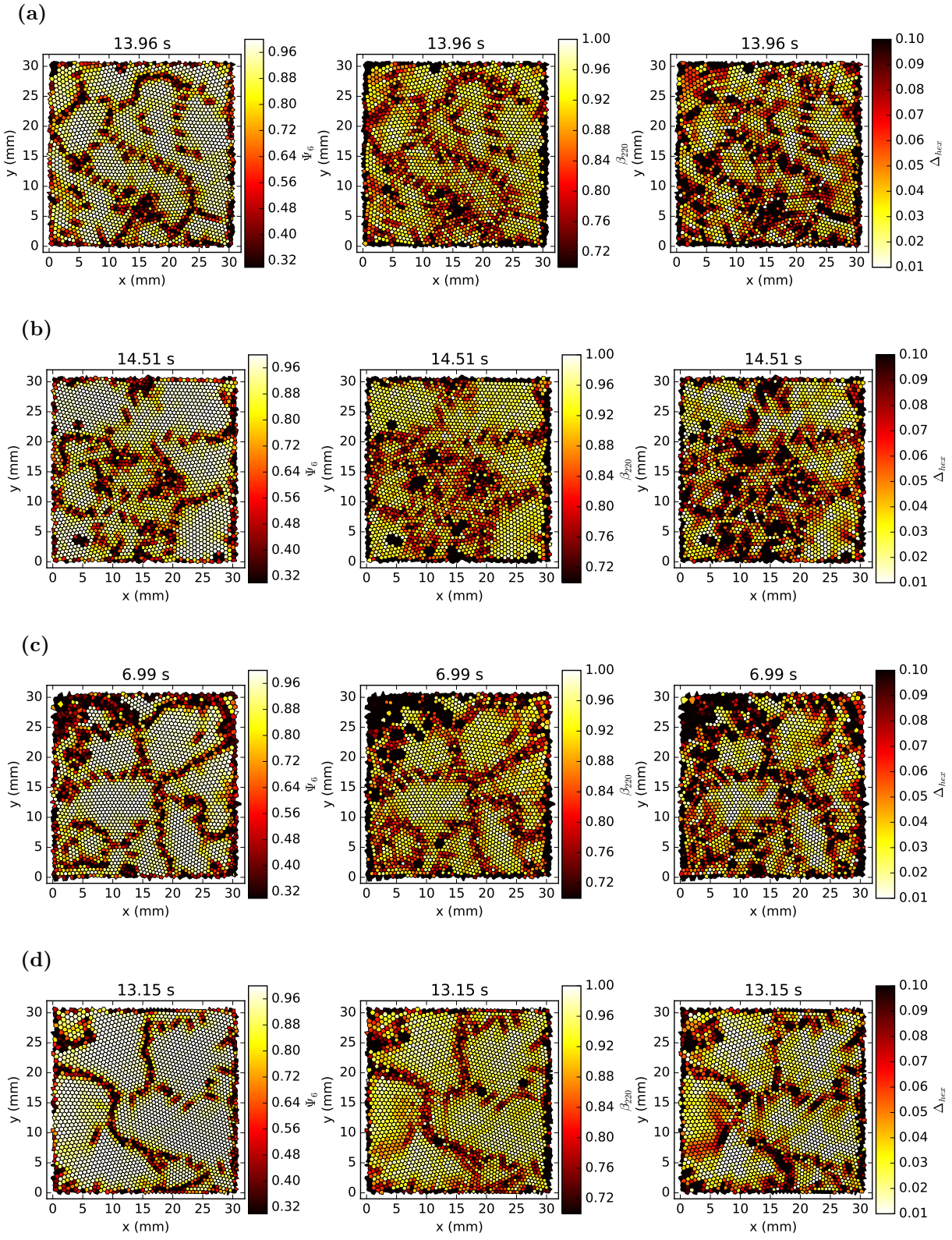

Figure B.1: Illustration of experiments I-IV. The Voronoi cells are color coded by Ψ_6 (left panels), $\beta_2^{2,0}$ (middle panels) and Δ_{hex} (right panels).

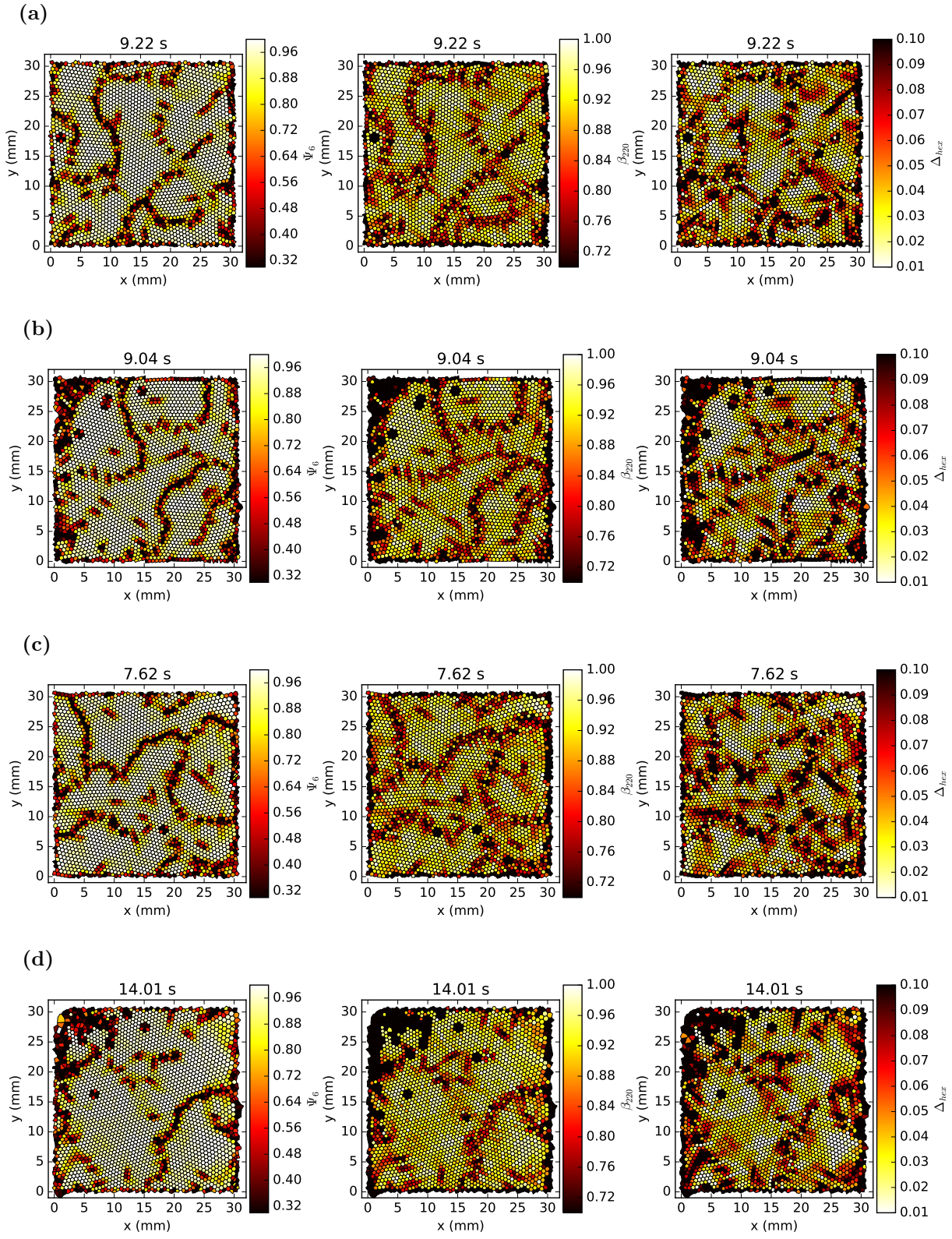

Figure B.2: Illustration of experiments V-VIII. The Voronoi cells are color coded by Ψ_6 (left panels), $\beta_2^{2,0}$ (middle panels) and Δ_{hex} (right panels).

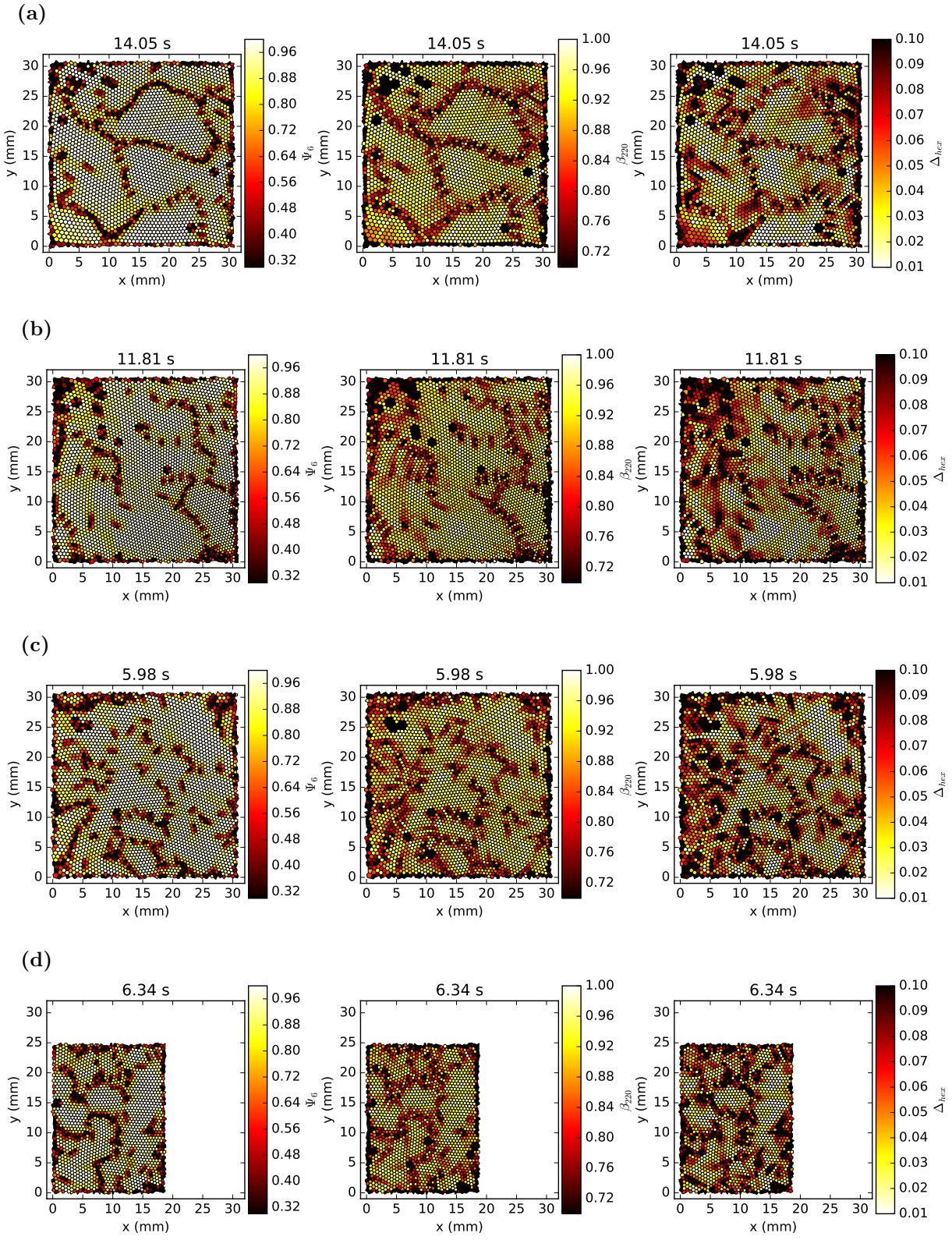

Figure B.3: Illustration of experiments IX-XII. The Voronoi cells are color coded by Ψ_6 (left panels), $\beta_2^{2,0}$ (middle panels) and Δ_{hex} (right panels).

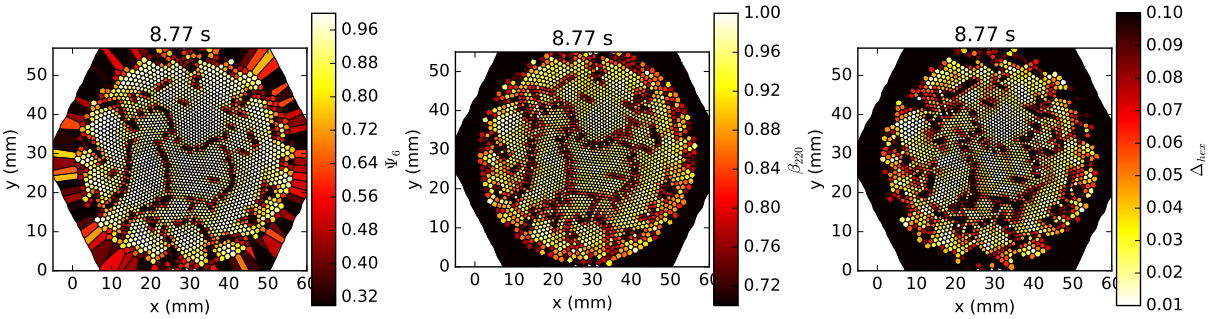

Figure B.4: Illustration of simulation S. The Voronoi cells are color coded by Ψ_6 (left panel), $\beta_2^{2,0}$ (middle panel) and Δ_{hex} (right panel).

Appendix C

Minkowski functionals for fluid demixing on spherical geometry

This section provides supplementary material to section 8.

The dependence of the Minkowski functionals on the threshold density ρ_{th} is presented in Fig. C.1 for the large sphere and in Fig. C.2 for the small sphere. The time t^* is color coded.

For the detailed analyses in 8 specific threshold values are chosen, such that the minimal number of active pixels is close to unity and the Minkowski functionals have their maximal scaling range as $\rho_{\mathrm{th}}/\rho_{\mathrm{th},100} \simeq x$. Such graphs are presented in Fig. C.3 and in Fig. C.4. In these graphs two demixing stages can be evidenced since they show a transition at the crossover time t_c^* when the domain interfaces form and coalescence begins. $t_c^* \simeq 2 \cdot 10^2$ in the case of $R = R_{11}$ and $t_c^* \simeq 2 \cdot 10^3$ in the case of $R = 2.5R_{11}$.

Logarithmic plots of the Minkowski functionals are presented in Fig. C.4.

The power-law exponents α, obtained by liner fits of the total power $(2l+1)C_l$, the average domain size obtained by the power spectrum L and $1/M_1$ and $1/\sqrt{M_2}$, are presented in table C.1.

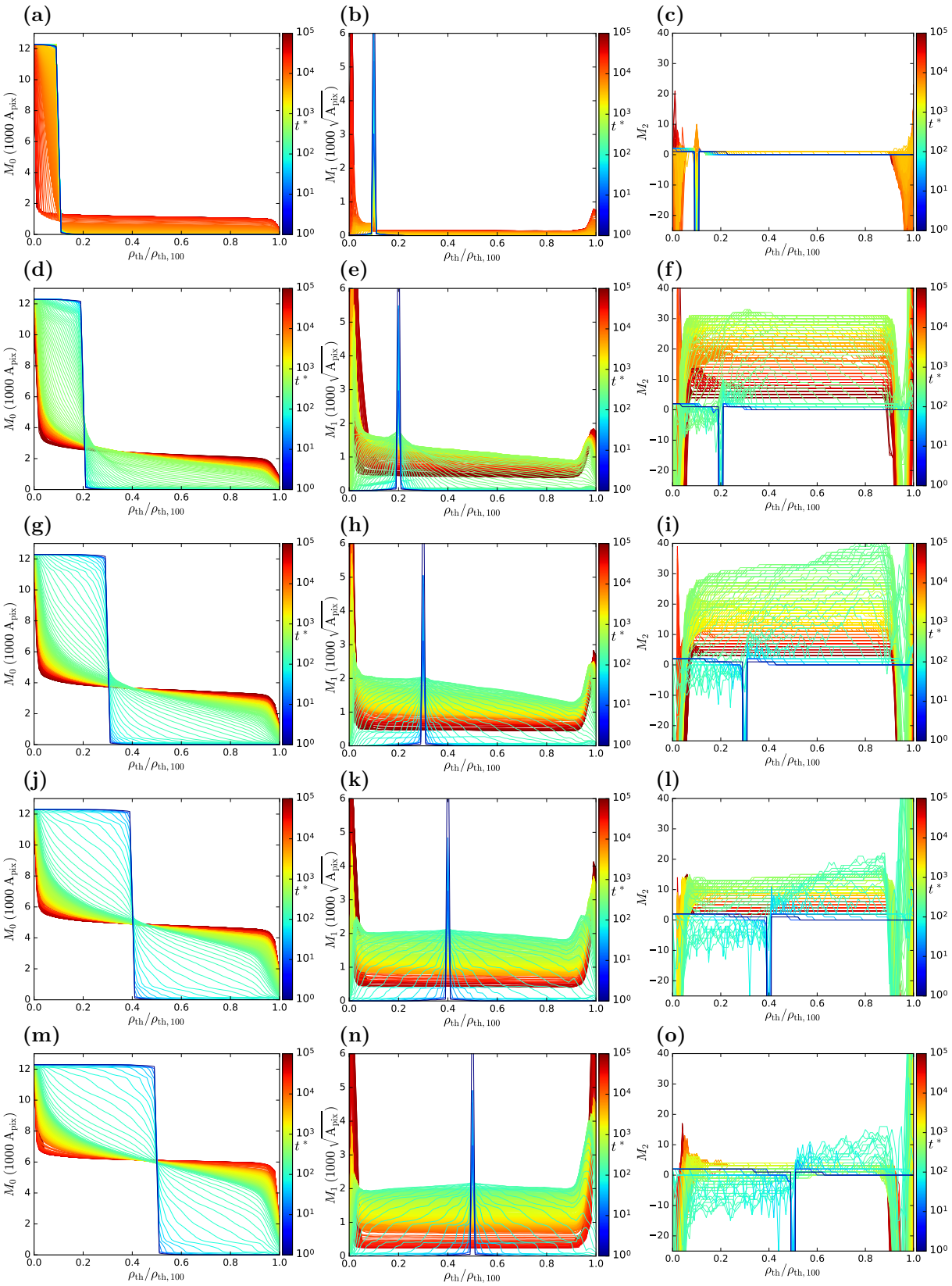

Figure C.1: Minkowski functionals dependence on the relative threshold density $\rho_{\mathrm{th}}/\rho_{\mathrm{th,100}}$ for the large sphere $R = 10R_{11}$. Time t^* is color coded. First column: Area functional M_0, second column: perimeter functional M_1, third column: euler functional M_2. First row: $x = 0.1$, second row: $x = 0.2$, third row: $x = 0.3$, fourth row $x = 0.4$, fifth row: $x = 0.5$.

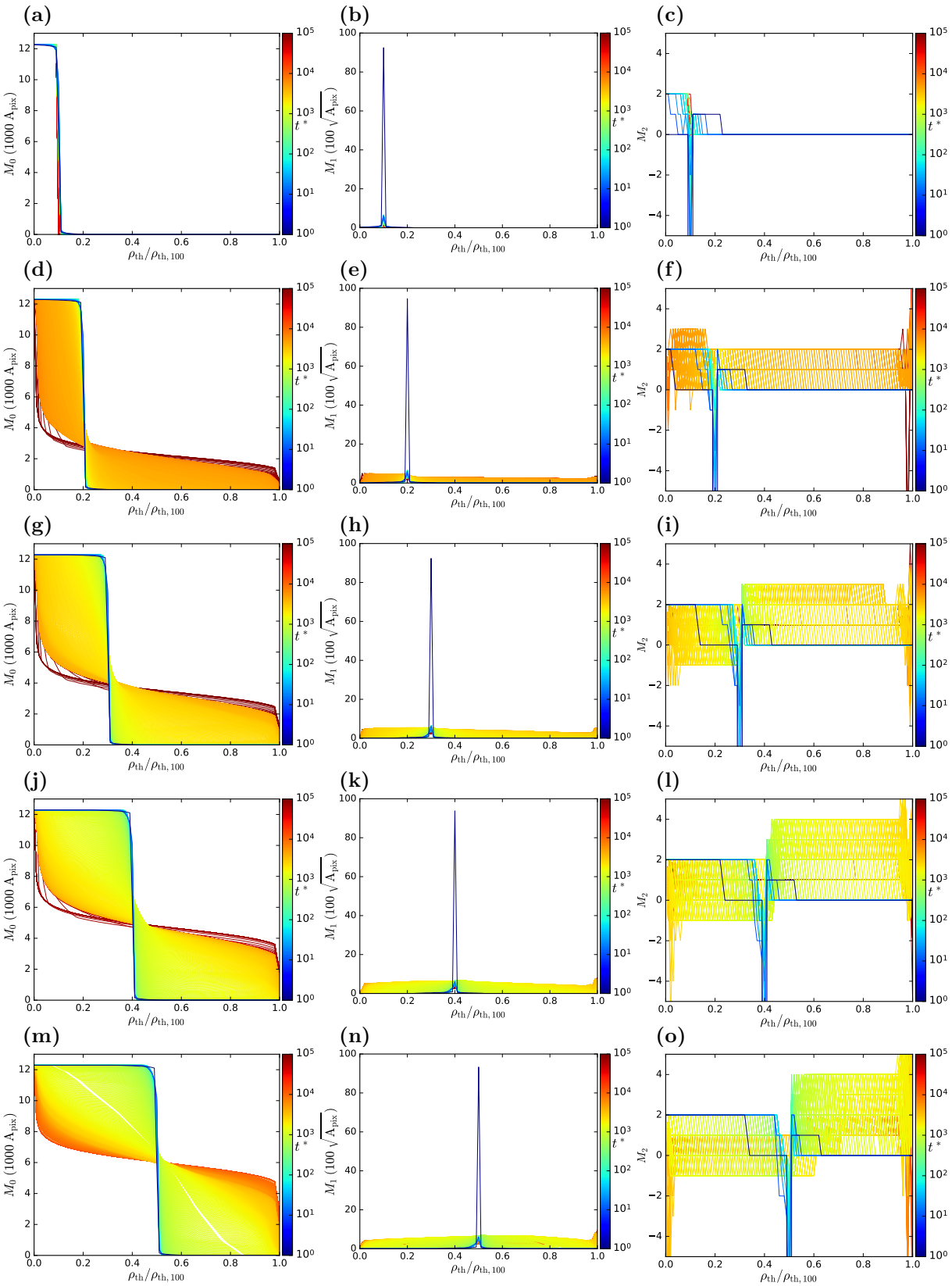

Figure C.2: Minkowski functionals dependence on the relative threshold density $\rho_{\mathrm{th}}/\rho_{\mathrm{th,100}}$ for the small sphere $R = 2.5R_{11}$. Time t^* is color coded. First column: Area functional M_0, second column: perimeter functional M_1, third column: euler functional M_2. First row: $x = 0.1$, second row: $x = 0.2$, third row: $x = 0.3$, fourth row $x = 0.4$, fifth row: $x = 0.5$.

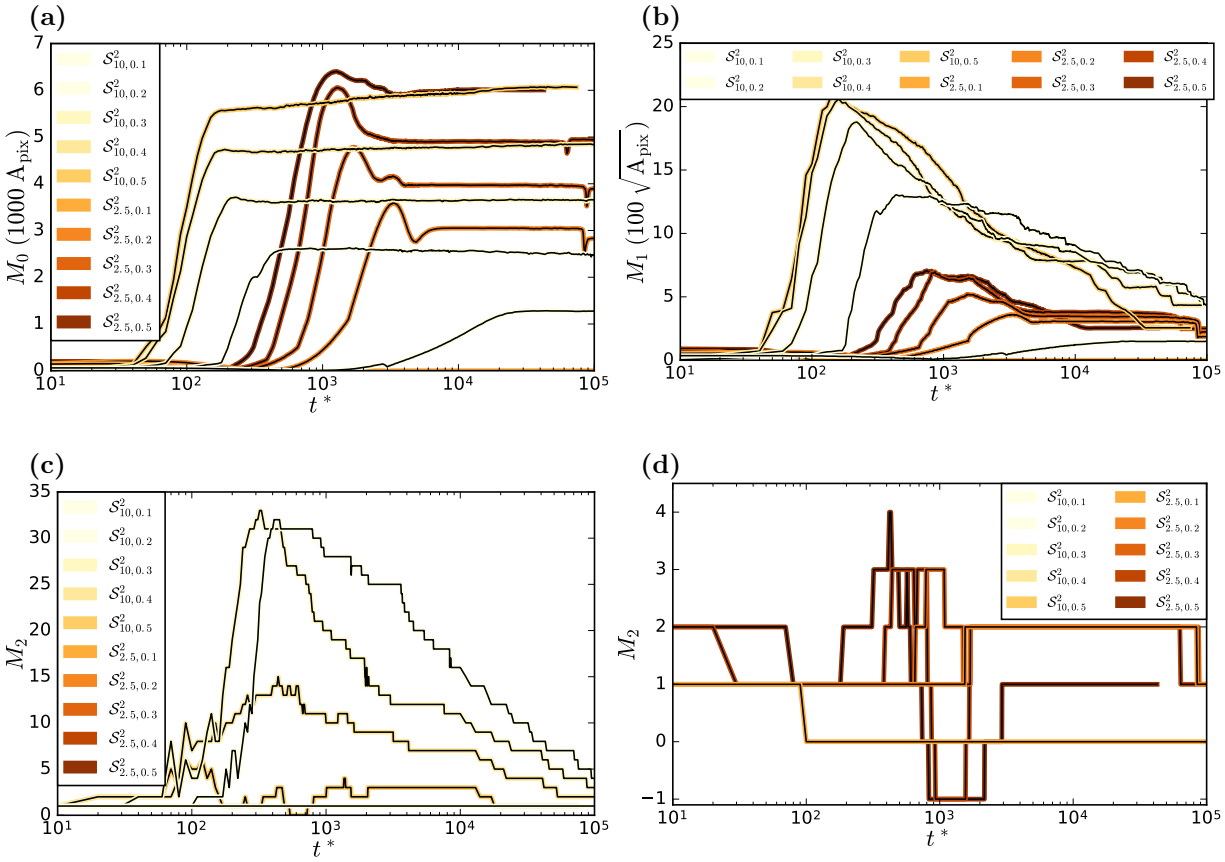

Figure C.3: Minkowski functionals for threshold values $\rho_{\mathrm{th}}/\rho_{\mathrm{th},100} \simeq x$. Exact threshold values are $\rho_{\mathrm{th}}/\rho_{\mathrm{th},100} \in [0.134, 0.212, 0.316, 0.416, 0.5154]$.

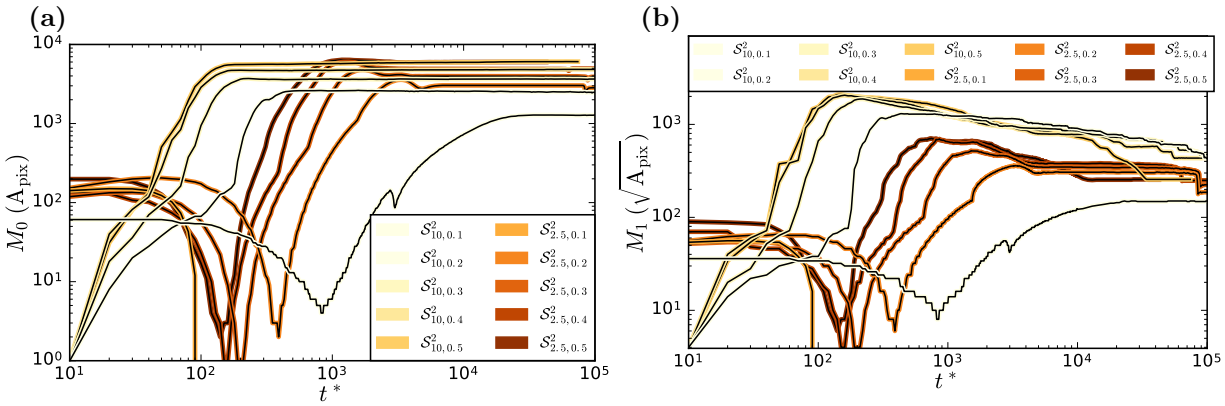

Figure C.4: Minkowski functionals for threshold values $T/T_{100} \simeq x$. Logarithmic plot. Exact threshold values are $\rho_{\mathrm{th}}/\rho_{\mathrm{th},100} \in [0.134, 0.212, 0.316, 0.416, 0.5154]$.

Table C.1: Power-law exponent α during the coalescence domain growth phase. Values are obtained via linear fits in the log-log plots in Fig. 8.4 and Fig. 8.7 for $t^* > t_c^*$.

$10000 \cdot \alpha$ for		$(2l+1)C_l$	L	$1/M_1$	$1/\sqrt{M_2}$
$R = 10\ R_{11}$					
	$x = 0.1$	–	6221 ± 23	–	–
	$x = 0.2$	2240 ± 24	2155 ± 24	2245 ± 13	2178 ± 13
	$x = 0.3$	2304 ± 23	2321 ± 27	1921 ± 12	1651 ± 19
	$x = 0.4$	2676 ± 28	2531 ± 28	2351 ± 14	2069 ± 26
	$x = 0.5$	2190 ± 57	2897 ± 38	3052 ± 21	946 ± 47
$R = 2.5\ R_{11}$					
	$x = 0.1$	–	–	–	–
	$x = 0.2$	–	1320 ± 160	792 ± 29	1200 ± 210
	$x = 0.3$	–	–	1330 ± 30	1000 ± 200
	$x = 0.4$	–	1500 ± 30	1894 ± 32	2230 ± 210
	$x = 0.5$	3254 ± 38	4511 ± 19	3052 ± 21	–

Appendix D

Enclosed publications

D.1 Scale-Free Crystallization of two-dimensional Complex Plasmas: Domain Analysis using Minkowski Tensors [24]

Scale-free crystallization of two-dimensional complex plasmas: Domain analysis using Minkowski tensors,
A. Böbel, C.A. Knapek and C. Räth, *Phys. Rev. E* **97** (2018), 053201

Scale-free crystallization of two-dimensional complex plasmas: Domain analysis using Minkowski tensors

A. Böbel,* C. A. Knapek, and C. Räth

Institut für Materialphysik im Weltraum, Deutsches Zentrum für Luft- und Raumfahrt (DLR), Münchner Strasse 20, 82234 Weßling

(Received 26 February 2018; published 3 May 2018)

Experiments of the recrystallization processes in two-dimensional complex plasmas are analyzed to rigorously test a recently developed scale-free phase transition theory. The "fractal-domain-structure" (FDS) theory is based on the kinetic theory of Frenkel. It assumes the formation of homogeneous domains, separated by defect lines, during crystallization and a fractal relationship between domain area and boundary length. For the defect number fraction and system energy a scale-free power-law relation is predicted. The long-range scaling behavior of the bond-order correlation function shows clearly that the complex plasma phase transitions are not of the Kosterlitz, Thouless, Halperin, Nelson, and Young type. Previous preliminary results obtained by counting the number of dislocations and applying a bond-order metric for structural analysis are reproduced. These findings are supplemented by extending the use of the bond-order metric to measure the defect number fraction and furthermore applying state-of-the-art analysis methods, allowing a systematic testing of the FDS theory with unprecedented scrutiny: A morphological analysis of lattice structure is performed via Minkowski tensor methods. Minkowski tensors form a complete family of additive, motion covariant and continuous morphological measures that are sensitive to nonlinear properties. The FDS theory is rigorously confirmed and predictions of the theory are reproduced extremely well. The predicted scale-free power-law relation between defect fraction number and system energy is verified for one more order of magnitude at high energies compared to the inherently discontinuous bond-order metric. It is found that the fractal relation between crystalline domain area and circumference is independent of the experiment, the particular Minkowski tensor method, and the particular choice of parameters. Thus, the fractal relationship seems to be inherent to two-dimensional phase transitions in complex plasmas. Minkowski tensor analysis turns out to be a powerful tool for investigations of crystallization processes. It is capable of revealing nonlinear local topological properties, however, still provides easily interpretable results founded on a solid mathematical framework.

DOI: 10.1103/PhysRevE.97.053201

I. INTRODUCTION

Complex plasmas are composed of a weakly ionized gas and microparticles that are highly charged due to absorption of the ambient electron and ion streams [1,2]. Complex plasmas constitute a model system that is well suited for studying the kinetics of fluids and crystallization processes at the individual particle level in three or two dimensions. Properties of pair interactions, such as the interaction range and strength, can be flexibly tuned. Also, the dynamics of particles at short timescales is practically undamped due to the low gas density in typical complex plasmas [2].

Because the Mermin-Wagner [3] theorem forbids any long-range order in only two dimensions, the existence of crystallization in two-dimensional phase transitions seemed thermodynamically impossible. However, Kosterlitz and Thouless (KT) proved [4–8] the possibility of a topological phase transition, from solid to liquid, in two-dimensional systems. This KT transition is mediated by lattice defects. Paired dislocations as initially bound defects dissociate into an intermediate hexatic phase that consists mainly of free dislocations, which then dissociate into free disclinations as the liquid state is reached. A disclination is a crystal defect for which rotational symmetry is broken. A dislocation is a type of defect that breaks translational symmetry. The general term defect refers to either or a combination of both types. In the KT transition, the long-range order typical to three-dimensional crystals is replaced by a quasi-long-range order. Thus, the Mermin-Wagner theorem [3] is not violated. Experimental evidence for such a topological phase transition is rare; examples are colloidal systems [9,10], the two-dimensional electron sheet on liquid helium [11], atomic gases [12], and superconducting vortex lattices [13]. However, only recently it was shown for a colloidal suspension system that the conventional Kosterlitz, Thouless, Halperin, Nelson, and Young (KTHNY) theory is not applicable on spherical geometry [14].

Whether a phase transition is of KTHNY type can be reduced to the question as to whether the pair correlation function $g(r)$ or the bond correlation function $g_6(r)$ follows a specific scaling behavior [15,16]. In Ref. [17] it is shown, by both experimental and simulated data, that the recrystallization of two-dimensional complex plasmas is not compatible with the KTHNY theory of phase transition due to different scaling behaviors in $g(r)$ and $g_6(r)$. In this work, a "fractal-domain-structure" (FDS) theory [2] based on the kinetic theory of Frenkel [18] is tested. It assumes the formation of homogeneous domains, separated by defect lines, during crystalliza-

*alexander.boebel@dlr.de

tion. Based on experimental evidence, a fractal relationship between domain area and boundary length is postulated. For the defect number fraction and system energy, a scale-free power-law relation is predicted.

The FDS theory is tested for experiments and a simulation of the crystallization process in two-dimensional complex plasmas. A layer of microparticles is levitated in the plasma sheath region and illuminated by a thin laser sheet. The crystalline particle system is melted by a short electric pulse and the recrystallization is captured by a high-speed camera.

Indications that this complex plasma phase transition data confirm the FDS theory were given in a first study [19]. There, defect numbers were counted as 5/7-dislocations. The hexagonal translational order in the solid state is violated by pairs of particles that have 5, respectively, 7 next neighbors instead of 6. A preliminary analysis of domain structure was done using the Ψ_6 bond-order parameter. However, various shortcomings of the Ψ_6 bond-order parameter have reported recently [20]: The choice of neighborhood definition has an impact on Ψ_6 beyond physical interpretation and its inherent discontinuity leads to a lack of robustness.

In this work, we verify previous results obtained via counting of 5/7-dislocations and the conventional Ψ_6 bond-order parameter and extend the Ψ_6 bond-order analysis to measure the defect number fraction. We proceed in the systematic testing of the FDS theory with unprecedented scrutiny: A morphological analysis of lattice structure is performed via Minkowski tensor methods [20–28]. Minkowski tensors are a tensorial extension of scalar Minkowski functionals. They form a complete family of additive, motion covariant and continuous morphological measures that are sensitive to nonlinear properties. They avoid the ambiguity, robustness, and discontinuity issues of the bond-order parameters and provide highly sensitive morphological measures with a wide range of applications.

As a first step in this work, it is confirmed that the complex plasma phase transitions are in fact not of KTHNY type. This is due to their long-range scaling behavior in the bond-order correlation function $g_6(r)$. Then the hypothesis of a fractal relationship between area and boundary length of crystalline domains is tested. Finally, the predicted scale-free relationship of defect fraction and system energy of the FDS theory is verified.

This paper is structured as follows: In Sec. II the theoretical foundations of the FDS theory are explained. Also theoretical predictions of the KTHNY theory on the bond-order correlation function are briefly reviewed. Section III describes the experiments and simulations that were performed and used to test the FDS theory. In Sec. IV, methods are presented: The traditional methods as the bond-order metric and the bond-order correlation function are described. Then the state of the art morphological analysis methods are introduced: Voronoi tessellations, Minkowski functionals, and Minkowski tensors. Based on this introduction an isotropy measure and a symmetry metric is derived. Also the method to cluster particles into homogeneous, ordered domains is explained, as is the method to calculate the particle kinetic energy. Section V presents the results obtained by both traditional analysis and Minkowski tensor analysis of the experimental and simulation data. The long-range decay scaling of the bond-order correlation function, and the fractal relationships for energy and defect fraction and for domain area and boundary length are shown. Finally, in Sec. VI results are discussed and conclusions are drawn.

II. THEORY

A. Fractal domain structure (FDS) theory

Experimental work, with complex plasmas as model systems [19], provided evidence that fundamental properties of a two-dimensional phase transition are not consistent with the usually assumed KT process. Rather, the findings support the recently developed FDS theory based on the kinetic theory of Frenkel [18]. The FDS theory was fist introduced in Refs. [2,17] and is revisited here. The model describes a scale-free phase transition of a two-dimensional N-particle system when the temperature is varied.

At a given energy $E = k_B T$, the N-particle system is divided into $z = N/\langle N_d \rangle$ homogeneous domains. Each domain contains $\langle N_d \rangle$ particles on average. The domain boundaries are defined by lattice defects (e.g., pairs of pentagons and septagons). The structural order in the individual domains is assumed to be uncorrelated with other domains in the system.

For a mean particle separation Δ, the mean domain radius $\langle r \rangle$ is determined by the domain area, consisting of all unit cell areas in the domain, as $\pi \langle r \rangle^2 = \pi(\Delta/2)^2(N/z)$ as

$$\langle r \rangle = 1/2(N/z)^{1/2}\Delta. \tag{1}$$

Neglecting the interaction between domains, the interface line energy of the boundaries is $\langle E \rangle = 2\pi \langle r \rangle z\sigma$, with the line tension σ. Substituting $\langle r \rangle$ gives

$$\langle E \rangle = \pi \Delta (Nz)^{1/2}\sigma. \tag{2}$$

Due to the arrangement possibilities of the domain structure, the system entropy increases with the number of domains z. The number of possible realizations P of the particles ordering characterizes the measure of disorder. It can be calculated by counting the number of possible realizations to distribute N distinguishable particles on z domains, each containing $\langle N_d \rangle$ particles. At first one can choose $\langle N_d \rangle$ distinguishable particles from an ensemble of N particles. Then, $\langle N_d \rangle$ particles are chosen from the remaining $N - \langle N_d \rangle$ particles with the number of possibilities p,

$$p = \binom{N - \langle N_d \rangle}{\langle N_d \rangle}. \tag{3}$$

Repeating this until all domains are completely occupied gives P as the product of all the independent numbers of possibilities:

$$P = \sum_{i=0}^{z-1} \binom{N - i\langle N_d \rangle}{\langle N_d \rangle} = N!/[(N/z)!]^z. \tag{4}$$

Using Stirlings formula for sufficiently large N and N/z yields $P \simeq z^N$. The entropy is $S = \ln(P)$ and the mean free Helmholtz energy is accordingly

$$\langle F \rangle = \pi \Delta (Nz)^{1/2}\sigma - NT \ln(z). \tag{5}$$

Assuming thermodynamic equilibrium at all times, it follows from $\partial\langle F\rangle/\partial z = 0$ that

$$z = (2T/\pi\Delta\sigma)^2 N. \tag{6}$$

The scaling nature of the domain structure is now introduced as a hypothesis:

$$\langle N_d\rangle \Delta^2 B = [\Delta\langle N_s\rangle]^{1+\alpha}, \tag{7}$$

with B and α constants depending on the shape of the domains. With the above definition $\alpha = 1$ if the domain is circular, for long narrow domains $\alpha \to 0$, suggesting $0 < \alpha < 1$ for fractal domains. Substituting this scaling in Eq. (6) yields the scaling for the total number of particles in all domain boundaries $N_T \equiv z\langle N_s\rangle$:

$$N_T/N \propto T^{2\alpha/(1+\alpha)} \propto E^{2\alpha/(1+\alpha)}. \tag{8}$$

B. Consequences of KTHNY on the bond correlation function $g_6(r)$

A well accepted theory for phase transitions of two-dimensional systems is the KTHNY theory [4–8], which describes the melting of two-dimensional systems with a continuous, second-order, defect-mediated phase transition.

The KTHNY theory makes predictions on the long-range decay behavior of the bond correlation function for orientational order $g_6(r)$. It can be defined as

$$g_6(r) = \sum_{r-\delta r \leqslant r < r+\delta r} \langle \Psi^*(\mathbf{r})\Psi(0)\rangle, \tag{9}$$

with $\Psi(r) = \exp[i\theta(\mathbf{r})]$, where $\theta(\mathbf{r})$ denotes the angle between a nearest-neighbor bond at position $\mathbf{r}$ and an arbitrary axis. It measures the correlation between the orientation of nearest-neighbor bonds separated by the distance r.

The KTHNY theory predicts a two-stage melting scenario with an intermediate phase between the solid and liquid state: the hexatic phase. In the solid phase $T < T_{c1}$ all dislocations are bound in pairs. Orientational order is preserved in the long-range limit: The bond correlation function $g_6(r)$ approaches a finite constant for large distances [6]. At T_{c1} the dislocation pairs start to dissociate and for $T > T_{c1}$ the orientational order persists with a slow power-law decay $g_6(r) \propto r^{\eta_6(T)}$ [6]. This transition if well known as the Kosterlitz-Thouless transition. A second transition was discovered by Halperin and Nelson at the temperature $T_{c2} > T_{c1}$: Here the dislocations break up and form free disclinations. The bond-order correlation function decays exponentially $g_6(r) \propto \exp[-r/\xi_6(T)]$ [6,7]. Table I summarizes these predictions.

TABLE I. Consequences of the KTHNY theory on the long-range scaling behavior of the bond correlation function $g_6(r)$ in different phase regimes.

Phase		$g_6(r)$ scaling
Liquid	$(T > T_{c2})$	$g_6(r) \propto \exp[-r/\xi_6(T)]$
Hexatic	$(T_{c1} < T < T_{c2})$	$g_6(r) \propto r^{-\eta_6(T)}$; $\eta_6 < 0.25$
Solid	$(T < T_{c1})$	$g_6(r) = \text{const.}$, const. $\neq 0$

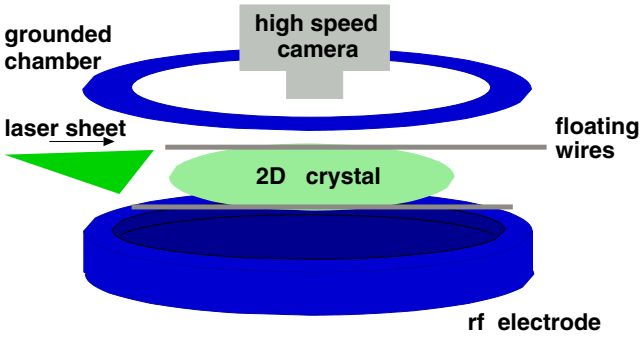

FIG. 1. Sketch of the experimental setup used for the presented crystallization experiments [17]. A two-dimensional crystal is levitated in the plasma sheath region above the lower rf electrode. A glass window in the upper chamber flange provides optical access for a high-speed camera from the top viewpoint. Particles are illuminated by a vertically thin, horizontally spread laser sheet. Two wires are mounted inside the chamber for electric particle manipulation. These are normally floating, but can be fed with a short electric pulse to melt the particle system.

III. EXPERIMENTS AND SIMULATION

To study the phase transition in a genuine two-dimensional system, experiments [19] were performed with two-dimensional complex plasmas: many-particle systems consisting of electrons, ions, neutral gas atoms, and charged micrometer-sized particles. A sketch of the experimental setup is provided in Fig. 1. An example image of an experimental data set is shown in Fig. 2. Movies for all data sets are provided in the Supplemental Material [29].

Melamine-formaldehyde particles with a diameter of 9.19 μm and a mass of 6.14×10^{-13} kg were injected into

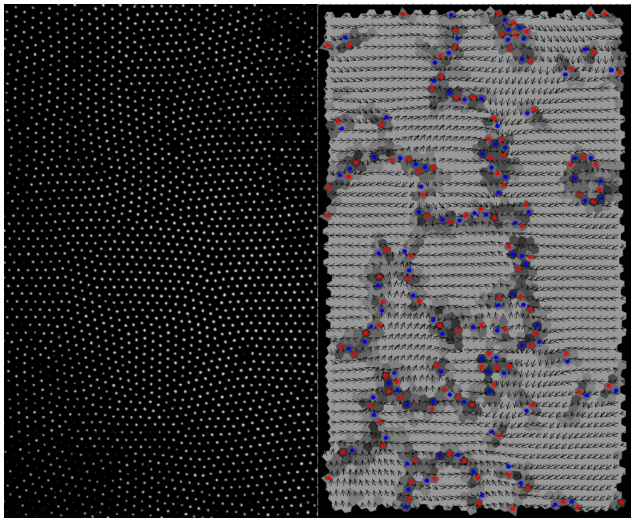

FIG. 2. Left: Image of a two-dimensional plasma crystal of the experimental data set XII for time $t = 6.0$ s. The field of view is 18×25 mm. Right: Gray scale plot of the Ψ_6 bond-order parameter. Dark Voronoi cells have low Ψ_6 values. The direction of the argument of Ψ_6 is indicated with arrows. Dislocations with 5 (respectively, 7) neighbors are marked with red (respectively, blue) dots.

an argon radio-frequency (rf) discharge ignited between a horizontal, capacitively coupled electrode mounted on the bottom of a vacuum chamber, and the grounded chamber walls. Due to the balance of electron- and ion-streams onto their surface, the particles acquired a negative charge. The electric fields in the plasma sheath region above the electrode then levitated particles against gravity (usually several millimeters above the electrode surface). Additionally, an elevated rim on the electrode provided a radial confinement by shaping the electric potential inside the chamber. The injected particles then formed a crystalline single layer with a hexagonal crystal structure, which could temporarily be destroyed by applying a negative electric pulse (duration: 0.2 s, amplitude: −250 V) to two parallel wires (58.7 mm apart from each other) mounted at approximately the levitation height of the monolayer. The particle system then was left to recrystallize under constant "environmental" conditions, i.e., pressure and rf power.

To obtain particle trajectories, the particle layer was illuminated by a 532 -nm Nd:YAG laser, adjusted to provide a vertically thin, horizontally spread sheet of light. The light reflected by the particles was then observed by a high-speed camera with a frame rate of 250 frames per second (fps) and a spatial resolution of 0.03 mm/px from the top viewpoint through a glass window. To reduce the effect of pixel noise during the image analysis, each two consecutive images were later averaged, yielding an effective frame rate of 125 fps [17]. The number of particles in the field of view of the camera was approximately 2000, which amounts to approximately 10–15% of the total number of particles in the monolayer.

Experiments were performed at 11 different plasma conditions: the neutral gas pressure was varied between 1.15 and 2.3 Pa and the peak-to-peak rf voltages U_{PP} at the electrode were chosen in the range [−134, −214] V.

Additionally, another data set from Ref. [30] was included in the analysis. Here, the gas pressure was 1.94 Pa, U_{PP} was −172 V, the recording frame rate was 500 fps (effective frame rate after averaging each three consecutive images: 166.667 fps), and the spatial resolution was 0.034 mm/px.

Details of the experimental setup are given in Refs. [17,30].

To complement the experimental results, the outcome of a molecular dynamics simulation of the crystallization of a monolayer of 3000 particles in a parabolic confinement is presented in addition. The simulation parameters were chosen to meet the experimental conditions: the damping rate was 2 Hz, the time step 0.01 s, particle mass and charge were 6.1×10^{-13} kg and −12 000 e, respectively. The particles were initially heated to 230 eV and then allowed to cool until they reached a crystalline state. The parabolic potential used in the simulation gives rise to deviations from the experiments. The confinement in the experiments is nonparabolic due to the presence of the electrodes used to induce the electric shock causing the melting. The nonparabolic confinement in the experiments leads to a constant particle density, whereas the parabolic confinement in the simulation gives rise to a radially decreasing particle density. Also, the expansion before melting and relaxation during crystallization of the system is affected by the difference in the confinement potential. Details of the simulation procedure are given in Ref. [31].

Here, the results of these earlier experiments and simulation are analyzed employing Minkowski tensor methods and compared with previous results. The particular parameters of each experiment are given in Table II.

TABLE II. Parameters of the experiments and the simulation. Neutral gas pressure p, Epstein damping coefficient ν, peak-to-peak rf voltage U_{PP} at the driven electrode, and the mean particle separation Δ obtained from the pair correlation functions. The Epstein damping coefficient ν, a measure for the damping rate of the particle motion due to scattering on neutral gas atoms, was calculated from the discharge parameters given in Ref. [32], using the reflection index $\delta = 1.26$ as measured in Ref. [33].

	p(Pa)	ν(Hz)	U_{PP}(V)	Δ(mm)
I	1.93	2.27	–138	0.60
II	1.36	1.60	–144	0.61
III	2.29	2.69	–134	0.61
IV	1.15	1.35	–184	0.60
V	1.36	1.60	–180	0.60
VI	1.68	1.97	–176	0.60
VII	2.12	2.49	–172	0.60
VIII	2.30	2.70	–172	0.60
IX	1.36	1.60	–214	0.57
X	1.93	2.27	–206	0.51
XI	2.30	2.70	–200	0.53
XII	1.94	2.28	–172	0.59
Simulation (S)	...	2	...	0.8

IV. METHODS

The bond-order parameters Ψ_6 were introduced in 1983 [34] and quickly became a standard tool to quantify crystalline structures. However, recent work [20] has shown that the calculation of Ψ_6 has some conceptual drawbacks. The choice of neighborhood definition causes an ambiguity of Ψ_6 beyond physical interpretation and its inherent discontinuity leads to a lack of robustness.

However, the Minkowski functionals are a continuous and robust tool for morphological data analysis, known since the early 20th century [35]. Only recently the hierarchy of Minkowski valuation was extended to tensor valued quantities called Minkowski tensors [36]. Minkowski functionals and tensors are sensitive to any n-point correlation function and thus can give new insights to processes beyond the capability of conventional (linear) methods, e.g., Ψ_6, $g(r)$ or $g_6(r)$. A commonly used method for quantifying the local structure of points (or discs) is by construction of a nearest-neighbor network on which quantitative structure metrics are computed (e.g., Ψ_6). The ambiguity of the neighborhood selection can be circumvented by using the method of the bijective Voronoi tessellation, based on the idea of a Wigner-Seitz cell for each particle.

In the following, the Ψ_6 bond-order metric, the bond orientational correlation function $g_6(r)$, Voronoi tessellation, Minkowski functionals and tensors, as well as a clustering algorithm via DBSCAN and the energy calculation via velocity distribution fits, are introduced as methods used throughout this paper.

A. Bond order parameter Ψ_6

In a fist step of a thorough investigation of the domain structure, irregular lattice sites are identified as defects via the Ψ_6 bond-order parameter [34]. It is defined as

$$\Psi_6 = 1/n_k \times \sum_{m=1}^{n_k} \exp(6i\Theta_{km}) \tag{10}$$

for each lattice site k. Here, n_k is the number of nearest neighbors of particle k, Θ_{km} is the angle of the bond between particles k and m to an arbitrary chosen axis (we chose the x axis), and i is the imaginary unit. For hexagonal ordered lattice sites, the modulus $|\Psi_6|$ is close to 1, whereas it tends to zero for distorted ones and therefore also for defects. To distinguish ordered from disordered sections, a cut off value of $\Psi_{6,\text{thresh}} > \Psi_{6,\text{defects}}$ (corresponding to Voronoi cells close to $|\Psi_6| = 1$ interpreted as in the crystalline state) is chosen. The specific value that is chosen for $\Psi_{6,\text{thresh}}$ is indicated in each case in the result Sec. V. The number fraction of these particles identified as in the crystalline state will be referred to as Ψ_6 measure in the following. Typical histograms for Ψ_6 for the analyzed recrystallization processes are shown in Fig. 3 for increasing time steps.

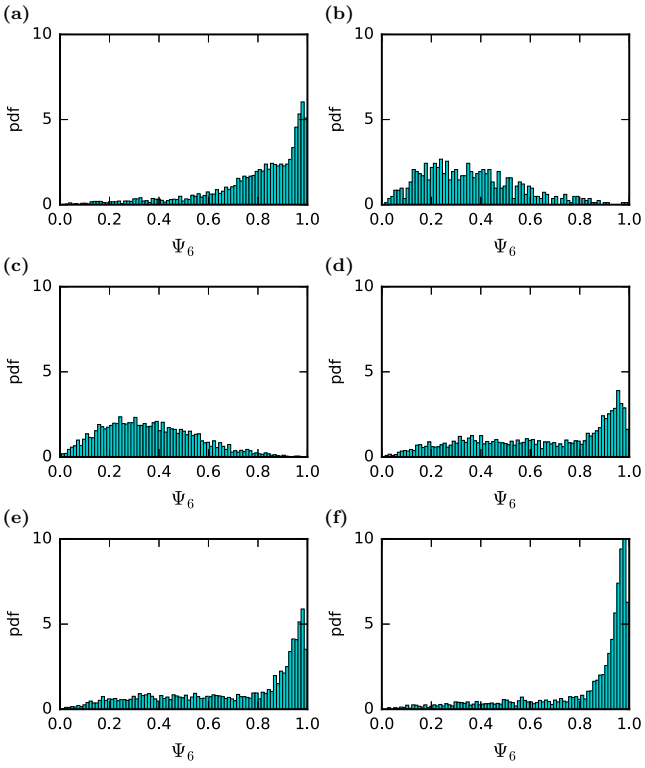

FIG. 3. Typical histograms for the Ψ_6 measure as time t evolves representatively shown for experiment X (see Table II). (a) $t = 3.00$ s: Before melting a large peak for Ψ_6 values close to $\Psi_6 = 1$ is a signature of the crystalline state. (b, c) $t = 3.30$ s, $t = 4.50$ s: The distribution broadens after melting. (d, e) $t = 6.00$ s, $t = 7.20$ s: During recrystallization the distribution shifts to larger Ψ_6 values. (f) $t = 12.00$ s: For late times the large peak for values close to $\Psi_6 = 1$ is recovered in the recrystallized state.

B. Bond correlation function $g_6(r)$

The bond correlation function $g_6(r)$ for the orientational order II B is calculated via

$$g_6(r) = \left| \frac{1}{N_B} \sum_{l=1}^{N_B} \frac{1}{n(l)} \sum_{k=1}^{n(l)} \exp\{6i[\theta(r_k) - \theta(r_l)]\} \right|. \tag{11}$$

Here, N_B is the total number of bonds in the crystal, $n(l)$ is the number of bonds at distance r from bond l, θ_i the angle of bond i at r_i to an arbitrary axis. For a perfect hexagon, $g_6(r) \equiv 1$. Since we are only interested in the long-range decay and not the exact shape of g_6 with its peaks in the close range regime, we choose large bins, i.e., large values of $n(l)$.

For a solid crystalline state $g_6(r)$ should be constant and close to 1 [6]. However, for the plasma crystal data sets analyzed here, we find $g_6(r)$ to be a linearly decaying function. This is because the crystal is made up of homogeneous domains, separated by defect lines, whose structural order is uncorrelated with neighboring domains. Since power law (respectively, exponential decay) is predicted in hexatic (respectively, liquid states) [6,7] for large r, following models are fitted to the experimental and simulation data sets: (a) linear decay $g_6(r) = A_1 + c_6 r$, (b) exponential decay $g_6(r) = A_2 \exp(-r/\xi_6)$, and (c) power-law decay $g_6(r) = A_3 r^{-\eta_6}$. To determine the best model the goodness of best fits is compared using the χ-squared χ^2 statistic. Lower values indicate a higher goodness of fit. This method was already applied to test for a hexatic phase [17,37].

C. Voronoi tessellation

An approach for quantifying local structure is provided by the analysis of the Voronoi diagram. The Voronoi diagram is the partition of space into the same number of convex cells as there are discs in the packing. The Voronoi cell of each disk is the region of space closer to that given disk than to any other disk. For the special case of three- or two-dimensional crystal lattices the Voronoi cell is called Wigner-Seitz cell. In the field of granular matter, Voronoi diagrams have been used to determine distributions of local packing fractions [38–40], spatial correlations [41], and correlations with particle motion [42].

Recently, studies provided insight into the local structure of sphere packings and sphere ensembles by analyzing the shape of Voronoi cells, in particular, their degree of anisotropy or elongation [23,43–45].

Here, the structure of the Voronoi tessellation, obtained from particle positions, is analyzed using Minkowski functional and tensor methods. The boundary particles were discarded from the analysis since they have no neighboring particles needed to define their Voronoi cells.

D. Minkowski functionals

For a body K with a smooth boundary contour ∂K embedded in D-dimensional euclidean space the $D+1$ Minkowski functionals are, up to constant factors, defined

as

$$W_0(K) = \int_K d^D r$$
$$W_\nu(K) = \int_{\partial K} G_\nu(r)\, d^{D-1} r \quad , \quad 1 \leqslant \nu \leqslant D \qquad (12)$$

$G_\nu(r)$ are the elementary symmetric polynomials of the local principal curvatures as defined in differential geometry.

In two-dimensional euclidean space the Minkowski functionals, up to constant factors, are $W_0(K)$ (area), $W_1(K)$ (circumference) and $W_2(K)$ (euler characteristic):

$$W_0(K) = \int_K d^2 r$$
$$W_1(K) = \int_{\partial K} dr$$
$$W_2(K) = \int_{\partial K} \kappa(r)\, dr \qquad (13)$$

Here, $\kappa(r)$ is the local curvature.

Minkowski functionals are motion invariant, additive and conditionally continuous. They form a complete family of morphological measures. Or vice versa: Any motion invariant, (conditionally) continuous and additive functional is a superposition of the (countably many) Minkowski functionals. They are nonlinear measures sensitive to higher order correlations. Applications are e.g. curvature energy of membranes [46], order parameter in Turing patterns [47], density functional theory for fluids (as hard balls or ellipsoids) [48,49], testing point distributions (find clusters, filaments, underlying point-process) or searching for non-Gaussian signatures in the CMB [50–54].

E. Minkowski tensors

To also account for directional properties it is natural to extend the scalar valued Minkowski functionals to tensor-valued quantities called Minkowski tensors. Applications of Minkowski tensors range from the analysis of cellular, granular, and porous structures to the classification of crystal types [22–28]. They are defined as [21]

$$W_0^{a,0}(K) := \int_K d^D r \;\; \mathbf{r}^{\odot a},$$
$$W_\nu^{a,b}(K) := 1/D \int_{\partial K} d^{D-1} r \;\; G_\nu(r) \;\; \mathbf{r}^{\odot a} \odot \mathbf{n}^{\odot b}. \qquad (14)$$

Here, $\odot$ denotes the symmetric tensor product $x \odot y = 1/2\,(x \otimes y + y \otimes x)$. Again $G_\nu(r)$ are the elementary symmetric polynomials of the local principal curvatures as defined in differential geometry. a counts the number of position vectors $\mathbf{r}$, b counts the number of normal vectors $\mathbf{n}$ in the tensor product. Thus, the rank of each tensor is the tuple (a,b).

Similar to Minkowski functionals the attractiveness of Minkowski tensors is due to their manifold applications. Further, they are founded on a solid mathematical framework: A strong completeness theorem by Alesker [36] states that all morphological information that is relevant for additive properties of a body K is represented by the Minkowski tensors. Any motion covariant, conditionally continuous and additive tensor valued functional is a superposition of the (countably many) Minkowski tensors.

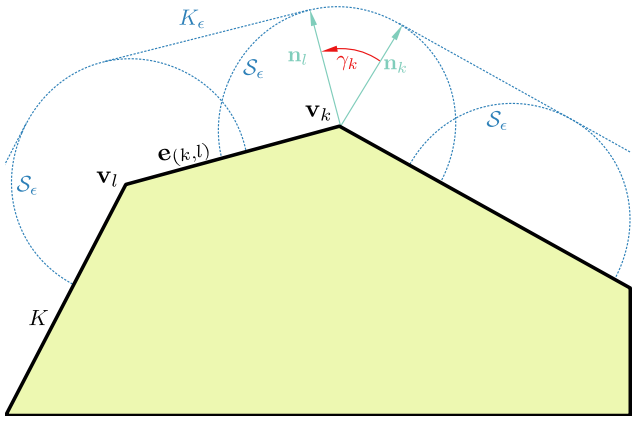

FIG. 4. Illustration for the explicit calculation of Minkowski tensors of a body K via K_ϵ.

The Minkowski tensors are defined as curvature integrals over smooth boundary surfaces. To calculate them for polygonal bodies P we consider the parallel body construction $P_\epsilon = P \uplus S_\epsilon$ [55]. S_ϵ is a disk of radius $\epsilon > 0$ and $\uplus$ is the Minkowski sum (defined as $K_1 \uplus K_2 = \{p_1 + p_2 \mid p_1 \in K_1, p_2 \in K_2\}$). Thus, P_ϵ is the union of all disks S_ϵ with origins at all points in P, illustrated in Fig. 4. Performing the limit $\epsilon \to 0$ then yields the tensor $W_\nu^{a,b}(P) = \lim_{\epsilon\to 0} W_\nu^{a,b}(P_\epsilon)$. Consider the polygonal representation of P by its vertices $\mathbf{v}_k$. Then the edges between vertices $\mathbf{v}_k$ and $\mathbf{v}_l$ are $\mathbf{e}_{(k,l)} = \mathbf{v}_l - \mathbf{v}_k$ with normal vectors $\mathbf{n}_{(k,l)} = R\,\mathbf{e}_{(k,l)}/|\mathbf{e}_{(k,l)}|$. $R = \left(\begin{smallmatrix} 0 & -1 \\ -1 & 0 \end{smallmatrix}\right)$ is the $\pi/2$ rotation matrix. γ_k is the angle between $\mathbf{n}_{(k-1,k)}$ and $\mathbf{n}_{(k,k+1)}$. Using these definitions we can obtain the explicit formula. Here we present formulas for the second rank in position vectors circumference [Eq. (15)] and the second rank in normal vectors euler tensors [Eq. (16)] as examples. E is the unit matrix:

$$W_1^{2,0}(P) = \lim_{\epsilon\to 0} \frac{1}{2} \int_{\partial P_\epsilon} dr \;\; \mathbf{r} \odot \mathbf{r} = \frac{1}{6} \sum_{(k,l)} |\mathbf{e}_{(k,l)}| \times \begin{pmatrix} v_{kx}^2 + v_{kx} v_{lx} + v_{lx}^2 & v_{kx} v_{ky} + v_{kx} v_{ly} + v_{lx} v_{ly} \\ v_{ky} v_{kx} + v_{ky} v_{lx} + v_{ly} v_{lx} & v_{ky}^2 + v_{ky} v_{ly} + v_{ly}^2 \end{pmatrix}, \qquad (15)$$

$$W_2^{0,2}(P) = \lim_{\epsilon\to 0} \frac{1}{2} \int_{\partial P_\epsilon} dr \;\; \kappa(r)\, \mathbf{n} \odot \mathbf{n} = 4\, W_2\, E. \qquad (16)$$

A list of expressions for two-dimensional tensors up to rank two is available in Ref. [55].

F. MT2 isotropy index

For a body K and each second-rank Minkowski tensor $W_\nu^{a,b}(K)$ an isotropy index β can be defined as the ratio between the smallest and largest eigenvalue $\lambda_{\min}$ and $\lambda_{\max}$ of

the $D \times D$ matrix representing each Minkowski tensor [21]:

$$\beta_\nu^{a,b}(K) := \frac{\lambda_{\min}\left[W_\nu^{a,b}(K)\right]}{\lambda_{\max}\left[W_\nu^{a,b}(K)\right]}. \tag{17}$$

The dimensionless isotropy index is a pure shape measure. It is invariant under isotropic scaling of K. For example, in two dimensions the isotropy index $\beta = 1$ is obtained for a circle or a square. For a rectangle one obtains $\beta =$ shorter/longer edge. Thus, this isotropy index is an isotropy measure only in the sense of elongation. β provides equivalent information as the improved, area weighted bond-order metric proposed in Ref. [20].

The rank-two Minkowski tensor analysis carried out in this study is done by calculating the isotropy index β Eq. (17) locally for every Voronoi cell and for every time step in the experimental and simulation data using the circumference Minkowski tensor $W_1^{2,0}$, since it is most sensitive to changes of elongation of Voronoi cells. To distinguish ordered from disordered Voronoi cells a cutoff value of $\beta_{\text{thresh}} > \beta_{\text{defects}}$ (corresponding to isotropic Voronoi cells interpreted as in the crystalline state) is chosen. The specific value that is chosen for β_{thresh} is indicated in each case in the result Sec. V. The number fraction of these particles identified as in the crystalline state will hereinafter be referred to as MT2 measure. Typical histograms for β for the analyzed recrystallization processes are shown in Fig. 5 as time evolves.

G. MT4 symmetry metric

To distinguish between structures of high symmetry, i.e., differentiate between crystalline structures (hcp, fcc, etc.), higher ranked tensors have to be applied. For rank four and higher, isotropic symmetry is distinct from cubic symmetry. (This is evidenced by the appearance of a second independent shear modulus when transitioning from isotropic to cubic symmetry in the theory of linear elasticity, which is formulated using a rank-four tensor [56].) This method has been used in hard sphere systems to characterize random close packings [23].

For brevity, only the simplest rank-four Minkowski tensor is considered:

$$W_1^{0,4}(K) = \frac{1}{2}\int_{\partial K} dr\ \mathbf{n}(\mathbf{r}) \otimes \mathbf{n}(\mathbf{r}) \otimes \mathbf{n}(\mathbf{r}) \otimes \mathbf{n}(\mathbf{r}). \tag{18}$$

In the polygonal representation its components, labeled $\mu,\nu,\tau,\sigma \in (x,y)$ are

$$\left[W_1^{0,4}(P)\right]^{\mu\nu\tau\sigma} = \frac{1}{2}\sum_{(k,l)} |\mathbf{e}_{(k,l)}| n^\mu_{(k,l)} n^\nu_{(k,l)} n^\tau_{(k,l)} n^\sigma_{(k,l)}. \tag{19}$$

Since it is translation invariant and symmetric (i.e., it holds for the components $[W_1^{0,4}]^{\mu\nu\tau\sigma} = [W_1^{0,4}]^{(\mu\nu\tau\sigma)}$), it has, in two dimensions, only 5 independent elements instead of 16. The round brackets denote cyclic permutation.

A morphological metric suitable for characterizing systems of spherical particles should be rotationally invariant since the physics does not a priori designate a preferred direction. Thus, the tensor W_1^{04} should not be directly used. Instead, rotational invariants are constructed [57]. This is done by borrowing ideas from the theory of the elastic stiffness tensor.

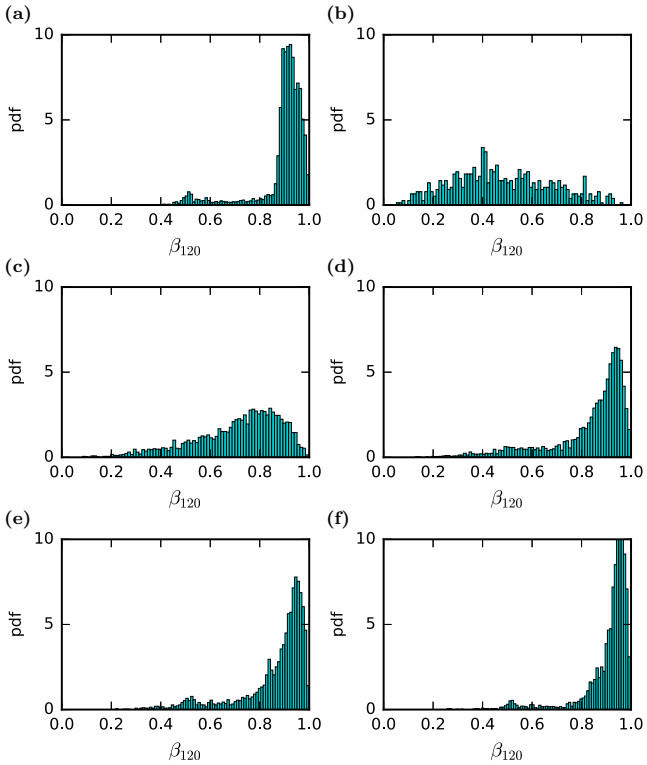

FIG. 5. Typical histograms for the MT2 measure as time t evolves representatively shown for experiment X (see Table II). (a) $t = 3.00$ s: Before melting a large peak for β values close to $\beta = 1$ is a signature of the crystalline state. (b) $t = 3.30$ s The distribution broadens after melting. (c–e) $t = 4.50$ s, $t = 6.00$ s, $t = 7.20$ s: During recrystallization the distribution shifts to larger β values. (f) $t = 12.00$ s: For late times the large peak for β values close to $\beta = 1$ is recovered in the recrystallized state.

The tensor $W_1^{0,4}(K)$ is rewritten in the Mehrabadi supermatrix notation [58] as a 3×3 matrix:

$$M = \begin{bmatrix} S_{xxxx} & S_{xxyy} & S_{xxzz} \\ S_{yyxx} & S_{yyyy} & \sqrt{2}\,S_{yyxy} \\ \sqrt{2}\,S_{xyxx} & \sqrt{2}\,S_{xyyy} & 2S_{xyxy} \end{bmatrix}, \tag{20}$$

where $S = W_1^{0,4}(K)/W_1(K)$.

Then, the three-tuple formed by the eigenvalues ζ_i of M (in descending order) may be considered a symmetry fingerprint of the polyhedron K. It is invariant under rotation, scaling, and translation of the polyhedron K. Using the signature eigenvalue tuple ζ_i of M, it is possible to define a distance measure on the space of bodies induced by the Euclidean distance:

$$\Delta(K_1,K_2) := \left\{\sum_{i=1}^{6} [\zeta_i(K_1) - \zeta_i(K_2)]^2\right\}^{1/2}. \tag{21}$$

$\Delta(K_1,K_2)$ is a pseudometric. It is positive definite, symmetric, the triangle inequality holds, however, the coincidence axiom $\Delta(K_1,K_2) = 0 \Leftarrow K_1 = K_2$ is only an implication and not an equivalence. For example, $\Delta(\text{sphere},\text{dodecahedron}) = 0$. To

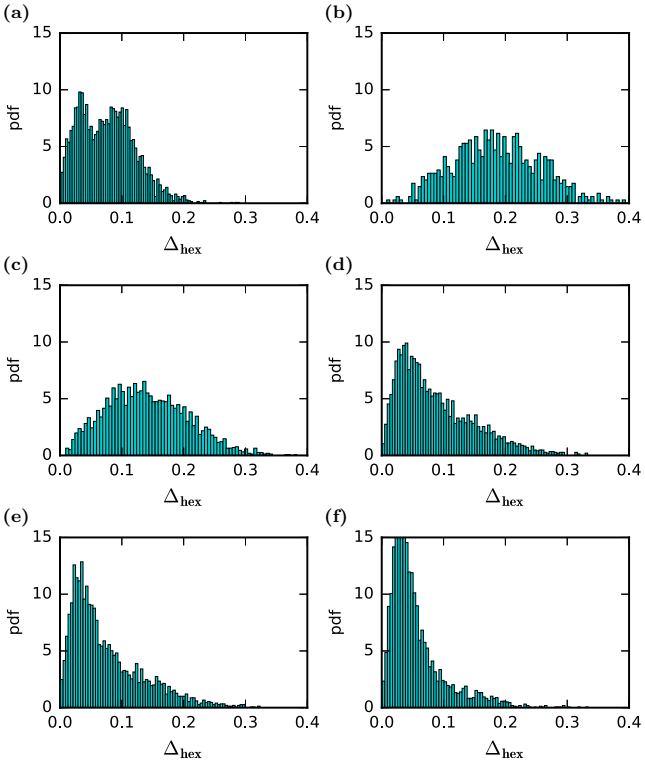

FIG. 6. Typical histograms for the MT4 measure as time t evolves representatively shown for experiment X (see Table II). (a) $t =$ 3.00 s: Before melting a large peak for small Δ_{hex} values is a signature of the crystalline state. (b) $t = 3.30$ s: The distribution broadens after melting. (c–e) $t = 4.50$ s, $t = 6.00$ s, $t = 7.20$ s: During recrystallization the distribution shifts to smaller Δ_{hex} values. (f) $t = 12.00$ s: For late times the large peak for small Δ_{hex} values is recovered in the recrystallized state.

distinguish dodecahedra from spheres one needs to employ even higher rank tensors.

The MT4 analysis carried out in this study is done in analogy to the MT2 analysis. The symmetry metric $\Delta_{hex} = \Delta(K_{voronoi\,cell}, K_{hex})$ Eq. (21) is calculated locally for every Voronoi cell $K_{voronoi\,cell}$ and for every time step in the simulation. K_{hex} denotes the ideal hexagonal unit cell. To distinguish ordered from disordered sections a cut off value of $\Delta_{thresh} < \Delta_{defects}$ (corresponding to Voronoi cells close to hexagonal symmetry interpreted as in the crystalline state) is chosen. The specific value that is chosen for Δ_{thresh} is indicated in each case in the result Sec. V. The number fraction of these particles identified as in the crystalline state will be referred to as MT4 measure in the following. Typical histograms for Δ_{hex} for the analyzed recrystallization processes are shown in Fig. 6 as time evolves.

H. Clustering

The area of ordered domains A_i is proportional to the number of particles in the domain N_d, weighted with the square of the particle separation Δ^2. The boundary length l_i is proportional to the number of particles N_s that the boundary line consists of, weighted with the particle separation Δ. It follows that the hypothesis Eq. (7) can be reduced to

$$\langle A_i \rangle \propto \langle l_i \rangle^{1+\alpha}. \tag{22}$$

To measure the area A_i and boundary length l_i of the ordered domains, the clustering algorithm density-based spatial clustering of applications with noise (DBSCAN) [59] was used. After sorting out the defect particles as identified by the Ψ_6 or Minkowski tensor methods, the remaining particles in the crystalline state domains where sorted in clusters via the DBSCAN algorithm. It sorts point clouds into clusters with at least n_{min} particles having at most d_{max} separation. To be able to disjoin clusters linked only by a small number of particles, the DBSCAN algorithm was run two consecutive times with adapted parameter n_{min}: In the second run, n_{min} was increased from $n_{min} = 3$ in the first run (i.e., the smallest clusters have at least four particles), to $n_{min} = 4$. The parameter d_{max} is set in the range of the mean particle displacement as $d_{max} = 0.75$mm (i.e., the largest particle distance within a cluster can not exceed 0.75 mm). Domains in contact with the image boundary were discarded. This restricts the maximum domain size, but for domains not completely within the field of view an estimate of their area and circumference is not possible.

After identifying the particles in domains separated by defect lines and associating them in clusters, as described in the paragraph above, the area and boundary length of each domain could be measured as follows: The concave hull (also known as "alpha shape") of the set of points was calculated as the polygon that represents the area occupied by this set of points in the plane. To achieve this, at first the convex hull and Delaunay triangulation is calculated. The convex hull is comprised of all triangles of the Delaunay triangulation. To get to a concave hull the largest triangles (i.e., the triangles at the boundary of the convex hull) are then discarded from the convex hull: All triangles (with edge lengths a,b,c and area A) with radius filter $r_f = abc/(4A) > 1/\gamma$ for an arbitrary parameter γ. The specific value that is chosen for $1/\gamma$ is indicated in each case in the result section V. Only values in the range $1/\gamma \in [0.04, 0.08]$mm are considered: For $1/\gamma >$ 0.08 mm, the algorithm breaks down since domains become internally disconnected until no connected regions can be found anymore. Domains for $1/\gamma < 0.04$ mm are unphysical, since the concave hull then includes particles that are not part of the domain as determined by the DBSCAN algorithm.

In a last step, the concave hull polygon is smoothed out by buffering it as a smooth contour constructed by discs with a radius r_b in the range of the mean inter-particle separation $r_b =$ 0.75 mm. An example of the clustering steps is given in Fig. 7.

I. Energy calculation

The velocities of every particle are obtained by tracking each particle frame by frame and comparing consecutive images. This provides trajectories in time from which the velocity of every particle is derived. After fitting a normal distribution to the histogram of velocities in x and y direction separately at every time step, the mean of the width of these histograms gives the particle kinetic energy E (representative of T from Sec. II) for each data set. With this method energies could be resolved down to a level of 0.1 eV.

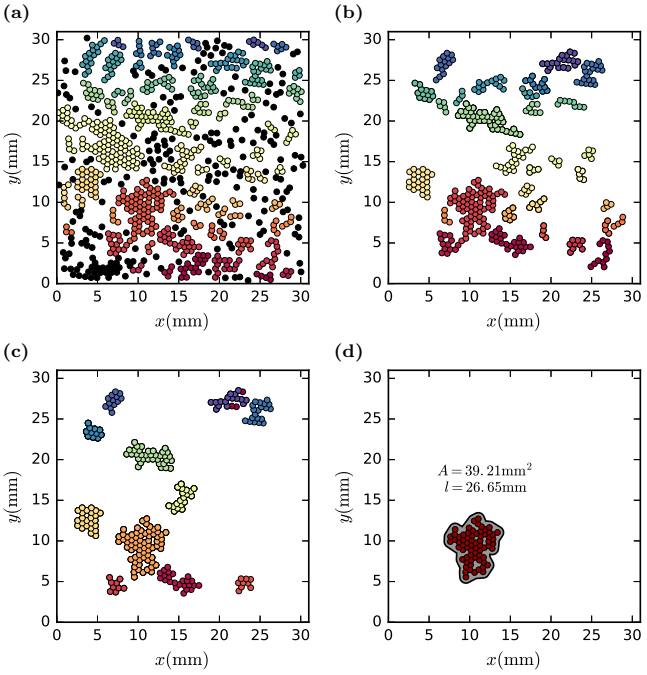

FIG. 7. Calculating the area and circumference of crystalline domains: (a) DBSCAN clustering for a specific time-step $t = 6.59$ s. Colors indicate different clusters, black are particles that are not considered as part of a cluster. (b) Clusters touching image boundary and particles not considered in a cluster are deleted. (c) The second DBSCAN clustering removes noise: Very small clusters, small cluster extensions and separates clusters connected by only few particles. (d) Estimate of the area and circumference of a specific domain via a concave hull algorithm. For details consult Sec. IV H.

V. RESULTS

A. Scaling behavior of the bond correlation function $g_6(r)$

The bond correlation function $g_6(r)$ was calculated for all time steps and datasets and fitted to a linear decay model (crystalline state), an exponential decay model (liquid state), and a power-law decay model (hexatic phase). For brevity of presentation only results of fits for experiment I are shown in Fig. 8. The findings, however, are qualitatively the same for all data sets. Figure 8(a) shows fits of the long-range decay behavior of $g_6(r)$ for different time steps. The goodness of fit χ^2 statistic is shown in Fig. 8(b). Small values indicate high goodness of fit and confidence of the validity of the underlying model. Figure 8(c) provides the values of the fit parameters c_6, ξ_6, and η_6.

For small times, before melting ($\sim$0 s $< t <$ 3 s), and for large times($\sim$7 s $< t <$ 12 s), after crystallization, we find the best model to be the linear decay. The linear decay evidences a state of crystalline domains that exhibit internal orientational order but have the freedom to rotate their orientation compared to neighboring domains [17].

For times directly before the linear decay ($\sim$ 5.5 s $< t <$ 7 s) evidences the crystalline state to be the best model, the exponential decay model provides the best goodness of fit (i.e., smallest χ^2 values in Fig. 8), indicating a liquid state [6,7]. This already excludes the possibility of a KTHNY-type

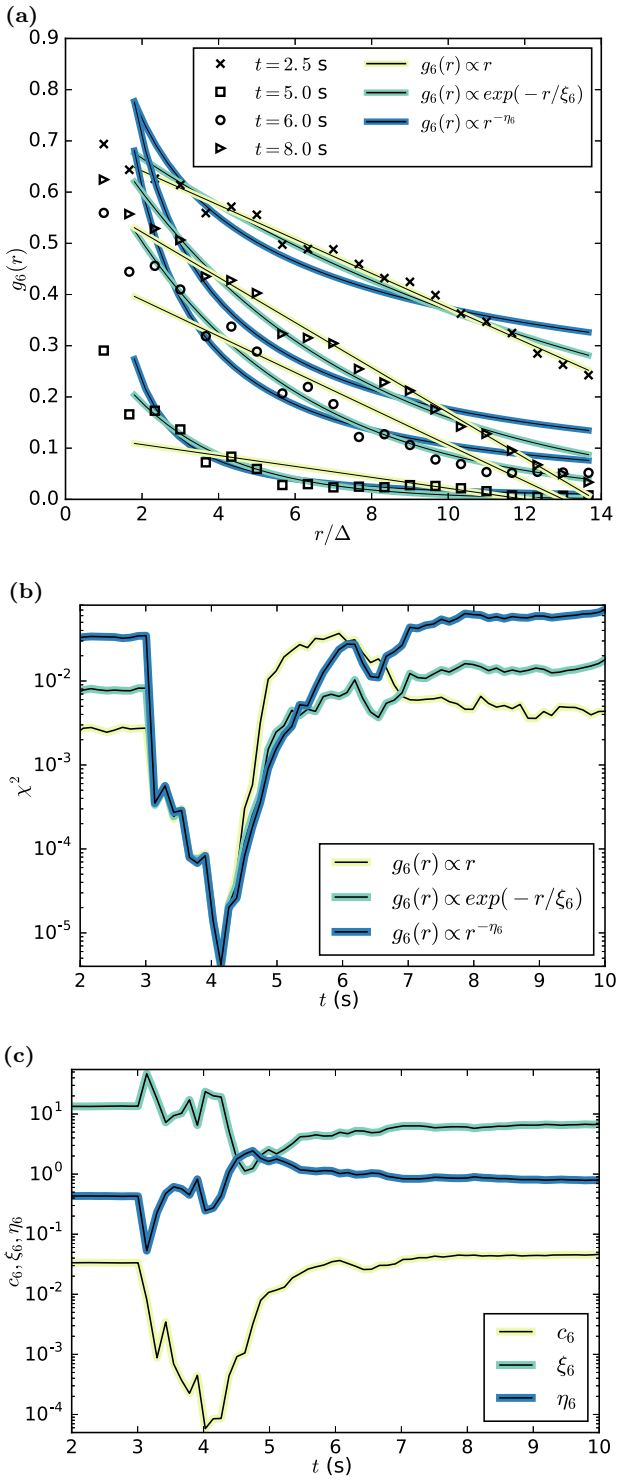

FIG. 8. Scaling behavior of the long-range decay of the bond correlation function $g_6(r)$. Shown for experimental data set I. (a) Different models are fitted to the long-range decay of $g(r)$ at different times t. Crystalline state: $g_6(r) \propto c_6 \cdot r$, liquid state: $g_6(r) \propto \exp(-r/\xi_6)$ and hexatic phase: $g_6(r) \propto r^{-\eta_6}$. (b) The chi-squared χ^2 statistic as a measure of the goodness of fit for different decay models. Small values indicate the best model. (c) Values of the best fit parameters for different models. To enhance the clarity of the strongly fluctuating figures during melting times ($\sim$ 3 s $< t <$ 5 s), panels (b) and (c) only show every 20th data point.

phase transition, since between the liquid and crystal state no evidence for the existence of a hexatic phase is found.

In a very short time frame between the chaotic melting and the liquid state (~ 4.5 s $< t < 5.5$ s), the power-law decay and exponential decay model both provide high goodness of fits values (i.e., low χ^2 values). The power-law decay would indicate a hexatic phase [6,7] in the KTHNY model. However, the KTHNY model predicts a power-law exponent of $\eta < 0.25$ for the hexatic phase. Here, we have much larger values of $\eta > 3$ for all times but the chaotic melting regime where no reliable fit could be performed. Also, the temperature regime does not correspond to a possible hexatic phase.

Thus, no hexatic state can be found for this phase transition. This implies that the two-dimensional complex plasma phase transitions analyzed in this study are not consistent with the KTHNY theory.

B. Relationship between domain area and boundary length

The results of the analysis with the above explained methods and measures are presented in the following. In this section, the hypothesis introduced in Eq. (7) and condensed to Eq. (22) is tested via plotting measured domain areas A_i against their circumferences l_i and thus possibly obtaining the power-law exponent α. To this end, first the defect Voronoi cells were detected via the Ψ_6 bond-order parameter (Sec. IV A), the MT2 (Sec. IV F), and the MT4 (Sec. IV G) method. Discarding these defects leaves ordered disjoint domains that are clustered using a DBSCAN clustering algorithm (IV H). The relation between the area of crystalline domains A_i and the boundary length l_i of defect lines separating the crystalline domains is shown in Fig. 9. All defect detection methods provide consistent results and every experiment is consistent with the scaling relation $\langle N_d \Delta^2 \rangle \propto [\Delta \langle N_s \rangle]^{1+\alpha}$. The exponents for the experiments are consistent with those found for the simulation data. The values of α obtained by least-square fits are listed in Table III and are consistent with the findings in Sec. V C.

In the simulation data we find small deviations. Since they are generated using a parabolic potential the particle density decreases in the radial direction. Thus, the density-based DBSCAN algorithm cannot as easily be applied to the simulation data as in the experimental case. For the Ψ_6 and MT2 metric in most cases a large cluster in the center is detected. For the MT4 metric predominantly very small clusters are detected.

It is noteworthy that the exponents are very stable (see Fig. 10): They are independent of the cutoff value used in the Minkowski methods to define crystalline cells and independent of the particular choice of Minkowski tensor metric and tensor rank. Even the Ψ_6 bond-order parameter gives a consistent result. Also, they depend only very weakly on the particular choice of parameters [reasonable values are discussed below and in Fig. 10(b)] in the DBSCAN clustering algorithm and the particular parameters in the calculation of the domain area and length via the convex hull algorithm. Varying the cutoff parameters in a large range only gives rises to very small changes in α. Variations are in the range of only a few percent and are listed in the caption of Fig. 10(a). In this figure the mean values $\langle \alpha \rangle$ are plotted for the whole range of cutoff values for the MT2, MT4 and Ψ_6 bond-order method, respectively.

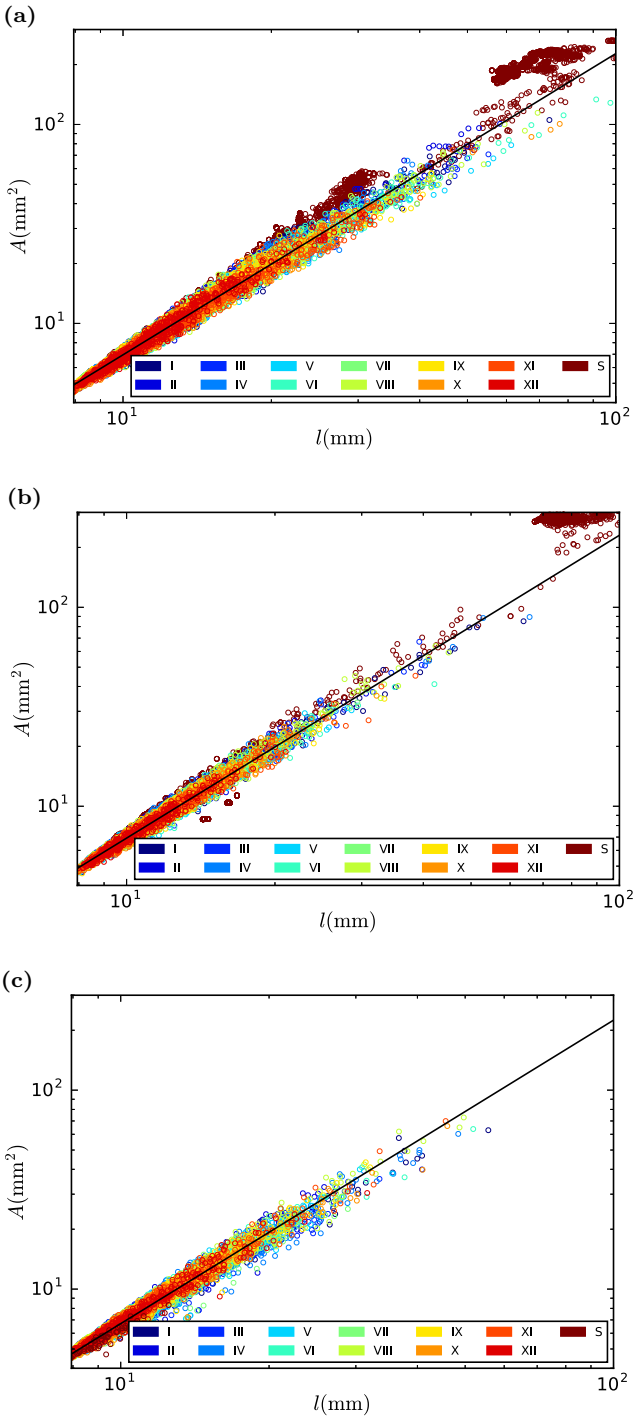

FIG. 9. The area A_i of crystalline domains plotted against their boundary length l_i. Different colors indicate different experiments and the simulation. The solid line is the mean of all least-square linear fits to the power-law Eq. (22) $\langle A_i \rangle \propto \langle l_i \rangle^{1+\alpha}$ for the experiments and the simulation. In panel (a) defects are identified via a Ψ_6 bond-order metric (Sec. IV A, $\Psi_{6,\mathrm{thresh}} = 0.5$), in panel (b) the particles in crystalline states are identified via the MT2 isotropy index method (Sec. IV F, $\beta_{\mathrm{thresh}} = 0.81$), and in panel (c) they are identified via the MT4 symmetry metric method as explained in Sec. IV G ($\Delta_{\mathrm{thresh}} = 0.18$). Area and boundary length are measured using a DBSCAN clustering algorithm as explained in Sec. IV H. Individual exponent values can be found in Table III.

TABLE III. Power-law exponent α for the area-length scaling in Fig. 9 measured via the Ψ_6 (IV A, $\Psi_{6,\mathrm{thresh}} = 0.7$), the MT2 (IV F, $\beta_{\mathrm{thresh}} = 0.88$), and the MT4 (IV G, $\Delta_{\mathrm{thresh}} = 0.12$) methods in Eq. (22) $\langle A_i \rangle \propto \langle l_i \rangle^{1+\alpha}$, for experiments I–XII and the simulation (III). For the corresponding graphs consult Fig. 9. The last row is the mean value of all above with the standard deviation as uncertainty. Area and circumference were measured via a DBSCAN algorithm [IV H, here $1/\gamma = 0.06$ mm, corresponding to the points in Fig. 10(b) marked with thick marker-edges.]

	α (Ψ_6)	α (MT2)	α (MT4)
I	0.526	0.505	0.519
II	0.569	0.550	0.570
III	0.503	0.535	0.539
IV	0.550	0.524	0.566
V	0.466	0.487	0.574
VI	0.485	0.494	0.547
VII	0.515	0.540	0.558
VIII	0.501	0.545	0.547
IX	0.527	0.518	0.570
X	0.488	0.545	0.545
XI	0.490	0.479	0.578
XII	0.548	0.543	0.560
S	0.752	0.856	0.529
⟨I...XII⟩	0.51 ± 0.02	0.52 ± 0.02	0.55 ± 0.02

Changing the smoothing parameter r_b over one order of magnitude has practically no effect. Varying the DBSCAN parameter $1/\gamma$ (it can be thought of as describing the raggedness of the concave hull) also gives only small changes in α as depicted in Fig. 10(b). The largest deviations are observed for values $1/\gamma < 0.04$ mm and $1/\gamma > 0.08$ mm. Yet, only values of $1/\gamma \in [0.04, 0.08]$mm are physically relevant since for too large values the domains become disconnected and for too small values the domains become more and more convex and include neighboring particles that are not part of the detected ordered domains. Averaging over all experiments, all defect detection methods with all threshold values and all physical DBSCAN parameters leads to a final value for the scaling exponent:

$$\alpha = 0.52 \pm 0.05. \tag{23}$$

This is the mean value (and uncertainty as standard deviation) of measurements as depicted in Fig. 10(b) for the range of physical values $1/\gamma \in [0.04, 0.08]$mm.

Detected domain sizes for different methods are compared in Fig. 11. Since multiple domains are detected during one point in time the comparison is only between the largest domain of each measure and point in time. With this method we only find few clusters that are detected consistently using different methods. Nevertheless, one can see that the Minkowski measures are more similar to each other than to the Ψ_6 bond-order metric, whereas the higher-rank Minkowski measure provides even less similar domains compared to the Ψ_6 measure than the lower-ranked Minkowski tensor measure.

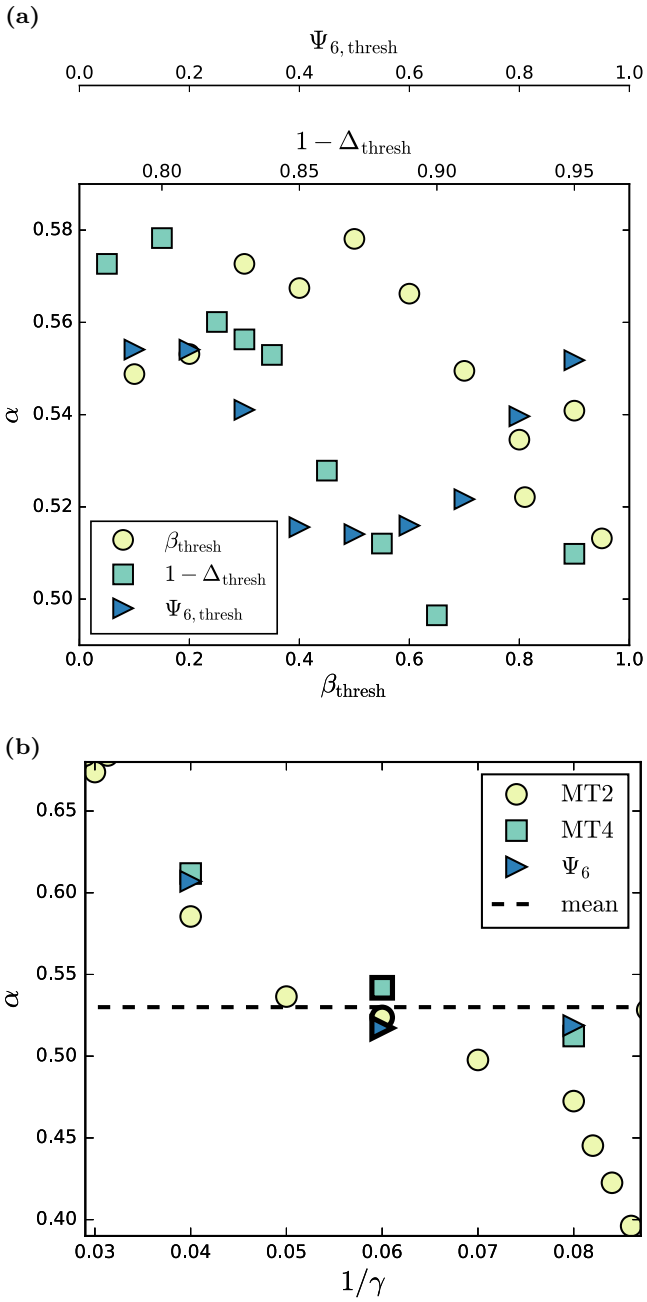

FIG. 10. (a) The exponents α from Eq. (22) $\langle A_i \rangle \propto \langle l_i \rangle^{1+\alpha}$, obtained by linear fits of the fractal relationship of domain area and circumference are plotted as the cutoff parameter of the particular measure is varied. α is found to be very stable: Varying the cutoff parameters in their whole range only gives rises to very small changes in α. We find variations of $\sqrt{Var[\alpha_\beta]}/\langle \alpha_\beta \rangle = 2.7\,\%$, $\sqrt{Var[\alpha_\Delta]}/\langle \alpha_\Delta \rangle = 4.3\,\%$ and $\sqrt{Var[\alpha_{\Psi_6}]}/\langle \alpha_{\Psi_6} \rangle = 1.9\,\%$. The DBSCAN parameters are constant, in particular, $1/\gamma = 0.06$ mm. (b) Variation of α from Eq. (22) $\langle A_i \rangle \propto \langle l_i \rangle^{1+\alpha}$ by variation of the DBSCAN parameter γ. (The cutoff parameter $\beta_{\mathrm{thresh}} = 0.81$ is constant.) The data points with thick marker-edges ($1/\gamma = 0.06$ mm) are the mean values of the individual α in Table III. The final mean value is indicated by a dashed line.

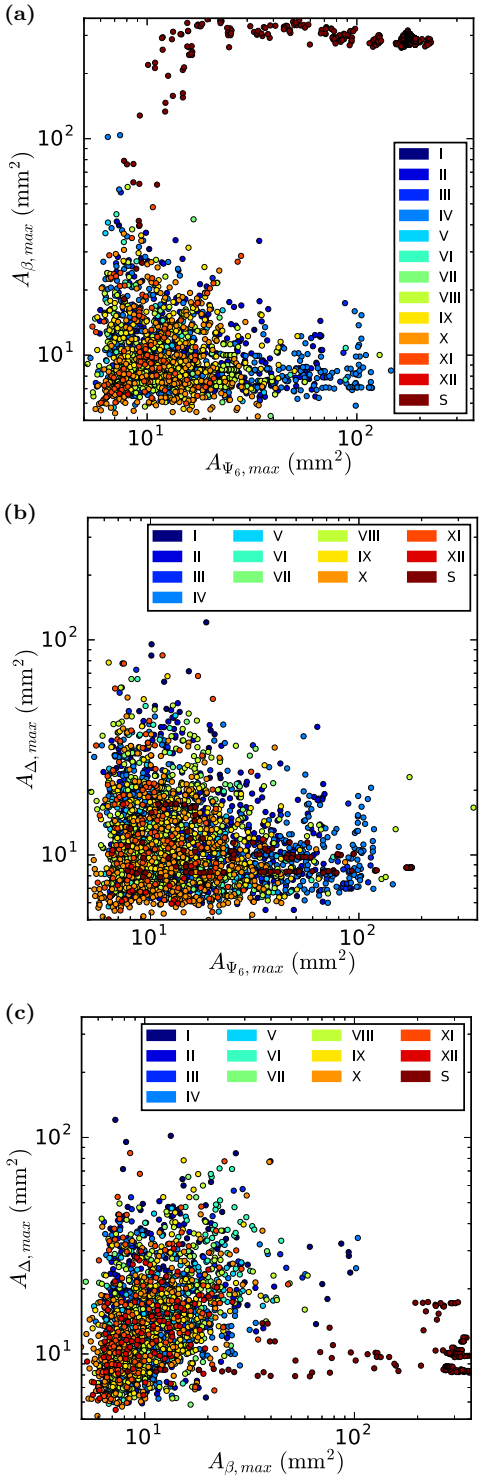

FIG. 11. A comparison of the detected domain areas A_i. For every point in time in which two measures both detect at least one crystalline domain the correlation between the largest domain of each measure is plotted. Comparison between the largest domains for (a) the MT2 and Ψ_6 measure, (b) the MT4 and Ψ_6 measure, and (c) the MT2 and MT4 measure. The Minkowski measures show the largest correlation, however, the data points are still widely spread. In all graphs (a–c) we find the simulation data points to be outliers. This is due to the fact that the clustering algorithm is not applicable in a straight forward way to this data, as discussed in the text.

TABLE IV. Power-law exponent α for the defect fraction-energy scaling in Fig. 12 measured via the MT2 (IV F, $\beta_{\text{thresh}} = 0.81$), MT4 (IV G, $\Delta_{\text{thresh}} = 0.18$), and Ψ_6 (IV A, $\Psi_{6,\text{thresh}} = 0.5$) methods in Eq. (8) $N_T/N \propto E^{2\alpha/(1+\alpha)}$, for experiments I–XII and the simulation (III). For the corresponding graphs, consult Fig. 12. The last row is the mean value of all above with the standard deviation as uncertainty.

	α (Ψ_6)	α (MT2)	α (MT4)
I	0.186	0.454	0.413
II	0.405	0.518	0.593
III	0.266	0.323	0.367
IV	0.295	0.416	0.473
V	0.362	0.618	0.605
VI	0.319	0.453	0.359
VII	0.336	0.573	0.317
VIII	0.405	0.526	0.418
IX	0.358	0.563	0.844
X	0.241	0.254	0.328
XI	0.263	0.103	0.677
XII	0.304	0.550	0.234
S	0.303	0.504	0.471
⟨I...XII⟩	0.31 ± 0.06	0.52 ± 0.18	0.47 ± 0.17

C. Relationship between energy and defect fraction

In this section the theoretical prediction of Eq. (8) $N_T/N \propto T^{2\alpha/(1+\alpha)} \propto E^{2\alpha/(1+\alpha)}$ of the FDS theory [2] is tested via plotting defect fractions N_T/N against the kinetic energy E of the particles. This is shown in Fig. 12. One can clearly see that the relation can well be described by a power law within a reasonable energy interval. After the detection of defects their number fraction N_T/N is obtained by simple division of the total defect number N_T and the total particle number N. The system temperature $E = k_B T$ is determined by fitting a normal distribution to the histogram of each component of the particle velocity vectors. Plotting these values in a log-log plot (Fig. 12) then gives the power-law exponent α for every data set and method. The exponents obtained in Secs. V B and V C are compared.

The dependence of the defect fraction N_T/N on the kinetic energy is shown in Fig. 12. Every measure and experiment is consistent with a power-law Eq. (8) $N_T/N \propto E^{\xi}$, with $\xi = 2\alpha/(1+\alpha)$. The exponents obtained by least-square fits are listed in Table IV. The exponents for the experiments are comparable with the exponents found for the simulation data: The line of best fit, shifted in a parallel fashion to simulation data energies, fits the data quite well. Thus, the simulation validates the experimental results. However, for very high energies the simulation curves deviate from the experimental fit. This can be explained by the dynamic difference in the system expansion during melting and the relaxation during crystallization due to the difference in the confinement potential of the experiments and simulation.

The exponents found via the MT2 and MT4 measures are consistent with the value obtained in the previous section [see Eq. (23)]. The only deviation found is for the mean exponent obtained via the Ψ_6 bond-order method. It is significantly smaller than all the other exponents obtained (with $\langle\alpha\rangle_{\Psi 6} \simeq 0.31$ by almost 40% compared to all other exponents $\langle\alpha\rangle \simeq$

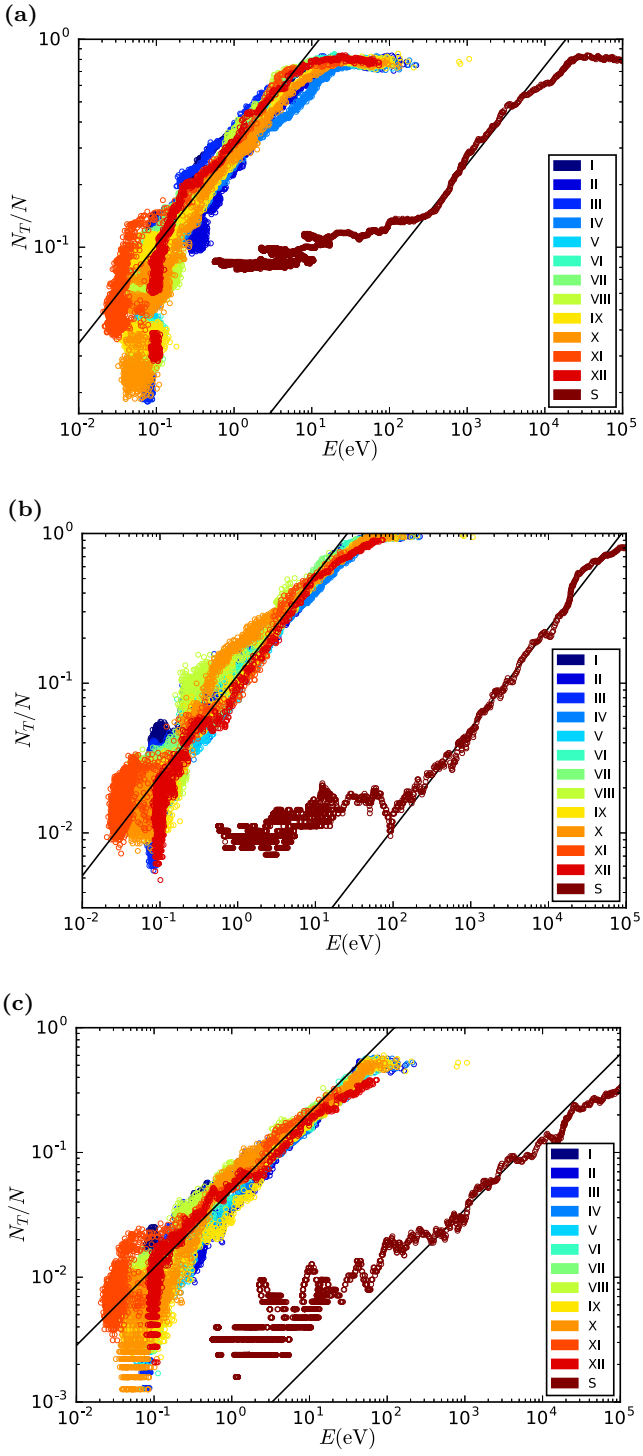

FIG. 12. The defect fraction N_T/N plotted against the particle kinetic energy E. Different colors indicate different experiments and the simulation. The solid line is the mean of all linear fits to the power-law $N_T/N \propto E^{\xi}$ for all experiments. The linear fit of the experimental data is shifted onto the simulation data in a parallel fashion. In panel (a) the defect fraction is obtained via the Ψ_6 method ($\Psi_{6,\text{thresh}} = 0.5$). The exponent is $\alpha_{\Psi 6} = 0.313$. The fit is constrained to energies in the interval $E \in [10^{-1}, 10^{1}]$ eV. (b) MT2 ($\beta_{\text{thresh}} = 0.81$); $\alpha_{\text{MT2}} = 0.518$; fit interval $E \in [10^{-1}, 10^{1.7}]$ eV. (c) MT4 method ($\Delta_{\text{thresh}} = 0.18$); $\alpha_{\text{MT4}} = 0.507$; fit interval $E \in [10^{-1}, 10^{2}]$ eV. Individual exponent values can be found in Table IV.

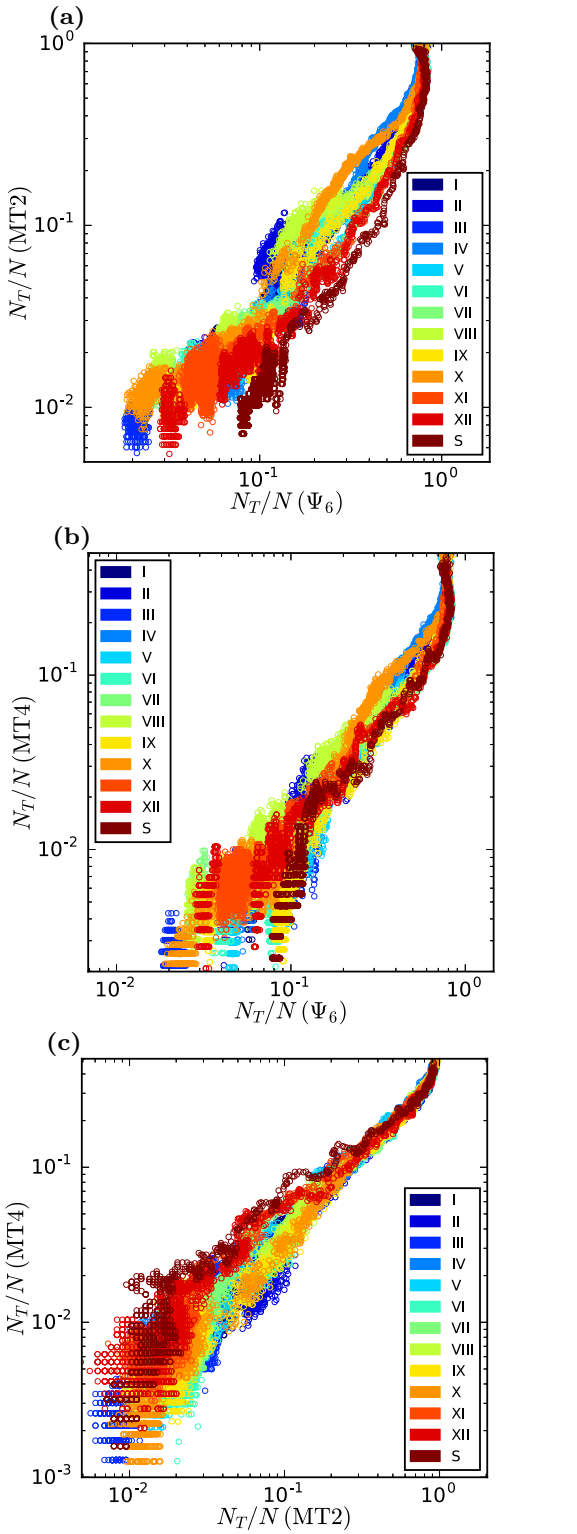

FIG. 13. A comparison of the detected defect fraction N_T/N at equal energies E. (a) MT2 vs Ψ_6, (b) MT4 vs Ψ_6, (c) MT2 vs MT4. The Minkowski measures resolve defect fractions for energy levels about one order of magnitude larger than the bond-order metric. The higher-rank Minkowski tensor measure resolves defect fractions even further than the lower ranked tensor measure. Compared to the Minkowski tensor measures the bond-order metric shows an early saturation for high energies.

0.5) in this and the previous section. The reason for the smaller Ψ_6 exponent likely lies in the fact that the Ψ_6 bond-order metric is less sensitive to lattice distortions compared to the Minkowski tensor measures and therefore less continuous in its nature, leading to a more binary, discontinuous form of defect/crystal state detection: Even for noisy data with larger distortions the Minkowski tensor method is able to distinguish more crystalline lattice structures form distorted ones, whereas the Ψ_6 bond-order metric only finds defects and can resolve crystalline structures only for smaller distortions. This can also be seen when comparing Fig. 3(c) with Fig. 5(c) [respectively, Fig. 6(c)]. After the melting the MT2 (respectively, MT4) measure starts to detect recrystallization much earlier than the Ψ_6 bond-order metric: The histogram of the Minkowski measure shifts noticeably to the right (respectively, left), whereas the bond-order metric histograms start to shift to crystalline values only at much later times.

The bond-order metric is obviously more binary in nature, allowing high values only for fairly perfect crystal structure and then changing rapidly to low values for distorted crystal structure. The Minkowski tensor metrics provide a means to probe and resolve the crystal structure continuously between those extremes. This allows the Minkowski tensor measures to confirm the scaling relation Eq. (8) for energy levels one order of magnitude larger (see also Fig. 13) than for the Ψ_6 bond-order metric and to confirm the FDS theory with unprecedented scrutiny.

VI. DISCUSSION AND CONCLUSION

Employing Minkowski tensor methods to the recrystallization process of experiments and simulation of two-dimensional complex plasma systems supports the FDS phase transition theory [2] based on the kinetic theory of Frenkel [18]. The analysis of the experimental and simulation data showed a scaling behavior in crystalline self-similar domains that is not consistent with the prominent KTHNY theory of phase transitions. The results of the Minkowski tensor analysis are consistent with the theoretically predicted power laws obtained from the scale-free theory and provide higher accuracy compared to results obtained by the commonly used bond-order metric Ψ_6 due to their capability to detect differences in defect fraction even for very high energies. Further, it is superior to the simple counting of paired 5/7-dislocations since it provides a more reliable statistic due to the much larger number of detected defects. All of the power-law exponents measured via Minkowski tensor metrics are consistent for all experiments and a simulation. Furthermore, they are also consistent for two different theoretical predictors: the scale-free behavior between defect fraction and particle energy, and the fractal relation between domain area and circumference. Summarized, this scale-free phase transition does not depend on experimental parameters but rather seems to be an inherent, universal feature of two-dimensional phase transitions as analyzed here.

The scaling relation introduced in Eq. (7) is confirmed by all experiments and the simulation for all applied defect measures (Ψ_6 bond-order metric, MT2 and MT4 measure). The straight lines in the log-log plots (Fig. 9) are reproduced extremely well. The power-law exponents are consistent for all measures and vary only marginally with changes of parameters in the methods of identifying defects and changes in the parameters of the DBSCAN clustering algorithm applied to measure the circumference and the area of crystalline domains. The DBSCAN clustering algorithm applied in this work measures this fractal behavior very precise and reproduces it even for the conventional Ψ_6 bond-order method. For this method deviations from the fractal behavior were found in an earlier study [19], where domain circumference and area where calculated by counting of particles. The DBSCAN method seems to be more accurate (holes in defect lines do not play an important role) and less tedious than only counting defects.

Also, the power-law Eq. (8) could be reproduced in with deviations only for very low and very high energies. This was already reproduced in a previous study, however, only by counting paired dislocation. The extended analysis in this work validated the predicted power law more rigorously, since the applied continuous measures (Ψ_6 bond-order metric, MT2 and MT4 measure) provide a significantly higher number of points in the defect-energy diagrams (Fig. 12) for the statistical analysis. The saturation in these diagrams can be explained by fact that for high energies all lattice sites in the system are distorted to fluid levels and an upper limit is reached. For low energies we only observe small deviations due to the thermodynamic occurrence of defects that are not domain boundaries and because of particles that leave the plane of observation due to oscillation in the vertical directions [60,61]. This causes artificial defects that can also be observed in the movies shown in the supplemental material [29]. The power-law exponents found for Eq. (8) are consistent with those for Eq. (7) for the Minkowski tensor methods. However, while the Ψ_6 measure reproduces a consistent exponent for Eq. (7) it yields a significantly smaller one for Eq. (8). This is due to the fact that the Ψ_6 measure is more binary in its nature than the Minkowski tensor measures. Therefore the dynamic range of the measured defect fraction is smaller which is reflected in the slope and the power-law exponent. The single measurement of the exponent α that does not fit into the other measurements in this work is, however, in the same range as the α obtained in a previous study [19] by considering defects only as 5/7-dislocations in a completely discrete fashion. The difference in these exponents might arise from this discreteness in counting defects in comparison to the more continuous Minkowski tensor methods. Here the Minkowski Tensor methods show promising potential for the analysis of crystal distortions: Where the Ψ_6 bond-order metric only scales over one order of magnitude and fails to detect changes in crystal defect numbers for very high energies, the Minkowski tensor methods provide one more order of magnitude in scaling range. Due to its continuous nature also the joint defect lines, forming the boarders of crystalline domains, can readily be detected leading to a more precise verification of the fractal relation 22 compared to defect detection via the Ψ_6 bond-order metric.

This study gives further evidence that Minkowski tensor methods are a powerful tool for morphological characterization of point sets. They are superior to conventional analysis methods in various respects. Minkowski tensor analysis is able to quickly reveal new aspects of interest in data, it is founded

on a solid mathematical framework, however it still provides easily interpretable results.

ACKNOWLEDGMENTS

We thank I. Laut for carefully checking this manuscript. We thank C. Durniak for providing the simulation data. The free software Qhull [62] was used to compute the Voronoi tessellation. Qhull uses the Quickhull algorithm for computing the convex hull. Some Minkowski tensors are calculated based on code of the free software package Karambola [63]. C. Knapek was financed by DLR/BMWi FKZ 50WM1441; A.B. was funded by the StMWi.

[1] V. E. Fortov, A. V. Ivlev, S. A. Khrapak, A. G. Khrapak, and G. E. Morfill, Phys. Rep. **421**, 1 (2005).
[2] G. E. Morfill and A. V. Ivlev, Rev. Mod. Phys. **81**, 1353 (2009).
[3] N. D. Mermin and H. Wagner, Phys. Rev. Lett. **17**, 1133 (1966).
[4] J. M. Kosterlitz and D. J. Thouless, J. Phys. C **5**, L124 (1972).
[5] J. M. Kosterlitz and D. J. Thouless, J. Phys. C **6**, 1181 (1973).
[6] B. I. Halperin and D. R. Nelson, Phys. Rev. Lett. **41**, 121 (1978).
[7] D. R. Nelson and B. I. Halperin, Phys. Rev. B **19**, 2457 (1979).
[8] A. P. Young, Phys. Rev. B **19**, 1855 (1979).
[9] K. Zahn, R. Lenke, and G. Maret, Phys. Rev. Lett. **82**, 2721 (1999).
[10] C. A. Murray and D. H. Van Winkle, Phys. Rev. Lett. **58**, 1200 (1987).
[11] C. C. Grimes and G. Adams, Phys. Rev. Lett. **42**, 795 (1979).
[12] Z. Hadzibabic, P. Kruger, M. Cheneau, B. Battelier, and J. Dalibard, Nature **441**, 1118 (2006).
[13] I. Guillamon, H. Suderow, A. Fernandez-Pacheco, J. Sese, R. Cordoba, J. M. De Teresa, M. R. Ibarra, and S. Vieira, Nat. Phys. **5**, 651 (2009).
[14] R. E. Guerra, C. P. Kelleher, A. D. Hollingsworth, and P. M. Chaikin, Nature **554**, 346 (2018).
[15] K. J. Strandburg, Rev. Mod. Phys. **60**, 161 (1988).
[16] C. Alba-Simionesco, B. Coasne, G. Dosseh, G. Dudziak, K. E. Gubbins, R. Radhakrishnan, and M. Sliwinska-Bartkowiak, J. Phys.: Condens. Matter **18**, R15 (2006).
[17] C. A. Knapek, *Phase Transitions in Two-Dimensional Complex Plasmas*, 1st ed., Springer Theses (Springer-Verlag, Berlin/Heidelberg, 2011).
[18] J. Frenkel, *Kinetic Theory of Liquids* (Dover Publications, Dover, 1955).
[19] C. A. Knapek, C. Durniak, D. Samsonov, and G. E. Morfill, Phys. Rev. Lett. **110**, 035001 (2013).
[20] W. Mickel, S. C. Kapfer, G. E. Schröder-Turk, and K. Mecke, J. Chem. Phys. **138**, 044501 (2013).
[21] G. E. Schröder-Turk, W. Mickel, S. C. Kapfer, F. M. Schaller, B. Breidenbach, D. Hug, and K. Mecke, New J. Phys. **15**, 083028 (2013).
[22] J. Hörrmann, D. Hug, M. A. Klatt, and K. Mecke, Adv. Appl. Math. **55**, 48 (2014).
[23] S. C. Kapfer, W. Mickel, K. Mecke, and G. E. Schröder-Turk, Phys. Rev. E **85**, 030301 (2012).
[24] F. M. Schaller *et al.*, Europhys. Lett. **111**, 24002 (2015).
[25] G. E. Schröder-Turk *et al.*, Adv. Mat. **23**, 2535 (2011).
[26] C. Dietz, T. Kretz, and M. H. Thoma, Phys. Rev. E **96**, 011301 (2017).
[27] M. A. Klatt, G. E. Schröder-Turk, and K. Mecke, Med. Phys. **44**, 3663 (2017).
[28] A. Böbel and C. Räth, Phys. Rev. E **94**, 013201 (2016).
[29] See Supplemental Material at http://link.aps.org/supplemental/10.1103/PhysRevE.97.053201 for movies S1–S13.
[30] C. A. Knapek, D. Samsonov, S. Zhdanov, U. Konopka, and G. E. Morfill, Phys. Rev. Lett. **98**, 015004 (2007).
[31] C. Durniak, D. Samsonov, N. P. Oxtoby, J. F. Ralph, and S. Zhdanov, IEEE Trans. Plasma Science **38**, 2412 (2010).
[32] S. Nunomura, J. Goree, S. Hu, X. Wang, and A. Bhattacharjee, Phys. Rev. E **65**, 066402 (2002).
[33] B. Liu, J. Goree, V. Nosenko, and L. Boufendi, Phys. Plasmas **10**, 9 (2003).
[34] P. J. Steinhardt, D. R. Nelson, and M. Ronchetti, Phys. Rev. B **28**, 784 (1983).
[35] H. Minkowski, Math. Ann. **57**, 447 (1903).
[36] S. Alesker, Geometriae Dedicata **74**, 241 (1999).
[37] P. Keim, G. Maret, and H. H. von Grünberg, Phys. Rev. E **75**, 031402 (2007).
[38] T. Aste, Phys. Rev. Lett. **96**, 018002 (2006).
[39] T. Aste, T. D. Matteo, M. Saadatfar, T. J. Senden, M. Schröter, and H. L. Swinney, Europhys. Lett. **79**, 24003 (2007).
[40] T. Aste and T. Di Matteo, Phys. Rev. E **77**, 021309 (2008).
[41] S.-C. Zhao, S. Sidle, H. L. Swinney, and M. Schröter, Europhys. Lett. **97**, 34004 (2012).
[42] S. Slotterback, M. Toiya, L. Goff, J. F. Douglas, and W. Losert, Phys. Rev. Lett. **101**, 258001 (2008).
[43] G. E. Schröder-Turk, W. Mickel, M. Schröter, G. W. Delaney, M. Saadatfar, T. J. Senden, K. Mecke, and T. Aste, Europhys. Lett. **90**, 34001 (2010).
[44] S. C. Kapfer, W. Mickel, F. M. Schaller, M. Spanner, C. Goll, T. Nogawa, N. Ito, K. Mecke, and G. E. Schröder-Turk, J. Stat. Mech. (2010) P11010.
[45] G. E. Schröder-Turk, R. Schielein, S. C. Kapfer, F. M. Schaller, G. W. Delaney, T. Senden, M. Saadatfar, T. Aste, and K. Mecke, AIP Conf. Proc. **1542**, 349 (2013).
[46] W. Helfrich, Z. Naturforsch. c **28**, 693 (1973).
[47] K. R. Mecke, Phys. Rev. E **53**, 4794 (1996).
[48] Y. Rosenfeld, Mol. Phys. **86**, 637 (1995).
[49] K. Mecke, in *Statistical Physics and Spatial Statistics*, Lecture Notes in Physics, Vol. 554, edited by D. S. K. R. Mecke (Springer, Berlin/Heidelberg, 2000), pp. 111–184.
[50] J. Schmalzing and K. M. Górski, Mon. Not. R. Astron. Soc. **297**, 355 (1998).
[51] S. Winitzki and A. Kosowsky, New Astron. **3**, 75 (1998).
[52] H. I. Modest, C. Räth, A. J. Banday, K. M. Górski, and G. E. Morfill, Phys. Rev. D **89**, 123004 (2014).
[53] G. Rossmanith, H. Modest, C. Räth, A. J. Banday, K. M. Górski, and G. Morfill, Phys. Rev. D **86**, 083005 (2012).

[54] H. I. Modest, C. Räth, A. J. Banday, G. Rossmanith, R. Sütterlin, S. Basak, J. Delabrouille, K. M. Górski, and G. E. Morfill, Mon. Not. R. Astron. Soc. **428**, 551 (2013).
[55] G. Schröder-Turk, S. Kapfer, B. Breidenbach, C. Beisbart, and K. Mecke, J. Microsc. **238**, 57 (2010).
[56] L. J. Walpole, J. Phys. D Appl. Phys. **19**, 457 (1986).
[57] S. Kapfer, Ph.D thesis, Friedrich-Alexander-Universität Erlangen-Nürnberg (FAU), 2012.
[58] M. Mehrabadi and C. C. Stephen, Quart. J. Mech. Appl. Math. **43**, 15 (1990).
[59] http://scikit-learn.org.
[60] D. Samsonov, S. Zhdanov, and G. Morfill, Phys. Rev. E **71**, 026410 (2005).
[61] S. V. Vladimirov, P. V. Shevchenko, and N. F. Cramer, Phys. Rev. E **56**, R74(R) (1997).
[62] http://www.qhull.org/.
[63] http://theorie1.physik.unierlangen.de/research/karambola/.

D.2 Kinetics of fluid demixing in complex plasmas: Domain growth analysis using Minkowski tensors [25]

Kinetics of fluid demixing in complex plasmas: Domain growth analysis using Minkowski tensors,
A. Böbel and C. Räth, *Phys. Rev. E* **94** (2016), 013201

Kinetics of fluid demixing in complex plasmas: Domain growth analysis using Minkowski tensors

A. Böbel* and C. Räth

Forschungsgruppe Komplexe Plasmen, Deutsches Zentrum für Luft- und Raumfahrt (DLR), Argelsrieder Feld 1a, 82234 Wessling, Germany

(Received 3 May 2016; published 11 July 2016)

A molecular dynamics simulation of the demixing process of a binary complex plasma is analyzed and the role of distinct interaction potentials is discussed by using morphological Minkowski tensor analysis of the minority phase domain growth in a demixing simulated binary complex plasma. These Minkowski tensor methods are compared with previous results that utilized a power spectrum method based on the time-dependent average structure factor. It is shown that the Minkowski tensor methods are superior to the previously used power-spectrum method in the sense of higher sensitivity to changes in domain size. By analysis of the slope of the temporal evolution of Minkowski tensor measures, qualitative differences between the case of particle interaction with a single length scale compared to particle interactions with two different length scales (dominating long-range interaction) are revealed. After proper scaling the graphs for the two length scale scenarios coincide, pointing toward universal behavior. The qualitative difference in demixing scenarios is evidenced by distinct demixing behavior: in the long-range dominated cases demixing occurs in two stages. At first, neighboring particles agglomerate, then domains start to merge in cascades. However, in the case of only one interaction length scale only agglomeration but no merging of domains can be observed. Thus, Minkowski tensor analysis is likely to become a useful tool for further investigation of this (and other) demixing processes. It is capable to reveal (nonlinear) local topological properties, probing deeper than (linear) global power-spectrum analysis, however, still providing easily interpretable results founded on a solid mathematical framework.

DOI: 10.1103/PhysRevE.94.013201

I. INTRODUCTION

When a binary fluid is forced into the immiscible state, it starts to dynamically demix until the thermodynamically stable state of two coexisting fluids is reached. This spinodal decomposition is accompanied by a domain growth that is believed to be selfsimilar in time; i.e., the domain morphology is preserved. This implies a single time-dependent characteristic length that obeys a power-law growth $L(t) \propto t^{\alpha}$ [1–7].

Competing interactions play an important role in the morphology of phase separation. They can lead to various domain patterns as, e.g., striped lamellar structures, hexagonal arrays of droplets [8], and clusters [9]. The dynamical evolution in systems with such interactions is governed by the competition between the long-range repulsion causing subdivision of domains and the short-range attraction resulting in the growth of interface energy. There has been a great deal of theoretical research of this process carried out in the mean-field framework [10,11]. However, there are few particle-resolved studies of such systems [12], in particular few studies exist addressing the role of competing interactions [6].

Complex plasmas are composed of a weakly ionized gas and microparticles that are highly charged due to absorption of the ambient electrons and ions [13,14]. Binary complex plasmas contain microparticles of two different sizes and constitute a model system that is well suited for studying the kinetics of fluid demixing at the individual particle level: properties of pair interactions, such as the interaction range, can be flexibly tuned. Also the dynamics of particles at short timescales is practically undamped due to the low density in the gas in typical complex plasmas [14].

The prevailing mechanism of interaction between charged microparticles in complex plasmas is electric repulsion [13,14]. At large distances r, the electrostatic potential of a particle can be represented in the asymptotic form $\Phi(r)$ [15]. Theory predicts a rich variety of screening mechanisms operating in complex plasmas [13,16]. The shape of $\Phi(r)$ can be affected by the plasma absorption on a particle, nonlinearity in plasma particle interactions, ionization loss balance, etc. Recently, it was shown that the plasma production and loss processes can play a crucial role in the long-range behavior of $\Phi(r)$ [17], resulting in the emergence of two dominating asymptotes that both have the Yukawa form:

$$\Phi(r) = \frac{1}{r}(Z^*_{\mathrm{SR}} e^{-r/\lambda_{\mathrm{SR}}} + Z^*_{\mathrm{LR}} e^{-r/\lambda_{\mathrm{LR}}}). \quad (1)$$

Here Z^* indicates effective charge, λ indicates the length scale for long-range (LR) and short-range (SR) interactions, respectively. The screening length ratio is defined as

$$\Lambda = \lambda_{\mathrm{LR}}/\lambda_{\mathrm{SR}}. \quad (2)$$

The following discussion will be based on simulations where Λ is varied since it was shown that the LR interactions can significantly enhance demixing [6].

To study the possibility of demixing in binary complex plasmas experiments with the PK-3 Plus rf discharge chamber [18] on board the ISS were performed earlier. After the injection of small particles in a stationary cloud of big ones an apparent phase separation was observed accompanied by the formation of a small particle droplet (Supplemental Material movie S1 in Ref. [6]). These experiments showed the strong tendency of binary complex plasmas to demix at time scales of seconds.

Since the early 20th Century [19] Minkowski functionals are a prominent tool for morphological data analysis. Only recently the hierarchy of Minkowski valuation was extended

*alexander.boebel@dlr.de

to tensor valued quantities called Minkowski tensors [20]. Minkowski functionals and tensors are sensitive to any n-point correlation function and thus can quickly give new insights to processes beyond the capability of power-spectrum methods as demonstrated for the demixing of a binary complex plasma in this paper.

This paper is structured as follows. Section II describes the simulations on which the Minkowski tensor analysis is performed upon. In Sec. III methods are presented: Voronoi tesselations (III A), Minkowski functionals (III B), and Minkowski tensors (III C) are introduced. Based on this introduction an isotropy measure (III D) and a symmetry metric (III E) is derived. Also, the previously used power-spectrum method (III F) is reviewed. Section IV presents the results obtained by Minkowski tensor analysis of the simulation data. The dynamic range (IV A) of the Minkowski measures, differences in demixed domain size (IV B) for different measures are discussed, and hints of universal behavior (IV C) can be found by analysis of local gradients of the temporal evolution of Minkowski measures. Finally, in Sec. V conclusions are drawn and a brief outlook on more detailed studies of this process is given.

II. SIMULATION

In order to investigate details of the particle dynamics accompanying the phase separation in binary complex plasmas and compare with theory, molecular dynamics (MD) simulations with the Langevin thermostat were employed previously: the growth of the minority phase (particle species 1) domains was analyzed for several combinations of short- and long-range interactions using a power-spectrum method based on the time-dependent average structure factor [6]. A binary mixture was composed of, in total, 729 000 particles (of species 1 and 2) at the off-critical particle composition $x_1 = 0.5$ (equal number of particles of species 1 and 2). The simulations were performed in a cubic box with the dimensions of 27 mm (corresponds to a mean interparticle distance of 0.3 mm) and periodic boundary conditions. The particles interacted via the potential Eq. (1). Following simulation parameters (approximately corresponding to the experiment) were used: The particle mass density $1.5\,\mathrm{g/cm^3}$ and diameters $2a_1 = 3.4\ \mu$m and $2a_2 = 9.2\ \mu$m, the actual charges $Z_1 = 4000e$ and $Z_2 = (a_2/a_1)Z_1 = 10824e$, the friction coefficients $\zeta_1 = 250\ \mathrm{s^{-1}}$ and $\zeta_2 = (a_1/a_2)\zeta_1 = 92.4\ \mathrm{s^{-1}}$, the SR (Debye-Hückel) screening length $\lambda_{\mathrm{SR}} = 150\,\mu$m, the mean interparticle distance $\Delta = 0.3$ mm, and the temperature $k_{\mathrm{B}}T = 0.024$ eV. A standard integration scheme was employed with a time step $\delta t = 0.0025 < \zeta_1^{-1} < \zeta_2^{-1}$ s to solve the equation of motion numerically. Further details can be found in the Supplemental Material of Ref. [6].

Here the results of these earlier simulations are analyzed in terms of Minkowski tensor methods and compared with previous results obtained by a power-spectrum analysis.

III. MINKOWSKI TENSOR METHODS

A. Voronoi tessellation

A commonly used method for quantifying the local structure of spheres is by construction of a nearest neighbor network on which quantitative structure metrics are computed (e.g., bond orientational order parameters [21]).

An alternative approach for quantifying local structure is provided by the analysis of the Voronoi diagram. The Voronoi diagram is the partition of space into the same number of convex cells as there are particles in the packing. The Voronoi cell of each particle is the region of space closer to that given particle than to any other particle. For the special case of three-dimensional crystal lattices the Voronoi cell is called Wigner-Seitz cell. In the field of granular matter, Voronoi diagrams have been used to determine distributions of local packing fractions [22–24], spatial correlations [25], and correlations with particle motion [26].

Recently, studies provided insight in the local structure of sphere packings and sphere ensembles by analyzing the shape of Voronoi cells, in particular their degree of anisotropy or elongation [27–30].

Here the shape of the Voronoi tessellation obtained from particle positions is analyzed using Minkowski functional and tensor methods. The boundary particles where discarded, the tessellation included only a center cube with an edge length of $16mm$.

B. Minkowski functionals

For a body K with a smooth boundary contour ∂K embedded in D-dimensional euclidean space the $D+1$ Minkowski functionals are, up to constant factors, defined as

$$\begin{aligned} W_0(K) &= \int_K d^D r, \\ W_\nu(K) &= \int_{\partial K} G_\nu(r)\, d^{D-1} r, \quad 1 \leqslant \nu \leqslant D, \end{aligned} \tag{3}$$

where $G_\nu(r)$ are the elementary symmetric polynomials of the local principal curvatures as defined in differential geometry.

The Minkowski tensor methods described in the following are also implemented for two-dimensional systems and thus can be applied to, e.g., experimental observations of slices of a three-dimensional system. In three-dimensional euclidean space the Minkowski functionals, up to constant factors, are $W_0(K)$ (volume), $W_1(K)$ (area), $W_2(K)$ (integrated mean curvature), and $W_3(K)$ (euler characteristic):

$$\begin{aligned} W_0(K) &= \int_K d^3 r, \\ W_1(K) &= \int_{\partial K} d^2 r, \\ W_2(K) &= \int_{\partial K} \kappa_1 + \kappa_2\, d^2 r, \\ W_3(K) &= \int_{\partial K} \kappa_1 \kappa_2\, d^2 r. \end{aligned} \tag{4}$$

Minkowski functionals are motion invariant, additive, and (conditionally) continuous. They form a complete family of morphological measures. Or vice versa: Any motion invariant (conditionally) continuous and additive functional is a superposition of the (countably many) Minkowski functionals. They are nonlinear measures sensitive to higher-order correlations. Known applications are, e.g., curvature energy of membranes

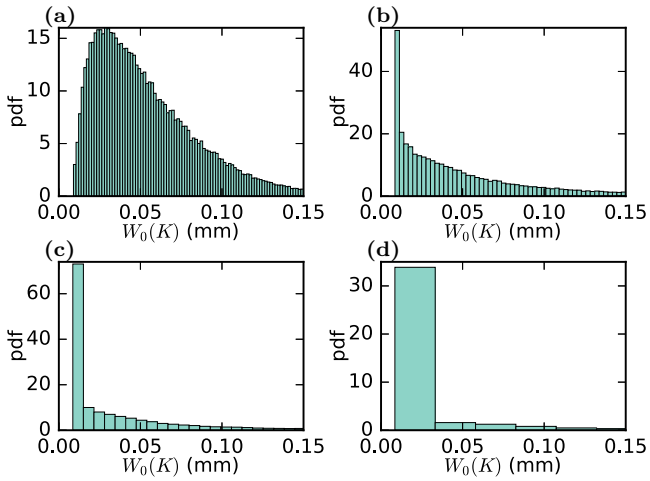

FIG. 1. Calculating the minority phase (particle species 1) domain size via a histogram method. The volume functional $W_0(K)$ Eq. (4) of species 1 particles is plotted for increasing time from the top left to the bottom right panel. (a) $t = 0.6\,s$, (b) $t = 0.6\,s$, (c) $t = 0.6\,s$, (d) $t = 0.6\,s$. The ever-increasing low-volume peak can be interpreted as ordered domains, whereas disordered particles that have not yet agglomerated correspond to larger Voronoi regions. These plots are obtained for simulations with screening length ratio $\Lambda = 12$. For other values of the screening length ratio similar plots are obtained.

[31], order parameter in Turing patterns [32], density functional theory for fluids (as hard balls or ellipsoids) [33,34], testing point distributions (find clusters, filaments, underlying pointprocess), or searching for non-Gaussian signatures in the CMB [35].

The Minkowski functional analysis carried out in this study is done by calculating the volume functional $W_0(K)$ Eq. (4) locally for every Voronoi region of the minority phase (particle species 1) and for every time step in the simulation. Then a histogram is calculated for every time step. As illustrated in Fig. 1 these histograms, as time progresses, separate into two parts: The narrow δ-shaped peak corresponding to the smallest volume becomes even more prominent and distinct from the larger-volume tail. It is reasonable to assume that the smallest volume peak corresponds to the homogeneous domains of agglomerating particles. To measure the size of these domains the number of Voronoi regions in the smallest volume peak of the histogram are counted. The hereby obtained value will hereinafter be referred to as MT0 measure.

C. Minkowski tensors

In order to account also for directional properties it is natural to abstract the scalar valued Minkowski functionals to tensor valued quantities called Minkowski tensors [36]:

$$\begin{aligned} W_0^{a,0}(K) &:= \int_K d^D r \;\; \mathbf{r}^{\odot a}, \\ W_\nu^{a,b}(K) &:= 1/D \int_{\partial K} d^{D-1} r \;\; G_\nu(r) \;\; \mathbf{r}^{\odot a} \odot \mathbf{n}^{\odot b}. \end{aligned} \tag{5}$$

Here $\odot$ stands for the symmetric tensor product. Again $G_\nu(r)$ are the elementary symmetric polynomials of the local principal curvatures as defined in differential geometry. a counts the number of position vectors $\mathbf{r}$, and b counts the number of normal vectors $\mathbf{n}$ in the tensor product. Thus, the rank of each tensor is the tupel (a,b). Their properties are as follows: they are isometry covariant; i.e., their behavior under translation and rotation is given by

$$\begin{aligned} W_\nu^{a,b}(K + \mathbf{t}) &= \sum_{i=0}^{a} \binom{a}{i} \mathbf{t}^i \; W_\nu^{a-i,b}(K), \\ W_\nu^{a,b}(\hat{O}\, K) &= \hat{O}_{a+b} \; W_\nu^{a,b}(K). \end{aligned} \tag{6}$$

They are additive,

$$W_\nu^{a,b}(K_1 \cup K_2) = W_\nu^{a,b}(K_1) + W_\nu^{a,b}(K_2) - W_\nu^{a,b}(K_1 \cap K_2), \tag{7}$$

and they are homogeneous of degree $3 + a - \nu$,

$$W_\nu^{a,b}(\lambda K) = \lambda^{3+a-\nu} \; W_\nu^{a,b}(K). \tag{8}$$

Similar to Minkowski functionals the attractiveness of Minkowski tensors is particularly due to a strong completeness theorem by Alesker [20]. It is stating that all morphological information that is relevant for additive material properties is represented by the Minkowski tensors. Any motion covariant, conditionally continuous and additive tensor valued functional is a superposition of the (countably many) Minkowski Tensors.

D. MT2 isotropy index

For a body K and each rank-two Minkowski tensor $W_\nu^{a,b}(K)$ an isotropy index can be defined as the ratio between the smallest and largest eigenvalue of the $D \times D$-matrix representing each Minkowski tensor [36]:

$$\beta_\nu^{a,b}(K) := \frac{\lambda_{\min}\left[W_\nu^{a,b}(K)\right]}{\lambda_{\max}\left[W_\nu^{a,b}(K)\right]}. \tag{9}$$

The dimensionless isotropy index is a pure shape measure. It is invariant under isotropic scaling of K. For example, in two dimensions the isotropy index $\beta = 1$ is obtained for a circle or a square. For a rectangle one obtains $\beta =$ shorter/longer edge. In three dimensions $\beta = 1$ is obtained for regular shapes ranging from a cube to a sphere. For a box the value is $\beta =$ shortest/longest edge. Thus, this isotropy index is an isotropy measure only in the sense of elongation.

The rank-two Minkowski tensor analysis carried out in this study is done by calculating the isotropy index β Eq. (9) locally for every Voronoi region of the minority phase (particle species 1) and for every time step in the simulation. Then a histogram is calculated for every time step. As illustrated in Fig. 2 these histograms are composed of two parts: The ordered, isotropic section (high β values) is separating from the disordered, anisotropic (small β values) section with increasing time steps. It is reasonable to assume that the isotropic Voronoi regions correspond to the homogeneous domains of agglomerating particles. To measure the size of these domains the number of Voronoi regions in the ordered, high-β section of the histogram are counted. To that purpose, in order to distinguish ordered from disordered sections a cutoff value ($\beta_{\text{thresh}} = 0.7$) is chosen as the intersection point of the two sections at late time steps when demixing is well progressed. For

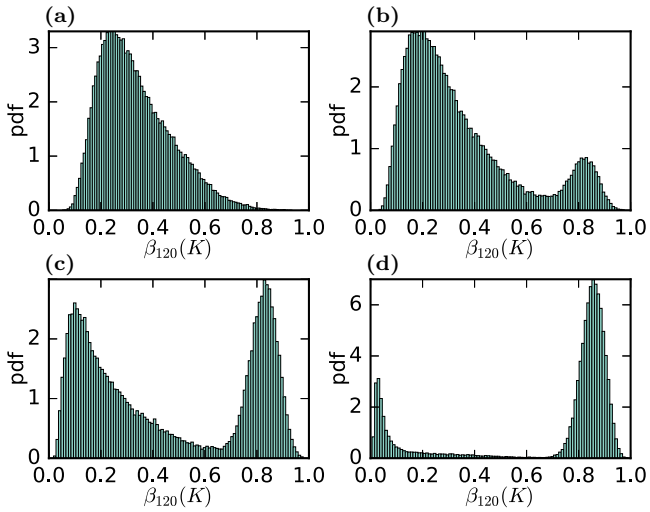

FIG. 2. Calculating the minority phase (particle species 1) domain size via a Histogram method. The isotropy index β Eq. (9) of minority phase particles is plotted for increasing time from the top left to the bottom right panel. (a) $t = 0.6\,s$, (b) $t = 0.6\,s$, (c) $t = 0.6\,s$, (d) $t = 0.6\,s$. The separating parts can be interpreted as ordered domains (high β values) and disordered particles that have not yet agglomerated (low β values) into a order domain. These plots are obtained for simulations with screening length ratio $\Lambda = 12$. For other values of the screening length ratio similar plots are obtained.

simplicity this measure will hereinafter be referred to as $MT2$ measure.

E. MT4 symmetry metric

In order to distinguish between structures of high symmetry, i.e., differentiate between crystalline structures (hcp, fcc, etc.) higher-order tensors have to be applied. For rank four and higher, isotropic symmetry is distinct from cubic symmetry. (This is evidenced by the appearance of a second independent shear modulus when transitioning from isotropic to cubic symmetry in the theory of linear elasticity, which is formulated using a rank-four tensor [37]. This method has been used in hard sphere systems to characterize random close packings [29].

For brevity, only the simplest rank-four Minkowski tensor is considered:

$$W_1^{04}(K) = 1/3 \int_{\partial K} d^2r\ \mathbf{n}(\mathbf{r}) \otimes \mathbf{n}(\mathbf{r}) \otimes \mathbf{n}(\mathbf{r}) \otimes \mathbf{n}(\mathbf{r}). \quad (10)$$

Since it is translation invariant and symmetric (i.e., it holds for the components $[W_1^{04}]_{ijkl} = [W_1^{04}]_{(ijkl)}$) it has only 15 independent elements instead of 81 in three dimensions.

A morphology metric suitable for the characterizing systems of spherical particles should be rotationally invariant since the physics do not *a priori* designate a preferred direction. Thus, the tensor W_1^{04} should not be directly used. Instead, rotational invariants are constructed. This is done by borrowing ideas from the theory of the elastic stiffness tensor.

The tensor $W_1^{04}(K)$ is rewritten in the Mehrabadi supermatrix notation [38] as a 6×6 matrix:

$$M = \begin{bmatrix} S_{xxxx} & S_{xxyy} & S_{xxzz} & \sqrt{2}\,S_{xxyz} & \sqrt{2}\,S_{xxxz} & \sqrt{2}\,S_{xxxy} \\ S_{xxyy} & S_{yyyy} & S_{yyzz} & \sqrt{2}\,S_{yyyz} & \sqrt{2}\,S_{yyxz} & \sqrt{2}\,S_{yyxy} \\ S_{xxzz} & S_{yyzz} & S_{zzzz} & \sqrt{2}\,S_{zzyz} & \sqrt{2}\,S_{zzxz} & \sqrt{2}\,S_{zzxy} \\ \sqrt{2}\,S_{xxyz} & \sqrt{2}\,S_{yyyz} & \sqrt{2}\,S_{zzyz} & 2\,S_{yzyz} & 2\,S_{yzxz} & 2\,S_{yzxy} \\ \sqrt{2}\,S_{xxxz} & \sqrt{2}\,S_{yyxz} & \sqrt{2}\,S_{zzxz} & 2\,S_{yzxz} & 2\,S_{xzxz} & 2\,S_{xzxy} \\ \sqrt{2}\,S_{xxxy} & \sqrt{2}\,S_{yyxy} & \sqrt{2}\,S_{zzxy} & 2\,S_{yzxy} & 2\,S_{xyxz} & 2\,S_{xyxy} \end{bmatrix}, \quad (11)$$

where $S = W_1^{04}(K)/W_1(K)$.

Then the six-tuple formed by the eigenvalues ζ_i of M (in descending order) may be considered a symmetry fingerprint of the polyhedron K. It is invariant under rotation, scaling, and translation of the polyhedron K. Using the signature eigenvalue tupel ζ_i of M, it is possible to define a distance measure on the space of bodies induced by the Euclidean distance:

$$\Delta(K_1, K_2) := \left\{ \sum_{i=1}^{6} [\zeta_i(K_1) - \zeta_i(K_2)]^2 \right\}^{1/2}, \quad (12)$$

where $\Delta(K_1, K_2)$ is a pseudometric. It is positive definite, symmetric, the triangle inequality holds, however, the coincidence axiom $\Delta(K_1, K_2) = 0 \Leftarrow K_1 = K_2$ is only an implication and not an equivalence. For example $\Delta(\text{sphere, dodecahedron}) = 0$. To distinguish dodecahedra from spheres one needs to employ even higher rank tensors.

The MT 4 analysis carried out in this study is done in analogy to the MT 2 analysis. The symmetry metric $\Delta(K_{\text{voronoi cell}}, K_{\text{hcp}})$ Eq. (12) is calculated locally for every Voronoi region of the minority phase (particle species 1) and for every time step in the simulation. Then a histogram is calculated for every time step. As illustrated in Fig. 3, these histograms are composed of two parts: the ordered, isotropic section (low Δ values) is separating from the disordered, anisotropic (small Δ values) section with increasing time steps. It is reasonable to assume that the isotropic Voronoi regions correspond to the homogeneous domains of agglomerating particles. To measure the size of these domains the number of Voronoi regions in the ordered, low Δ section of the histogram are counted. To that purpose, in order to distinguish ordered from disordered sections a cutoff value ($\Delta_{\text{thresh}} = 0.12$) is chosen as the intersection point of the two sections at late time steps when demixing is well progressed. For simplicity this measure will be referred to as MT4 measure in the following.

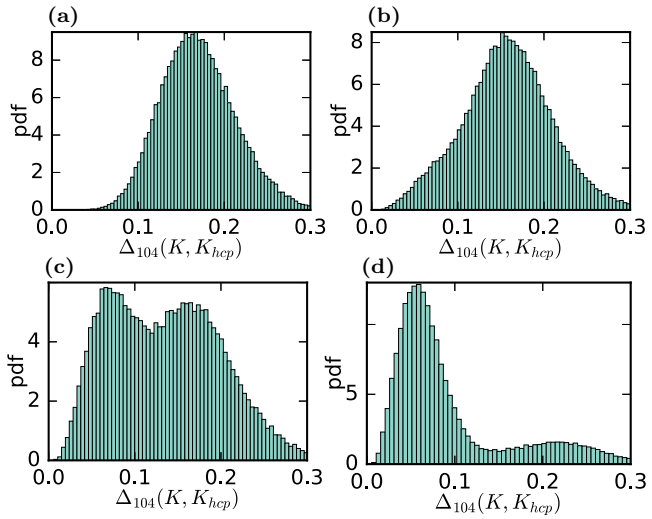

FIG. 3. Calculating the minority phase (particle species 1) domain size via a Histogram method. The pseudometric $\Delta(K_{\text{voronoi cell}}, K_{\text{hcp}})$ Eq. (12) of minority phase particles is plotted for increasing time from the top left to the bottom right panel. (a) $t = 0.6\,s$, (b) $t = 0.6\,s$, (c) $t = 0.6\,s$, (d) $t = 0.6\,s$. The separating parts can be interpreted as ordered domains (low Δ values) and disordered particles that have not yet agglomerated (high Δ values) into a order domain. These plots are obtained for simulations with screening length ratio $\Lambda = 12$. For other values of the screening length ratio similar plots are obtained.

F. PS method

In the underlying previous study the onset and the first stages of the phase separation were characterized by the evolving domain size L, which was deduced from the time-dependent average structure factor $S(k,t)$ [2,5,39] in a linear analysis. The position of the maximum of $S(k,t)$ was identified as $2\pi/L$. The position of maximum at each simulation time step was determined by fitting the off-critical function $S(k,t) \propto (kL/2\pi)^2/[2 + (kL/2\pi)^6]$.

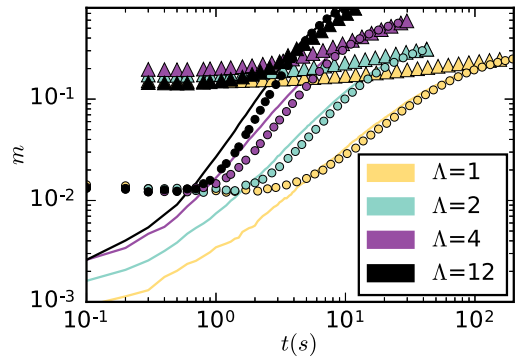

FIG. 4. Growth of the minority phase (particle species 1) domains. Different domain size measures $m \in \{\text{PS}, \text{MT0}, \text{MT2}\}$ are plotted as they change in time during the demixing simulation. (Details concerning measures and the simulation can be found in Sec. I.) Triangles are obtained by the PS method, lines by the volume MT0 method, dots by the MT2 isotropy index method. Different colors indicate different screening length ratios Λ. For better visibility only a subset of all data points are displayed so that all neighboring points have approximately equal spacing.

The results of this analysis are summarized in Fig. 4(a) (triangles); see also Supplemental Material movies S2 and S3 of Ref. [6]. In the SR-dominated case $\Lambda = 1$, when Eq. (1) is reduced to the regular Yukawa form, the growth of domains of the minority phase is rather slow, and the evolution of $L(t)$ is characterized by relatively small growth exponents. In this case domains remain fuzzy at the simulation timescales and their shape is irregular. The increase of Λ, and therefore of the interaction range, sharpens the interfaces and makes the domains grow faster. As Λ increases and LR interactions become more dominating they cause a large increase of the surface tension and faster demixing.

A more detailed description can be found in Ref. [6].

IV. RESULTS

The results of the analysis with above explained methods and measures are presented in the following. To allow for comparison some plotted results were scaled: Each time series obtained by the PS measure and MT0 measure was scaled by multiplication with a factor such that the last (and also highest) point of these time series have the same value as the corresponding (same Λ) time series of the MT2 measure.

A. Dynamic range

Comparing the graphs of the domain size measure obtained by using the original power-spectrum (PS) method (Fig. 4, triangles) with the graphs of volume Minkowski functional (MT0 measure) analysis (Fig. 4(a), lines) we find that the volume functional yields a more sensitive measure for the growth of the minority phase (particle species 1) domains. First, one notices that both graphs reproduce a power law indicated by the affine graph in the double logarithmic plot. Second, the significantly larger range of the volume curve and correspondingly its significantly steeper slope can be observed.

Furthermore, the MT0 measure is able to resolve the domain growth right from the beginning of the simulation, whereas the PS measure does not respond until a certain threshold is reached. This might be due to the local nature of the MT0 method. Further investigation is necessary. Resolving domain growth right at the beginning reveals distinct phases (indicated by distinct slopes) of slower power-law domain growth prior to the domain growth phase that was also found with the previous PS method.

Comparing the MT0 measure to the MT2 measure one can see that the capability of resolution in the beginning domain growth phases is lost (compare Fig. 4). However, when the main domain growth phase is reached the MT2 measure becomes similar to the MT0 measure.

Increasing the tensor rank of the Minkowski analysis and utilizing the MT4 measure we find similar results to the MT2 measure. The most significant difference is, however, the smaller dynamic range (and therefore also sensitivity) of the MT4 domain-size measure (compare Fig. 5). This might be due to the fact that only particle number or volume is required for any domain-size analysis, but the higher-rank MT4 analysis also incorporates anisotropies that are not relevant in this regard. The Minkowski tensor measures contain more

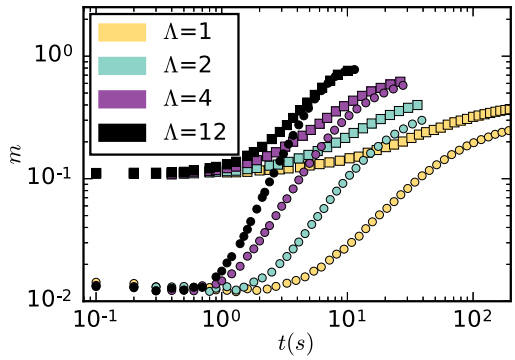

FIG. 5. Growth of the minority domains. Different domain-size measures $m \in \{MT2, MT4\}$ are plotted as they change in time during the demixing simulation. (Details concerning measure and the simulation can be found in Sec. I.) Dots are obtained by the $MT2$ isotropy index method, crosses by the MT4 symmetry metric method. Different colors indicate different screening-length ratios Λ. For increasing values of Λ (corresponding to slower demixing), an increasing difference can be observed in the maximal absolute level between the MT2 and MT4 measure. For better visibility only a subset of all data points are displayed as in Fig. 4.

information that is needed, when calculating back to domain size from higher-rank tensors some of this information is lost.

In conclusion, it was found that increasing the tensor rank of the Minkowski analysis from rank one to rank two and four results in ever-decreasing dynamical range and therefore sensitivity. However, even the rank-four Minkowski tensor method performs better in terms of sensitivity than the previously used linear power-spectrum methods.

B. Difference in demixed domain size

Comparing graphs of the MT2 and MT4 analysis we not only find differences in dynamical range and sensitivity as discussed in the previous chapter but also a difference in the absolute level these measures maximally yield. This might be another hint to the fact that the higher-rank tensor analysis utilizes structural information beyond the mere volume information needed to calculate the domain size. However, it is more likely that this difference is just an artifact due to the simple method of separating the two histogram parts of the MT4 pseudometric Δ via a cutoff value. Using Gaussian mixture methods might be preferable for future calculations with this measure. A cutoff value approach was sufficient for the MT2 isotropy index β since the ordered and disordered parts in the β histogram are much further apart in the demixed state (compare Fig. 2).

C. Hints of universal behavior

Qualitative differences in the demixing behavior for different combinations of long- and short-range interaction can be found by analyzing the local gradients $d = \Delta m/\Delta t$ (Fig. 6) and local power-law scaling behavior $d_{\mathrm{LL}} = \Delta \log(m \times 1s)/\Delta \log(t/1s) = (\Delta m \times t)/(\Delta t \times m)$ (Fig. 7) of Minkowski measures $m \in \{MT0, MT2, MT4\}$. In the unscaled plots (left columns) of Figs. 6 and 7, a qualitatively different behavior between the case $\Lambda = 1$ and the cases

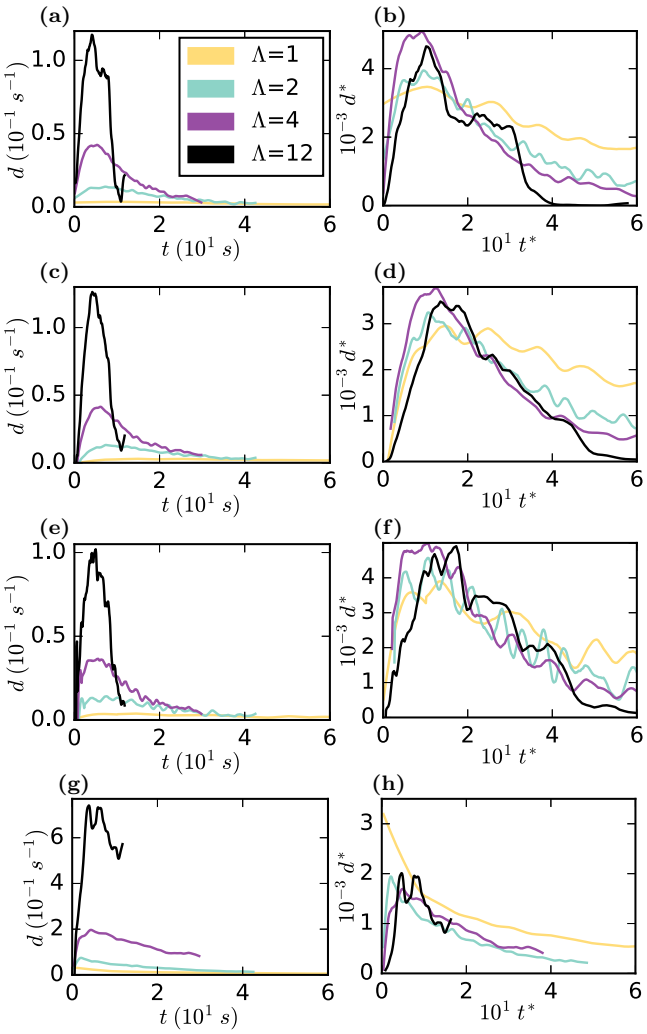

FIG. 6. Left column: local gradients $d = \Delta m/\Delta t$ are plotted against time t. (a) $m = MT0$; (c) $m = MT2$; (e) $m = MT4$; (g) $m = PS$. Right column: Scaled local gradients $d^* = (d \times 1s)^{\Lambda^\mu}$, $\mu \in \mathbb{R}$ are plotted against scaled time $t^* = (t/1s)^{\Lambda^\tau}$, $\tau \in \mathbb{R}$. (b) $m = MT0$, $\mu = 0.37$, $\tau = 0.20$; (d) $m = MT2$, $\mu = 0.405$, $\tau = 0.24$; (f) $m = MT4$, $\mu = 0.34$, $\tau = 0.23$; (h) $m = PS$, $\mu = 0.35$, $\tau = 0.05$. The graphs are obtained by calculating the simple difference quotient $\Delta m/\Delta t$ for every point of the different MT and PS measures. Before and after differentiation the measure data was smoothed using a Savitzky-Golay filter [40] of order 1 and window sizes w depending on the length of the time series ($\Lambda = 1$, $w = 7$; $\Lambda = 2$, $w = 17$; $\Lambda = 4$, $w = 23$; $\Lambda = 12$, $w = 101$). The legend for all panels is identical to panel (a).

$\Lambda = 2, 4, 12$ can be observed: For $\Lambda = 2, 4, 12$ a significant increase and, after reaching a maximum, a significant decline in d and d_{LL} can be observed. However, for $\Lambda = 1$ the local gradients d and local power-law exponents d_{LL} do not show a significant decline after reaching their maximal level and remain almost constant.

This qualitative difference is also evident by considering scaled graphs of d and d_{LL} (right columns of Figs. 6 and 7, respectively). After finding a suitable scaling $\mu \in \mathbb{R}$ for d [in the form $d^* = (d \times 1s)^{\Lambda^\mu}$] and a timescale factor $\tau \in \mathbb{R}$

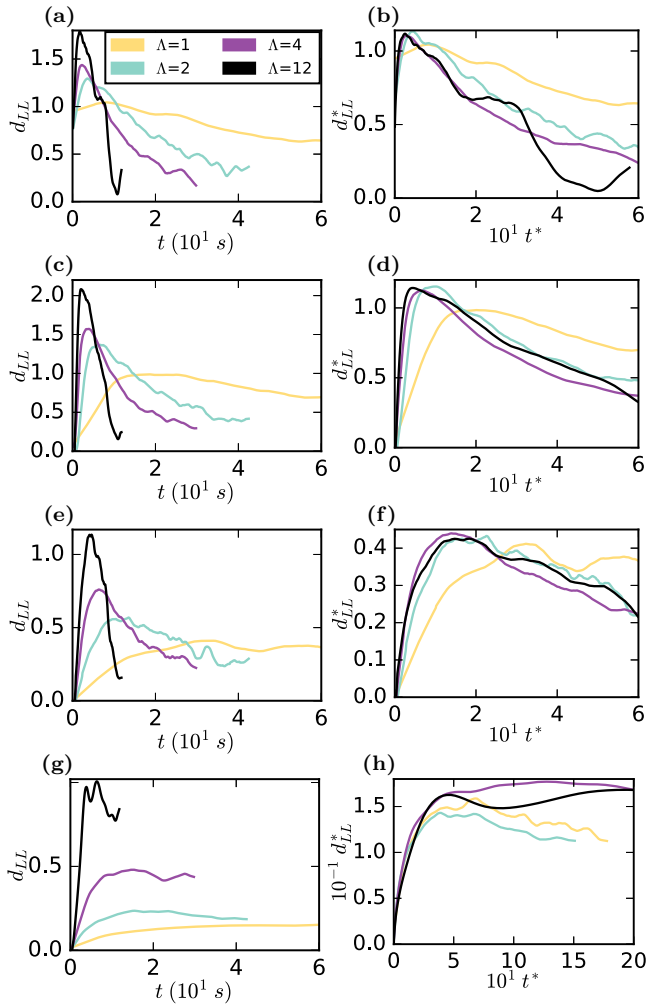

FIG. 7. Left column: local power-law exponents $d_{\mathrm{LL}} = \Delta\log(m \times 1s)/\Delta\log(t/1s)$ are plotted against time t. (a) $m = MT0$; (c) $m = MT2$; (e) $m = MT4$; (g) $m = PS$. Right column: Scaled local gradients $d^*_{\mathrm{LL}} = d_{\mathrm{LL}}/\Lambda^{\nu}$, $\nu \in \mathbb{R}$ are plotted against scaled time $t^* = (t/1s)^{\Lambda^{\rho}}$, $\rho \in \mathbb{R}$. (b) $m = MT0$, $\nu = 0.19$, $\rho = 0.20$; (d) $m = MT2$, $\nu = 0.24$, $\rho = 0.26$; (f) $m = MT4$, $\nu = 0.495$, $\rho = 0.26$; (h) $m = PS$, $\nu = 0.78$, $\rho = 0.25$. The graphs for the different MT and PS measures are obtained by calculating $(\Delta m \times t)/(\Delta t \times m)$ for every point, which is equivalent to the simple difference quotient $\Delta\log(m \times 1s)/\Delta\log(t/1s)$. Smoothing was done as described in the legend of Fig. 6. The legend for all panels is identical to panel (a).

for $t[t^* = (t/1s)^{\Lambda^{\tau}}]$ the curves $d^*(t^*)$ tend to collapse onto one curve for the cases with $\Lambda \neq 1$. The scaled curves for $\Lambda = 1$, however, do not follow the same behavior: the scaled local gradient curves $d^*(t^*)$ for $\Lambda = 1$ do not reach a maximal level comparable to the cases $\Lambda = 2, 4, 12$ and also decline much slower after reaching their maximal value. The same procedure is applicable to the local power-law scaling exponent d_{LL}: By using the scaling $d^*_{\mathrm{LL}} = d_{\mathrm{LL}}/\Lambda^{\nu}$, $\nu \in \mathbb{R}$ and $t^* = (t/1s)^{\Lambda^{\rho}}$, $\rho \in \mathbb{R}$ the curves $d^*_{\mathrm{LL}}(t^*)$ tend to collapse onto one curve for cases $\Lambda \neq 1$. The scaled local power-law exponent curves $d^*_{\mathrm{LL}}(t^*)$ for $\Lambda = 1$ reach their maximal level at later times (for MT2 and MT4 analysis) compared to the cases $\Lambda = 2, 4, 12$ and also decline slower after reaching their maximal value.

This qualitatively different demixing behavior can also be observed in the data of particle position of detected demixed domains when compared during common scaled times t^* as in Fig. 8 (or in the Supplemental Material movies in the online version of this paper [41]).

In the long-range dominated cases ($\Lambda = 2, 4, 12$) demixing seems to occur in two stages: at first neighboring particles agglomerate (scaled times $t^* \lesssim 10$, before gradient or power-law exponent reaches maximal value) then the agglomerated domains start to merge in cascades at scaled times $t^* \sim 10$ when the gradient or power-law exponent of the Minkowski measures reach their maximal level. When the domains start to merge, after the agglomeration phase, the number of demixed particles is only growing slowly and correspondingly the graphs of gradient and power-law exponent start to decay. In this cascade phase the main demixing mechanism is the merging of already demixed domains. The higher the screening length ratio is, the more cascades are happening and the larger are the resulting domains. For the screening length ratio $\Lambda = 1$, however, there is only agglomeration and no cascades are happening in which these agglomerated domains merge explaining the qualitatively different behavior of gradient and power-law exponent curves in Figs. 6 and 7.

As illustrated in Fig. 9 the quotient of the difference quotients of the Minkowski measures and the PS measure is not constant and thus provides new information about the demixing behavior. For $\Lambda > 1$ the graphs are rising until they reach a maximal value and then decline again. For the MT0 and MT4 measure there is an additional peak right at the beginning for $\Lambda = 12$. Discarding this additional peak, the times when the maximal value is reached correspond approximately to the $t^* = 15$, the time where the demixing changes from only agglomeration to the merging cascade dominated regime. This is plausible since the Minkowski measures are measuring the total volume of demixed regimes, whereas the PS measure measures the mean length scale of demixed regimes: when the merging cascade phase begins, the length scale of domains increases much faster compared to the agglomeration phase. However, the total volume still only increases due to residual agglomeration and does not change due to merging of already demixed domains.

For $\Lambda = 1$ the graphs are increasing in the beginning, however, they do not decline after reaching their maximal value but stay approximately constant again indicating a qualitatively different behavior. Note that the quotient of local power-law scaling exponents is reminiscent to the box counting dimension [42] (also known as MinkowskiBouligand dimension) as defined in fractal geometry due to the fact that it is equivalent to the quotient $\log(V)/\log(L)$ if self similar growth of domains is assumed. Since here L is the mean domain size and not the box size, the quotient of local power-law exponents is not the same as the box counting dimension. Similar behavior to the behavior of the quotient of gradients is found for the quotient of local power-law exponents (Fig. 10). Additionally, one can conclude that the MT0 measure has a much higher local power-law exponent at the onset of demixing. This higher sensitivity will be advantageous for future studies of the onset of the demixing process.

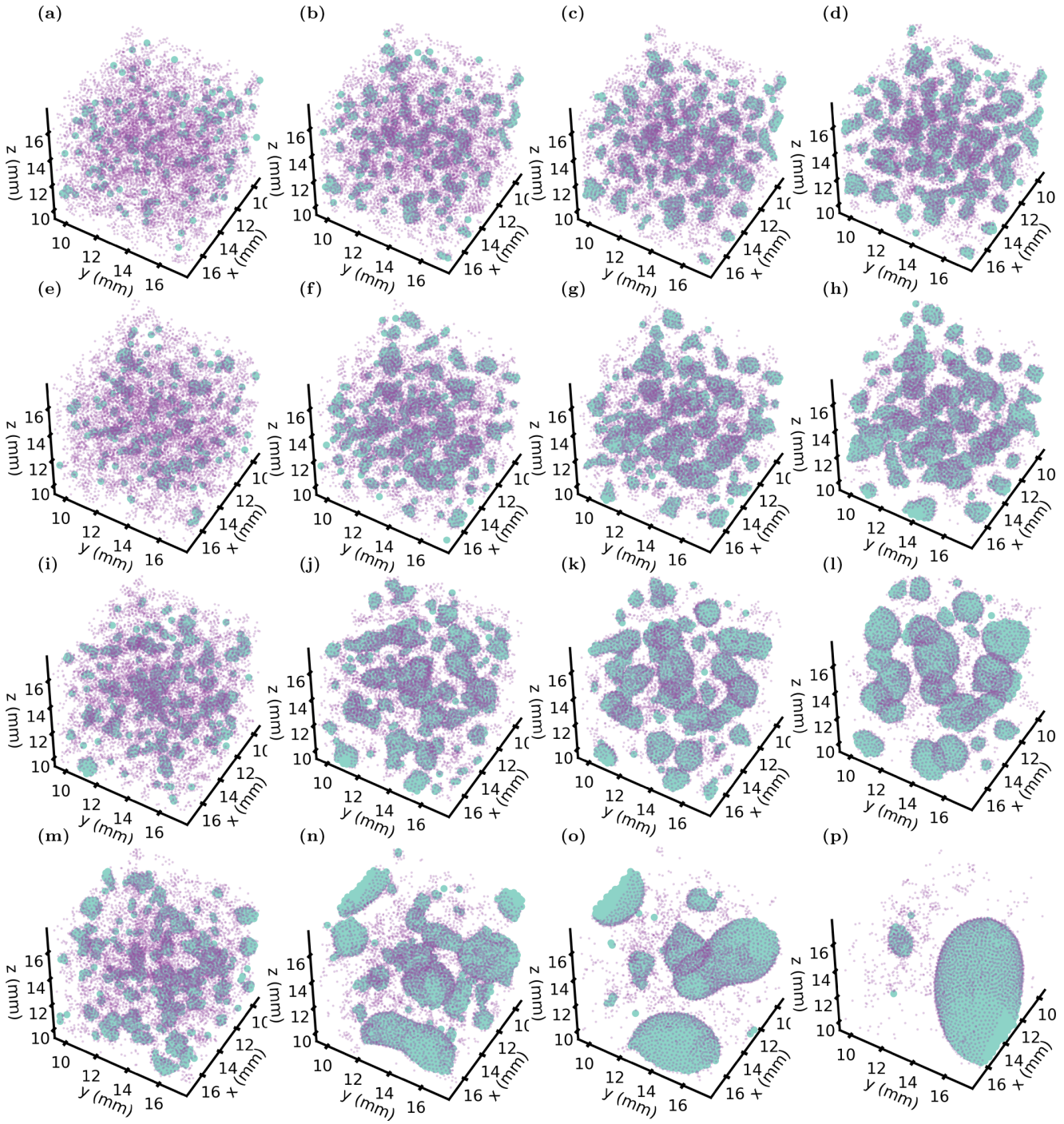

FIG. 8. Particles of the minority phase (species 1) detected by the MT2 analysis as contributions to demixed domains are color coded in turquoise, the remaining species 1 particles are color coded in violet and are smaller in size. To assure visibility of the demixing process the particles of species 2 are not shown. They are homogeneously dispersed around the particles of species 1. The rows indicate different screening-length ratios (The first row corresponds to $\Lambda = 1$, the second row to $\Lambda = 2$, the third row to $\Lambda = 4$, and the fourth row to $\Lambda = 12$). The first column corresponds to the scaled time $t^* = 5$ (corresponding to the agglomeration phase), the second column to $t^* = 15$ (agglomeration phase finished for $\Lambda = 2, 4, 12$ and first merging cascade processes begin), the third column to $t^* = 25$ (early merging cascades for $\Lambda = 2, 4, 12$ finished), and the fourth column to $t^* = 50$. (end stages of merging cascades for for $\Lambda = 2, 4, 12$). The case $\Lambda = 1$ is qualitatively different: Only agglomeration but no merging cascades of demixed domains can be observed. The scaled times given here are mean values of the different scaling times provided in Figs. 6 and 7. These illustrations can be viewed as video files in the Supplemental Material of the online version of this paper [41].

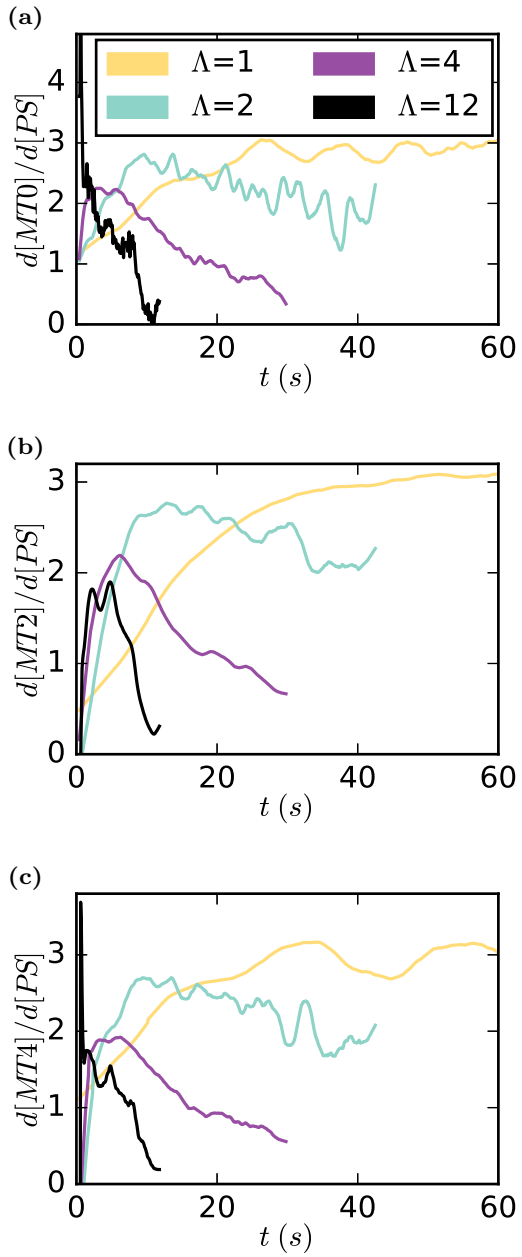

FIG. 9. Quotient of difference quotients d of Minkowski measures m and the PS measure. (a) $m = MT0$; (b) $m = MT2$; (c) $m = MT4$. Calculation and smoothing was done as described in the legend of Fig. 6.

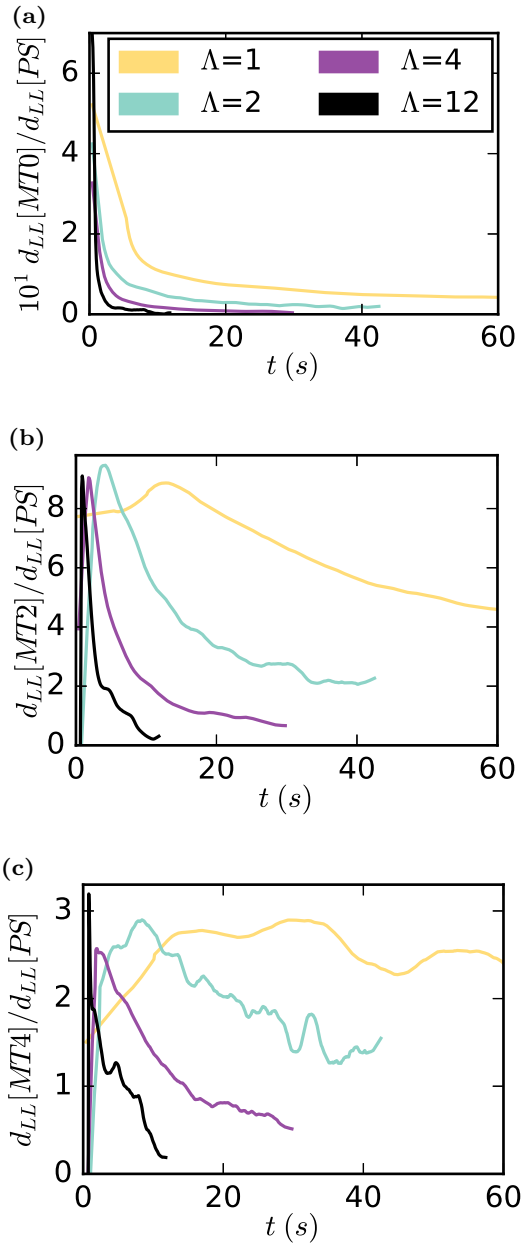

FIG. 10. Quotient of local power-law exponents d_{LL} of Minkowski measures m and the PS measure. (a) $m = MT0$; (b) $m = MT2$; (c) $m = MT4$. Calculation and smoothing was done as described in the legend of Fig. 7.

V. CONCLUSION AND OUTLOOK

Minkowski Tensor methods are a powerful tool for morphological characterization and analysis. They can be superior to methods only utilizing the linear PS since they are inherently sensitive to nonlinear properties. They exhibit a higher sensitivity to changes in domain size and the measures exhibit a larger dynamical range. However, utilizing the potential of higher-rank tensors might not always prove to be worthwhile if not all the symmetry information they provide is needed. In this study, employing rank-four tensors proved to be unnecessary in order to obtain simple domain-size information.

Employing Minkowski tensor methods reveals two qualitatively different demixing scenarios for simulations employing interactions with only one length scale ($\Lambda = 1$) and different length scales ($\Lambda = 2, 4, 12$), which power-spectrum analysis was not able to detect. Demixing occurs even for small screening-length ratios $\Lambda = 1$. However, it is not only slower compared to long-range dominated ($\Lambda = 2, 4, 12$) regimes but also shows qualitatively different behavior. In the long-range dominated cases ($\Lambda = 2, 4, 12$) demixing seems to occur in two stages: at first neighboring particles agglomerate then the agglomerated domains start to merge in cascades. In this cascade phase the main demixing mechanism is merging of

already demixed domains. The higher the screening-length ratio is, the more cascades are happening and the larger are the resulting domains. For the screening-length ratio $\Lambda = 1$, however, there is only agglomeration and no cascades are happening in which these agglomerated domains merge. This is also evidenced by the universal behavior of domain-size measures based on Minkowski functionals and tensors. Further study of the universality is necessary. Future studies will try to concretise the hints of universal behavior and qualitative differences for different screening length ratios. The questions as to how the transition between qualitatively different demixing behavior depends on other values for the screening-length ratio, and how this transition occurs, can be answered by means of more extensive simulations. More extensive simulations can also be used to investigate the effects of demixing in not perfectly monodisperse complex plasmas and how strongly demixing effects depend on the particle size distribution.

It might be beneficial to further investigate the onset of this process. There, the discreteness effects play an essential role and might require separate particle-resolved studies focused on the comparison with the results of the coarse-grained approach used in the simulations that provided data for this study [6]. As demonstrated in this study, morphological Minkowski tensor analysis could be superior to PS methods in the investigation of the onset of demixing. The (linear) scaling behavior for the domain growth of a binary Lennard-Jones (LJ) liquid is well known [4]. To further test the efficiency of the Minkowski tensor analysis methods and to shed new light on demixing processes in systems with LJ-like interactions we will apply MT analysis to these classical systems as well. The demixing process of binary complex plasmas is a subject of current scientific interest: only recently new experimental evidence gained via means of new visualization techniques, based on the use of fluorescent dust particles, was published [43]. A clear trend toward phase separation even for smallest-size (charge) disparities was observed. Further research in this direction can benefit from Minkowski tensor analysis as presented here since it is sensitive to nonlinear properties and capable of quickly revealing new aspects of interest in data. Minkowski tensor analysis is probing deeper than linear power-spectrum analysis, however, still providing easily interpretable results founded on a solid mathematical framework.

ACKNOWLEDGMENTS

We thank Adam Wysocki for providing the simulation data. The free software Qhull [44] was used to compute the Voronoi tesselation. Qhull uses the Quickhull algorithm for computing the convex hull. Some Minkowski tensors are calculated based on code of the free software package Karambola [45].

[1] A. J. Bray, Adv. Phys. **51**, 481 (2002).
[2] D. G. A. L. Aarts, R. P. A. Dullens, and H. N. W. Lekkerkerker, New J. Phys. **7**, 40 (2005).
[3] A. E. Bailey, W. C. K. Poon, R. J. Christianson, A. B. Schofield, U. Gasser, V. Prasad, S. Manley, P. N. Segre, L. Cipelletti, W. V. Meyer, M. P. Doherty, S. Sankaran, A. L. Jankovsky, W. L. Shiley, J. P. Bowen, J. C. Eggers, C. Kurta, T. Lorik, P. N. Pusey, and D. A. Weitz, Phys. Rev. Lett. **99**, 205701 (2007).
[4] A. K. Thakre, W. K. den Otter, and W. J. Briels, Phys. Rev. E **77**, 011503 (2008).
[5] K. Jiang, L.-J. Hou, A. V. Ivlev, Y.-F. Li, C.-R. Du, H. M. Thomas, G. E. Morfill, and K. R. Sütterlin, Europhys. Lett. **93**, 55001 (2011).
[6] A. Wysocki, C. Räth, A. V. Ivlev, K. R. Sütterlin, H. M. Thomas, S. Khrapak, S. Zhdanov, V. E. Fortov, A. M. Lipaev, V. I. Molotkov, O. F. Petrov, H. Löwen, and G. E. Morfill, Phys. Rev. Lett. **105**, 045001 (2010).
[7] S. N. Weber, C. A. Weber, and E. Frey, Phys. Rev. Lett. **116**, 058301 (2016).
[8] S. Michael and A. David, Science **267**, 476 (1995).
[9] A. Stradner, H. Sedgwick, F. Cardinaux, W. C. K. Poon, S. U. Egelhaaf, and P. Schurtenberger, Nature **432**, 492 (2004).
[10] C. Sagui and R. C. Desai, Phys. Rev. E **49**, 2225 (1994).
[11] K.-O. Ng and D. Vanderbilt, Phys. Rev. B **52**, 2177 (1995).
[12] C. P. Royall, D. G. A. L. Aarts, and H. Tanaka, J. Phys.: Condens. Matter **17**, S3401 (2005).
[13] V. E. Fortov, A. V. Ivlev, S. A. Khrapak, A. G. Khrapak, and G. E. Morfill, Phys. Rep. **421**, 1 (2005).
[14] G. E. Morfill and A. V. Ivlev, Rev. Mod. Phys. **81**, 1353 (2009).
[15] A. V. Ivlev, S. K. Zhdanov, H. M. Thomas, and G. E. Morfill, Europhys. Lett. **85**, 45001 (2009).
[16] S. A. Khrapak, B. A. Klumov, and G. E. Morfill, Phys. Rev. Lett. **100**, 225003 (2008).
[17] S. A. Khrapak, A. V. Ivlev, and G. E. Morfill, Phys. Plasmas **17**, 042107 (2010).
[18] H. M. Thomas, G. E. Morfill, V. E. Fortov, A. V. Ivlev, V. I. Molotkov, A. M. Lipaev, T. Hagl, H. Rothermel, S. A. Khrapak, R. K. Sütterlin, M. Rubin-Zuzic, O. F. Petrov, V. I. Tokarev, and S. K. Krikalev, New J. Phys. **10**, 033036 (2008).
[19] H. Minkowski, Math. Ann. **57**, 447 (1903).
[20] S. Alesker, Geometriae Dedicata **74**, 241 (1999).
[21] P. J. Steinhardt, D. R. Nelson, and M. Ronchetti, Phys. Rev. B **28**, 784 (1983).
[22] T. Aste, Phys. Rev. Lett. **96**, 018002 (2006).
[23] T. Aste, T. D. Matteo, M. Saadatfar, T. J. Senden, M. Schröter, and H. L. Swinney, Europhys. Lett. **79**, 24003 (2007).
[24] T. Aste and T. Di Matteo, Phys. Rev. E **77**, 021309 (2008).
[25] S.-C. Zhao, S. Sidle, H. L. Swinney, and M. Schröter, Europhys. Lett. **97**, 34004 (2012).
[26] S. Slotterback, M. Toiya, L. Goff, J. F. Douglas, and W. Losert, Phys. Rev. Lett. **101**, 258001 (2008).
[27] G. E. Schröder-Turk, W. Mickel, M. Schröter, G. W. Delaney, M. Saadatfar, T. J. Senden, K. Mecke, and T. Aste, Europhys. Lett. **90**, 34001 (2010).
[28] S. C. Kapfer, W. Mickel, F. M. Schaller, M. Spanner, C. Goll, T. Nogawa, N. Ito, K. Mecke, and G. E. Schröder-Turk, J. Stat. Mech. Theo Exp. (2010) P11010.
[29] S. C. Kapfer, W. Mickel, K. Mecke, and G. E. Schröder-Turk, Phys. Rev. E **85**, 030301 (2012).

[30] G. E. Schröder-Turk, R. Schielein, S. C. Kapfer, F. M. Schaller, G. W. Delaney, T. Senden, M. Saadatfar, T. Aste, and K. Mecke, AIP Conf. Proc. **1542**, 349 (2013).
[31] W. Helfrich, Z. Naturforsch. **28c**, 693 (1973).
[32] K. R. Mecke, Phys. Rev. E **53**, 4794 (1996).
[33] Y. Rosenfeld, Mol. Phys. **86**, 637 (1995).
[34] K. Mecke, in *Statistical Physics and Spatial Statistics*, edited by D. S. K. R. Mecke, Lecture Notes in Physics Vol. 554 (Springer, Berlin/Heidelberg, 2000), pp. 111–184.
[35] M. Kerscher, in *Statistical Physics and Spatial Statistics*, edited by D. S. K. R. Mecke, Lecture Notes in Physics Vol. 554 (Springer, Berlin/Heidelberg, 2000), pp. 36–71.
[36] G. E. Schröder-Turk, W. Mickel, S. C. Kapfer, F. M. Schaller, B. Breidenbach, D. Hug, and K. Mecke, New J. Phys. **15**, 083028 (2013).
[37] L. J. Walpole, J. Phys. D Appl. Phys. **19**, 457 (1986).
[38] M. Mehrabadi and C. C. Stephen, Quart. J. Mech. Appl. Math. **43**, 15 (1990).
[39] H. Furukawa, Physica A: Stat. Mech. Appl. **123**, 497 (1984).
[40] A. Savitzky and M. J. E. Golay, Anal. Chem. **36**, 1627 (1964).
[41] See Supplemental Material at http://link.aps.org/supplemental/10.1103/PhysRevE.94.013201 for movies S1–S4.
[42] B. B. Mandelbrot, *The Fractal Geometry of Nature*, 1st ed. (W.H. Freeman, London, 1982).
[43] C. Killer, T. Bockwoldt, S. Schütt, M. Himpel, A. Melzer, and A. Piel, Phys. Rev. Lett. **116**, 115002 (2016).
[44] http://www.qhull.org/.
[45] http://theorie1.physik.uni-erlangen.de/research/karambola/.

D.3 Fluid demixing kinetics on spherical geometry: Power spectrum and Minkowski functional analysis

Fluid demixing kinetics on spherical geometry: Power spectrum and Minkowski functional analysis

A. Böbel, M. C. Bott, H. Modest, J. M. Brader and C. Räth, submitted to the *New Journal of Physics*

Fluid demixing kinetics on spherical geometry: Power spectrum and Minkowski functional analysis

A. Böbel[1], M. C. Bott[2], H. Modest[1], J. M. Brader[2], C. Räth[1]

[1]Institut für Materialphysik im Weltraum, Deutsches Zentrum für Luft- und Raumfahrt (DLR), Münchener Str. 20, 82234 Weßling
[2]Soft Matter Theory, University of Fribourg, Switzerland

E-mail: alexander.boebel@dlr.de

Abstract. Dynamic density functional theory (DDFT) calculations of fluid-fluid demixing on spherical geometries are characterized via their angular power spectrum as well as via the Minkowski functionals of their binarized fluid density fields. Minkowski functionals form a complete set of additive, motion invariant and continuous morphological measures sensitive to nonlinear (spatial) correlations. The temporal evolution of the fluid density fields is analysed for different sphere sizes and mixing compositions. The demixing process in the stages of early spinodal decomposition and consecutive domain growth can be characterized by both methods and a power-law domain growth $L(t) \propto t^{\alpha}$ is evidenced for the Minkowski functional measures. The average domain size obtained by the structure factor only responds to the late stage domain growth of the demixing process. Minkowski functionals provide refined insights into the demixing process: They allow the detection of distinct stages in the early spinodal decomposition, provide a precise measure of the relative species composition of the mixture and, most importantly: After a proper rescaling, they allow the detection of a universal demixing behavior for a wide range of mixture fractions and for different sphere sizes.

Keywords: Article preparation, IOP journals Submitted to: *New J. Phys.*

1. Introduction

If a binary fluid mixture is in the immiscible state it will start to dynamically demix in order to reach the thermodynamically stable state of two coexisting phases. This phase separation can be split in two consecutive regimes [1, 2, 3]: The spinodal decomposition in the early stage, followed by the domain growth stage. During spinodal decomposition fluid density fluctuations increase exponentially and neighboring particles agglomerate to form disjoint domains. In the domain growth stage the size of these initial domains increases further and they start to coalesce with neighboring domains in order to reduce the energy costs of the interface areas. As the domain morphology is preserved, this

domain growth is self-similar in time. The self-similarity implies a time-dependent characteristic length of the mean domain size that can be described by a power-law growth $L(t) \propto t^{\alpha}$.

When the system is spatially confined, the phase separation kinetics are less well understood. Spatial confinement can be imposed by obstacles and external fields [4, 5]. Another form of spatial confinement can be achieved via the geometry of space itself [6]. Recently, the study of statistical physics processes on curved surfaces, in particular on the sphere, has attracted growing interest and showed the richness of physical phenomena that are influenced by their embedding on non-flat geometries. The crystallization of a colloidal suspension on a sphere was explained via a icosahedrically symmetric order parameter that revealed the long-range order of the crystal on the curved surface [7]. The projection of inhomogeneous crystals onto homogeneous ones on curved surfaces enabled the prediction of defect distributions [8]. Also, unusual emergent structures due to advection were demonstrated on a spherical geometry [9].

Common methods for the characterization of demixing dynamics are based on linear measures: The mean domain size is measured via the first zero crossing of the radial correlation function or equivalently via the first maximum of the power spectral structure factor [10, 11, 12]. However, this method is computationally expensive [13]. Another drawback lies in the linearity of the method. The mean domain size is not a sufficient descriptor of the domain morphology [14, 15, 3]. Thus, it is beneficial to extend the description of the demixing system to morphological measures, which are sensitive to higher order correlations.

Morphological measures that capture the complete nonlinear structural information of a system are the Minkowski functionals [16]. They became a prominent tool for morphological data analysis since they form a complete family of structural descriptors sensitive to nonlinear properties. Minkowski functionals are well suited for the investigation of demixing processes [3, 15, 14] and can readily be applied on spherical geometry [17, 18, 19]. In two-dimensional flat and curved spaces the Minkowski functionals are easily interpretable measures connected to concepts as area, perimeter and the Euler characteristic. The Euler characteristic is a measure for the connectivity of a spatial structure.

In this work we aim to systematically study the properties of dynamic density functional theory calculations (DDFT) of fluid demixing on a spherical geometry with both linear and nonlinear measures. The DDFT calculations were already utilized as the basis for the studies in [6] and are reused here as a convenient starting point for the first ever Minkowski functional analysis of fluid-fluid demixing on spherical geometries. Initially we apply the conventional linear method known in the flat space case to the spherical data: We calculate the angular power spectral density and fit it to a general structure factor function in order to calculate the average domain size L. These results are then compared with the Minkowski functional measures.

This paper is structured as follows: In Section 2 we explain the methods and results for the calculation of the phase separation dynamics on the spherical body.

Section 3 describes the method of the structure factor calculation based on the angular power spectral density and the implementation of the Minkowski functional calculation. The results of power spectral density and Minkowski functional analysis for DDFT calculations with different sphere sizes and mixture parameters are presented in section 4. Finally, in section 5 results are discussed and conclusions drawn.

2. Dynamic density-functional theory calculations

This section is intended to give a brief overview of the methods and results found about phase separation on a large spherical particle [6]. The data for the evolution of the density distribution during spinodal decomposition forms the basis for the Minkowski functional analysis discussed in this manuscript.

In order to avoid any confusion with terminology, we will henceforth refer to the large particle as the 'meso-particle' and the smaller, mobile particles constituting the fluid on its surface as the 'surface particles'.

2.1. The Gaussian Core Model

To represent the surface particles, we consider a model binary mixture, thus two particle species, in which the particles interact via the soft repulsive pair potential

$$\beta v_{ij}(r) = \beta\epsilon_{ij}\exp\{-r^2/R_{ij}^2\}. \tag{1}$$

Here the non-negative parameters ϵ_{ij}, R_{ij} and $\beta=(k_BT)^{-1}$ determine the strength and range, respectively, of the interaction between species i and j. The Gaussian core model (GCM) was introduced by Stillinger [20] to study phase separation in binary mixtures and has since been studied intensively, both in bulk and at interfaces [21]. The model has the advantage that a simple mean-field approximation to the free energy provides good agreement with computer simulation data [22] and is therefore straight forward to incorporate in a density functional theory.

2.2. Mean-field free energy functional

To describe the collective behavior of the surface particles we use an approximation to the two-dimensional Helmholtz free energy functional

$$\begin{aligned}\beta\mathcal{F}[\{\rho_i(\mathbf{r})\}] = &\sum_i \int d\mathbf{r}\rho_i(\mathbf{r})\big(\ln(\rho_i(\mathbf{r})) - 1\big) \\ &+ \frac{1}{2}\sum_{ij}\int d\mathbf{r}\int d\mathbf{r}'\rho_i(\mathbf{r})\rho_j(\mathbf{r}')\beta v_{ij}(|\mathbf{r}-\mathbf{r}'|),\end{aligned} \tag{2}$$

where the first and second terms provide the ideal and excess (over ideal, describing the particle interactions) contributions, respectively. The subscripts i and j are species labels and the notation $[\{\rho_i(\mathbf{r})\}]$ indicates a functional dependence on the one-body

density profiles of all species. We set the (physically irrelevant) thermal wavelength λ equal to unity. For a binary mixture the species indicies are restricted to the values $i, j = 1, 2$. In bulk, the number density of species i is $\rho_i = N_i/V$, where V is the area in the 2d case and N_i the number of particles of species i. The total density is of the surface particles $\rho = \rho_1 + \rho_2$.

It is convenient to introduce a concentration variable, the mixture parameter $x = N_2/N$, with the total number of particles N. This enables the species labeled densities to be expressed as $\rho_1 = (1-x)\rho$ and $\rho_2 = x\rho$. In these variables the bulk free energy per particle consists of a sum of two terms, $f \equiv F/N = f_{\rm id} + f_{\rm ex}$. The ideal part is given by

$$\beta f_{\rm id} = \ln(\rho) - 1 + (1-x)\ln(1-x) + x\ln(x), \tag{3}$$

and the reduced bulk excess free energy per particle can be written as

$$\beta f_{\rm ex} = \frac{1}{2\rho}\big(\rho_1\rho_1\hat{v}_{11} + 2\rho_1\rho_2\hat{v}_{12} + \rho_2\rho_2\hat{v}_{22}\big). \tag{4}$$

where $\hat{v}_{ij} = \epsilon^*_{ij} R^2_{ij}\pi$ and $\epsilon^*_{ij} = \beta\epsilon_{ij}$. In [6] the parameters $R_{11} = R_{22} = R_{12} = 1$, $\epsilon^*_{11} = \epsilon^*_{22} = 2$ and $\epsilon^*_{12} = 1.035\epsilon^*_{11}$ were chosen and the phase diagram for an infinite planar system has been calculated. This phase diagram is shown in Fig. 1 and indicates the five states that will be analyzed in this study for a large $R = 10R_{11}$, respectively a small $R = 2.5R_{11}$ sphere. Even though the mesosphere represents a finite size system the phase diagram for the bulk system offers a useful guide. When the total density ρ becomes sufficiently large the GCM demixes.

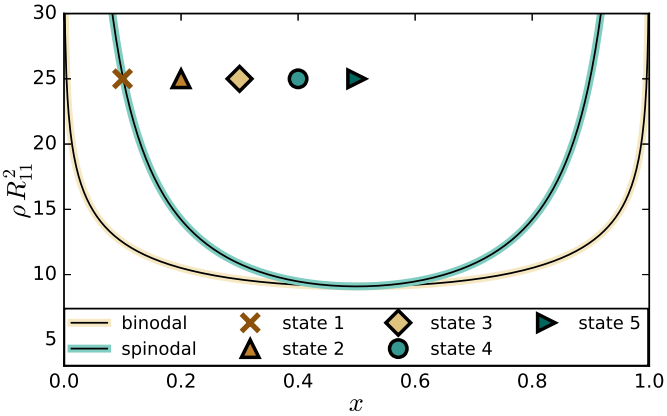

Figure 1. Phase diagram for the planar system as a reference point. Binodal and spinodal curves, as well as the states analyzed in this study are indicated. The states are $x \in \{0.1, 0.2, 0.3, 0.4, 0.5\}$ for $\rho R^2_{11} = 25$. Parameters are $R_{11} = R_{22} = R_{12} = 1$, $\epsilon^*_{11} = \epsilon^*_{22} = 1$, $\epsilon^*_{12} = 1.035\epsilon^*_{11}$. The critical point is found at $\rho R^2_{11} = 9.094568$ and $x = 0.5$.

2.3. Dynamical density-functional theory and numerical implementation

To study phase separation on the surface of a meso-particle we will focus on the dynamics of the one-body density of the surface particles. This can be obtained using dynamical density functional theory (DDFT) [23, 24]. Within this approach the time evolution of the density of species i is given by a

$$\gamma^{-1}\frac{\partial\rho_i(\mathbf{r},t)}{\partial t} = \frac{\partial}{\partial\mathbf{r}}\cdot\left[\rho_i(\mathbf{r},t)\frac{\partial}{\partial\mathbf{r}}\frac{\delta\mathcal{F}[\{\rho_i(\mathbf{r},t)\}]}{\delta\rho_i(\mathbf{r},t)}\right]. \tag{5}$$

Here γ is the mobility and it is related to the diffusion coefficients D as $\gamma = \beta D$. The DDFT equation of motion (5) is a generalized diffusion equation. The one-body density is driven by gradients in the local chemical potential which arise from the particle interaction described by the functional for the free energy (2). If we insert the functional of the ideal gas, we recover the well known diffusion equation for a non interacting gas.

To solve the DDFT equation of motion (5) on the surface of a meso-sphere we chose to parametrize the sphere using the spherical polar angles θ and ϕ. With this approach we have an accurate finite-difference scheme for calculating the gradient and divergence of scalar- and vector fields. In addition we make use of the convolution theorem on the unit-sphere [25, 6] to efficiently compute the convolution of two scalar fields in the space of spherical harmonic functions. The numerical methods for solving equation 5 on the surface of a sphere are described in more detail in reference [6].

2.4. DDFT calculation Results

For larger meso-sphere radii ($R = 10R_{11}$) we find standard spinodal decomposition dynamics for an equal mixture, $x = 0.5$, leading to a 'half-half' final state. As the value of x is reduced towards the spinodal, then the phase separation dynamics are given by the Ostwald ripening scenario [26], where islands of the minority phase form, which then slowly merge together (see Fig. 2). For the phase separation on the smaller meso-particle ($R = 2.5R_{11}$) finite-size effects become more important. In contrast to the behavior on the larger meso-sphere, the density evolves here in most cases into a 'band' state, where two islands with species 1 form, separated by a band of species 2 particles. This state is stable over a long time. The smaller we chose the mixture parameter x the longer the metastable band state lives. This enhanced stability of the band structure can be attributed to the fact that the distance between the interfaces increases as the surface coverage of the minority phase is reduced by reducing x. In the following analyses we only consider one of the species and call its density field $\rho_2(\mathbf{r},t^*) \equiv \rho(\mathbf{r},t^*)$. Since their contributions are mirror images their information content is redundant. t^* is the dimensionless time given by $t^* = tD/R_{11}^2$, where D is the bare diffusion coefficient.

Movies for all DDFT calculations are provided in the supplemental material at [27].

2.5. Equal Area Pixelisation

Using the python library healpy [28] for HEALPix the spherical coordinate grid ($181 \cdot 92 = 16652$ pixel) was interpolated on a equal area pixel grid with $N_{pix} = 12288$ pixel in order to apply the Minkowski functional analysis straightforwardly. The HEALPix pixelisation scheme is a partition of a spherical surface into exactly equal area quadrilateral pixels of varying shape [29] but uniform area A_{pix}. The pixel size depends on the HEALPix resolution parameter of the grid equal to $N_{\text{side}} = 1, 2, 4, 8, ...$ corresponding to a total number of pixels of $N_{\text{pix}} = 12 \times N_{\text{side}}^2 = 12, 48, 192, 768, ...$ In this work we use a resolution parameter of $N_{\text{side}} = 32$, since this is the closest match to the raw data in the spherical coordinate grid. In further studies much higher resolutions can be obtained. In Fig. 2 the pixelization of the density fields $\rho(\mathbf{r}, t^*)$ is shown for both sphere sizes during the evolution of time t^*.

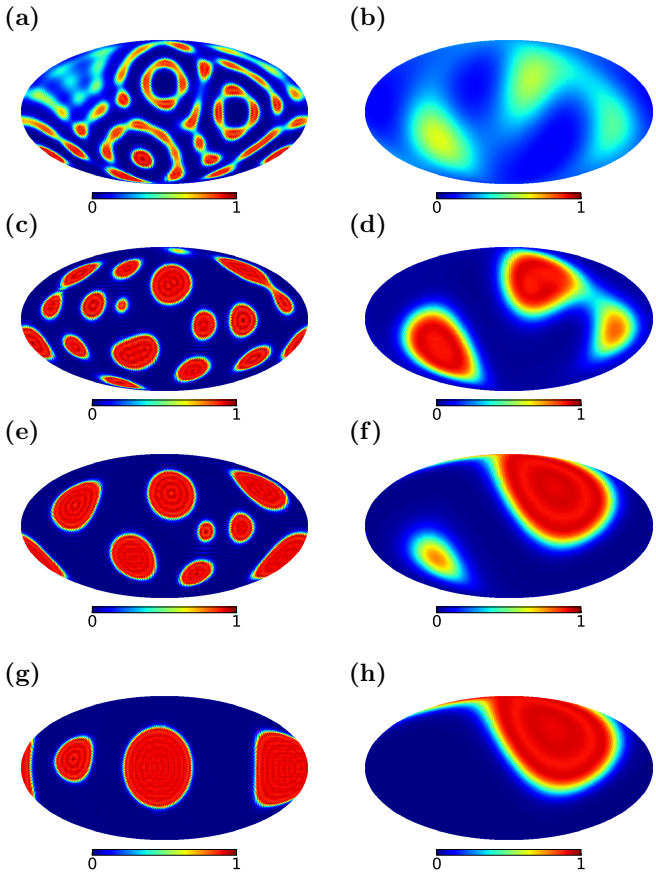

Figure 2. Mollweide projection of equal area pixelisation for the DDFT calculation data for $x = 0.3$. Left column: (a)-(c)-(e)-(g) Evolution of the particle density $\rho_2(\mathbf{r}, t^*)$ of species two for the large sphere $R = 10R_{11}$. Right column: (b)-(d)-(f)-(h) Evolution of the particle density for the small sphere $R = 2.5R_{11}$.

3. Spatial statistics

3.1. Angular power spectral density

Any scalar function $\rho(\mathbf{n})$ on a spherical geometry, where $\mathbf{n}(\theta, \phi)$ is a direction on the sphere, can be decomposed into its spherical harmonics representation. The spherical harmonics Y_{lm} form an orthonormal base on the unit sphere. They are given by:

$$Y_{lm} = \sqrt{\frac{2l+1}{4\pi}\frac{(l-m)!}{(l+m)!}} P_l^m(\cos(\theta))e^{im\phi} \tag{6}$$

With indices $l \in \mathcal{N}$ and $-l \leq m \leq l$. P_l^m are the Legendre polynomials. l is the multipole. The average solid angle Ω corresponding to a specific l is $\Omega = 4\pi/2l$. Considering the division of the sphere in $2l$ equal slices, the widest part of these slices corresponds to an angle $\gamma = \pi/l$. This translates into a length scale $L = R \cdot \pi/l$, with the sphere radius R.

Then $\rho(\mathbf{n})$ can be expanded as:

$$\rho(\mathbf{n}) = \sum_{l \geq 0} \sum_{|m| \leq l} a_{lm} Y_{lm}(\mathbf{n}), \tag{7}$$

with harmonic coefficients a_{lm} given by the projection

$$a_{lm} = \int \mathrm{d}\Omega \; \rho(\mathbf{n}) Y_{lm}^*(\mathbf{n}). \tag{8}$$

$\circ^*$ denotes the complex conjugate of $\circ$. The power spectrum C_l of the scalar field $\rho(\mathbf{n})$ can be defined as the variance of the harmonic coefficients $\langle a_{lm} a_{l'm'}^* \rangle = \delta_{ll'}\delta_{mm'}C_l$ with

$$C_l = \frac{1}{2l+1} \sum_{|m| \leq l} \langle |a_{lm}|^2 \rangle. \tag{9}$$

The C_l are called the angular power spectral density. Since for any l there exist $2l+1$ modes of m the total power for the multipole l is given by $(2l+1) \cdot C_l$.

In the following we analyze the position $l_{\max}$ and value $C_{l,\max}$ of the maximum of the power spectral density. $l_{\max}$ is a measure for the length scale of the most dominant pattern. This quantity is the standard metric to characterize the domain growth of demixing processes [2, 13, 30, 12, 3]. Here we also introduce the power $C_{l,\max}$ as a measure for the domain growth. $C_{l,\max}$ is a measure for the dominance of the most predominant pattern (in terms of spherical harmonics) of the function on the sphere.

The position of the maximum is determined, using the standard procedure, via fitting the off-critical fitting function $S(l,t) \propto (l \cdot L_{\mathrm{PS}}(t)/2\pi)^2 \,/\, \left[2 + (l \cdot L_{\mathrm{PS}}(t)/2\pi)^6\right]$ [31] and the average domain size L_{PS} is identified as $R\pi/l_{\max}$.

3.2. Minkowski functionals

Since the early 20th century [16] Minkowski functionals have been known in integral geometry [32, 33] and became a prominent tool for morphological data analysis [34].

They are able to characterize the geometry and shape of structural data as well as their topology and connectedness. Minkowski functionals are sensitive to any n-point correlation function and thus can provide new insights into physical processes beyond the capability of linear methods, e.g. power spectral density measures.

On the two-dimensional sphere $\mathcal{S}^2$ with radius R in $D = 2$ dimensions the $D + 1$ Minkowski functionals $M_\nu, \nu \in \{0, 1, 2\}$ for a set $K \subseteq \mathcal{S}^2$ are the area M_0, the perimeter M_1 and the Euler characteristic M_2. They are defined as:

$$\begin{aligned} M_0(K) &= \int_K \mathrm{d}^2 r \\ M_1(K) &= \frac{1}{4} \int_{\partial K} \mathrm{d}r \\ M_2(K) &= \frac{1}{2\pi} \int_{\partial K} \kappa(r)\, \mathrm{d}r \end{aligned} \tag{10}$$

Here, $\kappa(r)$ is the local Gaussian curvature.

Minkowski functionals are motion invariant, additive and conditionally continuous. They form a complete family of morphological measures. Or vice versa: Any motion invariant, conditionally continuous and additive functional is a superposition of the countably many Minkowski functionals [35]. They are nonlinear measures sensitive to any higher order correlations. They are homogeneous functions of order $D - \nu$:

$$M_\nu(\lambda K) = \lambda^{D-\nu} M_\nu(K) \tag{11}$$

There is a broad range of applications of Minkowski functionals, e.g. curvature energy of membranes [36], order parameter in Turing patterns [37], density functional theory for fluids (as hard balls or ellipsoids) [38, 39], testing point distributions (find clusters, filaments, underlying point-process) or searching for non-Gaussian signatures in the cosmic microwave background [40, 41, 19, 17, 18].

In order to study the morphology of the smooth, scalar density fields $\rho(\mathbf{r}, t^*)$, the Minkowski Functionals (MFs) of the excursion sets K_{th} of the equal area pixelization of the simulation data are calculated. K_{th} is the set of all pixels with density values $\rho(\mathbf{r}, t^*)$ that are higher or at least equal to a threshold value ρ_{th}: $K_{\mathrm{th}} = \{\mathbf{r} \in \mathcal{S}^2 | \rho(\mathbf{r}, t^*) \geq \rho_{\mathrm{th}}\}$. These pixels mark the regions $\mathbf{r}$ on $\mathcal{S}^2$ that have a density $\rho(\mathbf{r}, t^*)$ greater or equal to the threshold density ρ_{th}, at the time t^*.

By running over 101 equidistant threshold steps $\rho_{\mathrm{th},k}$ (with $k \in \{0, ..., 100\}$) the density fields are binarized into an active and a non-active part. The first threshold step $\rho_{\mathrm{th},0}$ is chosen such that every pixel on $\mathcal{S}^2$ is active. The last step $\rho_{\mathrm{th},100}$ is reached when all pixels are excluded and inactive.

For the implementation of the explicit calculation the algorithm proposed in [42] is adapted to compute Minkowski functionals of pixelized maps: Due to the additivity of the MFs the calculation can be performed by the summation of local contributions. Individual pixels are considered to be composed of 4 vertices, 4 edges and their interior area. The total number of active pixels n_s, the number of edges n_e and vertices n_v at

the interface of active and inactive pixels is counted. Then the area M_0, the integral mean curvature (or perimeter) M_1 and the Euler characteristic M_2 can be calculated as sums:

$$\begin{aligned} M_0 &= n_s \\ M_1 &= -4n_s + 2n_e \\ M_2 &= n_s - n_e + n_v. \end{aligned}$$

In order to avoid any double counting of edges or vertices the original field is built up iteratively by adding active pixels to the initially empty temporary field individually. Only if all neighboring pixels have already been built into the temporary field the edges and vertices are added to the total sum. The number of arithmetic operations required to compute the MFs scales linearly with the number of active pixels and the total number of pixels of the image.

4. Results

4.1. Power spectral density

The angular power spectral densities obtained for the DDFT calculations on different sphere sizes R and with different mixture parameters x are presented in the supplementary material.

The graphs for the average domain size, measured as the characteristic length scale $L_{\mathrm{PS}} = R\pi/l_{\max}$, derived from the positions of maximal power spectrum amplitudes $l_{\max}$ are presented in Fig. 3. In these graphs the initial spinodal decomposition phase of nucleation cannot be observed. L_{PS} is blind for the initial demixing stage (exponential growth of density fluctuations) where yet no domain growth can be observed. However, in the coalescence stage, an increase of L_{PS} is found that can be fitted to a power-law. The power law is better reproduced in the large sphere graphs, since they allow for more individual domains, more coalescence events and therefore provide a more constant slope in the log-log plot. The small sphere graphs show plateaus between power law growth. During plateau phases no coalescence of domains happens because of the low number of individual domains on the small sphere. The onset of demixing is much later for the small sphere compared to the large sphere. Also smaller mixture parameters correlate with later times for the onset of demixing. In particular for $R = 2.5R_{11}$ and $x = 0.1$ no demixing is observed during the complete DDFT calculation, ending at $t^* = 10^5$. The domain growth is faster for higher mixture parameters, the exception being $x = 0.1$: Here the demixing processes starts late but domain growth is fast.

4.2. Minkowski functionals

The dependence of the Minkowski functionals on the threshold density ρ_{th} is presented in the supplementary material.

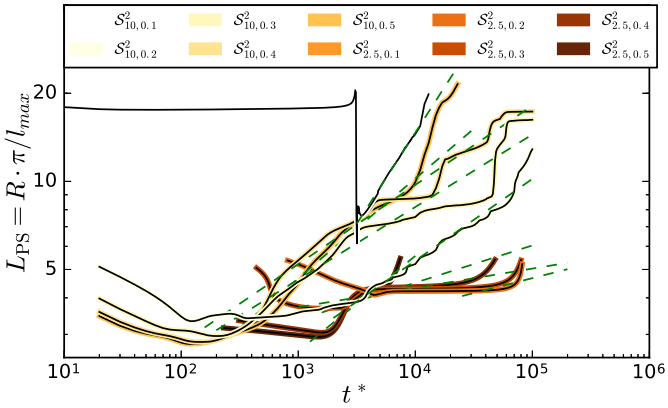

Figure 3. Power spectrum analysis: The characteristic length scale $L_{\mathrm{PS}} = R\pi/l_{\mathrm{max}}$ is identified via the position of the maximum of the angular power spectrum $l_{\mathrm{max}} = l|_{C_l = C_{l,\mathrm{max}}}$. It is the standard measure for the average domain size. Different sphere radii R and mixture parameters x are color coded. Their values are indicated in the legend by $\mathcal{S}^2_{R/R_{11},x}$. $\mathcal{S}^2$ denotes the two-dimensional sphere. As a guide to the eye power-law fits are presented as green dashes lines. The signal for $\mathcal{S}^2_{2.5,0.1}$ is not shown. It is very small since no demixing occurs during the calculation time.

The temporal evolution of the Minkowski functionals is also presented in the supplementary material. Here two plots are shown representatively: Fig. 4 shows the area functional M_0 for the mixing fractions $x = 0.3$ in panel (a) and $x = 0.5$ in panel (b). The relative threshold value $\rho_{\mathrm{th}}/\rho_{\mathrm{th},100}$ is color coded. For early times there is a qualitative difference for the regimes $\rho_{\mathrm{th}}/\rho_{\mathrm{th},100} < x$ and $\rho_{\mathrm{th}}/\rho_{\mathrm{th},100} > x$ for M_0. (Also $M_1(\rho_{\mathrm{th}})$ and $M_2(\rho_{\mathrm{th}})$ have a higher variance in the early time phase during spinodal decomposition. See supplementary material.) The functional at the crossover value $\rho_{\mathrm{th}}/\rho_{\mathrm{th},100} \simeq x$ deviate significantly from the functional values at neighboring threshold values. Any other threshold variations only show small changes in the shape of the curve. In the initial mixture the density is $\rho/\rho_{\mathrm{th},100} \simeq x$, all relative threshold values below x result in almost no active pixels after binarization, but most pixels are active for higher thresholds. This leads to a sharp transition of the Minkowski functionals from detecting almost all pixels as active to detecting almost no active pixels at $\rho_{\mathrm{th}}/\rho_{\mathrm{th},100} \simeq x$. Thus it is easy to detect the composition parameter x via the shape of Minkowski functional curves even only analyzing the initial phase of spinodal decomposition.

After a certain point in time, however, the curves are essentially the same. This point can be identified as the time t_c^* where the spinodal decomposition transitions from the early nucleation stage to the late stage coalescence regime. With these curves t_c^* can easily be determined. In particular using non-morphological measures like e.g. the correlation function the determination of t_c^* proves to be more difficult and computationally expensive [13].

The Minkowski functional graphs obtained on the sphere are in qualitative

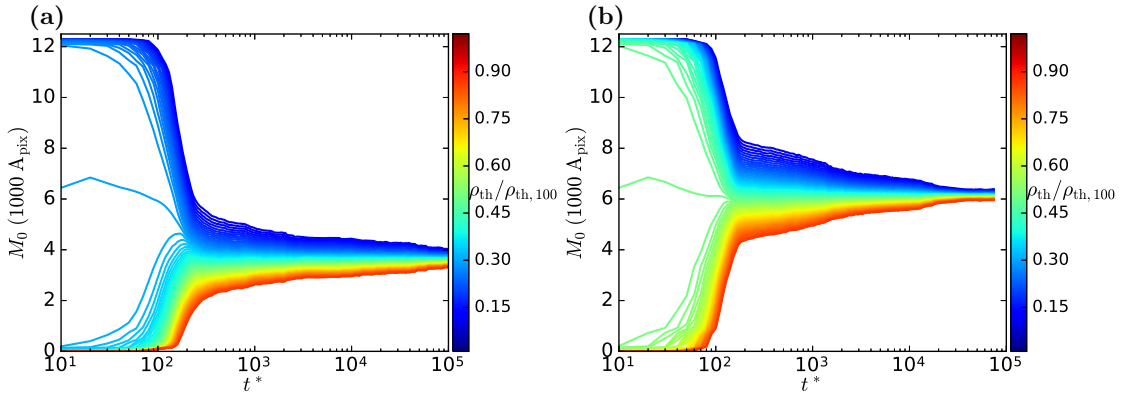

Figure 4. Area Minkowski functional M_0, dependent on the relative threshold density $\rho_{\mathrm{th}}/\rho_{\mathrm{th},100}$, for large sphere $R = 10R_{11}$. Threshold values $\rho_{\mathrm{th}}/\rho_{\mathrm{th},100}$ are color coded. (a) $x = 0.3$, (b) $x = 0.5$.

agreement with Minkowski functional calculated for spinodal decomposition in flat two-dimensional geometry [15, 14].

4.3. Stages during spinodal decomposition

In the following analysis a specific threshold value ρ_{th} is chosen for any DDFT calculation. It is choosen such that the minimal detected number of active pixels is close to 1. (This happens at $\rho_{\mathrm{th}}/\rho_{\mathrm{th},100} \simeq x$.) Then the Minkowski functionals have a maximal dynamic range. These Minkowski functional graphs are presented, for the area functional M_0, in Fig. 5. In all functional graphs both, the spinodal decomposition and the subsequent coalescence stage of demixing can be evidenced. During spinodal decomposition the M_0 area functional follows a power law. In the coalescence stage it assumes a constant value since the individual domains only grow by merging with neighboring domains. M_1 also grows fast during spinodal decomposition. However, during the coalescence stage it drops again, thus providing a means to easily determine the crossover time t_c^*. (Compare Fig. 6, or consult the supplementary material.) We obtain $t_c^* \simeq 2 \cdot 10^2$ in the case of $R = 10R_{11}$ and $t_c^* \simeq 2 \cdot 10^3$ in the case of $R = 2.5R_{11}$.

A difference in the shape of the graphs for the large and small sphere can be observed: In the large sphere graphs M_0 has a small, non-vanishing slope before the main growth phase evidences the initial nucleation. This can not be observed for the small sphere, where the slope changes rapidly from its zero value in the beginning to a high value in the initial nucleation phase of the spinodal decomposition. (M_1 shows the same behavior, shown in the supplementary material.)

In comparison to the power spectrum measure presented in Fig. 3, the Minkowski functional graphs are not as smooth since they are more sensitive to dynamical changes in the structure of density profiles. This allows the Minkowski functionals to detect features of the demixing process that is not accessible via power spectrum

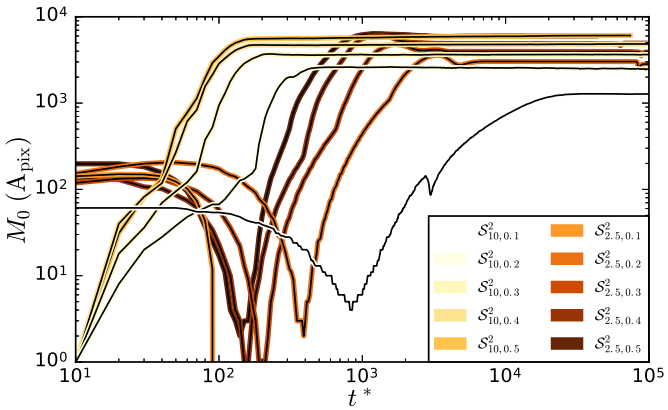

Figure 5. Area Minkowski functional M_0 for threshold values $\rho_{\mathrm{th}}/\rho_{\mathrm{th},100} \simeq x$. Exact threshold values are $\rho_{\mathrm{th}}/\rho_{\mathrm{th},100} \in [0.134, 0.212, 0.316, 0.416, 0.5154]$. Different sphere radii R and mixture parameters x are color coded. Their values are indicated in the legend by $\mathcal{S}^2_{R/R_{11},x}$. $\mathcal{S}^2$ denotes the two-dimensional sphere.

analysis. The Minkowski functionals resolve three distinct phases in the early stage of spinodal decomposition with different domain growth rates: (1) prior to the spinodal decomposition, (2) initial spinodal decompostion, (3) main spinodal decomposition. None of these stages can be detected with the standard demixing metric $L(t)$ obtained by the position of the maximum of the power spectral density as can be seen in Fig. 3. When plotting the maximum of the angular power spectrum $C_{l,\mathrm{max}}$ phases (1) and (2) can also be detected. (Shown in the supplementary material.) Thus, the maximum of the power spectral density is, in contrast to measures obtained by its position, able to detect the density fluctuation growth characteristic to the spinodal decomposition in the early stage of demixing.

The dynamical range of the Minkowski functionals depends only on the resolution of the data, since one can always find a threshold value, such that the minimal number of active pixels is close to one. The upper limit is determined by the number of active pixels after spinodal decomposition which scales with the resolution of the data. The power spectrum analysis does not show such a resolution dependence that provides a higher dynamical range proportional to the resolution. For the power spectral density a higher resolution only provides further modes l.

4.4. Characteristic Length Scale L

Since the Minkowski functional $M_\nu(K)$ are homogeneous function of order $D - \nu$ (Eq. (11)) one can expect a scaling behavior of the Minkowski functionals for the scaling length L:

$$M_0 \propto 1,\ M_1 \propto L^{-1},\ M_2 \propto L^{-2} \tag{12}$$

L can be interpreted as the characteristic size of demixed domains. Note that L can of be defined via different methods, e.g. as the first zero crossing of the correlation function or as the first moment of the wavelength distribution [10, 11]. These widely used methods are, however, computationally expensive [13]. The scaling behavior of $1/M_1 \propto L$ is presented in 6. (For the plot of $1/\sqrt{M_2} \propto L$ consult the supplementary material.) It evidences the power law growth of domain size $L \propto t^{*\alpha}$ during the coalescence phase after spinodal decomposition. The transition from spinodal decomposition to coalescence happens at about $t_c^* \simeq 2 \cdot 10^2$ in the case of $R = 10R_{11}$ and $t_c^* \simeq 2 \cdot 10^3$ in the case of $R = 2.5R_{11}$.

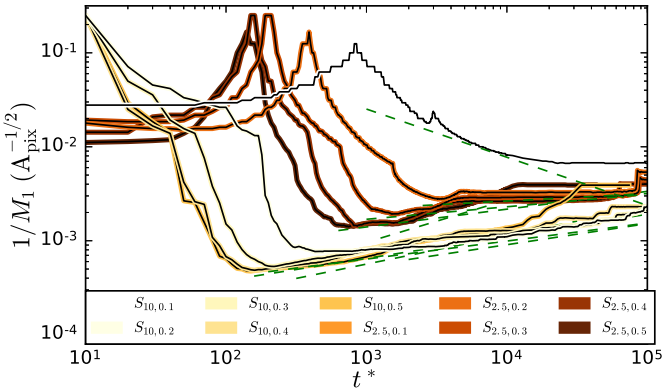

Figure 6. Scaling behaviour of $1/M_1 \propto L$ reveal power law domain growth $L \propto t^{*\alpha}$ after spinodal decomposition. Different sphere radii R and mixture parameters x are color coded. Their values are indicated in the legend by $\mathcal{S}^2_{R/R_{11},x}$. $\mathcal{S}^2$ denotes the two-dimensional sphere. As a guide to the eye power-law fits are presented as green dashes lines. They are shifted in a parallel fashion (by multiplication with the factor 0.8) to enhance visibility.

For the small sphere only few disjoint domains exist and thus only few coalescence events happen where L changes rapidly. The power law can however still be detected via the mean slope in $1/M_1$. For $1/\sqrt{M_2}$ the few coalescence events result in non-smooth graphs resulting in poor linear fits.

Power-law exponents α obtained by linear fits to the domain growth stages ($t^* > t_c^*$) in Fig. 3 and Fig. 6 are presented in table 1 for the large sphere and respectively in table 2 for the small sphere. Also the fit values for the power spectrum measures, the total power $(2l+1)C_{l,\max}$ and the average domain size L_{PS} are presented. Uncertainties are given by the fit routine. Statistics generally are better for the Minkowski functionals, in particular $1/M_1$ gives the smallest statistical errors and provides the most comparable curves to a power-law. The angular power spectral density based measures have high uncertainties and in particular for the small sphere they only provide few curves that allow for a power-law fit.

The power-law exponents are found to be close to $\alpha \simeq 0.2$. This is close to the predicted value in [43]. It is smaller than the value of 1/3 that is predicted in the

diffusive domain growth regime of the Lifshitz-Slyozov growth law [44, 30]. Only in the case of the mixture parameter $x = 0.5$ the power-law exponent gets close to the prediction in the diffusive regime.

Table 1. Power-law exponent α during domain growth phase for the large sphere $R = 10R_{11}$. Values are obtained via linear fits in the log-log plots in Fig. 3 and Fig. 6 for $t^* > t_c^*$.

$10000 \cdot \alpha$ for $R = 10R_{11}$				
	$(2l+1)C_{l,\max}$	L_{PS}	$1/M_1$	$1/\sqrt{M_2}$
$x = 0.1$	–	6221 ± 23	–	–
$x = 0.2$	2240 ± 24	2155 ± 24	2245 ± 13	2178 ± 13
$x = 0.3$	2304 ± 23	2321 ± 27	1921 ± 12	1651 ± 19
$x = 0.4$	2676 ± 28	2531 ± 28	2351 ± 14	2069 ± 26
$x = 0.5$	2190 ± 57	2897 ± 38	3052 ± 21	946 ± 47

Table 2. Power-law exponent α during domain growth phase for the small sphere $R = 2.5R_{11}$. Values are obtained via linear fits in the log-log plots in Fig. 3 and Fig. 6 for $t^* > t_c^*$.

$10000 \cdot \alpha$ for $R = 2.5R_{11}$				
	$(2l+1)C_{l,\max}$	L_{PS}	$1/M_1$	$1/\sqrt{M_2}$
$x = 0.1$	–	–	–	–
$x = 0.2$	–	1320 ± 160	792 ± 29	1200 ± 210
$x = 0.3$	–	–	1330 ± 30	1000 ± 200
$x = 0.4$	–	1500 ± 30	1894 ± 32	2230 ± 210
$x = 0.5$	3254 ± 38	4511 ± 19	3052 ± 21	–

4.5. Hints towards universal behavior

Motivated by findings in [3] universal features in the demixing behavior on spherical geometries are investigated. We hypothesise that the temporal development of the structure parameters becomes independent of the mixture parameter and sphere size by a suitable rescaling of axis. The rescaled time t_{r}^* is a function $t_{\mathrm{r}}^* = f(t^*, x, R)$ and the rescaled measures m_r are transformed via $m_r = g(M, x, R)$ for different measures M. The specific scalings are obtained by empirically testing simple functions f and g. In order to remove possible scaling effects due to the mixture parameter x and the sphere size R, that influence the otherwise universal dynamics, the simplest rescaling functions are products of the form $f(t^*, x, R) = t^* x^{\omega} (R/R_{11})^{\Omega}$ and $g(M, x, R) = M x^{\sigma} (R/R_{11})^{\Sigma}$ with real exponents $\omega, \Omega, \sigma, \Sigma \in \mathbb{R}$. We find universal behavior for the Minkowski

functionals M_0 and M_1. This is presented in Fig. 7 where, after rescaling, the graphs for M_0 and M_1 coincide well for all sphere sizes and mixture parameters $x > 0.1$. The time axis was scaled by $t^* \to t^* \cdot x^{-2/3} \cdot (R/R_{11})^{3/2}$. M_0 was scaled by the mixture parameter as $M_0 \to M_0/x$ in Fig. 7 (b). M_1 was scaled by the mixture parameter and the sphere Radius as $M_1 \to M_1/\sqrt{x}/(R/R_{11})^{0.8}$ in Fig. 7 (c). This hints towards a universal demixing behavior for these systems. Only the graphs for $x = 0.1$ show a different behavior due to their very late start of the demixing process and thus may have qualitatively different demixing behavior. The specific scaling of axis is obtained by empirical testing of simple functions.

For the power spectral measures no rescaling of the axis could be found that leads to uniform graphs, see Fig. 7 (a). Since this could easily be achieved via Minkowski functional measures this suggests that nonlinear properties play a role in the demixing process and that hence nonlinear measures, such as the Minkowski functionals, are a more suitable means for the analysis of demixing processes.

5. Conclusion and Outlook

An angular power spectrum analysis for DDFT calculations of the demixing processes on a sphere is able to detect different stages in the demixing process: The onset of spinodal decomposition, the main spinodal decomposition stage and the coalescence stage after spinodal decomposition. A scale-free power law growth $L \propto t^\alpha$ could be found for the domain size of demixed domains in the coalescence stage. The onset of the main spinodal decomposition phase is much later on the small sphere with $R = 2.5R_{11}$ compared to the large sphere with $R = 10R_{11}$. The same behavior is found for the crossover time between spinodal decomposition and coalescence. Also the mixture parameter x influences these times: Smaller x shifts the onset of the spinodal decomposition and also the crossover time to coalescence to later times. In the large sphere case many nucleation sites in the spinodal decomposition phase provide a large number of initially demixed domains. Thus during the growth and coalescence phase the domain size power law yields a smooth function. However, in the small sphere case only few nucleation sites exist and therefore also only few initially demixed domains exist after spinodal decomposition and prior to coalescence. This leads to a worse statistic in detecting the domain growth power law in the case of the small sphere.

The main spinodal decomposition stage cannot be detected with the standard method of analyzing the average domain size L_{PS} provided by the structure factor $S(l, t)$. This measure is only responsive to the domain coalescence in the late stage of demixing. Using the maximum of the the structure factor, the power $(2l + 1)C_{l,\max}$, one can observe the spinodal decomposition stage prior to the coalescence of domains. The Minkowski functionals provide even further insight: they reveal that the main spinodal decomposition stage actually is composed of two parts: at first the functional measures M_0 and M_1 show a slow growth and after a specific value start to grow faster until the beginning of the coalescence stage. Minkowski functionals are able to resolve

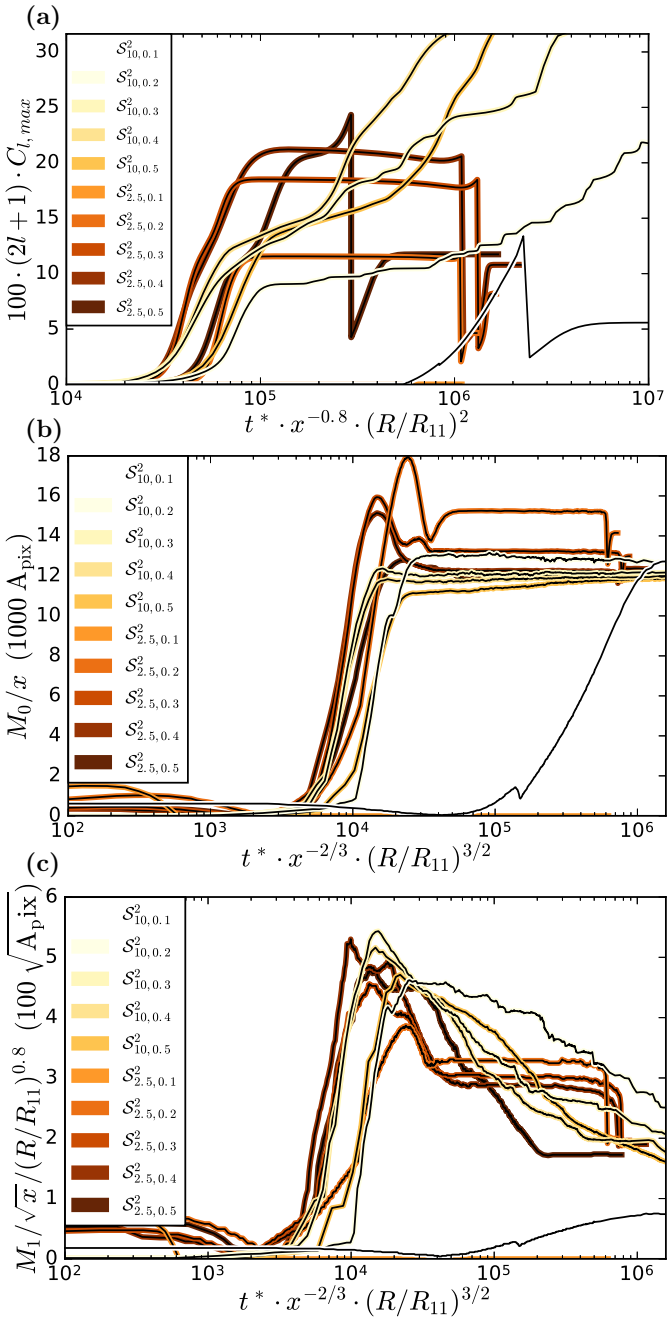

Figure 7. After a rescaling of axis hints of universal behavior are found in panel (b) for M_0 and in panel (c) for M_1. However, in panel (a), no universal behavior is found for power spectral density $(2l+1) \cdot C_{l,\max}$. Different sphere radii R and mixture parameters x are color coded. Their values are indicated in the legend by $\mathcal{S}^2_{R/R_{11},x}$. $\mathcal{S}^2$ denotes the two-dimensional sphere.

a further level of detail in the spinodal decomposition process. A systematic evaluation of the Minkowski functionals on further demixing systems might shed new light on the

early stage spinodal decompostion dynamics.

Another advantage of Minkowski functionals is their scaling behavior during the coalescence stage: The domain growth power-laws are reproduced with higher precision than using the angular power spectrum method. The Minkowski functionals seem to be a convenient measure to efficiently determine domain growth power-law exponents and shed light on a possible connection between the growth rate and the domain morphology.

The Minkowski functionals allow the precise measurement of the mixture parameter x only observing the early stage spinodal decomposition without knowledge of the demixed end state. Since the density in the initial mixture is $\rho/\rho_{\mathrm{th},100} \simeq x$, all relative threshold values below x result in almost no pixels being active after binarization, but almost all pixels are active for higher thresholds. This leads to a sharp transition of the value of the Minkowski functionals at $\rho_{\mathrm{th}}/\rho_{\mathrm{th},100} \simeq x$.

The most interesting new insight gained by a morphological Minkowski functional analysis is their universal behavior. By applying a suitable rescaling, all Minkowski functionals collapse onto a single master curve. The only exception being the curve for the smallest mixture parameter $x = 0.1$, suggesting a qualitatively different demixing scenario with a much later onset of phase separation. For higher mixture parameters this shows that the analysed demixing process has a universal, parameter independent domain evolution. For the angular power spectrum measures no suitable rescaling of the axis could be found. This suggests that nonlinear properties play an important role in the demixing process and thus that the inherently nonlinear Minkowski functionals are a suitable tool for the characterization of this process. In further studies we will use surrogates [17, 18, 19] in order to disentangle the linear and nonlinear effects of the demixing process and their impact on the behavior of the Minkowski functionals.

This result immediately suggest further analysis of the binary demixing system on spherical geometry: What are the differences between the low and high mixture parameter classes and how is the transition between these classes? Other questions worth of further examination are: Is this behavior influenced by the interaction potential, and is there a connection to the flat three-dimensional case?

Hints towards universal behavior in demixing systems via Minkowski functional (and tensor) analysis were already discovered in previous studies [3]. Here simulations of a three dimensional system with a binary complex plasma were analysed. A universal behavior was found for different screening length rations of a double Yukawa interaction potential. There, also an exception of the universal behavior was found for a single screening length interaction potential. Further investigation of the universal behavior of demixing processes on various geometries, boundary conditions and with various interaction potentials are vital in order to obtain a thorough understanding of the fundamental properties of demixing systems. The preliminary analyses in this work and in [3] suggest that further investigation will lead to deeper insight into the physical mechanisms of the demixing of binary systems.

Applying higher ranked (tensor) Minkowski valuations to demixing DDFT calculations on spherical geometries in further studies may shed further light on

the features of the universal properties of the demixing process. Tensor Minkowski functional on the two-sphere $\mathcal{S}^2$ were introduced and applied in [45, 46]. Higher ranked Minkowski tensor measures already proved to be useful in characterizing the solid-liquid phase transition in a two-dimensional flat complex plasma [47]. Also the resolution of the DDFT calculations can be significantly improved in further studies.

This study gives further evidence that Minkowski functional methods are a powerful tool for morphological characterization of physical processes. They are superior to conventional analysis methods in various respects: They directly provide information on the morphology of structures, are inherently nonlinear, and are fast and easy to compute (by only counting pixels) compared to correlation function measures. They allow the measurement of the characteristic length scale L with high statistical reliability even for low resolution data. Minkowski functional analysis is able to quickly reveal new aspects of interest in particular in nonlinear (non-Gaussian) data. It is founded on a solid mathematical framework, however it still provides easily interpretable results.

ACKNOWLEDGMENTS

We thank I. Laut for carefully checking this manuscript. A. Böbel was funded by the StMWi. M. C. Bott acknowledges funding provided by the Swiss National Science Foundation through the National Center of Competence in Research Bio-Inspired Materials.

References

[1] JD Gunton M Miguel P S 1983 The dynamics of first order phase transitions *Phase Transitions and Critical Phenomena* ed C Domb J (New York: Academic Press)

[2] Bray A J 1994 *Advances in Physics* **43** 357–459 URL https://doi.org/10.1080/00018739400101505

[3] Böbel A and Räth C 2016 *Phys. Rev. E* **94**(1) 013201 URL https://link.aps.org/doi/10.1103/PhysRevE.94.013201

[4] Li W H and Lee J 1994 *Physica A: Statistical Mechanics and its Applications* **202** 165 – 174 ISSN 0378-4371 URL http://www.sciencedirect.com/science/article/pii/0378437194901724

[5] Lee J 1994 *Physica A: Statistical Mechanics and its Applications* **210** 127 – 138 ISSN 0378-4371 URL http://www.sciencedirect.com/science/article/pii/0378437194001111

[6] Bott M C and Brader J M 2016 *Phys. Rev. E* **94**(1) 012603 URL https://link.aps.org/doi/10.1103/PhysRevE.94.012603

[7] Guerra R E, Kelleher C P, Hollingsworth A D and Chaikin P M 2018 *Nature* **554** 346 EP – URL http://dx.doi.org/10.1038/nature25468

[8] Soni V, Gómez L R and Irvine W T M 2018 *Phys. Rev. X* **8**(1) 011039 URL https://link.aps.org/doi/10.1103/PhysRevX.8.011039

[9] Krause A L, Burton A M, Fadai N T and Van Gorder R A 2018 *Phys. Rev. E* **97**(4) 042215 URL https://link.aps.org/doi/10.1103/PhysRevE.97.042215

[10] Stanley H E 1987 *Introduction to Phase Transitions and Critical Phenomena*

[11] Allen M P and Tildesley D J 1987 *Computer Simulation of Liquids* (New York: Oxford University Press)

[12] Wysocki A, Räth C, Ivlev A V, Sütterlin K R, Thomas H M, Khrapak S, Zhdanov S, Fortov V E,

Lipaev A M, Molotkov V I, Petrov O F, Löwen H and Morfill G E 2010 *Phys. Rev. Lett.* **105**(4) 045001 URL http://link.aps.org/doi/10.1103/PhysRevLett.105.045001

[13] Velasco E and Toxvaerd S 1996 *Phys. Rev. E* **54**(1) 605–610 URL https://link.aps.org/doi/10.1103/PhysRevE.54.605

[14] Mecke K R and Sofonea V 1997 *Phys. Rev. E* **56**(4) R3761–R3764 URL https://link.aps.org/doi/10.1103/PhysRevE.56.R3761

[15] Sofonea V and Mecke K 1999 *The European Physical Journal B - Condensed Matter and Complex Systems* **8** 99–112 ISSN 1434-6036 URL https://doi.org/10.1007/s100510050672

[16] Minkowski H 1903 *Mathematische Annalen* **57** 447–495 URL http://eudml.org/doc/158108

[17] Rossmanith G, Modest H, Räth C, Banday A J, Górski K M and Morfill G 2012 *Phys. Rev. D* **86**(8) 083005 URL https://link.aps.org/doi/10.1103/PhysRevD.86.083005

[18] Modest H I, Räth C, Banday A J, Rossmanith G, Sütterlin R, Basak S, Delabrouille J, Górski K M and Morfill G E 2013 *Monthly Notices of the Royal Astronomical Society* **428** 551–562 URL http://dx.doi.org/10.1093/mnras/sts056

[19] Modest H I, Räth C, Banday A J, Górski K M and Morfill G E 2014 *Phys. Rev. D* **89**(12) 123004 URL https://link.aps.org/doi/10.1103/PhysRevD.89.123004

[20] Stillinger F H 1976 *The Journal of Chemical Physics* **65** 3968 ISSN 0021-9606 URL http://dx.doi.org/10.1063/1.432891

[21] Archer A J and Evans R 2001 *Phys. Rev. E* **64** ISSN 1095-3787 URL http://dx.doi.org/10.1103/PhysRevE.64.041501

[22] Louis A A, Bolhuis P G and Hansen J P 2000 *Phys. Rev. E* **62** 79617972 ISSN 1095-3787 URL http://dx.doi.org/10.1103/PhysRevE.62.7961

[23] Archer A J and Evans R 2004 *The Journal of Chemical Physics* **121** 4246–4254 (*Preprint* https://doi.org/10.1063/1.1778374) URL https://doi.org/10.1063/1.1778374

[24] Marconi U M B and Tarazona P 1999 *The Journal of Chemical Physics* **110** 8032 ISSN 0021-9606 URL http://dx.doi.org/10.1063/1.478705

[25] Driscoll J and Healy D 1994 *Advances in Applied Mathematics* **15** 202250 ISSN 0196-8858 URL http://dx.doi.org/10.1006/aama.1994.1008

[26] Onuki A 2002 *Phase transition dynamics* (Cambridge University Press)

[27] *see supplementary material at [...]*

[28] *https://healpy.readthedocs.io* URL https://healpy.readthedocs.io

[29] Górski K M, Hivon E, Banday A J, Wandelt B D, Hansen F K, Reinecke M and Bartelmann M 2005 *The Astrophysical Journal* **622** 759 URL http://stacks.iop.org/0004-637X/622/i=2/a=759

[30] Thakre A K, den Otter W K and Briels W J 2008 *Phys. Rev. E* **77**(1) 011503 URL http://link.aps.org/doi/10.1103/PhysRevE.77.011503

[31] Furukawa H 1984 *Physica A: Statistical Mechanics and its Applications* **123** 497 – 515 ISSN 0378-4371 URL http://www.sciencedirect.com/science/article/pii/0378437184901687

[32] Weil W 1983 *Stereology: A Survey for Geometers* (Basel: Birkhäuser Basel) pp 360–412 ISBN 978-3-0348-5858-8 URL https://doi.org/10.1007/978-3-0348-5858-8_15

[33] Schneider R 2013 *Convex Bodies: The BrunnMinkowski Theory* 2nd ed Encyclopedia of Mathematics and its Applications (Cambridge University Press)

[34] Mecke K R, Buchert T and Wagner H 1994 *Astron. Astrophys.* **288** 697–704 URL http://adsabs.harvard.edu/abs/1994A%26A...288..697M

[35] Hadwiger H 1957 *Vorlesungen über Inhalt, Oberfläche und Isoperimetrie* (Berlin: Springer-Verlag)

[36] Helfrich W 1973 *Z. Naturforsch.* **28c** 693703

[37] Mecke K R 1996 *Phys. Rev. E* **53** 4794–4800 URL http://link.aps.org/doi/10.1103/PhysRevE.53.4794

[38] Rosenfeld Y 1995 *Mol. Phys.* **86** 637–647 URL http://dx.doi.org/10.1080/00268979500102241

[39] Mecke K 2000 Additivity, convexity and beyond: Applications of minkowski functionals in statistical physics *Statistical Physics and Spatial Statistics* (*Lecture Notes in Physics* vol 554) ed K R Mecke D S (Springer Berlin Heidelberg) pp 111–184 ISBN 978-3-540-67750-5 URL

http://dx.doi.org/10.1007/3-540-45043-2_6

[40] Schmalzing J and Górski K M 1998 *Monthly Notices of the Royal Astronomical Society* **297** 355–365 URL http://dx.doi.org/10.1046/j.1365-8711.1998.01467.x

[41] Winitzki S and Kosowsky A 1998 *New Astronomy* **3** 75 – 99 ISSN 1384-1076 URL http://www.sciencedirect.com/science/article/pii/S1384107697000468

[42] Michielsen K and Raedt H D 2001 *Physics Reports* **347** 461 – 538 ISSN 0370-1573 URL http://www.sciencedirect.com/science/article/pii/S037015730000106X

[43] Binder K and Stauffer D 1974 *Phys. Rev. Lett.* **33**(17) 1006–1009 URL https://link.aps.org/doi/10.1103/PhysRevLett.33.1006

[44] Lifshitz I and Slyozov V 1961 *Journal of Physics and Chemistry of Solids* **19** 35 – 50 ISSN 0022-3697 URL http://www.sciencedirect.com/science/article/pii/0022369761900543

[45] Chingangbam P, Yogendran K, Joby P, Ganesan V, Appleby S and Park C 2017 *Journal of Cosmology and Astroparticle Physics* **2017** 023 URL http://stacks.iop.org/1475-7516/2017/i=12/a=023

[46] Ganesan V and Chingangbam P 2017 *Journal of Cosmology and Astroparticle Physics* **2017** 023 URL http://stacks.iop.org/1475-7516/2017/i=06/a=023

[47] Böbel A, Knapek C A and Räth C 2018 *Phys. Rev. E* **97**(5) 053201 URL https://link.aps.org/doi/10.1103/PhysRevE.97.053201

Bibliography

[1] *http://scikit-learn.org*. 59

[2] *https://healpy.readthedocs.io*. 76

[3] D.G.A.L. Aarts, R.P.A. Dullens und H.N.W. Lekkerkerker, *New. J. Phys.* **7** (2005), 40. 39, 68

[4] F.F. Abraham, *The Journal of Chemical Physics* **64** (1976), 2660. 17

[5] J.M. Aguilera und P.J. Lillford: *Food Materials Science: Principles and Practice*. Food Engineering Series. Springer, New York, 2007. 1, 33

[6] S. Alesker, *Geometriae Dedicata* **74** (1999), 241. 2, 49

[7] J. Allen, *Physica Scripta* **45** (1992), 497. 26

[8] S.M. Allen, *Acta Metall.* **27** (1979), 1085. 17

[9] A.V.G. Alpert Y. L. und L.P. Pitaevsky: *Space physics with artificial satellites*. Consultants Bureau, New York, 1965. 27

[10] A.J. Archer und R. Evans, *Phys. Rev. E* **64** (2001). 30

[11] A.J. Archer und R. Evans, *J. Phys.: Condens. Matter* **14** (2002), 11311141. 30

[12] A.J. Archer und R. Evans, *The Journal of Chemical Physics* **118** (2003), 9726. 4, 29, 30, 76

[13] A.J. Archer und R. Evans, *The Journal of Chemical Physics* **121** (2004), 4246. 31

[14] A.J. Archer, R. Evans, R. Roth und M. Oettel, *The Journal of Chemical Physics* **122** (2005), 084513. 30

[15] A.J. Archer, C.N. Likos und R. Evans, *J. Phys.: Condens. Matter* **16** (2004), L297L303. 30

[16] A.J. Archer, M. Schmidt und R. Evans, *Phys. Rev. E* **73** (2006). 30

[17] M. Baaden, R. Schurhammer und G. Wipff, *The Journal of Physical Chemistry B* **106** (2002), 434. 4

[18] M. Barbosa, R. Natoli, K. Valter, J. Provis und T. Maddess, *Biomedical optics express* **5** (2014), 2317. 33

[19] T. Baum, M. Gräbeldinger, C. Räth, E.G. Garcia, R. Burgkart, J.M. Patsch, E.J. Rummeny, T.M. Link und J.S. Bauer, *Journal of bone and mineral metabolism* **32** (2014), 56. 1, 33

[20] C. Beisbart, M.S. Barbosa, H. Wagner und L.d.F. Costa, *The European Physical Journal B-Condensed Matter and Complex Systems* **52** (2006), 531. 33

[21] K. Binder, *Physical Review B* **15** (1977), 4425. 20

[22] K. Binder, *Reports on progress in physics* **50** (1987), 783. 4, 20

[23] K. Binder und D. Stauffer, *Phys. Rev. Lett.* **33** (1974), 1006. 84

[24] A. Böbel, C.A. Knapek und C. Räth, *Phys. Rev. E* **97** (2018), 053201. vii, 14, 25, 57, 108

[25] A. Böbel und C. Räth, *Phys. Rev. E* **94** (2016), 013201. vii, 21, 41, 49, 67, 125

[26] M.C. Bott und J.M. Brader, *Phys. Rev. E* **94** (2016), 012603. 4, 29, 31, 75

[27] G. Box und G. Jenkins: *Time Series Analysis, Forecasting and Control.* Holden-Day, San Francisco, 1976. 34

[28] A. Bray, *Journal of Physics A: Mathematical and General* **23** (1990), L67. 17

[29] A.J. Bray, *Advances in Physics* **43** (1994), 357. 41

[30] A.J. Bray, *Advances in Physics* **51** (2002), 481. 16, 18, 19

[31] I. Buttinoni, J. Bialké, F. Kümmel, H. Löwen, C. Bechinger und T. Speck, *Phys. Rev. Lett.* **110** (2013), 238301. 4

[32] J. Cahn, *J. Chem. Phys.* **31** (1959), 688. 17

[33] J.W. Cahn, *Acta metallurgica* **9** (1961), 795. 17

[34] M. Chaudhuri, S. Khrapak und G. Morfill, *Physics of Plasmas* **15** (2008), 053703. 27

[35] F.F. Chen und S.E. von Goeler, *Physics Today* **38** (1985), 87. 23

[36] J. Chu und I. Lin, *Phys. Rev. Lett.* **72** (1994), 4009. 23, 24

[37] S. Chui, *Physical Review B* **28** (1983), 178. 3

[38] P.M. Chung, L. Talbot und K.J. Touryan: *Electric probes in stationary and flowing plasmas: theory and application*, Band 11. Springer Science & Business Media, 2013. 26

[39] S.C. Cowin und S.B. Doty: *Tissue mechanics*. Springer Science & Business Media, 2007. 1, 33

[40] J. Daugherty, R. Porteous, M. Kilgore und D. Graves, *Journal of applied physics* **72** (1992), 3934. 26

[41] A. Derossi, T. De Pilli und C. Severini, *Food biophysics* **7** (2012), 258. 1, 33

[42] J.K. Dhont, *The Journal of chemical physics* **105** (1996), 5112. 17

[43] C. Dietz, T. Kretz und M.H. Thoma, *Phys. Rev. E* **96** (2017), 011301. 3, 49

[44] G. Dougherty: *Medical image processing: techniques and applications*. Springer Science & Business Media, 2011. 1, 33

[45] J. Driscoll und D. Healy, *Advances in Applied Mathematics* **15** (1994), 202250. 31

[46] D. Else, R. Kompaneets und S. Vladimirov, *Physical Review E* **80** (2009), 016403. 27

[47] D.L. Ermak und H. Buckholz, *Journal of Computational Physics* **35** (1980), 169. 68

[48] R. Evans und M. Telo da Gama, *Molecular Physics* **38** (1979), 687. 17, 19

[49] P.M. Falcone, A. Baiano, F. Zanini, L. Mancini, G. Tromba, D. Dreossi, F. Montanari, N. Scuor und M.A.D. Nobile, *Journal of Food Science* **70** (2005), E265. 1, 33

[50] F.J. Fattoyev, C.J. Horowitz und B. Schuetrumpf, *Phys. Rev. C* **95** (2017), 055804. 1, 33

[51] A. Filippov, A. Zagorodny, A. Momot, A. Pal und A. Starostin, *Journal of Experimental and Theoretical Physics* **104** (2007), 147. 27

[52] V.E. Fortov, A.V. Ivlev, S.A. Khrapak, A.G. Khrapak und G.E. Morfill, *Phys. Rep.* (2005). 3, 4, 23

[53] J. Frenkel: *Kinetic Theory of Liquids*. Dover Publications. Dover, 1955. 3, 10, 12

[54] H. Furukawa, *Physica A: Statistical Mechanics and its Applications* **123** (1984), 497 . 39, 40, 41, 68

[55] J.W. Gibbs, *Transactions of the Connecticut Academy of Arts and Sciences* **3** (1874-78), 108. 15

[56] J. Goldstone, A. Salam und S. Weinberg, *Physical Review* **127** (1962), 965. 7

[57] J. Goree, *Plasma Sources Science and Technology* **3** (1994), 400. 26

[58] K.M. Górski, E. Hivon, A.J. Banday, B.D. Wandelt, F.K. Hansen, M. Reinecke und M. Bartelmann, *The Astrophysical Journal* **622** (2005), 759. 76

[59] C.C. Grimes und G. Adams, *Phys. Rev. Lett.* **42** (1979), 795. 3, 24

[60] R.E. Guerra, C.P. Kelleher, A.D. Hollingsworth und P.M. Chaikin, *Nature* **554** (2018), 346 EP . 4, 75

[61] H. Hadwiger: *Vorlesungen über Inhalt, Oberfläche und Isoperimetrie.* Springer-Verlag, Berlin, 1957. 45

[62] Z. Hadzibabic, P. Krüger, M. Cheneau, B. Battelier und J. Dalibard, *Nature* **441** (2006), 1118. 3, 24

[63] B.I. Halperin und D.R. Nelson, *Phys. Rev. Lett.* **41** (1978), 121. 3, 7, 37

[64] J.P. Hansen und H. Löwen, *Annual Review of Physical Chemistry* **51** (2000), 209. 4

[65] J.P. Hansen und I.R. McDonald: *Theory of simple liquids.* Elsevier, 1990. 4, 20, 21

[66] P. Hartmann, A. Douglass, J.C. Reyes, L.S. Matthews, T.W. Hyde, A. Kovács und Z. Donkó, *Phys. Rev. Lett.* **105** (2010), 115004. 3

[67] Y. Hayashi und K. Tachibana, *Japanese journal of applied physics* **33** (1994), L804. 23, 24

[68] P. Heiney, R. Birgeneau, G. Brown, P. Horn, D. Moncton und P. Stephens, *Physical Review Letters* **48** (1982), 104. 3, 24

[69] W. Helfrich, *Z. Naturforsch.* **28c** (1973), 693703. 2, 45

[70] P. Hopkins, A.J. Archer und R. Evans, *The Journal of chemical physics* **124** (2006), 054503. 21

[71] J. Hörrmann, D. Hug, M.A. Klatt und K. Mecke, *Adv. Appl. Math.* **55** (2014), 48 . 3, 49

[72] S. Hyde, Z. Blum, T. Landh, S. Lidin, B. Ninham, S. Andersson und K. Larsson: *The language of shape: the role of curvature in condensed matter: physics, chemistry and biology.* Elsevier, 1996. 2, 33

[73] H. Ikezi, *Phys. Fluids* **29** (1986), 1764. 24

[74] A. Ivlev, L. Hartmut, G. Morfill, C.P. Royall et al. : *Complex plasmas and colloidal dispersions: particle-resolved studies of classical liquids and solids*, Band 5. World Scientific Publishing Company, 2012. 3, 4, 20, 23

[75] A.V. Ivlev, S.K. Zhdanov, H.M. Thomas und G.E. Morfill, *EPL* **85** (2009), 45001. 4

[76] P.S. J.D. Gunton, M. Miguel. In *Phase Transitions and Critical Phenomena*, herausgegeben von J. C. Domb, Band 8. Academic Press, New York (1983), Seite 267. 16, 17

[77] K. Jiang, L.J. Hou, A.V. Ivlev, Y.F. Li, C.R. Du, H.M. Thomas, G.E. Morfill und K.R. Sütterlin, *EPL* **93** (2011), 55001. 68

[78] Y. Jiao, T. Lau, H. Hatzikirou, M. Meyer-Hermann, J.C. Corbo und S. Torquato, *Physical Review E* **89** (2014), 022721. 33

[79] B. Julesz, *Nature* **290** (1981), 91. 43

[80] B. Julesz, *Rev. Mod. Phys.* **63** (1991), 735. 43

[81] S. Kapfer: Friedrich-Alexander-Universität Erlangen-Nürnberg (FAU), Ph.d thesis, 2012. 55

[82] S.C. Kapfer, W. Mickel, K. Mecke und G.E. Schröder-Turk, *Phys. Rev. E* **85** (2012), 030301. 3, 49, 53

[83] A. Kashlinsky und B.J. Jones, *Nature* **349** (1991), 753. 1, 33

[84] S. Khrapak und G. Morfill, *Physics of plasmas* **13** (2006), 104506. 27

[85] S.A. Khrapak, A.V. Ivlev und G.E. Morfill, *Physical Review E* **70** (2004), 056405. 26

[86] S.A. Khrapak, A.V. Ivlev und G.E. Morfill, *Phys. Plasmas* **17** (2010). 27

[87] S.A. Khrapak, B.A. Klumov und G.E. Morfill, *Phys. Rev. Lett.* **100** (2008), 225003. 4

[88] C. Killer, T. Bockwoldt, S. Schütt, M. Himpel, A. Melzer und A. Piel, *Phys. Rev. Lett.* **116** (2016), 115002. 4

[89] M.A. Klatt: Friedrich-Alexander-Universität Erlangen-Nürnberg (FAU), Ph.d thesis, 2016. 1, 33

[90] M.A. Klatt, G.E. Schröder-Turk und K. Mecke, *Med. Phys.* **44** (2017), 3663. 3, 49

[91] C. Knapek, D. Samsonov, S. Zhdanov, U. Konopka und G. Morfill, *Physical review letters* **98** (2007), 015004. 3

[92] C.A. Knapek: *Phase Transitions in Two-Dimensional Complex Plasmas*. Springer Theses, 1. Auflage. Springer-Verlag Berlin Heidelberg, 2011. 3, 12, 58

[93] C.A. Knapek, C. Durniak, D. Samsonov und G.E. Morfill, *Phys. Rev. Lett.* **110** (2013), 035001. 3, 12, 57

[94] J.M. Kosterlitz und D.J. Thouless, *Journal of Physics C: Solid State Physics* **6** (1973), 1181. 3, 7

[95] A.L. Krause, A.M. Burton, N.T. Fadai und R.A. Van Gorder, *Phys. Rev. E* **97** (2018), 042215. 5, 75

[96] S. Kumari, A.S. Nunes, N.A. Araújo und M.M. Telo da Gama, *The Journal of Chemical Physics* **147** (2017), 174702. 4

[97] M. Lampe, G. Joyce, G. Ganguli und V. Gavrishchaka, *Physics of plasmas* **7** (2000), 3851. 27

[98] L.D. Landau, E.M. Lifshitz und L. Pitaevskii: *Statistical physics, part I*. Pergamon, Oxford, 1980. 15, 16, 21

[99] J. Langer, *Physica* **73** (1974), 61. 20

[100] J. Langer, M. Bar-On und H.D. Miller, *Physical Review A* **11** (1975), 1417. 20

[101] J.L. Lebowitz und O. Penrose, *Journal of Mathematical Physics* **7** (1966), 98. 20

[102] J. Lee, *Physica A: Statistical Mechanics and its Applications* **210** (1994), 127 . 4

[103] W.H. Li und J. Lee, *Physica A: Statistical Mechanics and its Applications* **202** (1994), 165 . 4

[104] I. Lifshitz und V. Slyozov, *Journal of Physics and Chemistry of Solids* **19** (1961), 35 . 19, 84

[105] E. Lima, P. Pereira, H. Löwen und S. Apolinario, *Journal of Physics: Condensed Matter* **30** (2018), 325101. 2, 33

[106] F. Lindemann, *Physik. Zeits.* (1910), 609612. 56

[107] B. Liu, J. Goree, V. Nosenko und L. Boufendi, *Phys. Plasmas* **10** (2003), 9. 59

[108] A.A. Louis, P.G. Bolhuis und J.P. Hansen, *Phys. Rev. E* **62** (2000), 79617972. 30

[109] U.M.B. Marconi und P. Tarazona, *The Journal of Chemical Physics* **110** (1999), 8032. 4, 29, 31, 76

[110] J. Marro, A. Bortz, M. Kalos und J. Lebowitz, *Physical Review B* **12** (1975), 2000. 4, 20

[111] S.R. McCandlish, A. Baskaran und M.F. Hagan, *Soft Matter* **8** (2012), 2527. 4

[112] K. Mecke. In *Statistical Physics and Spatial Statistics*, herausgegeben von D. S. K. R. Mecke, Band 554 von *Lecture Notes in Physics*. Springer Berlin Heidelberg (2000), Seiten 111–184. 2, 45

[113] K.R. Mecke, *Phys. Rev. E* **53** (1996), 4794. 2, 45

[114] K.R. Mecke, T. Buchert und H. Wagner, *Astron. Astrophys.* **288** (1994), 697. 2, 44, 45

[115] K.R. Mecke und V. Sofonea, *Phys. Rev. E* **56** (1997), R3761. 84

[116] M. Mehrabadi und C.C. Stephen, *Quart. J. Mech. Appl. Math.* **43** (1990), 15. 55

[117] N.D. Mermin und H. Wagner, *Phys. Rev. Lett.* **17** (1966), 1133. 3, 7, 24

[118] K. Michielsen und H.D. Raedt, *Physics Reports* **347** (2001), 461 . 46, 47, 77

[119] W. Mickel, S.C. Kapfer, G.E. Schröder-Turk und K. Mecke, *J. Chem. Phys.* **138** (2013), 044501. 3, 37

[120] H. Minkowski, *Mathematische Annalen* **57** (1903), 447. 2, 44

[121] H.I. Modest, C. Räth, A.J. Banday, K.M. Górski und G.E. Morfill, *Phys. Rev. D* **89** (2014), 123004. 2, 45, 87

[122] H.I. Modest, C. Räth, A.J. Banday, G. Rossmanith, R. Sütterlin, S. Basak, J. Delabrouille, K.M. Górski und G.E. Morfill, *Monthly Notices of the Royal Astronomical Society* **428** (2013), 551. 2, 45, 87

[123] R. Morf, *Physical Review Letters* **43** (1979), 931. 3, 24

[124] G.E. Morfill und A.V. Ivlev, *Rev. Mod. Phys.* **81** (2009), 1353. 3, 4, 23

[125] G.E. Morfill und A.V. Ivlev, *Rev. Mod. Phys.* **81** (2009), 1353. 3, 12, 65

[126] V. Mukhanov: *Physical foundations of cosmology*. Cambridge university press, 2005. 1, 33

[127] D. Müller, I. Sidorenko, C. Räth und J. Bauer: *Evaluation der trabekulären Knochenstruktur des Skelettsystems anhand von Micro-CT (μCT)-Bilddaten an unterschiedlichen Skelettlokalisationen. Evaluation der trabekulären Knochenstruktur des Skelettsystems anhand von Micro-CT (μCT)-Bilddaten an unterschiedlichen Skelettlokalisationen*, In *RöFo-Fortschritte auf dem Gebiet der Röntgenstrahlen und der bildgebenden Verfahren*, Band 185. (2013) Seite WI_PO36. 1, 33

[128] C. Murray, W. Sprenger und R. Wenk, *Physical Review B* **42** (1990), 688. 3

[129] C.A. Murray und D.H. Van Winkle, *Phys. Rev. Lett.* **58** (1987), 1200. 3

[130] S. Nachtrab, S.C. Kapfer, C.H. Arns, M. Madadi, K. Mecke und G.E. Schröder-Turk, *Advanced Materials* **23** (2011), 2633. 1

[131] D.R. Nelson und B.I. Halperin, *Phys. Rev. B* **19** (1979), 2457. 3, 7, 37

[132] V. Nosenko, S.K. Zhdanov, A.V. Ivlev, C.A. Knapek und G.E. Morfill, *Phys. Rev. Lett.* **103** (2009), 015001. 3, 11

[133] S. Nunomura, J. Goree, S. Hu, X. Wang und A. Bhattacharjee, *Phys. Rev. E* **65** (2002), 066402. 59

[134] A. Onuki: *Phase transition dynamics*. Cambridge University Press, 2002. 16, 17, 18

[135] Q. Ouyang und H.L. Swinney, *Chaos: An Interdisciplinary Journal of Nonlinear Science* **1** (1991), 411. 2, 33

[136] C. Park, J. Yoon und E.L. Thomas, *Polymer* **44** (2003), 6725. 2, 33

[137] L. Pauchard, D. Bonn und J. Meunier, *Nature* **384** (1996), 145 EP . 3, 24

[138] A. Pelissetto und E. Vicari, *Physics Reports* **368** (2002), 549. 16, 84

[139] O. Penrose und J.L. Lebowitz, *Journal of Statistical Physics* **3** (1971), 211. 20

[140] T. Ramakrishnan und M. Yussouff, *Physical Review B* **19** (1979), 2775. 3

[141] C. Räth: *Decoding Complex Structures in Medical Physics, Plasma Physics and Astrophysics*. Ludwig–Maximilians–Universität, habilitation, 2017. 42

[142] C. Räth, T. Baum, R. Monetti, I. Sidorenko, P. Wolf, F. Eckstein, M. Matsuura, E.M. Lochmüller, P.K. Zysset, E.J. Rummeny et al. , *Bone* **57** (2013), 377. 1, 33

[143] N. Rivas, S. Ponce, B. Gallet, D. Risso, R. Soto, P. Cordero und N. Mujica, *Phys. Rev. Lett.* **106** (2011), 088001. 4

[144] Y. Rosenfeld, *Mol. Phys.* **86** (1995), 637. 2, 45

[145] G. Rossmanith, H. Modest, C. Räth, A.J. Banday, K.M. Górski und G. Morfill, *Phys. Rev. D* **86** (2012), 083005. 2, 45, 87

[146] J.S. Rowlinson und F. Swinton: *Liquids and liquid mixtures: Butterworths monographs in chemistry*. Butterworth-Heinemann, 2013. 4, 21

[147] F.M. Schaller, S.C. Kapfer, J.E. Hilton, P.W. Cleary, K. Mecke, C.D. Michele, T. Schilling, M. Saadatfar, M. Schrter, G.W. Delaney und G.E. Schrder-Turk, *EPL* **111** (2015), 24002. 3, 49

[148] J. Schmalzing und K.M. Górski, *Monthly Notices of the Royal Astronomical Society* **297** (1998), 355. 2, 45

[149] R. Schneider: *Convex Bodies: The BrunnMinkowski Theory*. Encyclopedia of Mathematics and its Applications, 2. Auflage. Cambridge University Press, 2013. 2, 44

[150] G. Schröder-Turk, S. Kapfer, B. Breidenbach, C. Beisbart und K. Mecke, *Journal of Microscopy* **238** (2010), 57. 50, 91

[151] G.E. Schröder-Turk, W. Mickel, S.C. Kapfer, M.A. Klatt, F.M. Schaller, M.J.F. Hoffmann, N. Kleppmann, P. Armstrong, A. Inayat, D. Hug, M. Reichelsdorfer, W. Peukert, W. Schwieger und K. Mecke, *Adv. Mat.* **23** (2011), 2535. 3, 49

[152] G.E. Schröder-Turk, W. Mickel, S.C. Kapfer, F.M. Schaller, B. Breidenbach, D. Hug und K. Mecke, *New J. Phys.* **15** (2013), 083028. 2, 48, 52, 91

[153] E.D. Siggia, *Phys. Rev. A* **20** (1979), 595. 19

[154] O. Sigmund und S. Torquato, *Journal of the Mechanics and Physics of Solids* **45** (1997), 1037. 1

[155] V. Sofonea und K. Mecke, *The European Physical Journal B - Condensed Matter and Complex Systems* **8** (1999), 99. 84

[156] V. Soni, L.R. Gómez und W.T.M. Irvine, *Phys. Rev. X* **8** (2018), 011039. 4, 75

[157] P.J. Steinhardt, D.R. Nelson und M. Ronchetti, *Phys. Rev. B* **28** (1983), 784. 3, 36

[158] J. Stenhammar, R. Wittkowski, D. Marenduzzo und M.E. Cates, *Phys. Rev. Lett.* **114** (2015), 018301. 4

[159] F.H. Stillinger, *The Journal of Chemical Physics* **65** (1976), 3968. 4, 29, 30, 76

[160] K.J. Strandburg, *Rev. Mod. Phys.* **60** (1988), 161. 7

[161] Y. Tang, A. Armstrong, R. Mockler und W. Osullivan, *Physical review letters* **62** (1989), 2401. 3

[162] A.K. Thakre, W.K. den Otter und W.J. Briels, *Phys. Rev. E* **77** (2008), 011503. 41, 84

[163] H. Thomas, *Phys. Rev. Lett.* **73** (1994), 652. 23, 24

[164] S. Torquato, *International Journal of Solids and Structures* **37** (2000), 411. 1

[165] S. Torquato: *Random heterogeneous materials: microstructure and macroscopic properties*, Band 16. Springer Science & Business Media, 2013. 1

[166] V.N. Tsytovich, *Physics-Uspekhi* **40** (1997), 53. 27

[167] J.H. Van't Hoff: *Etudes de dynamique chimique*, Band 1. Muller, 1884. 11

[168] B. Vasilić, C.S. Rajapakse und F.W. Wehrli, *Medical physics* **36** (2009), 3280. 1, 33

[169] E. Velasco und S. Toxvaerd, *Phys. Rev. E* **54** (1996), 605. 2, 33, 41

[170] C. Wagner, *Zeitschrift für Elektrochemie, Berichte der Bunsengesellschaft für physikalische Chemie* **65** (1961), 581. 19

[171] D.C. Wallace: *Statistical Physics of Crystals and Liquids*. WORLD SCIENTIFIC, 2003. 35

[172] L.J. Walpole, *J. Phys. D Appl. Phys.* **19** (1986), 457. 53

[173] G. Watanabe, K. Iida und K. Sato, *Nuclear Physics A* **676** (2000), 455. 1, 33

[174] S.N. Weber, C.A. Weber und E. Frey, *Phys. Rev. Lett.* **116** (2016), 058301. 4

[175] W. Weil. *Stereology: A Survey for Geometers*. Birkhäuser Basel, Basel, 1983. Seiten 360–412. 2, 44

[176] P. Whittle: *Hypothesis testing in time series analysis.* Almqvist & Wiksells boktr., Uppsala, 1951. 34

[177] S. Winitzki und A. Kosowsky, *New Astronomy* **3** (1998), 75 . 2, 45

[178] A. Wysocki, C. Räth, A.V. Ivlev, K.R. Sütterlin, H.M. Thomas, S. Khrapak, S. Zhdanov, V.E. Fortov, A.M. Lipaev, V.I. Molotkov, O.F. Petrov, H. Löwen und G.E. Morfill, *Phys. Rev. Lett.* **105** (2010), 045001. 41, 68

[179] A.P. Young, *Phys. Rev. B* **19** (1979), 1855. 3, 7

[180] K. Zahn, R. Lenke und G. Maret, *Phys. Rev. Lett.* **82** (1999), 2721. 3

Danksagung

Mein Dank gilt meiner Frau Lena die mich jederzeit unterstützt hat und die es mir ermöglichte diese Arbeit auch während unserer Familiengründung fertigzustellen. Du bist mir ein unersätzlicher sicherer Hafen, mein Ein und Alles. Meine Tochter Emilia motiviert mich täglich rechtzeitig meine Arbeit zu beenden um sie bald wieder sehen zu können. Mein Engel, ich freue mich schon darauf dass bald auch deine kleine Schwester auf der Welt sein wird.

Auch möchte ich meinen Eltern und Großeltern dafür danken, dass sie mir diese Ausbildung ermöglichten. Eure Bereitschaft bedingungslos in mich zu investieren erfüllt mich mit tiefer Dankbarkeit.

Aller Anfang ist schwer. Doch die in mir bis heute nicht schwindende Begeisterung für die Wissenschaft zu entfachen, vermochten auf unnachahmliche Art und Weise nur die Professoren Christoph Gerz und Michael Sachs, und das bereits zu Beginn meines Studiums. Durch Sie entwickelte ich das analytische Denken, das nötig war um so weit zu kommen. Danke auch an meinen Schwiegervater Friedrich Böbel für kurzfristige und kurzweilige Nachhilfestunden. Während meiner Masterarbeit konnte Filipe Tostevin mir, einem bis dahin hoffnungslosen Fall, das Programmieren nahe bringen und mir damit eine neue spannende Welt eröffnen, vielen Dank.

Danken möchte ich insbesondere meinem Betreuer Christoph Räth für sein Engagement im Voranbringen meiner Doktorarbeit, für die vielen hilfreichen Diskussionen und das sorgfältige Prüfen meiner Arbeiten. Dank dir entstand diese Doktorarbeit und auch dank dir konnte sie einem erfolgreichen Ende zugeführt werden. Meinem Doktorvater Gregor Morfill bin ich zu großem Dank verpflichtet. Seine außergewöhnliche Fähigkeit komplizierte Probleme zu durchschauen und sogleich elegante Lösungen zu erkennen, haben mich weit vorangebracht. Danken möchte ich Ihnen weiter für die Bereitschaft meine Promotion zu vertreten und für die Sicherheit die Sie mir auch in Fragen bezüglich der Formalitäten vermitteln konnten. Hubertus Thomas schenkte mir Vertrauen, indem er mir die Doktorandenstelle am DLR anbot. Du hast mich bei der Fertigstellung meiner Arbeit sowie bei der Vertragsverlängerung immer unterstützt, vielen Dank. Christina Knapek hat mir bei physikalischen Fragestellen immer weiterhelfen können, auch wenn Sie sich doch selbst nie über zu viel Freizeit beklagen konnte. Danke auch für deine Hilfe vor und während der Parabelflugkampagne. Daniel Mohr und Peter Huber standen mir in IT Fragen kompetent zur Seite und haben darüber hinaus jedes Mittagessen mit anregenden Gesprächsthemen aufgewertet. Mein Dank gilt auch allen weiteren, unerwähnten Mitarbeitern der Arbeits-

gruppe Komplexe Plasmen, die immer für ein angenehmes Arbeitsklima gesorgt haben.

Professor Hartmut Löwen war ohne Umschweife bereit kurzfristig das Zweitgutachten zu dieser Dissertation zu verfassen. Vielen Dank für Ihren Einsatz.

I want to thank Professor David Graves for giving me the opportunity to join his group at UC Berkeley as a visiting researcher and Mierk Schwabe for initiating this contact.

Dank Waldemar Wiederspan, Thomas Hopfner und meiner Frau war es mir jederzeit möglich im Taekwondo Training einen überaus willkommenen Ausgleich zur wissenschaftlichen Arbeit zu finden.

Zu guter Letzt sind hier meine "Leidensgenossen" Meike Müller und Erich Zähringer sowie Ingo Laut gesondert zu erwähnen. Dank euch war der Aufenthalt im Büro, allein schon der Stimmung wegen, eine Freude.